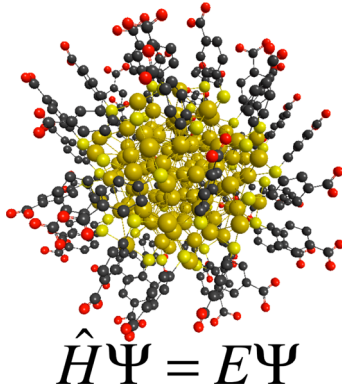


Quantum Mechanical Studies of Large Metal, Metal Oxide, and Metal Chalcogenide Nanoparticles and Clusters

Amendra Fernando, K. L. Dimuthu M. Weerawardene, Natalia V. Karimova, and Christine M. Aikens*

Department of Chemistry, Kansas State University, Manhattan, Kansas 66506, United States



CONTENTS

1. Introduction	B
1.1. General Background	B
1.2. Scope	B
1.3. Theoretical Methods	C
1.4. General Comments	C
2. Transition Metal Clusters	D
2.1. Group 10	D
2.1.1. Ni Clusters	D
2.1.2. Pd Clusters	F
2.1.3. Pt Clusters	I
2.2. Group 11	L
2.2.1. Gold	L
2.2.2. Silver	Q
2.2.3. Copper	U
2.2.4. Thiolate-Protected Gold Nanoparticles	W
2.2.5. Halogen-Stabilized Gold Nanoparticles	AE
2.2.6. Phosphine-Passivated Gold Nanoparticles	AE
2.2.7. Iron–Carbonyl Ligands on Gold Nanoparticles	AG
2.2.8. Thiolate-Protected Silver and Copper Nanoparticles	AH
2.3. Group 12	AH
2.3.1. Zn Clusters	AH
2.3.2. Cd Clusters	AI
2.3.3. Hg Clusters	AI
2.4. Other 3d Transition Metal Clusters	AI
2.4.1. Sc Clusters	AJ
2.4.2. Ti Clusters	AK
2.4.3. V Clusters	AL
2.4.4. Cr Clusters	AM
2.4.5. Mn Clusters	AN
2.4.6. Fe Clusters	AO
2.4.7. Co Clusters	
2.5. Other 4d Transition Metal Clusters	

2.5.1. Ru Clusters	AP
2.5.2. Rh Clusters	AP
2.6. Other 5d Transition Metal Clusters	AR
3. Main Group Metal Clusters	AR
3.1. Group 13	AR
3.1.1. Al Clusters	AR
3.1.2. Ga Clusters	AU
3.2. Group 14	AV
3.2.1. Sn Clusters	AV
3.2.2. Pb Clusters	AW
4. Transition Metal Oxides	AX
4.1. Group 3 Oxides	AX
4.1.1. Scandium Oxides	AX
4.1.2. Yttrium Oxides	AX
4.2. Group 4 Oxides	AY
4.2.1. Titanium Oxides	AY
4.2.2. Zirconium Oxides	BD
4.3. Group 5 Oxides	BE
4.3.1. Vanadium Oxides	BE
4.3.2. Niobium Oxides	BH
4.4. Group 6 Oxides	BH
4.4.1. Chromium Oxides	BH
4.4.2. Molybdenum Oxides	BI
4.4.3. Tungsten Oxides	BI
4.5. Group 7 Oxides	BJ
4.5.1. Manganese Oxides	BJ
4.6. Group 8 Oxides	BM
4.6.1. Iron Oxides	BM
4.6.2. Ruthenium Oxides	BO
4.7. Group 9 Oxides	BO
4.7.1. Cobalt Oxides	BO
4.7.2. Rhodium Oxides	BQ
4.7.3. Iridium Oxides	BQ
4.8. Group 10 Oxides	BR
4.8.1. Nickel Oxides	BR
4.8.2. Palladium Oxides	BR
4.8.3. Platinum Oxides	BR
4.9. Group 11 Oxides	BR
4.9.1. Copper Oxides	BR
4.9.2. Silver Oxides	BS
4.10. Group 12 Oxides	BS
4.10.1. Zinc Oxides	BS
4.10.2. Cadmium Oxides	BX
4.10.3. Mercuric Oxides	BX
4.11. Polyoxometalates	BX
5. Semiconducting Metal Chalcogenide Clusters	BZ

Special Issue: Calculations on Large Systems

Received: September 15, 2014



5.1. Group 12: A ^{II} B ^{VI} (A ^{II} = Cd, Zn, Hg; B ^{VI} = S, Se, Te)	BZ
5.1.1. Cadmium Chalcogenides: CdS, CdSe, and CdTe	BZ
5.1.2. Zinc Chalcogenides: ZnS, ZnSe, and ZnTe	CH
5.1.3. Mercury Chalcogenides: HgS, HgSe, and HgTe	CI
5.2. Group 13: A ^{III} B ^{VI} (A ^{III} = Ga; B ^{VI} = S, Te)	CJ
5.2.1. Gallium Sulfide	CJ
5.2.2. Gallium Telluride	CJ
5.3. Group 14: A ^{IV} B ^{VI} (A ^{IV} = Ge, Pb; B ^{VI} = S, Se, Te)	CJ
5.3.1. Germanium Chalcogenides: GeS and GeSe	CJ
5.3.2. Lead Chalcogenides: PbS, PbSe, and PbTe	CK
6. Summary	CL
Author Information	CL
Corresponding Author	CL
Notes	CL
Biographies	CL
Acknowledgments	CM
Abbreviations	CM
References	CM

1. INTRODUCTION

1.1. General Background

Metal, metal oxide, and metal chalcogenide materials have a wide variety of applications. For example, many metal clusters and nanoparticles are used as catalysts for reactions varying from the oxidation of carbon monoxide to the reduction of protons to hydrogen gas. Noble metal nanoparticles have unique optical properties such as a surface plasmon resonance for large nanoparticles that yield applications in sensing and photonics. In addition, a number of transition metal clusters are magnetic. Metal oxide clusters and surfaces are commonly used as catalysts for reactions such as water splitting. Both metal oxide and metal chalcogenide materials can be semiconducting, which leads to applications in sensors, electronics, and solar cells.

Many researchers have been interested in studying nanoparticles and/or small clusters of these materials. Some of the system sizes under investigation have been experimentally synthesized, which enables direct theory–experiment comparison. Other clusters that have been examined theoretically are of interest as models of larger systems or surfaces. Often, the size-dependence of their properties such as their HOMO–LUMO gap, magnetic properties, optical properties, etc., is of interest.

Metals can be divided into the alkali and alkaline earth (s-block) metals, transition (d-block) metals, and p-block metals. In these systems, the s (and p, if applicable) electrons are very loosely held, which leads to delocalized bonding characteristics for clusters comprised of these metals. Several decades ago, Knight, de Heer, and co-workers observed electron shell behavior in alkali metal clusters that could be attributed to electrons confined within a roughly spherical potential well.^{1,2} In a spherical jellium model, the lowest energy electronic orbitals are 1S, 1P, 1D, 2S, 1F, 2P, etc., where the capital letters denote orbitals with symmetry similar to atomic orbitals but delocalized throughout the entire metal cluster (now called

“superatom” orbitals). Systems with approximate spherical symmetry with a number of electrons corresponding to closed electronic shells (2, 8, 20, ...) were found to be “magic” clusters with special stability measured via mass spectrometry abundance, ionization potential, etc.² Clusters with a number of electrons varying significantly from these spherical magic numbers were determined to have lower symmetry. Systems with p-block elements that have filled electronic shells such as Al₁₃⁻ and Si@Al₁₂ also have enhanced stability as compared to their neighbors.^{3–6} Moreover, systems such as Al₁₃ that are missing one electron as compared to a filled electronic shell are predicted to behave similarly to halogen atoms; this led to the term “superatom”, which implies that a cluster may have chemical behavior similar to that of elements in the periodic table.⁵ Early alkali metal work has been extensively reviewed by Bonačić-Koutecký et al.,⁷ and the superatom concept has been reviewed recently by Castleman, Khanna, and Jena.^{8,9} In 2008, Walter et al. extended the superatom model to consider the effects of ligands on the electronic structure of metal nanoparticles, especially those composed of gold and silver.¹⁰

For transition metals with an unfilled d shell, directional bonding and magnetic effects can dominate the properties of these systems. This directional bonding can be contrasted with the delocalized bonding in s- and p-block elements, and yields very different structures as a result. Also in consequence, the structures for these systems can vary widely from related clusters with different occupations of d shells. In addition, the magnetic moments of these systems are of great interest because these systems often have several unpaired electrons and may experience either ferromagnetic or antiferromagnetic coupling of the unpaired electrons.

Metal oxide clusters also typically exhibit directional bonding. The band gaps of these systems are also size dependent, which has garnered significant interest among researchers. In particular, these systems are of interest as models of catalytic systems, especially of active sites involving defects or other low-coordinated atoms. Furthermore, the magnetic properties of these systems have been studied by many groups.

Semiconductor clusters have received great attention due to their unusual electronic and optical properties. The properties of these materials can be transformed by changing the cluster size and the ratio of the elements that compose the cluster. Compound semiconductors are materials that contain several elements from one, two, or more groups of the periodic table. These types of semiconductors can be classified as binary systems (two elements) and “alloy” (ternary, quaternary, etc.). Size, shape, and composition have a great effect on the structural, electronic, and optical properties of these semiconductors. When the size of the semiconductor system decreases from bulk to the atomic level, new unique characteristics can be observed. These features make semiconductor nanoclusters an extremely interesting research area.

1.2. Scope

This Review examines quantum mechanical calculations on large metal, metal oxide, and metal chalcogenide clusters. The focus of this Review is on the theoretical calculations and not on the related experimental studies, although theory–experiment interaction has been extremely valuable in many of these investigations. Studies on transition and main group metal clusters and nanoparticles with over 10 metal atoms (20 atoms for coinage metal clusters without ligands) are described and analyzed. Transition metal oxide investigations involving at

least four metal oxide units ($\text{MO}_x)_n$ ($n \geq 4$) are also examined. For metal chalcogenides, the focus of this Review is on semiconducting systems, which include both transition metal and main group metal chalcogenides. Metal chalcogenide systems with $(\text{AB})_n$ ($n \geq 6$) are of interest in this work. The choice of sizes described here accounts for many interesting studies on, for example, 13-atom metal clusters, metal oxide tetramers, and metal chalcogenide hexamers. Periodic studies of bulk or surface properties are not considered in this Review. This paper primarily focuses on the structure and physical properties of these metal-containing clusters rather than chemical reactivity such as catalytic properties.

1.3. Theoretical Methods

Most quantum mechanical studies on metal, metal oxide, and metal chalcogenide clusters employ density functional theory (DFT), although some work discussed in this Review has also been performed with the Hartree–Fock (HF) self-consistent field (SCF) method, second-order Møller–Plesset (MP2) perturbation theory, or coupled cluster (CC) theory at the level of single and double excitations (CCSD) or singles and doubles with perturbative triples (CCSD(T)). Multireference methods such as complete active space SCF (CASSCF) are occasionally used to treat near-degeneracies that often occur within transition metal-containing systems. Within DFT, exchange correlation functionals that utilize the local density approximation (LDA) or the generalized gradient approximation (GGA) are the most common, although meta-GGA and hybrid functionals are also frequently used. The local spin density (LSD) approximation (LSDA) approach accounts for polarization of electrons, that is, uses an unrestricted formalism with separate alpha and beta electron densities. Common LDA functionals include X α , Ceperley–Alder (CA),¹¹ Perdew–Zunger (PZ),¹² and Vosko–Wilk–Nusair (VWN).¹³ GGA functionals often employed are BP86,^{14,15} PW91,¹⁶ and PBE,¹⁷ among others. Hybrid functionals discussed in this Review include B3LYP^{18,19} and PBE0,²⁰ and meta-GGA functionals include TPSS²¹ and M06.²² Hubbard-corrected DFT functionals are represented as DFT+U.

Most excited-state calculations employ time-dependent density functional theory (TDDFT) using either the linear response (LR) formalism of Casida²³ or a real-time (RT) approach. TDDFT calculations usually employ the adiabatic local density approximation (ALDA), and this approach is sometimes referred to as the time-dependent local density approximation (TDLDA). Model potentials used in TDDFT calculations include the asymptotically correct exchange functional of Van Leeuwen and Baerends (LB94)²⁴ and the statistical average of orbital potentials (SAOP).^{25,26} A variety of long-range corrected (LC) functionals including CAM-B3LYP²⁷ are also used in TDDFT calculations. Other excited-state calculations can be performed using configuration interaction (CI), usually at the singles excitation level (CIS), or with equations-of-motion (EOM) CC approaches.

Although not the focus of this Review, other calculations on large systems utilize empirical potentials (EP) such as the Gupta potential or tight binding (TB) semiempirical methods such as density functional tight binding (DFTB). A few studies employing EP or semiempirical methods will be discussed in this Review for comparison with results from full quantum mechanical methods.

Because systems involving metal atoms possess many electrons, the basis sets employed often utilize pseudopotentials

(PP) or effective core potentials (ECP) that replace many of the core electrons with nodeless potentials; these potentials are usually derived with scalar relativistic effects included. Common PP or ECP basis sets include LANL2DZ,^{28–30} SKBJ (or SBKJC),^{31–33} etc. Basis sets used in these calculations may involve Gaussian-type orbitals (GTOS), Slater orbitals, or plane waves. Plane wave calculations often utilize the projector augmented wave (PAW) approach. For atomic orbital basis sets, a variety of double- ζ (DZ) and triple- ζ (TZ) quality basis sets are employed in the work described in this Review; these may be double- ζ or triple- ζ only in the functions describing the valence electrons. Polarization functions are often added. Because of the wide variety of basis set abbreviations employed in the work discussed in this Review (including some with the same abbreviation for different basis sets), it is recommended that the reader refer to the original literature for further details on individual basis sets.

Levels of theory are often represented as method/basis, where the method may be DFT, MP2, etc., and the basis set is provided after the slash. In this work, different basis sets may be employed for different atom types, and this will be occasionally denoted as method/basis1,basis2. The notation method2//method1 implies that a geometry optimization was employed with method1 followed by an energy calculation with method2.

1.4. General Comments

Because of the sizes of the systems of interest in this work, most of the calculations reviewed utilize DFT. In consequence, the results obtained depend strongly on the exchange-correlation functional used as well as the basis set employed. Some general trends about the ability of DFT calculations are well established. For example, bond lengths of clusters (or lattice parameters for periodic systems) are often slightly underestimated by LDA functionals. On the other hand, GGA functionals typically overestimate these bond lengths. Results with hybrid functionals can depend on the degree of Hartree–Fock exchange incorporated in the calculation. In consequence, the type of exchange-correlation functional employed can affect whether or not the bond lengths are over- or underestimated as compared to experiment. Even within a certain class of exchange-correlation functionals, the results predicted can vary somewhat: BP86 and PBE calculations on the same cluster would provide slightly different bond distances.

In addition to the structural effects, the exchange-correlation functional affects the predicted isomer energies. GGA, meta-GGA, and hybrid calculations typically provide much better relative energies as compared to simpler LDA calculations, but calculations with all four types of functionals can still be found in the literature. As for the structural parameters, the predicted isomer energies will vary on the basis of the class of exchange-correlation functional as well as the particular functional chosen. Because of the wide variation in relative energies that can be predicted using different functionals and the large number of low energy isomers that are present in the systems discussed in this work, it is not possible to confidently assign the lowest energy isomer unless additional data about experimental properties such as vibrational spectra or optical spectra are also available; even then, questions can arise because experiments can trap higher energy isomers and can not guarantee that the observed properties are those of the lowest energy isomers. However, combined theory–experiment investigations have had significant success at predicting the lowest energy isomers.

In addition to challenges of predicting isomer energies for isomers with the same spin state, DFT can have trouble predicting the relative energies of states with different spin multiplicities. The energy difference between, for example, a singlet and triplet state arising from the same electron configuration would be given by an exchange integral in HF theory, but is given by the exchange-correlation functional in DFT and is thus very dependent on the functional used. This can be an issue for transition metal systems in which several low-energy spin states are often available. In addition, a broken-symmetry approach is often used to calculate low spin states. Although this approach can provide a qualitative picture of the antiferromagnetic coupling between two spin centers, it is not as rigorous as multireference calculations. Since multireference calculations are often not practical for the system sizes examined in this Review, many calculations employ broken-symmetry DFT.

Another consideration regarding DFT calculations relates to self-interaction error. The Coulomb part of the electron–electron repulsion depends on the electron density. In consequence, there is a nonzero electron–electron Coulomb repulsion even for a one-electron system. Although the exchange energy should exactly cancel the self-interaction energy for a one-electron system (as well as for many-electron systems), the approximate exchange-correlation functionals used in actual DFT calculations do not necessarily have this property. This self-interaction error affects quantities such as orbital energies, excitation energies, and charge-transfer interactions.

In DFT, Koopman's theorem does not hold unless the exact exchange-correlation functional is used.³⁴ Occupied orbital energies can vary significantly from ionization potentials when self-interaction error in the exchange-correlation functions is high. In addition, unoccupied orbital energies in DFT are determined in a field of $N - 1$ electrons (as compared to N electrons in Hartree–Fock theory), so they do not correspond closely to electron affinities but are more closely associated with excitation energies. In general, unoccupied orbital energies in DFT tend to be much lower than the corresponding HF ones. In consequence, predicted HOMO–LUMO gaps are also much smaller with DFT than with HF. LDA functionals often drastically underestimate HOMO–LUMO gaps, leading to notable failures such as the prediction of metallic behavior for particular semiconducting materials such as carbon nanotubes. More sophisticated GGA and meta-GGA functionals can more accurately predict the HOMO–LUMO gaps as compared to LDA, although underestimations are still quite common. In contrast, hybrid functionals that include HF exchange can potentially overestimate HOMO–LUMO gaps similar to HF theory, but this depends on the system and the degree of HF exchange incorporated.

In cases in which orbital energy gaps are underestimated (or overestimated), optical gaps determined by TDDFT often follow the same trends. LDA is rarely used for excitation energy prediction because it often leads to drastically underestimated energies. GGA functionals appear to have better success, but may still underestimate energies. Hybrid functionals can predict excitation energies within 0.2 eV of experiment for some cases,³⁵ but in other cases can be 1 eV or more too high.³⁶ As with all DFT calculations, the results depend on the type of system and the particular exchange-correlation functional employed.

Recently, asymptotically corrected functionals have been of interest for excitations because they correct problems with standard DFT functionals for Rydberg and charge-transfer excited states. In addition, these functionals appear to predict fewer excitation peaks than standard functionals. However, those with large HF contributions can sometimes predict excitation energies that are much higher than experiment.³⁶

Although this section outlines some of the potential issues with DFT calculations, DFT has also had many successes in the prediction of structure and properties of large systems with many heavy atoms. As the following sections demonstrate, DFT and other quantum mechanical calculations have been applied to a wide variety of systems. Although experimental verification is not available for a large number of the studies presented in this work, we hope that this Review will provide a useful overview of past work for researchers interested in these areas. Throughout the remainder of this Review, the general comments related to the theoretical methods described above should be kept in mind when assessing the quality or utility of a particular study.

2. TRANSITION METAL CLUSTERS

2.1. Group 10

2.1.1. Ni Clusters. Nickel clusters are of interest for their applications in, for example, catalysis and hydrogen chemisorption. Several theoretical investigations on pure and doped Ni clusters have been performed during the past two decades. Reuse and Khanna performed the first theoretical study on geometry, electronic structure, and magnetism of small Ni_n ($n = 2\text{--}6, 8, 13$) clusters using a linear combination of atomic orbitals molecular orbital (LCAO-MO) approach within the density functional formalism and using the exchange correlation functional proposed by Ceperley and Alder (CA).³⁷ It was reported that the ground-state Ni_{13} has an icosahedral structure with a total spin of $S = 4$, whereas $S = 5$ and $S = 6$ states lie marginally above the ground state.

These authors carried out further investigations to study the electronic structure,³⁸ magnetic behavior,³⁸ and photoabsorption spectrum³⁹ of Ni_{13} by means of the same theoretical procedure. They compared the relative energy of states of the icosahedral and octahedral geometry with several different total spins and found that the distorted D_{3d} icosahedron is the most stable structure,³⁸ in agreement with their previous study.³⁷ It was also noted that the icosahedral geometries are more stable than the cuboctahedral clusters for all spin states.³⁸ They calculated the magnetic moment of Ni_{13} and found that it is closer to the bulk value and also lower than some of the smaller and bigger Ni clusters. However, it was reported that the magnetic moment changes significantly with the size of the cluster and the lower magnetic moment of Ni_{13} is mostly due to its high symmetry. Moreover, Reuse and Khanna were the first to calculate the theoretical photoabsorption spectra of Ni_{13} . An angular momentum decomposition around the center of mass of the cluster was carried out to analyze the electronic states and label the various transitions.³⁹ They reported that the photoabsorption spectra not only depend on the cluster size, but are also sensitive to the geometrical arrangement. This fact suggests that photoabsorption can be used as an effective tool to differentiate various isomers that otherwise cannot be distinguished by their magnetic moments or other properties.

Reddy et al. performed calculations of equilibrium geometries, binding energies, ionization potentials, and magnetic

moments of Ni_n clusters containing up to 21 atoms.⁴⁰ The geometries of the clusters were obtained using molecular dynamics simulations, while the electronic structure, ionization potentials, and magnetic moments were calculated self-consistently within the framework of molecular orbital theory and the density functional method. They used both LDA and GGA exchange correlation functionals. The comparison between calculated and experimental ionization potentials and magnetic moments revealed the general trend of the size dependence of these properties. In agreement with the experimental results, the calculated ionization potentials showed little fluctuation with the cluster size from $n = 11$ –21. The magnetic moments were found to have enhanced values over the bulk value and vary monotonically as a function of cluster size. The molecular orbital energy levels of these Ni clusters were studied, and a band-like form was identified at $n = 14$.

DFT-LSDA calculations have been performed to study the ground-state electronic structure and the magnetic properties of relatively larger Ni_n clusters, $n = 2$ –39 and 55.⁴¹ Duan et al. observed a similarity between the overall features of density of states (DOS) for the clusters and the bulk. As was reported in the study of Reddy et al.,⁴⁰ Duan et al.⁴¹ also found magnetic moments larger than the bulk value. In addition, they reported a monotonic variation of the magnetic moments, which agrees well with the experimental results. The general trend to have enhanced magnetic moments on the surface of the clusters is not applicable to small Ni_n clusters ($n = 14$ –39), because they observed higher average moments for core atoms than those for surface atoms. This observation has been attributed to charge transfer from inner atoms to the surface atoms.

Entel and co-workers carried out a similar investigation to obtain the lowest energy structures, magnetic moments, binding energies, and HOMO–LUMO gaps of Ni_n clusters in the range of $2 \leq n \leq 16$ with the PAW/GGA level of theory.⁴² The calculated magnetic moments and the binding energies were comparable to the results obtained by Reddy et al.⁴⁰ and Duan et al.⁴¹ and also agreed with the experiments. A higher HOMO–LUMO gap was obtained for Ni_{13} , indicating its higher stability. Furthermore, the discrepancies of HOMO–LUMO gaps in the present study and in the study of Reddy et al. were attributed to the use of different levels of theory.⁴² Longo and Gallego studied the structure and magnetic moment of the Ni_{13} cluster by means of PBE/TZ2P level of theory and reported that it is most stable in the icosahedral geometry.⁴³ Aguilera-Granja et al. also studied the 13- and 23-atom Ni clusters using DFT-PBE and reported that these Ni clusters tend to adopt more compact structures.⁴⁴

DFT calculations have been done to study structure, binding energy, and bond lengths of Ni_{13} with the B3LYP level of theory using three different basis sets.⁴⁵ Onal et al. optimized the 13-atom Ni cluster energetically and obtained the icosahedral geometry in agreement with the previous theoretical and experimental studies. The correlation between the binding energy per atom and $n^{-1/3}$, where n is the number of atoms, has been used to estimate the binding energy of bulk Ni for an infinite number of atoms. The calculated binding energy of bulk Ni was very close to the experimental value. This group performed another theoretical study to investigate the geometry, binding energy, and ethylene adsorption of the Ni_{55} nanocluster using the B3LYP/86-411(41d)G level of theory.⁴⁶ In accordance with the experimental findings, they found a distorted icosahedral geometry for Ni_{55} and the lowest binding

energy as compared to the theoretical literature. By including the binding energy of Ni_{55} , they obtained a slightly overestimated bulk binding energy as compared to the previous study. They reported that there are two alternative adsorption sites for ethylene adsorption, and the adsorption energy is higher for Ni having a coordination number (CN) of 6 than that with CN 8.

Ni clusters having 13, 55, and 147 atoms have been probed to study their structural, electronic, and magnetic properties by means of PAW/GGA.⁴⁷ Singh and Kroll considered anti-ferromagnetic (AFM) and ferromagnetic (FM) coupling between the center atom and surrounding atoms in their cluster calculations. It was found that the icosahedral structures are more stable than cuboctahedral and anticuboctahedral structures for all cluster sizes and at all total magnetic moments. Both the cohesive energy of the cluster and the nearest neighbor bond length were found to increase with the increasing cluster size. They reported that the cluster size, its intrastructure, and the geometrical structure symmetries are all important factors that determine the magnetic and electronic structure of a cluster.

The lowest energy structures, binding energies, second differences in energy, and magnetic properties of Ni_n ($n = 20$ –30) clusters have been calculated by means of a genetic algorithm coupled with a tight-binding (TB) interatomic potential search followed by DFT-PBE-based optimizations.⁴⁸ Song et al. found that the Ni clusters having 20–30 atoms favor the double icosahedron-based motif, which can be formed by adding atoms one by one on the side face of Ni_{19} . The thermodynamic stability of Ni clusters was found to have an oscillatory behavior, because Ni_{20} , Ni_{23} , Ni_{26} , and Ni_{29} showed extra stability as compared to their neighbors. Furthermore, they reported that the binding energy of the studied clusters increases monotonically as a function of cluster size. In contrast with the work of Duan et al.,⁴¹ it was found that the surface atoms exhibit larger magnetic moments than the core atoms.⁴⁸ They also observed decreasing magnetic moments with the increasing number of atoms in the cluster. It was also reported that their calculated trend in magnetic moment has a better agreement with the experiment⁴⁸ as compared to that of Duan et al.

Song et al. continued their work on neutral Ni clusters using the same theoretical method, to investigate the lowest-energy structures, energetic stability, and magnetic properties of clusters having 31–35 Ni atoms.⁴⁹ The growth behavior and the evolution of properties of Ni_n ($n = 31$ –35) clusters seem to be analogous to that of Ni_n ($n = 20$ –30) clusters. It was found that the double-icosahedron-like structures dominate for Ni clusters in the size range of 31–35 atoms and the binding energy per atom increases monotonically as a function of cluster size.⁴⁹ Similar to the previous study,⁴⁸ they observed the surface atoms to have more magnetic character than the core atoms.

Ni nanoclusters are well-known catalysts employed in single-wall carbon nanotube (SWCNT) growth. Both experimental and theoretical investigations have been carried out to find out whether the carbon atom adsorption energy varies with the size of the Ni cluster, whether there are any preferences for different facets of the nanoclusters, or whether the carbon atom diffuses into the nanoclusters or stays on the surface once adsorbed. Zhang et al. performed DFT-PW91 calculations on the Ni_{38} cluster and reported that the lowest-energy structure of Ni_{38} is a truncated octahedron and the preferred adsorption facet is

(100).⁵⁰ Furthermore, it was reported that the C atom tends to have a coordination number of 4. Chen and co-workers performed theoretical investigations to study C adsorption on four Ni_n ($n = 13, 15, 38, 55$) clusters.⁵¹ They found that Ni₁₃ and Ni₅₅ adopt icosahedral geometries and Ni₁₅ has a hexagonal antiprism, while in accordance with the previous study, Ni₃₈ has a truncated octahedral geometry (Figure 1). It was observed

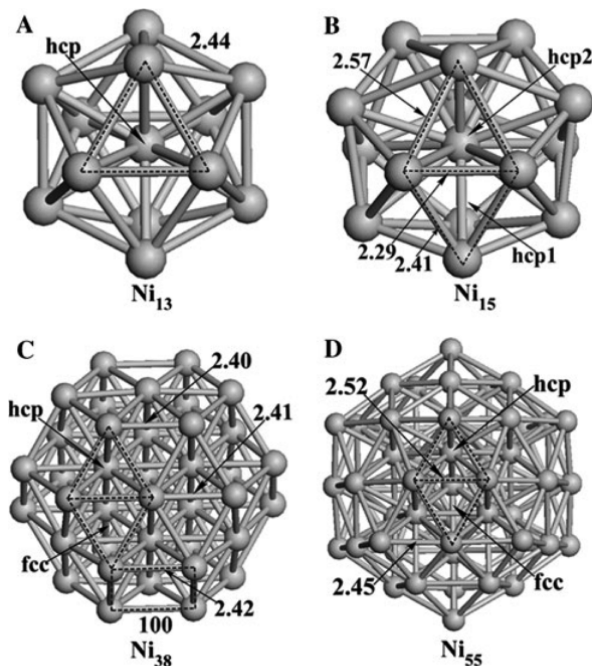


Figure 1. Ni clusters: (A) Ni₁₃, (B) Ni₁₅, (C) Ni₃₈, and (D) Ni₅₅. Surface adsorption sites are depicted on the models with Ni–Ni bond lengths shown in angstroms. Reproduced with permission from ref 51. Copyright 2011 Springer.

that the C atoms preferably adsorb on highly coordinated sites and C adsorption is stronger on smaller clusters. Moreover, the migration of surface C atom into the underlying interstitial subsurface positions was found to be energetically and kinetically feasible, indicating that both surface and subsurface C atoms are involved in carbon nanotube growth.

As Wang and Johnson predicted using the DFT-PAW/GGA level of theory, Ni clusters having Au, Ag, Cu, Pt, or Pd impurities in 55-atom binary nanoclusters are preferably formed.⁵² They have also suggested stable configurations for core–shell nanoclusters: Ir and Os core with Ni shell or Ni core with Ag, Cu, Au, Pd, or Pt shell.

Das and Shoji studied geometries, orbital interactions, and oxygen chemisorption properties of pure and chromium-doped Ni clusters having up to 13 atoms by means of the PW91/DNP level of theory.⁵³ It was found that the Cr-doped clusters having 10–13 atoms are more stable than the pure Ni clusters with the same number of atoms. The cluster binding energy monotonically increases as a function of cluster size, while Ni₁₀ and Ni₁₃ show higher stability than their neighbors. Cr atoms showed a higher preference to be in the center than at the edge. Ni₁₂Cr was found to have the highest stability, while icosahedral Ni clusters having more than four Cr atoms exhibited lower stability than their pure counterparts. A strong interaction between Ni 4s and Cr 3d orbitals was observed, while a decrease in the metal 3d orbital peak with an increasing amount of Cr was also identified. The oxygen chemisorption energy was

found to be always higher in Cr-doped Ni clusters than pure Ni clusters, and the preferred oxygen chemisorption site for Ni₁₃, Ni₁₀Cr, Ni₁₁Cr, and Ni₁₂Cr was the hollow site.

Recently, Das and Shoji performed a similar investigation with the same level of theory to study structure, orbital interactions, and atomic oxygen and OH adsorption on Mo-, Sc-, and Y-doped nickel clusters having up to 13 atoms.⁵⁴ They found that the icosahedral Ni₁₂Mo cluster is the most stable one where Mo sits at the center. However, it was observed that Sc and Y preferably occupy the edge. The analysis of the second-order energy differences and fragmentation energies suggested that Ni₁₂Mo, Ni₁₁Sc, and Ni₁₂Y would be the magic clusters. It was found that the oxygen atom prefers to adsorb on the top Mo site for Ni₁₀Mo, whereas in the case of Ni₁₁Mo, Ni₁₂Mo, Ni₁₂Sc, and Ni₁₂Y the oxygen atom preferentially occupies the hollow site in accordance with the previous study. Mo-doped nanoclusters showed the highest oxygen and OH chemisorption energies. Upon OH chemisorption, Sc and Y doped clusters exhibited larger distortions as compared to Mo doped and pure Ni clusters.

Structures and magnetic moments of the Ni₁₂Y (Y = Fe, Co, Ru, Rh, Pd, and Pt) binary clusters have been studied with PBE/DZ2P level and compared to the properties of the pure Ni₁₃ clusters.⁵⁵ It was found that, although Ni₁₂Rh, Ni₁₂Pd, and Ni₁₂Pt have the same hcp structure as pure Ni₁₃, in contrast Ni₁₂Fe, Ni₁₂Co, and Ni₁₂Ru have icosahedral geometries. Furthermore, it was reported that the binding energy of Ni₁₂Ru is higher, whereas Ni₁₂Pd is lower than the binding energy of pure Ni₁₃. Aguilera-Granja et al. predicted a remarkable magnetic behavior for Ni₁₂Rh, which can be attributed to electronic effects due to Ni–Rh hybridization.

2.1.2. Pd Clusters. Palladium is of intense interest due to its many uses in applications such as catalytic converters and fuel cells. In consequence, many researchers have studied the properties of palladium clusters and nanoparticles. Reddy and Khanna were the first to study 13-atom Pd metal clusters. They used the linear combination of atomic orbitals method for their calculations within the density functional formalism. They used the von Barth–Hedin form to include the exchange correlation effects in their calculations. It was established that the icosahedral geometry is more stable for Pd₁₃ than the face-centered cubic (fcc) octahedron, and it has a nonzero magnetic moment unlike the bulk, which is nonmagnetic. Furthermore, they calculated the binding energy per atom of the 13-atom Pd cluster and compared this to the bulk cohesive energy.⁵⁶ In accordance with Reddy and Khanna, Estiu and Zerner also reported that the icosahedron is the most stable isomer for Pd₁₃.⁵⁷ However, their final structure was found to be a distorted icosahedron with D_{5d} symmetry with a zero magnetic moment. They analyzed the mutual dependence between electronic structure and geometric characteristics of small Pd clusters using the self-consistent-field/configuration interaction (SCF/CI) level of theory.

Watari and Ohnishi analyzed the cuboctahedral and icosahedral symmetries of Pd₁₃ to explore its atomic and electronic structures by means of the linear combination of norm-conserving pseudopotential atomic orbitals (LCPSAO) method with both PZ and PBE exchange correlation functionals.⁵⁸ It was found that the cuboctahedral Pd₁₃ is more stable with a small spin polarization, $S = 3$. This fact is in contrast with the previously discussed studies; Watari and Ohnishi attributed this difference to the accuracy of the numerical calculation and the treatment of the core electrons.

The structures and magnetism of neutral and anionic 13-atom Pd clusters have been studied with the Born–Oppenheimer local-spin-density molecular dynamics (BO LSD MD) method, and it has been found that the icosahedral Pd_{13} is the most stable with a magnetic moment of $0.62 \mu_{\text{B}}$ /atom.⁵⁹ Pd_{13} and Pd_{13}^- are rather similar and follow the same binding energy evolution as a function of the spin multiplicity of the cluster. Moseler et al. calculated remarkably consistent vertical electron detachment energies with the values obtained in the photo-electron spectroscopy (PES) measurements. Interestingly, Chang and Chou found a new buckled biplanar (BBP) structure that has a C_{2v} symmetry and higher s–d hybridization for Pd_{13} in their DFT-PW91/plane wave basis calculations.⁶⁰ It was observed that the spin magnetic moment of the BBP structure is generally smaller than that of the icosahedron.

Kumar and Kawazoe performed calculations based on PW91/plane wave basis and predicted a tricapped pentagonal bipyramid with a $6 \mu_{\text{B}}$ magnetic moment as the lowest energy isomer of Pd_{10} , incomplete icosahedra each with a $6 \mu_{\text{B}}$ magnetic moment for Pd_{11} and Pd_{12} , and for Pd_{13} an icosahedral isomer with an $8 \mu_{\text{B}}$ magnetic moment⁶¹ in agreement with the earlier studies.^{59,60} In contrast to the frequent assumptions in literature, Futschek et al. reported that the stable structures of the clusters with $n = 11, 12$, and 13 are based neither on icosahedral nor cuboctahedral motifs, but octahedral with adatoms.⁶² They found a polyoctahedral cluster that has an $S = 3$ spin configuration at the PAW/PZ level of theory. Rogan et al. studied the physical properties of small Pd clusters with several phenomenological many-body potentials and the LSDA-PZ/DZP method.⁶³ They found geometric structures with minor differences similar to the findings of Kumar and Kawazoe.

Wang and Johnson proposed that the 13-atom Pd clusters tend to adopt low symmetry, open structures rather than high symmetry, compact ones.⁶⁴ A low symmetry structure with relatively close packing has been identified as the lowest energy isomer using the DFT-PW91 level of theory. They mentioned that the structural habit of Pd closely resembles that of noble metals rather than transition metals due to the complete filling of the d orbitals. For Pd_{13} , a distorted icosahedron has been reported with an $8 \mu_{\text{B}}$ magnetic moment by Sun et al.,⁶⁵ while in a subsequent study the same authors reported that two different density functionals can lead to two global minimum structures that are very close in energy and have the same spin states. The PBE functional has favored the icosahedrons, whereas a structure that is similar to the one proposed by Wang and Johnson has been preferred by the B3LYP functional.⁶⁶

Recently, Köster et al. performed DFT-PBE calculations to study the electronic structure and magnetic properties of Pd_{13} .⁶⁷ Unlike the previous theoretical studies, they found a bilayer structure that can be considered as a relaxed bulk fragment with a spin magnetic moment of $6.0 \mu_{\text{B}}$. The icosahedral cluster was found to be slightly above the ground state. The stabilization by the p- or d-like cluster orbitals caused the near degeneracy of the bilayer or icosahedral clusters, respectively. The low-lying spin states were found to be important in controlling the electronic and magnetic properties of the cluster. Recently, Reveles et al. used the linear combination of atomic orbitals-molecular orbital approach at the PBE/DZVP level of theory to learn the structural changes of bilayer C_s ground state and the octahedron of Pd_{13} upon charging and oxidation or reduction.⁶⁸ It was observed that the bare Pd_{13} has a C_s geometry, whereas Pd_{13}O_2 has an icosahedral

Pd_{13} core, indicating an interesting structural change during an oxidation/reduction reaction. The location of 1P, 1D, and 2P cluster orbitals and the amount of hybridization between the atomic p orbitals and the cluster 1D orbitals determine the order of stability of the isomers. Park et al. calculated the adsorption geometry and binding affinity of Pd_{13} nanoparticle onto the surface of carbon nanotubes (CNT) using both GGA and LDA functionals and a plane wave basis set. It was found that unlike Al and Au, 13-atom Pd nanoparticles have a strong binding to the CNT.⁶⁹

Combined ab initio DFT-PZ/DZP and semiempirical tight-binding (TB) model calculations have been performed on small Pd clusters containing up to 21 atoms to study their structural and magnetic properties.⁷⁰ Aguilera-Granja et al. observed an icosahedral growth pattern with some structural disorder. They compared these results to the studies of Futschek et al.⁶² and Kumar and Kawazoe.⁶¹ The structures of Pd_n clusters with $n = 16–18, 20$, and 21 were found to be different⁷⁰ from those of Kumar and Kawazoe. Aguilera-Granja et al. found structures with 5-fold symmetry for $n = 10, 11, 12$, and 13 ⁷⁰ in contrast with the results of Futschek et al. It was found that the TB and DFT results are in fairly good qualitative agreement, and hence the reliability of TB method for this type of calculation was established. Later, these authors studied the structural and magnetic properties of Pd_{12}Y ($\text{Y} = \text{Fe}, \text{Ni}, \text{Co}, \text{Ru}, \text{Rh}$, and Pt) clusters.⁵⁵ It was found that the binding energies of the bimetallic clusters having icosahedral geometries with the impurity atom at the center are larger than the pure Pd_{13} , which is a fragment of the double icosahedron.

The total energies and the relaxed geometries of Pd_n ($n = 55, 135, 140$) clusters have been studied using the LDA-PZ level of theory.⁷¹ The 55- and 135-atom clusters have been selected due to the simultaneous cuboctahedral (fcc) and icosahedral (icos) subshell closings. Jennison et al. concluded that both Pd_{55} and Pd_{135} prefer the icos geometries, and the transition from icos to fcc occurs near $n = 140$. However, they treated these clusters as nonmagnetic. It has also been established that the icos structures show large core compressions to obtain better interatomic spacing of the surface atoms, while fcc structures exhibit considerable surface compressions.

DFT theory calculations within the spin-polarized generalized gradient approximation (GGA) have been performed by Kumar and Kawazoe to study the evolution of the atomic and electronic structure and also the magnetism of Pd clusters having $2–23, 55$, and 147 atoms.⁶¹ Moreover, they focused on the changes in the magnetic behavior of clusters due to H and O adsorption. They found that there is an icosahedral growth pattern where the atomically closed-shell 13-, 55-, and 147-atom clusters have higher magnetic moments that gradually decrease with the increasing cluster size. Furthermore, they observed that the binding energy increases monotonically toward the bulk value with the increasing cluster size. The second-order energy differences showed that the 10-, 13-, 15-, 18-, 21-, and 22-atom clusters are magic. Kumar and Kawazoe observed that the impurities and reactants on clusters have a significant effect on their magnetic behavior.

Nava et al. investigated the structure and properties of neutral, bare Pd_n clusters $n = 2–309$ by means of DFT-BP86/SVP.⁷² Numerous isomeric structures that are very close in energy were found for small Pd_n clusters $n \leq 15$, which prefer high spin states with small HOMO–LUMO gaps. Pd clusters having more than 100 atoms in the fcc arrangement showed

higher cohesive energies than icosahedra and decahedra, suggesting an early preference for the bulk packing.

Yudanov et al. performed a series of DFT investigations to explore size-dependent geometric parameters, binding energies, electronic structure, and CO and C adsorption properties as well as the light element atom impurities on the subsurfaces of relatively large Pd clusters containing 100–200 atoms.^{73–77} They used the linear combination of Gaussian-type orbitals fitting-functions density functional (LCGTO-FF-DF) method for their calculations. The geometry optimizations have been performed using the local density approximation, whereas the generalized gradient approximation has been used in the energy calculations (GGA//LDA). The following calculations have been performed at the BP86//VWN level of theory.^{73–77}

In two subsequent studies, Yudanov et al. studied the octahedral and truncated octahedral Pd_n ($n = 55, 79, 85, 116, 140, 146, 147, 148$) clusters (Figure 2),^{73,74} the size

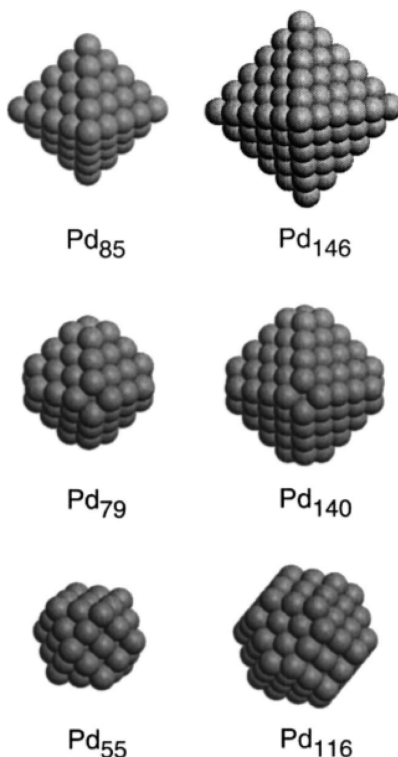


Figure 2. Octahedral and truncated octahedral Pd_n clusters. Reprinted with permission from ref 73. Copyright 2002 AIP Publishing LLC.

dependence of bond lengths, cohesive energy, and adsorption properties of bare Pd_n clusters,⁷³ and the energetics of CO adsorption at different sites of Pd nanoparticles.⁷⁴ In the former study, they considered the adsorption of CO molecules only at isolated 3-fold hollow positions in the center of Pd(111) facets and observed that the CO adsorption energy varies in a small range except for Pd_{55} , which is notably lower.⁷³ It was concluded that the Pd clusters with about 80 atoms are capable of reproducing structural features and vibrational frequencies of adsorption complexes on the corresponding sites of the infinite substrate. Afterward, they addressed CO adsorption at other sites of Pd nanoparticles at the same level of theory and found that the 3-fold hollow position is energetically favored over bridge, on-top sites, and the sites in the vicinity of cluster edges and corners.⁷⁴ However, it was found that CO bonds strongest

at bridge positions of cluster edges where it binds to low-coordinated Pd centers.

The occupation of Pd(111) surface and the octahedral and tetrahedral subsurface holes by atomic H, C, N, and O species in octahedral Pd_{79} and Pd_{116} clusters that represent the face centered cubic lattice has been explored.⁷⁵ The migration of adsorbed atoms at the 3-fold hollow sites to the subsurface sites has also been considered, and N and O showed higher endothermicity, whereas H is slightly endothermic and C is isoenergetic. It has been found that the subsurface C impurities reduce the CO adsorption energy at Pd clusters. Later, Neyman et al. performed an extended work to study the C adsorption on Pd using Pd_n ($n = 55, 79, 85, 116, 140, 146$) nanoparticles that are fragments of bulk Pd in the form of three-dimensional octahedral or cubooctahedral crystallites.⁷⁶ The calculations revealed that the surface C atoms preferably adsorb as carbide species, which carries a negative charge. The 3-fold hollow sites in the center of (111) facets are energetically favored, and the migration of adsorbed C to the facet borders is slightly less stable.

The C–O bond scission of methoxide is an intermediate step of methanol decomposition at the surface of Pd nanoparticles.⁷⁷ Yudanov et al. used Pd_{79} as a model cluster compound to study the different locations of adsorbed intermediates and the transition state of C–O bond scission. To do this, they reduced the overall symmetry of the model from O_h to D_4 . The C–O bond breaking results in the formation of a residual CH_3 , and the on-top position at a cluster edge between two (111) facets has been calculated as the most favorable position for CH_3 binding. Nevertheless, the high activation barrier suggested that the methoxide decomposition via C–O bond breaking on Pd is a very slow process, even with the edge sites.

Later, Neyman and co-workers performed DFT calculations using a plane wave basis set and the PAW method with PW91//VWN to study size-dependent geometric parameters, binding energies, and electronic structures of Pd clusters.⁷⁸ A series of model octahedral and cubooctahedral Pd_n ($n = 38, 44, 55, 79, 85, 116, 140, 146$) crystallites that were cut from the Pd bulk were used to evaluate the aforementioned properties. The calculated results then were compared to their previous theoretical studies that used the LCGTO-FF-DF method. It was observed that the structure and energetics of the crystallites approach the values of bulk material around $n = 80$. It has been reported that the plane-wave method has high performance for transition-metal nanoparticle calculations. The authors used the same theoretical method to study bimetallic, cubooctahedral $Pd_{140-n}Zn_n$ ($n = 0, 8, 24, 32$) nanoclusters and their adsorption complexes with CO molecules.⁷⁹ It was found that the average cluster cohesive energy decreases as a function of the number of Zn atoms added. The adsorption of CO molecules on 3-fold hollow sites at the center of (111) facets was considered, and the CO adsorption energy was found to decrease when the Zn atoms located in the subsurface layers in the cluster, whereas the Zn atoms in the surface layer were found to induce slight changes to the CO adsorption energy.

Six different structural motifs (four with 38 atoms, one with 39, and another with 40 atoms of Pd) have been considered to investigate the adsorption of CO molecules and atomic hydrogen on these clusters.⁸⁰ Paz-Borbón et al. performed all of the optimizations at the PW91/DZ level of theory, whereas the TZP basis set was used for energy calculations. The chemisorption of CO flattened the metal cluster potential energy surface while favoring the noncrystalline structures.

However, H adsorption is mostly related to the release of surface stress while favoring 5-fold symmetry motifs. The adsorption of up to 32 CO molecules or the H atoms has altered the DFT energy ordering of the bare structural motifs.

A number of theoretical studies have been performed to explore binary metal nanoclusters during the past few years. Wang and Johnson predicted that the formation of Pd core–Au/Ag shell nanoparticles and Fe/Ru/Os/Co/Rh/Ir/Ni/Pt/Cu core–Pd shell nanoparticles is energetically favorable.⁵² A lot of theoretical investigations on Pd–Pt bimetallic nanoclusters have been performed, and most of the recent studies were discussed under the “Pt clusters” section of this Review.

There are several DFT studies reported on Pd–Au nanoparticles due to their higher catalytic activities for various chemical reactions. Combined empirical potential (EP)/DFT calculations have been performed to study Pd–Au bimetallic clusters containing up to 50 atoms.^{81,82} Paz-Borbón et al. found that the truncated octahedron is favorable for all compositions at $n = 38$, where Pd atoms occupy the core and Au atoms segregate to the shell.⁸² They performed DFT calculations at the PW91/DZ level of theory. Subsequently, Yudanov et al. performed PW91//VWN calculations to study the distribution of Au atoms in truncated octahedral shaped $\text{Pd}_{79-n}\text{Au}_n$ clusters, where n changes from 1 to 60.⁸³ In agreement with the earlier studies, it was found that the segregation of Au atoms into the particle surface is thermodynamically more stable. Furthermore, the cluster edges were found to stabilize gold atoms more than do the sites inside the (111) cluster facets. The strain induced by Au atoms is larger due to its larger atomic radius. The cluster edges have more flexibility for the relaxation and to minimize this larger strain caused by Au atoms.

The B3LYP/LANL2DZ level of theory has been used to study structural, electronic, and energetic properties of smaller Pd_nAu_m ($n + m \leq 14$) clusters as a function of size ($n + m$).⁸⁴ Zanti and Peeters found that the clusters having more Pd atoms favor three-dimensional structures, whereas the clusters enriched in Au prefer planar structures with deviation from planarity near Pd centers. At a given size, the ground-state spin multiplicity increased with an increasing number of Pd atoms. This was due to the promotion of part of the 4d electrons to the 5s orbital in Pd to obtain stable metal–metal bonds. It was found that the Pd_nAu_m mixed clusters are more stable than their monometallic counterparts.

Liu et al. studied the geometry and stability of Pd_nAu_m clusters ($n + m = 38, 55, 79$; $m/n \approx 2:1$ and $5:1$) using the PAW/GGA-PW91 level of theory.⁸⁵ The truncated octahedral or cubooctahedral clusters were examined, and it was demonstrated that the Pd:Au (m/n) atomic ratio of 2:1 forms more stable clusters than the 5:1 ratio. It was also reported that $\text{Au}_{24}\text{Pd}_{14}$ is the most stable bimetallic cluster that has a total of 38 atoms. The Pd_nAu_m clusters with $m/n \approx 2:1$ were found to have delocalized d electron characteristics and shifted d band centers to the Fermi level of the clusters as compared to the pure Pd and Au metal clusters. Thus, Pd_nAu_m clusters with $m/n \approx 2:1$ were expected to bond with gas molecules more easily. Furthermore, it was mentioned that the Pd_nAu_m clusters ($m/n \approx 2:1$) would be able to preserve their initial shape under catalytic conditions due to the higher thermodynamic stability. The aforementioned authors performed a subsequent investigation to study the stability and H_2 adsorption activity of bimetallic, truncated octahedral $\text{Au}_{79-n}\text{Pd}_n$ ($n = 1–55$) clusters using the same computational method.⁸⁶ Yudanov et al. reported the following stability order

for four Pd substitution types, face > midedge > corner > edge. The stability of the clusters increased with an increasing amount of Pd for the same substitution type. In contrast with the above stability order, the H_2 adsorption activity was found to be corner \approx edge > midedge > face. The $\text{Au}_{36}\text{Pd}_{43}$ cluster showed a higher stability and H_2 nonactivated dissociation activity.

Recently, Bruma et al. studied the structures and energetics of 98-atom AuPd clusters using a combined EP/DFT approach. The PBE/plane wave basis relaxations revealed that the fcc-hcp and Marks decahedron structural motifs are more stable than Leary tetrahedron and icosahedron structures, which is in good agreement with the experimental results.⁸⁷

The structures and magnetic properties of small Pd clusters doped with Fe and Mn atoms have been studied using the PAW-PBE level of theory.^{88,89} It was found that the doping increases the stability and the magnetic moment of the clusters with respect to the pure Pd clusters. The geometries did not change significantly after the addition of an Fe atom, except for $n = 11$ and 12 ,⁸⁸ whereas the Mn doping gave rise to a geometry reconstruction for $n > 9$.⁸⁹

Wei et al. used the LDA-VWN/DNP level of theory to study the effects of doped Pb atoms on Pd_n clusters ($13 \leq n \leq 116$).⁹⁰ The doped Pb atoms changed the thickness of surface phase and surface morphology of Pd clusters. Moreover, the doped Pb atoms reduced the HOMO–LUMO gap of the clusters as compared to the pure Pd clusters; hence, they enhanced the chemical reactivity of larger clusters. Pd_{12}Pb and $\text{Pd}_{36}\text{Pb}_{19}$ are two of the exceptions, which are relatively smaller in size and have higher energy gaps. Negreiros et al. used a combined EP/DFT approach to study AgPd nanoclusters having up to 400 atoms,^{91,92} adsorbed on MgO(100).⁹² The plane wave-based calculations were performed with the PBE exchange correlation functional.^{91,92} The truncated octahedral (TO) form was found to be the global minimum for the 38-atom metal cluster, a capped icosahedra for size 60, and decahedra for size 100.⁹¹ Although pure Ag and Pd clusters prefer fcc structure on MgO(100), the AgPd clusters were found to create a pocket of stability for polyicosahedral structures.⁹²

2.1.3. Pt Clusters. Platinum clusters have also been of intense interest due to their applications in catalysis. In most of the earliest investigations, semiempirical methods were used or very small clusters such as dimers or trimers were studied due to limited computational resources. The self-consistent-field-X α scattered wave (SCF-X α -SW) approach to molecular orbital (MO) theory was used to study the electronic structure of Pt_{13} cluster with the cubooctahedral geometry in 1976.⁹³ The overlap of d-band by the s, p band and the sharp peak in the density of states around the Fermi level of Pt_{13} exhibited the main features of the Pt-bulk band structure. Messmer et al. also reported that the ionization potential of the Pt_{13} cluster is about 2 eV greater than the average bulk work function.

Goepel and co-workers performed ab initio (SCF/MP2) calculations to study the size-dependent electronic structures of Pt_n clusters up to $n = 12$ and their bond properties.⁹⁴ It was found that the Pt atom at the unsaturated coordination site has lower Pt_{6s} electron occupancy and is also energetically unstable. With increasing cluster size, the occupancy of Pt_{6s} increases and the Pt reactivity decreases. Furthermore, the electronic structure trend found here is qualitatively consistent with the former experimental data.

Several different studies on the geometry,^{65,95,96} electronic structure,^{58,96,97} and hydrogen adsorption⁹⁷ of the Pt₁₃ cluster have been performed during the past two decades. Aprà and Fortunelli studied the structure and energetics of cubooctahedral Pt₁₃ and Pt₅₅ by means of the DFT-BPW91 level of theory and compared the results to the Hartree–Fock (HF) approximation and a hybrid method, which uses a mixture of the Hartree–Fock and BPW91 functionals.⁹⁵ Even though the failure of the HF approach on metallic systems is well-known, they checked whether that fact applies to relatively small metal clusters as well. The cubooctahedral Pt₅₅ was found to undergo a strange structural rearrangement toward a spherical configuration. A huge spin contamination clearly showed that the HF approach could not describe the Pt₅₅ cluster sufficiently. The plots of the DOS of Pt₁₃ and Pt₅₅ obtained with DFT were found to qualitatively agree with the previous semiempirical curves better than the ones obtained with the hybrid method.

In a subsequent DFT study carried out using the BPW91 functional by the same authors, a truncated octahedral geometry for Pt₃₈ and icosahedral, truncated decahedral, and cubooctahedral geometries for Pt₁₃ and Pt₅₅ have been considered to study their structures, energetics, and electronic structures.⁹⁶ They reported that the Pt_n clusters in this size range from $n = 13\text{--}55$ start developing metallic characteristics, which is evident from the vanishing gap at the Fermi level. The introduction of a single positive or negative charge on these clusters has small effects on the optimized geometries, and the electronic structures only change in the orbitals directly involved in the charging process most of the time. The binding energy per atom, the ionization potential, and the electron affinity were found to extrapolate fairly well to the bulk value.

Watari and Ohnishi studied the electronic structures of icosahedral and cubooctahedral Pt₁₃ clusters and the 8, 12, 14, and 20 hydrogen atoms adsorbed systems.⁹⁷ They used the LCPSAO method with both PZ and PBE exchange correlation functionals. They found that the cubooctahedron cluster is the most stable for Pt₁₃ clusters in contrast to the oblate, multiply capped trigonal prism reported by Sun et al.⁶⁵ The calculated H–Pt binding energy was found to be comparable with the experimental results.⁹⁷ The cluster–H equilibrium bond length remains constant, while the Pt–H equilibrium distances vary, suggesting the “giant atom” nature of the Pt₁₃ cluster. Furthermore, the electronic shell structure of Pt₁₃ was found not to change upon adsorption of H. These authors performed a subsequent study to explore the equilibrium cluster size, the total energy, and the HOMO–LUMO orbitals of the 13-atom Pt cluster using the LCPSAO method with PZ exchange correlation functional.⁵⁸ They reported that the Fermi level of the Pt cluster is located in the d-band unlike Au₁₃.

Lin et al. evaluated the effect of cluster size on the adsorption energies of O and S atoms on small Pt clusters.⁹⁸ They performed a series of DFT calculations applying both PW91 and PBE functionals and the plane wave basis sets on the Pt clusters having 3–25 atoms and a Pt(111) slab, with and without O and S adsorbates. The adsorption energies varied significantly with the cluster size, while Pt₁₀ was shown to have the largest variation from the adsorption energies of the Pt(111) slab indicating that it is a poor model for the Pt(111) slab. They found that the difference in the binding energy per atom between bulk Pt and small clusters is proportional to the (cluster size)^{-1/3}. It was reported that the adsorption energy of S is greater than that of O on the Pt clusters as well as on the semi-infinite slab.

Theoretical investigations on X-ray absorption near edge structure (XANES) of Pt clusters have been done to study their sensitivity toward the size and shape of small Pt_n clusters.^{99,100} Bazin et al. used a non self-consistent FEFF7 code for their calculations and covered only Pt clusters of 13, 19, 43, 55 atoms with fcc structure (O_h symmetry).⁹⁹ However, Ankudinov et al. performed their calculations with an improved, ab initio relativistic, self-consistent code FEFF8, which is based on a full multiple scattering, real-space Green’s function formalism.¹⁰⁰ Therefore, they obtained more reliable results for the intensity of the white line as a function of the cluster size and extended the studies to Pt clusters with various symmetries.

The PW91 level of theory along with a plane wave basis set has been used to study Pt clusters up to 55 atoms, and these systems have been compared for their stabilities, HOMO–LUMO gaps, and magnetic moments.¹⁰¹ Xiao et al. found that the binding energy increases; however, the relative stability of the Pt clusters is not affected by the consideration of spin–orbit coupling. They also found that out of several different isomers of 10-atom Pt clusters, the tetrahedral Pt₁₀ is the most stable, whereas Pt₅₅ is most stable in the icosahedral geometry. Moreover, they found more stable isomers for Pt₁₃ other than the icosahedron and the cubooctahedron.¹⁰¹ Yang et al. also confirmed this fact in an earlier study on small Pt clusters that was performed with the CA exchange correlation functional within LDA.¹⁰² Xiao et al. reported that most of the Pt clusters are ferromagnetic and the highly magnetic clusters tend to have large HOMO–LUMO band gaps.¹⁰¹ They correlated the binding energy, HOMO–LUMO gap, and magnetic moment of the Pt clusters with their size as well as their structure.

Chang and Chou performed PW91/plane wave basis calculations to study the atomic geometry, electronic structure, and magnetic moment of 4d transition-metal clusters with 13 atoms.⁶⁰ Pt₁₃ is of particular interest because it corresponds to the first atomic or geometric shell closure for both icosahedral and cubooctahedral structures. However, Chang and Chou suggested a low-lying structure with a buckled biplanar arrangement that has a C_{2v} symmetry for Pt and other late transition metals with more than half-filled d shells.⁶⁰ They found a smaller spin magnetic moment for this new structure as compared to that of the icosahedron and also reported that their spin magnetic moments are in better agreement with the available experimental values. It was also suggested that the buckled biplanar structure with a larger and irregular surface area is likely to offer a higher catalytic activity to the cluster. This lowest energy buckled biplanar geometry for Pt₁₃ has been confirmed by a later study carried out by Futschek and co-workers within the DFT-PAW/PZ level of theory with a plane wave basis.¹⁰³

A combined molecular dynamics simulations and DFT calculations study has been carried out to investigate the amorphization mechanism of icosahedral Pt nanoclusters.¹⁰⁴ Aprà et al. used the Becke functional to describe exchange and Perdew–Wang functional for correlation with a GTO basis set. The authors proposed an amorphization mechanism of icosahedral (I_h) clusters where the rosettelike structural excitations at the 5-fold vertices take place. In the icosahedral 55-atom cluster, a vertex atom is inserted between the five neighbors on the surface, to form a 6-fold ring centered around the original position of the vertex. The bond directionality effects due to d–d interactions increase the favorability of the rosette for Pt clusters.

Kumar and Kawazoe performed GGA calculations with PAW on the atomic growth pattern of Pt_n clusters up to nanoparticles having a diameter of ~ 3 nm.¹⁰⁵ In agreement with the results of Xiao et al.,¹⁰¹ Kumar and Kawazoe also obtained a stable Pt_{10} with the tetrahedral geometry.¹⁰⁵ The decahedral isomers were reported to be more stable in the range of $20 < n < 25$. The simple cubic structures are generally favorable up to $n = 38$. They observed that the triangle of Pt_6 and the square of Pt_9 are the most significant structural units in the most stable Pt clusters. The octahedral clusters have been found to be more stable beyond $n = 40$, and this trend continued for at least $n \approx 350$. The small magnetic moments of Pt clusters, which are in good agreement with the experiments, tend to decrease with an oscillatory behavior as the cluster size increases.

Six different structural motifs, four with 38 atoms and the other two with 39 atoms of Pt, have been considered to investigate the adsorption of CO molecules and atomic hydrogen on these systems.⁸⁰ Paz-Borbón et al. used GTO basis sets of double- ζ quality along with the PW91 functional. The adsorption of up to 32 CO molecules or H atoms altered the DFT energy ordering of the six structural motifs. The chemisorption of CO flattened the metal cluster potential energy surface while favoring noncrystalline structures, whereas H adsorption released the surface stress while favoring 5-fold symmetry motifs. The experimental findings of structural changes upon catalytic conditions agreed well with these theoretical predictions. The PW91 calculations of Ryu et al. also found a ligand-induced structural evolution of Pt_{55} nanoparticles as the number and the species of the ligand changed.¹⁰⁶ The cuboctahedral structure was found to change into a I_h -based structure through a Mackay transformation mechanism upon addition of 18 methylamines. As more methylamine ligands were added, this structure was observed to return into the original cuboctahedral structure due to the directional orbital hybridization between d-orbitals in the Pt atoms and p-orbitals in the N atoms. However, they observed that the methylthiol-ligated systems do not undergo structural transformations.

PBE calculations with PAW have been performed to study Pt–O bonding interaction on pure Pt and Ni@Pt clusters composed of 55 atoms.¹⁰⁷ The Mackay icosahedron was found to be the most stable isomer for Pt_{55} . Because it has been found that the Pt:Ni ratio should be close to 3:1 to achieve high catalytic activity in oxygen reduction reaction (ORR), Oemry et al. considered only that atomic ratio for the 55-atom cluster in this theoretical study. They constructed the Ni@Pt cluster such that 42 Pt atoms accommodate the cluster surface and a 13-atom Ni icosahedron is positioned in the center. The global trend of Pt–O bonding strength in the pure Pt and Ni@Pt clusters was found to vary significantly with the oxygen adsorption site.

Bimetallic nanoparticles are of special interest due to their novel chemical and physical properties. Such nanoparticles containing Pt have been reported to show better catalytic activities. Most of the earlier theoretical studies on binary nanoalloys Ni–Pt, Pd–Pt, Cu–Pt, Pt–Ag, Pt–Au, and many more have been reviewed by Ferrando et al.,¹⁰⁸ and thus will not be discussed here. Recently, Wang and Johnson investigated 132 binary-alloyed nanoparticle systems using the GGA level of theory and compared their segregation energies to determine core–shell preferences.⁵² It was found that having Au, Ag, Cu, and Pd as an impurity and Pt as the majority is preferred in 55-atom binary alloy nanoparticles. Furthermore,

they found that the binary alloys with a Fe, Co, Ni, Rh, Ru, Ir, or Os core and a Pt shell are stable.⁵²

A combined empirical potential (EP)/DFT method has been used to study 38-atom Pd–Pt and Ag–Pt nanoalloys.⁸² Paz-Borbón et al. used the GTO basis sets of double- ζ quality along with the PW91 functional in the DFT calculations. Figure 3 shows the 11 structural motifs considered in this study.

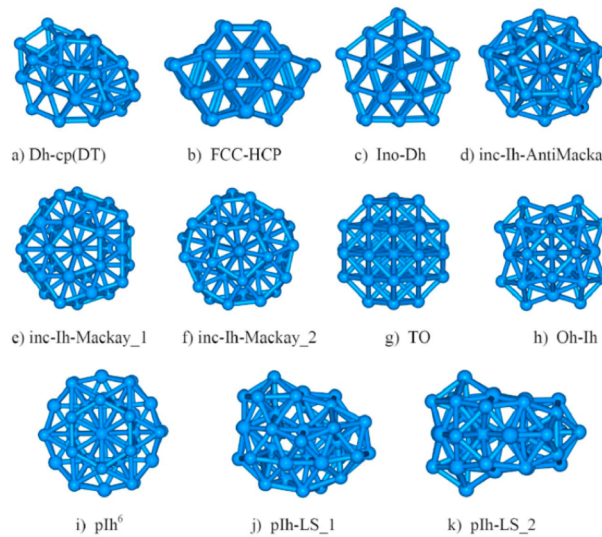


Figure 3. Eleven structural motifs studied for 38-atom binary clusters composed of elements from groups 10 and 11 of the periodic table. Reprinted with permission from ref 82. Copyright 2008 AIP Publishing LLC.

The DFT calculations suggested that the novel O_h – I_h mixed arrangement is a low energy isomer for both Pd–Pt and Ag–Pt pairs at composition 24–14. Even though $n = 38$ is a magic number for truncated octahedral (TO), the favorability toward O_h – I_h arrangement suggests that Pd–Pt and Ag–Pt at this size range prefer to obtain mixed 5-fold symmetric/close-packed or decahedral arrangements. When charge-transfer effects are not strong, segregation is mainly determined by minimization of surface energy and maximization of the strongest bond interactions. The preferred segregations were found to be $\text{Pd}_{\text{shell}}\text{Pt}_{\text{core}}$ and $\text{Ag}_{\text{shell}}\text{Pt}_{\text{core}}$. They reported that the “stickier” third-row transition metals tend to occupy the core, while the “less sticky” second-row transition metals grow on the surface forming 5-fold-symmetric motifs.⁸²

Pd–Pt core–shell type nanoclusters have been studied by means of UB3LYP/LANL2DZ, and Pt_{13} , Pd/Pt_{12} , and $\text{Pd}_6/\text{Pt}_{32}$ clusters have been considered.¹⁰⁹ Okumura et al. observed that the surface charge density distribution of these core–shell clusters is significantly different from that of their monometallic clusters. In a heterojunction site of a core–shell cluster, a charge polarization is induced due to the charge transfer from a Pd to a Pt atom. Hence, it was reported that these heterojunctions play a vital role in modifying the electronic state of the cluster surface.

Barcaro et al. studied $\text{MgO}(100)$ supported CoPt nanoclusters with a total number of atoms $n = 20, 40, 48, 50, 62, 64$, and 80.¹¹⁰ First, they carried out global search optimizations with a tight-binding empirical potential and then DFT calculations using the PBE exchange correlation functional. For $n = 20$, they found a global minimum of a double icosahedron with 19 atoms plus a lateral atom. The 40-atom

CoPt cluster is most stable in the polyicosahedral (pIh) structure exhibiting a 6-fold symmetry axis ($\text{pIh}6$) plus two lateral Co atoms. Even for larger clusters, occurrence of pIh motifs in the lowest energy isomers has been identified.

Plane-wave DFT calculations combined with symmetry orbit approach have been performed to investigate face-centered-cubic-like PdPt nanoparticles with 38–201 atoms. In contrast to the previous theoretical studies^{82,109} and despite the larger Pt bulk energy, Barcaro et al. found a strange Pt surface segregation in Pd-rich particles (Figure 4). They attributed

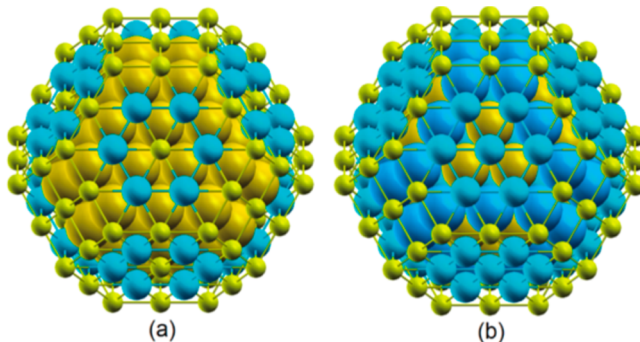


Figure 4. Optimal chemical ordering of (a) $\text{Pd}_{153}\text{Pt}_{48}$ and (b) $\text{Pd}_{110}\text{Pt}_{91}$ (around 1:1) nanoparticles. The different sizes of atoms highlight the patchy multishell pattern in the 1:1 composition. The yellow atoms represent Pd and blue is for Pt. Reprinted with permission from ref 111. Copyright 2011 American Chemical Society.

this unusual behavior to the interplay of metal–metal homo and hetero interactions. Furthermore, they observed a novel multishell pattern of the compositions around 1:1 in which each shell is decorated by “patches” of like atoms.¹¹¹

2.2. Group 11

2.2.1. Gold. Gold has been of interest to researchers for many decades due to its wide variety of applications in catalysis, sensing, and biotagging. The properties of gold nanoparticles and clusters are known to vary widely as the size of the system decreases, so many researchers have examined the structures and properties of gold clusters as a function of size.

2.2.1.1. Geometric Structures. The structures of pure gold clusters and especially the two-dimensional to three-dimensional structural transition have been of interest to researchers for many years. Many studies have examined small clusters with fewer than 20 atoms, as reviewed recently.¹¹² In this Review, we focus on systems with at least 20 gold atoms.

Some of the earliest work on large systems focused on symmetrical structures. In 1994, Häberlen et al. examined octahedral and icosahedral Au_{55} using the VWN functional and found that the Kohn–Sham orbitals and their energy orderings agreed well with a jellium model once energy level splittings due to symmetry reduction were considered.¹¹³ They found that relativistic calculations lowered the energy levels arising from s orbitals toward the d-band. In 1997, Häberlen et al. examined O_h -symmetric Au_{38} , Au_{44} , and Au_{55} , as well as I_h -symmetric Au_{55} and Au_{147} .¹¹⁴ They found that the VWN functional predicts average gold–gold distances whose extrapolated values are in better agreement with experiment than BP86. However, the cohesive energies per atom were found to be better for BP86. The energy differences between the two Au_{55} structures were found to be small, although the icosahedral structure was preferred by <0.1 eV.

In 1998, Garzón et al. employed a genetic algorithm using a Gupta n -body potential followed by LDA calculations and determined that the lowest energy isomers of Au_{38} and Au_{55} are amorphous or disordered structures instead of O_h - or I_h -symmetric clusters; however, the difference in energy was found to be less than 0.4 meV/atom for Au_{38} and 9.4 meV/atom for Au_{55} .¹¹⁵ On the other hand, for Au_{75} the decahedral structure was found to be 5.7 meV/atom lower in energy than the closest amorphous structure.¹¹⁵ They later attributed the disordered structures for gold to be due to the short-range nature of its interatomic potential, whereas nickel and silver have a longer range potential that leads to more ordered structures.^{116,117} They employed the concept of local stress to explain the physical nature of the amorphization; they found that the compact ordered structures are destabilized by the tendency of the metallic bonds to contract at the surface because of decreased coordination.¹¹⁸ In 2002, Garzón et al. found a disordered structure for the lowest-energy structure of Au_{28} as well as thiol-passivated $\text{Au}_{28}(\text{SCH}_3)_{16}$ and $\text{Au}_{38}(\text{SCH}_3)_{24}$.¹¹⁹ Using the Hausdorff chirality measure, they predicted that the cores of passivated clusters are more chiral than bare clusters.

Häkkinen et al. presented a combined theory-experiment investigation of Au_n^- , Ag_n^- , and Cu_n^- ($n = 53–58$), and ascertained that Au_{55}^- does not adopt icosahedral symmetry, unlike Ag_{55}^- and Cu_{55}^- , which they attributed to relativistic effects that lead to significant s–d hybridization and direct d–d bonding effects.^{120,121} Huang et al. later studied Au_n^- ($n = 55–64$) in a combined PES-theory examination.¹²² They found that although all of these clusters possess low (C_1) symmetry, these nanoparticles have a core–shell structure. Au_{58}^- was found to be nearly spherical with an inner core of 12 atoms. All larger clusters were found to arise from capping square defects on the Au_{58}^- surface. Later work by Dong and Gong also suggested a core–shell structure for neutral Au_{58} , but found that its inner shell consists of 10 atoms.¹²³

2.2.1.1.1. Neutral Structures. Early work on Au_{20} using an LDA functional found compact, low-symmetry structures to be the lowest in energy.¹²⁴ However, in 2003, Li et al. showed using a combined experiment–theory investigation that the lowest energy structure of the Au_{20} cluster is tetrahedral with a face-centered cubic structure.¹²⁵ They examined six structures using PW91/TZ2P and found that the tetrahedral structure was calculated to have an electron affinity of 2.61 eV without spin–orbit coupling or 2.741 eV with spin–orbit coupling; the latter was in excellent agreement with the measured experimental electron affinity of 2.745 eV from photoelectron spectroscopy (PES). Tetrahedral Au_{20} was also computed to have a HOMO–LUMO gap of 1.818 eV, which was in very good agreement with experimental estimates.

Numerous groups have since examined tetrahedral Au_{20} . Wang et al. examined Au_{20} , Ag_{20} , and Cu_{20} with PW91 and suggested that Au_{20} and Ag_{20} adopt a tetrahedral structure, whereas Cu_{20} is compact with low symmetry.¹²⁶ Later calculations by Fernández et al. agreed with Wang that the tetrahedral structure is lowest energy for Au_{20} , but found amorphous-like structures for Ag_{20} and Cu_{20} using the PBE functional that were lower in energy than the tetrahedral structures.¹²⁷ Wu et al. optimized the structure of Au_{20} using PW91 and incorporated scalar relativistic effects using the zero-order regular approximation (ZORA).¹²⁸ They then calculated its static polarizability and hyperpolarizability using the LB94 functional and predicted that the hyperpolarizability of this system is several times larger than values for typical

organometallic systems with extensive π -conjugation. Xie et al. calculated the optical absorption spectrum for Au_{20} using TDDFT with BP86 and found several peaks below 3 eV.¹²⁹ Aikens and Schatz also found several low-energy excited states arising from intraband excitations, as well as a number of peaks with significant interband character.¹³⁰ Idrobo et al. later agreed that d orbitals are much more important in the spectrum of Au_{20} than the corresponding spectrum of Ag_{20} .¹³¹ In 2008, Castro et al. showed that spin-orbit coupling effects have very small effects on the optical absorption spectrum of Au_{20} .¹³² In 2012, Koppen et al. demonstrated that long-range corrected functionals lead to absorption spectra for Au_{20} that have a strong peak around 3.4–3.7 eV with a few additional peaks in the 2.7–4.1 eV range, but many fewer peaks than previous LDA and GGA functionals.¹³³ Recently, Anak et al. examined the optical absorption spectrum of Au_{20} using LC-M06L, CAM-B3LYP, SAOP, and SAOP with spin-orbit coupling.¹³⁴ They also found that the inclusion of spin-orbit coupling led to minor changes in the optical absorption spectrum and that long-range corrected spectra are somewhat cleaner than the corresponding LDA and GGA spectra.

In 2007, Yoon et al. showed that the d-band states for Au_{20} are very localized, whereas the states arising from the 6s and 6p orbitals of gold yield very free-electron-like, delocalized Kohn-Sham orbitals that can be described with approximate spherical harmonics 1S, 1P, 2S, 1D, 1F, etc. (Figure 5).¹³⁵ The delocalized orbitals have energies below and above the d-band.

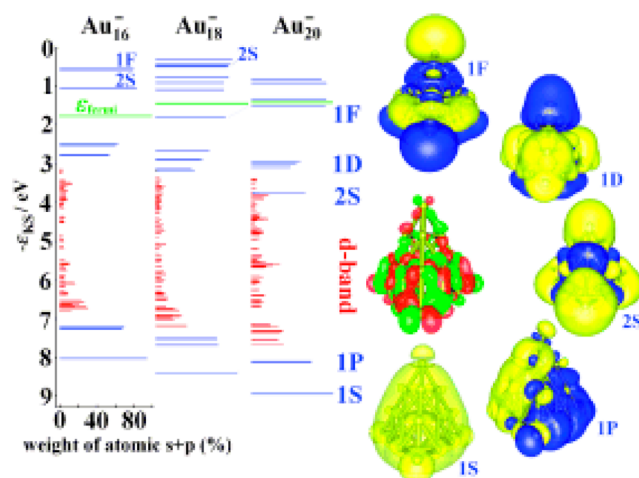


Figure 5. Kohn-Sham orbitals (with labels corresponding to approximate spherical harmonics) and orbital energies for the Au_{20}^- tetrahedron. Reprinted with permission from ref 135. Copyright 2007 John Wiley and Sons.

King et al. described the bonding in Au_{20} as arising from four-center two-electron bonds in each of 10 tetrahedral cavities within the cluster.¹³⁶ A similar partitioning was also proposed by Zubarev and Boldyrev using an adaptive natural density partitioning method.¹³⁷

Using a comparison between TIED data and TPSS/TZVPP calculations, Lechtken et al. showed that Au_{20} , Au_{20}^- , and Au_{20}^+ have tetrahedral-based structures.¹³⁸ Kryachko and Remacle considered the doubly charged clusters Au_{20}^{2-} and Au_{20}^{2+} .¹³⁹ They found that they were stable, although neither was determined to have tetrahedral symmetry.

Many researchers have proposed structures for larger neutral gold clusters in the past decade. Fa et al. calculated structures

for neutral Au_n ($n = 21–26$) using GGA.¹⁴⁰ They found bulk-like geometries (tetrahedral structures plus adatoms) for $n = 21–23$ and 25 and hollow tube-like structures for $n = 24$ and 26. Shortly thereafter, Fa and Dong also found tube-like structures for $n = 26–28$.¹⁴¹ Tian and Zhao examined Au_n ($n = 21–28$) in 2008 using PBE and found bulk-like structures for $n = 21–23$, a tubular structure for Au_{24} , a double-layered structure for Au_{25} , a pyramidal structure for Au_{26} , and tubular structures for Au_{27} and Au_{28} .¹⁴² The Au_{25} and Au_{26} structures they found varied from the previous work of Fa et al. In 2010, Zhao et al. revisited the neutral cluster structures using both PW91 and PBE and agreed with previous results from Fa et al. that the lowest energy Au_n ($n = 21–23$) structures are based on the pyramidal structure, with a tube-like structure for Au_{24} in agreement with Tian and Zhao; for $n = 27–28$, they found hollow columnar structures with a single additional atom on the axis instead of hollow tube-like configurations.¹⁴³ Yang, Fa, and Dong later found a new pyramidal isomer for Au_{23} , which was predicted to be 0.05 eV lower in energy than the previous pyramidal Au_{23} isomer at the PBE level of theory; they calculated IR spectra for Au_n structures up to $n = 26$.¹⁴⁴

Au_{32} has been a cluster of particular interest ever since Johansson et al. and Gu et al. predicted that this system would have a fullerene-like form with icosahedral symmetry.^{145,146} Using BP86 and PBE0, Johansson et al. showed that this cluster would be 7–10 kJ/mol/atom more stable than Au_{20} .¹⁴⁵ Gu et al. also examined Au_n ($n = 33–35$) with atoms inside the Au_{32} icosahedral cage and predicted that Au_{32} does not want to accept another atom.¹⁴⁶ A year later, Ji et al. revisited the Au_{32} system and found that, although the icosahedral structure is the most stable geometry at 0 K, vibrational entropy contributions mean that a C_1 structure becomes lowest in energy above about 300 K;¹⁴⁷ this will be discussed further below. In 2010, Zhao et al. calculated structures for Au_n ($n = 29–32$) including structures motivated by fullerenes.¹⁴³ They found that the lowest energy isomers were indeed hollow cage fullerene-like structures, although with lower symmetry. A year later, Tian et al. agreed that the Au_n ($n = 29–32$) structures consist of hollow cages, and proposed that the lowest energy geometries of $n = 33–35$ are amorphous core-shell structures.¹⁴⁸

Since the prediction of I_h symmetry for Au_{32} , additional icosahedral gold clusters have been proposed. In 2005, Gao and Zeng calculated an I_h -symmetric structure for Au_{42} using both the BP86 and the B3LYP functionals.¹⁴⁹ They found that this structure was about 0.7 eV higher in energy than two compact structures and did not satisfy the $2(N + 1)^2$ for spherical aromaticity, but it was predicted to have a HOMO-LUMO gap of 0.4–0.9 eV. Wang et al. evaluated the structures of neutral gold clusters including Au_{50} and predicted that a C_2 -symmetric hollow cage structure would be more stable than compact forms; they calculated a HOMO-LUMO gap of 0.83 eV using the PBE functional.¹⁵⁰ In 2007 using the same level of theory, Tian et al. computed a new D_{6d} cage for Au_{50} , which possessed a HOMO-LUMO gap of 1.07 eV and was determined to lie 0.255 eV lower in energy than the C_2 cage.¹⁵¹ Karttunen et al. then predicted an icosahedral, chiral structure for Au_{72} (Figure 6), which fulfilled the $2(N + 1)^2$ rule for aromaticity.¹⁵² At the BP86/def2-TZVP level of theory, this structure is calculated to have a HOMO-LUMO gap of 0.72 eV and to be 23.4 kJ/mol/atom more stable than tetrahedral Au_{20} ; using MP2/def2-TZVP single point energy calculations, this structure is predicted to be 51.3 kJ/mol/atom more stable than Au_{20} .

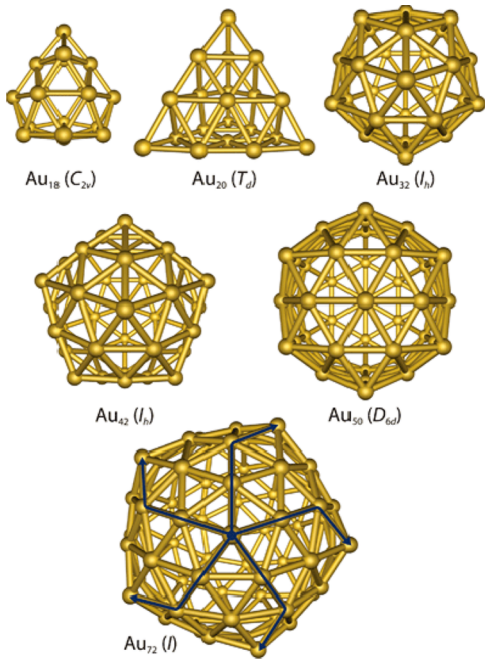


Figure 6. Optimized structures of Au_n cages. The chirality of Au_{72} is shown on the figure. Reprinted with permission from ref 152. Copyright 2008 Royal Society of Chemistry.

In 2011, Jiang and Walter examined structures for Au_{40} using a PBE-based basin-hopping search.¹⁵³ They found that the lowest energy isomer with C_1 symmetry has a HOMO–LUMO gap of 0.69 eV. A C_3 isomer was found to be only 0.15 eV higher in energy with a HOMO–LUMO gap of 0.85 eV. Both isomers can be described as twisted pyramids: the top three layers look like tetrahedral Au_{20} . The angular momentum projected density of states showed that the HOMO has F-like symmetry whereas the LUMO has G-like symmetry, as expected for a cluster with 40 delocalized electrons.

Also in 2011, Liu et al. examined helical Au_n ($n = 24, 32, 40$) with three, four, and five atoms in the central core surrounded by 21, 28, and 35 atoms, respectively.¹⁵⁴ Using a variety of density functionals including BP86 and B3P86, they found that their helical Au_{40} structure was competitive energetically with a more compact Au_{40} structure. They also predicted that it would have a larger HOMO–LUMO gap than the compact Au_{40} isomer.

Wang et al. proposed hollow tube-like structures for Au_n ($n = 37, 42, 47, 52, 57, 62, 67, 72, \dots$) based on a (5,5) single-wall gold nanotube capped on both ends by one-half of a fullerene-like Au_{32} using the PBE, PW91, BP86, and BLYP functionals.¹⁵⁵ They found that their proposed Au_{42} structure is lower in energy than the icosahedral structure previously examined, although their Au_{72} nanotube structure is higher in energy than the icosahedral form.

Zhao et al. considered hollow tube-like structures for Au_n ($n = 14, 20, 26, 32, 38, 44, 50$, and 74) built by adding rows of six atoms to a D_{6h} structure of Au_{14} .¹⁵⁶ They found that all geometries are local minima. Their Au_{14} , Au_{26} , and Au_{44} systems were found to have the highest HOMO–LUMO gaps, with a gap of 0.70 eV for Au_{44} .

2.2.1.2. Anionic Structures. Because of the success of photoelectron spectroscopy in elucidating the structure of Au_{20} and other smaller clusters, a number of researchers have investigated anionic gold clusters. Xing, Yoon, and co-workers

used a Born–Oppenheimer (BO) local spin-density functional (LSD) molecular dynamics (MD) simulation method with the PBE functional and scalar relativistic pseudopotentials to predict structures for Au_n^- ($n = 21–24$).^{135,157} They found that the electron diffraction pattern of Au_{21}^- is radically different from that for Au_{20}^- ; they found an elongated cage structure to be the best fit for the experimental diffraction pattern, although this structure was predicted to lie 0.16 eV above the ground-state structure consisting of a tetrahedron with an adatom. For Au_{24}^- , Xing, Yoon, and co-workers predicted that an elongated cage-like structure is the lowest energy and provides the best fit to the diffraction pattern.^{135,157} For Au_{22}^- and Au_{23}^- , they found a novel “pita-pocket-like” double-layer structure with several close-lying isomers.

About the same time, an independent study by Bulusu et al. on Au_n^- ($n = 21–25$) also predicted that the lowest energy isomer for Au_{21}^- is a tetrahedral structure with an adatom.¹⁵⁸ However, MP2 single point calculations at the PBE geometries predicted that this structure would lie 1.15 eV higher in energy than a structure created by fusing two planar gold structures at an edge; they also suggested that the planar-fused isomer provided the best agreement with experimental PES data, although the agreement was only moderate. Hollow tubular structures were found to lie 0.4–0.5 eV higher in energy than the ground state at both the PBE and the MP2 levels of theory. For Au_{22}^- , they calculated that the planar-fused structure, which was the second lowest energy isomer after the pyramidal ground-state geometry, gave the best agreement with PES data. For Au_{23}^- , the pyramidal ground state gave good agreement with the experimental PES data but could not fully explain all peaks, which suggested the presence of multiple isomers as found for smaller clusters. For Au_{24}^- , the lowest energy isomers and the best matches to the PES data were found to be hollow tube-like structures. Interestingly, they found a different structure from the one predicted by Xing and co-workers. For Au_{25}^- , they predicted the lowest energy isomer to be a hollow structure, but the best match to the PES data was provided by the second lowest energy isomer, which was a core–shell structure with an endohedral atom. They emphasized that different levels of theory provide different results, so additional calculations should be performed on these systems to fully elucidate the isomers present experimentally.

In 2005, a combined PES-theoretical investigation examined the Au_{32} cluster.¹⁴⁷ In addition to revisiting the neutral structure, the authors examined the structure of Au_{32}^- and determined that the hollow icosahedral structure with a slight Jahn–Teller distortion to D_{3d} was predicted to be the lowest energy isomer at the PW91/TZ2P level of theory. They found several other cage-like isomers that were also calculated to lie very close ($\Delta E \geq 0.01$ eV) in energy. On the basis of the calculated adiabatic and vertical detachment energies and HOMO–LUMO gaps, the icosahedral structure was shown to not match experimental PES data. The authors instead ascertained that a compact C_1 cluster that was 0.4 eV higher in energy than the lowest energy structure was likely the isomer observed experimentally. Vibrational entropy contributions calculated using harmonic frequencies of each isomer suggested that the C_1 isomer became favored at about 300 K. Jalbout et al. later showed that the global minimum structure for Au_{32}^- at the PBE level of theory is a C_1 isomer, which is 0.67 eV lower in energy than the icosahedral cage structure.¹⁵⁹ The HOMO–LUMO gap of 0.34 eV for this C_1 isomer was found to be in good agreement with the experimental HOMO–LUMO gap of

0.30 eV. This distorted structure was also determined to be the lowest energy structure for Au_{32}^+ , whereas the icosahedral cage structure was confirmed to be the global minimum for neutral Au_{32} .

In 2007, Lechtken et al. examined the Au_{34}^- cluster using both experiment and theory and proposed a chiral C_3 structure for the global minimum.¹⁶⁰ This structure has four interior atoms and has a symmetry reminiscent of a slightly distorted modified truncated octahedron. Other isomers were found to lay only 0.05 eV higher in energy. The authors calculated PES spectra using TDDFT and found moderate agreement between the C_3 structure and experiment. Gu et al. also considered the structure of Au_{34}^- and predicted that the lowest energy structure is a C_1 structure with four interior atoms.¹⁶¹ These authors considered the PW91, PBE, and MP2 levels of theory with a variety of basis sets. They also found a C_3 structure, although it was predicted to lay 0.09 eV higher in energy than their lowest energy C_1 structure. The lowest energy structures they found also had four interior atoms in agreement with the results of Lechtken et al. Because of the wide variety of structures with similar energies, Gu et al. suggested that the cluster was likely fluxional. They calculated PES spectra for their nine lowest energy isomers and determined that the lowest energy C_1 structure agreed best with experiment. A later study by Santizo et al. using the PBE functional agreed that C_1 and C_3 isomers for Au_{34}^- are nearly degenerate, with the C_1 isomer 0.03 eV lower in energy.¹⁶² They then calculated optical absorption and circular dichroism spectra for these isomers and suggested that circular dichroism (CD) spectra may provide a way to distinguish the isomers experimentally,¹⁶² although it should be noted that this would require that the structures be rigid enough that their enantiomers can be separated.

Shao et al. later considered the structures of Au_n^- ($n = 27$ – 35) in a combined PES-theory investigation.¹⁶³ They found that all structures in this range exhibit core–shell type structures. Au_{27}^- , Au_{28}^- , and Au_{30}^- contain one core atom, Au_{32}^- has three core atoms, and Au_{33 – $35}^-$ have four core atoms. This group later examined Au_n^- ($n = 36$ – 38) and ascertained that these systems have pyramidal, fcc-like geometries.¹⁶⁴ The pyramidal, bulk-like structures are similar to the neutral Au_{40} structure discussed above that was suggested by Jiang and Walter.¹⁵³

2.2.1.2. Optical Absorption. As discussed in the last section, TDDFT calculations are often employed as one means of determining the experimentally relevant structure or structures. Although many of the studies of bare gold clusters have focused on determining the global energy minima for these systems, other studies have examined the properties of symmetric bare gold clusters as models for larger systems; these structures may not be global minimum for the sizes of interest, but the trends in their optical absorption spectra are useful.

In 2007, Stener et al. published the optical excitation spectra of octahedral Au_6^{4+} , Au_{44}^{4+} , and Au_{146}^{2+} clusters using the VWN functional with both double and triple- ζ basis sets.¹⁶⁵ They found that the optical absorption spectra of these systems were quite broad, which can be attributed to the small 6s–5d gap, with significant intensity starting around 3 eV. They determined that the spectra are red-shifted as the particle size increases. Later, Durante et al. compared the optical absorption of the octahedral Au_{146}^{2+} , cuboctahedral $\text{Au}_{147}^{5+,1+}$, icosahedral Au_{147}^{5-} , and cubic Au_{172}^{4+} nanoparticles calculated with the LB94 and VWN functionals.¹⁶⁶ They found that LB94 yielded excitation energies in better agreement with experiment than

VWN. The spectra of these systems were again quite broad, with high intensity around 3 eV calculated with the LB94 functional.

Using RT-TDDFT, Weissker and Mottet examined the optical absorption spectra of Au_{13} , Au_{38} , Au_{55} , and Au_{140} with cuboctahedral, icosahedral, and truncated octahedral symmetries.¹⁶⁷ They found very few strong peaks in the absorption spectra, which they attributed to damping from the d electrons. Burgess and Keast likewise studied the optical absorption spectrum of cuboctahedral and icosahedral Au_{55} ; they too found a very broad absorption spectrum for this system.¹⁶⁸

One of the earliest systems examined was atomic chains of gold atoms. Lian et al. calculated the absorption spectrum for linear gold chains up to 20 atoms using TDDFT with PW91/LANL2DZ.¹⁶⁹ They found that the longitudinal plasmon resonance red-shifted with increasing size, and that peaks in the 1.3–3.0 eV region have some oscillator strength. Guidez and Aikens examined similar systems using SAOP and LB94 model potentials.¹⁷⁰ They determined that the first peak red-shifts with increasing length, but found that this red-shift was not linearly dependent on length due to mixing with excitations out of the d band. They found that the peaks in the 1.5–3.5 eV region are primarily due to excitations out of the d band.

In 2010, Liao et al. performed TDDFT calculations using the BP86 functional with a double- ζ basis set on the hollow tube-like Au_n ($n = 14, 20, 26, 32, 38, 44, 50, 74$) proposed by Zhao et al. and on a series of cigar-like structures Au_n ($n = 12, 18, 24, 30, 36, 42, 48, 54, 66, 78, 84$).¹⁷¹ They found very broad spectra for systems with a smaller number of atoms, which was again attributed to mixing between the d and s bands, and a sharp longitudinal plasmon peak only arose for $n > 36$.

In 2013, Guidez and Aikens investigated the TDDFT optical absorption spectra of a series of gold nanorods with increasing diameters.¹⁷² Using LB94/DZ calculations, they computed the excitation energies of systems with a six-atom pentagonal cross section Au_n ($n = 19, 31, 43, 55, 67$), an 11-atom star-shaped cross section Au_n ($n = 18, 29, 40, 51, 62, 73$), and a 16-atom pentagonal cross section Au_n ($n = 23, 39, 55, 71$). They ascertained that the orbitals near the HOMO–LUMO gap have delocalized cylindrical symmetry arising from the sp atomic orbitals, with localized d-band orbitals slightly lower in energy (Figure 7). They observed broadened spectra relative to the corresponding silver nanoparticles, which was due to strong contributions from transitions arising from the d band. For a given diameter, the sharpest longitudinal peaks were observed for the longest diameters.

Shortly thereafter, Piccini et al. examined the optical absorption spectra of a series of linear atomic wires Au_n ($n = 14, 20, 30$) and thicker nanorods Au_n ($n = 32, 50, 68, 86, 122$) grown along the $\langle 110 \rangle$ direction, and nanorods Au_n ($n = 38, 76, 114$) grown along the $\langle 111 \rangle$ direction.¹⁷³ They found that a sharp longitudinal peak occurs for the atomic wires, but for systems with a thicker diameter, a sharp longitudinal peak only appears for the two longest nanorods Au_{86} and Au_{122} . A sharp longitudinal peak was also observed for Au_{66} with an intermediate diameter.

Around the same time, López-Lozano et al. published a real-time TDDFT study of gold nanorods with a six-atom pentagonal cross section and a 16-atom pentagonal cross section.¹⁷⁴ They found that the longitudinal peak becomes sharper as the length increases for a given diameter and that the d band of the larger nanorods is smoother than that in the thinner rods. Snapshots of the electron density for an Au_{145}

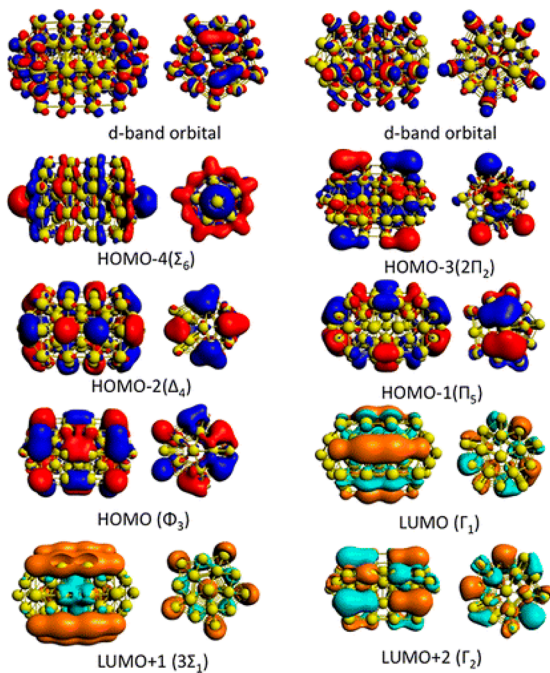


Figure 7. Side and end views of Kohn–Sham orbitals of Au_{71}^{3-} near the HOMO–LUMO gap showing delocalized sp-band orbitals with cylindrical symmetry and localized d-band orbitals. Reprinted with permission from ref 172. Copyright 2013 American Chemical Society.

nanorod show a very clear dipolar motion of the electrons along the long axis of the nanoparticle as expected for a longitudinal dipolar plasmon resonance.

Burgess and Keast performed a RT-TDDFT study of gold clusters cut from the bulk with up to 171 atoms.¹⁷⁵ A variety of symmetries were examined, including systems with very low symmetry. The calculated optical absorption spectra were found to be very broad.

2.2.1.3. Magnetic Properties. In 2007, Magyar et al. examined the magnetic properties of symmetric gold nanoclusters with up to 68 atoms using PBE, B3LYP, and PBE1PBE.¹⁷⁶ They predicted that the magnetism is localized to the surface of the nanoparticles, whereas the core of the nanoparticles is essentially diamagnetic. They found that the magnetic moment per atom will decrease as the cluster size increases.

Luo et al. examined the magnetic properties of icosahedral Au_{13} , Au_{55} , and Au_{147} and of octahedral and truncated octahedral Au_6 , Au_{13} , Au_{19} , Au_{38} , Au_{44} , and Au_{55} using the Perdew–Zunger LDA and Perdew–Wang GGA functionals.¹⁷⁷ They predicted a magnetic moments of $5 \mu_B$ for icosahedral Au_{13} , which was attributed to degenerate D-like superatom orbitals composed of Au 6s orbitals.

In 2011, Pundlik et al. examined the magnetic properties of Au_n clusters ($n = 12, 13, 24, 25$).¹⁷⁸ They found that Jahn–Teller distortion in cuboctahedral Au_{12} and Au_{13} clusters leads to induced magnetism in these systems. They predicted magnetic moments up to $5 \mu_B$ for icosahedral Au_{13} when only scalar relativistic effects were included. Inclusion of spin–orbit coupling led to substantially decreased magnetic moments for Au_{12} and Au_{13} ; the magnetic moment for Au_{13} with SOC was predicted to be $1 \mu_B$. They also found that the electrons responsible for magnetism in these clusters have sp character and not purely s character.

2.2.1.4. Electronic Properties. Gusso calculated electron energy loss spectra (ELNES) of cuboctahedral gold clusters.¹⁷⁹ The author computed the ground-state charge density and the Kohn–Sham effective potential using the VWN functional. A Green’s function multiple scattering approach then was employed to determine the ELNES spectra. The ELNES spectra did not change systematically as the cluster size increased, which made identification of size-dependent trends challenging.

Majumdar et al. investigated a series of cubic gold clusters with up to 2016 atoms, where DFT calculations (B3LYP/SBKJC) were employed on the Au_{63} and Au_{126} clusters as calibration for PM6 and molecular mechanics calculations.¹⁸⁰ They calculated the HOMO–LUMO gaps of Au_{63} and Au_{126} to be 1.06 and 0.50 eV, respectively, using DFT. DFT-calibrated PM6 values led the authors to predict a HOMO–LUMO gap of 0.26 eV for Au_{1512} .

2.2.1.5. Adsorbate Binding. A number of studies have examined ligand binding to gold clusters. In 2004, Zhang et al. synthesized a $\text{Au}_{20}(\text{PPh}_3)_8$ complex and measured its stoichiometry via mass spectrometry; they found that four of the triphenylphosphine compounds were labile in collision-induced dissociation experiments.¹⁸¹ They optimized the structure of $\text{Au}_{20}(\text{PPh}_3)_4$ and model $\text{Au}_{20}(\text{PH}_3)_4$ and $\text{Au}_{20}(\text{PH}_3)_8$ compounds using the PW91 functional and calculated the HOMO–LUMO gaps to be 1.44, 1.82, and 1.55 eV, respectively. They also observed that the face-centered atoms moved outward slightly upon PH_3 binding.

Aikens and Schatz examined NH_3 and PH_3 binding to the tetrahedral Au_{20} cluster.¹⁸² Using BP86/TZP, they calculated that PH_3 ligands bind to vertex and face sites with an average binding energy of 0.81 and 0.43 eV, respectively. In contrast, NH_3 ligands were predicted to bind with average binding energies of 0.61 and 0.19 eV, respectively; however, if four ligands were bound to the vertex sites, the binding energies to the face sites dropped to 0.00–0.05 eV. Amine ligands were found to only slightly change the TDDFT absorption spectrum as compared to the bare Au_{20} cluster, whereas phosphine ligands lead to the disappearance of the Au_{20} intraband peak at 2.89 eV and the appearance of a large peak at 3.27 eV.

Provorse and Aikens examined the binding of carboxylates to the Au_{20} nanoparticle using BP86 with DZ and TZP basis sets.¹⁸³ They found that only two anionic formate species would bind in the gas phase. In continuum water solvent, up to four formate ions could bind to the system. Shortly thereafter, Hull et al. investigated the binding of neutral carboxyl radicals to Au_{20} using the same level of theory.¹⁸⁴ They found that at least eight formyloxyl radicals can bind favorably to the nanoparticle. Binding of four or more formyloxyl radicals was determined to induce a structural distortion in the cluster so that the core loses its tetrahedral symmetry.

Early work on thiolate binding to gold nanoparticles has examined the interactions between methylthiolate and benzenethiolate with an octahedral Au_{13} cluster.¹⁸⁵ This group found that significant structural distortions occur when a thiolate is bound to the cluster, but observed few differences between the two thiolates. Shortly thereafter, Genest et al. examined the interactions of 4, 6, and 8 SR ($R = \text{H}, \text{CH}_3$) groups with an octahedral Au_{13} cluster.¹⁸⁶ They determined that the SCH_3 groups bind less strongly to the core than the SH groups. In 2010, Periyasamy et al. considered the binding of 42 SCH_3 groups to icosahedral and cuboctahedral Au_{55} using PW91/plane wave and B3LYP/LANL2MB,6-31+G(d) calcu-

lations.¹⁸⁷ Although previous crystal structures of thiolate-stabilized nanoparticles had shown bridging SR–Au–SR groups (see section 2.2.4), structures with these bridging units were not considered. They predicted that an initial icosahedral structure of Au₅₅ would be preserved with ligation and solvation. Later, Barnsgrover and Aikens examined thiol (HSCH₃) binding to gold clusters including 2D and 3D Au₁₂ and Au₁₃ clusters, T_d Au₂₀, and TO Au₃₈⁴⁺.¹⁸⁸ They found that the barrier to S–H bond dissociation is less than the adsorption energy of the thiol. The hydrogen atom was determined to be relatively mobile on the gold cluster so that two hydrogen atoms from different adsorbed thiols can eventually find each other and evolve H₂. Staple-like SCH₃–Au–SCH₃ groups were ascertained to form on the surface of the gold nanoparticle similar to those observed for thiolate-stabilized nanoparticles (see section 2.2.4).

López-Lozano et al. examined the adsorption of cysteine on a chiral Au₅₅ cluster using the PBE functional.¹⁸⁹ They found that the most favorable adsorption structures had both the thiolate and the amino groups adsorbed to the cluster, preferably at low-coordinated metal atoms. The difference in adsorption energies between left- and right-handed cysteine enantiomers was found to be negligible. Pérez et al. later examined cysteine adsorption on icosahedral and chiral Au₅₅ clusters and found that higher adsorption energies are observed when cysteine adsorbs on asymmetrical bridge sites of low-coordinated gold atoms.¹⁹⁰ Tlahuice-Flores later investigated zwitterionic L-cysteine adsorbed on the Au₂₀ cluster using PBE/DNP with a continuum solvent model.¹⁹¹ He found that adsorption to vertex sites was energetically preferred over binding to face sites; binding of several functional groups was not reported. Four IR peaks of cysteine were found to become 4–7× more intense upon binding to the gold cluster. Hidalgo et al. studied SCH₃ bound to icosahedral Au₅₅ and Ag₅₅ clusters with the PBE functional.¹⁹² They found that thiolate binding distorts the gold cluster more than the silver cluster, which leads to stronger CD signals.

Although not the focus of our Review, a number of researchers have examined catalysis such as CO oxidation on gold clusters. For example, Gao et al. examined the binding of CO and O₂ to neutral and anionic gold clusters with up to 35 atoms.¹⁹³ They found that both molecules adsorb more strongly to anionic gold clusters. This leads to lower barriers in the catalytic reaction. They also observed that the coadsorption energies of the molecules decrease as the cluster size increases, except for the magic cluster Au₃₄ that has additional electronic stability. They found that reasonably strong adsorption of the two molecules leads to higher efficiency for CO oxidation. Kanoun and Cavallo examined O₂ dissociation on a cuboctahedral Au₃₈ nanoparticle.¹⁹⁴ Using revPBE/TZP with dispersion corrections, they found that the O₂ dissociation barrier is only 11.4 kcal/mol, so it is easily achievable under normal conditions.

Sánchez-González et al. examined a perylene diimide (PDI) dye attached to tetrahedral Au₂₀ and Ag₂₀ nanoparticles using a polarizable continuum model to represent the solvent and/or the metal nanoparticle.¹⁹⁵ They employed B3LYP/6-31+G(d) for PDI and LANL2DZ for the metal atoms. They found that the solvatochromic shift is smaller for gold than for silver, and thus the excitation energy transfer rates are affected differently by solvation.

2.2.2. Silver. Silver nanoparticles and clusters have many uses, especially in optical sensing applications such as surface-

enhanced Raman scattering (SERS). In consequence, their structures, optical properties, and adsorbate binding have been studied by many researchers.

2.2.2.1. Geometric Structures. As for gold, some of the earliest work on large systems focused on symmetrical clusters. In 1997, Jennison et al. examined Ag₅₅, Ag₁₃₅, and Ag₁₄₀ with icosahedral and/or cuboctahedral structures using the Perdew–Zunger LDA parametrization.¹⁹⁶ They found that icosahedral structures are energetically preferred. The central atoms in icosahedral structures were computed to have compressions in atomic distances of up to 6% as compared to bulk, but small surface compressions of ~1%, whereas the cuboctahedral structures were found to have core compressions of 1% and surface compressions of 2–3%.

In 2004, a combined theory–experiment investigation of Ag₅₅[−] demonstrated that the photoelectron spectrum of Ag₅₅[−] is well-reproduced by an icosahedral structure, which was also found to be the lowest energy isomer for this cluster size.¹²⁰ Schooss et al. then examined the structures of Ag₅₅[−] and Ag₅₅⁺ using both DFT (BP86 with a SVP basis set) and trapped ion electron diffraction (TIED).¹⁹⁷ Their reduced molecular scattering functions were found to be in excellent agreement with those predicted for icosahedral structures. The lowest energy isomer for Ag₅₅[−] is predicted to be a slightly Jahn–Teller distorted singlet icosahedral structure, although a triplet state with D_{5h} symmetry was found to be almost isoenergetic.

Xing et al. also employed a combination of TIED with DFT calculations using the PBE functional to examine Ag_n⁺ (*n* = 36–46, 55).¹⁹⁸ They found that although clusters with fewer than 55 atoms do not have an icosahedral structure, they do have local 5-fold symmetry. For Ag₃₈⁺, their ground-state structure had truncated octahedral symmetry, but their isomer that best fit the experimental data had 5-fold symmetry. Blom et al. then expanded the combined DFT and TIED studies to investigate the structures of Ag₁₉⁺, Ag₃₈⁺, Ag₅₅⁺, Ag₅₉⁺, Ag₇₅⁺, and Ag₇₉⁺.¹⁹⁹ They found a truncated decahedral structure that was predicted to be 0.26 eV lower in energy than the truncated octahedral structure at the TPSS/TZVP level of theory. They ascertained that icosahedral-based structures were lowest in energy for the other cluster sizes studied in that work.

In 2002, Bonačić-Koutecký et al. investigated the structure of Ag₂₀ using BLYP and predicted that a C₃ structure is lower in energy than T_d or C_{2v} structures.²⁰⁰ Shortly thereafter, Wang et al. found that the C₃ structure was not stable at the PW91/DNP level of theory and predicted that the lowest energy structure of Ag₂₀ is tetrahedral (similar to the recently established¹²⁵ T_d structure of Au₂₀), with a C_s structure only 0.06 eV higher in energy.¹²⁶ However, using PBE Fernández et al. predicted that the lowest energy structure of Ag₂₀ is amorphous with C₁ symmetry and that the T_d structure lies 0.76 eV higher in energy and is the third most stable.¹²⁷ In 2006, Yang et al. also employed PBE using starting structures from corresponding copper clusters and found that the T_d structure of Wang et al. is 0.63 eV less stable than their lowest energy structure and that the distorted tetrahedral structure of Fernández et al. is 0.24 eV less stable than their ground-state structure.²⁰¹ Two years later, Baishya et al. computed TDLDA absorption spectra for the structures of Yang et al. and determined that the shape of the absorption spectrum for their ground-state structure best matched experiment; the theoretical absorption energy was found to be 0.25 eV lower in energy than experiment.²⁰²

In 2007, Tian et al. revisited the structure of Ag_{20} using PW91/DNP and found that the tetrahedral structure is 0.045 eV lower in energy than a C_s structure; however, energies of C_1 structures were not reported.²⁰³ They also examined the structures of Ag_{21} and Ag_{22} and predicted that these are compact. Pereiro and Baldomir investigated Ag_n ($n \leq 23$) clusters and predicted icosahedral-based structures for $n = 20-23$.²⁰⁴ Harb et al. then calculated the structures and optical absorption spectra of Ag_{20} and Ag_{22} using BP86/LANL2DZ.²⁰⁵ They found compact structures for these systems with a 13-atom icosahedral core for Ag_{20} and a 19-atom double icosahedral core for Ag_{22} . Two nearly degenerate isomers (with C_s and C_1 symmetries) were calculated for Ag_{20} , and both exhibited absorption spectra in good agreement with the experimental spectral shape; as for Baishya et al., the theoretical spectra were red-shifted as compared to experiment by about 0.2 eV. Anak et al. later calculated TDDFT absorption spectra for the C_s isomer using CAM-B3LYP/SDD and LC-M06L/SDD and found a broad peak around 4.0 eV that was well-separated from other electronic transitions.¹³⁴

The structures of positively and negatively charged Ag_{20}^{\pm} were calculated by Lechtken et al. using TPSS/TZVPP.¹³⁸ They found that the minimum energy structure of Ag_{20}^+ is based on an incomplete double icosahedron and has C_s symmetry. Several other isomers with structures based on icosahedra were also found within 0.42 eV, and the calculated molecular scattering functions of these systems matched TIED data. For Ag_{20}^- , the lowest energy structure was ascertained to be a distorted decahedral structure with C_s symmetry; five icosahedral-based structures were found within 0.11 eV. The calculated molecular scattering functions of one of the distorted icosahedral structures matched the TIED data slightly better than the distorted decahedral structure, so it was suggested to be a major species present in the ensemble.

In 2012, Yan et al. examined the structures of Ag_n^z ($n = 21-29$; $z = 0, \pm 1$) using PW91/DNP.²⁰⁶ They found that the ground states of Ag_{21-23} generally have cores based on a 13-atom icosahedron or a 19-atom double icosahedron. They found that bulk-like stacking patterns arise for Ag_{24-27} . For Ag_{28} and Ag_{29} , the ground-state structures were predicted to have a C_6 axis of symmetry, with bulk-like structures somewhat higher in energy. They calculated TDDFT absorption spectra for the ground-state structures and found excellent agreement with available experimental data for Ag_{21} , Ag_{23} , Ag_{25} , and Ag_{27} .

Chen et al. calculated the structures of Ag_n ($n < 100$) using an embedded atom potential for $n > 20$ and DFT optimizations for $n \leq 20$.²⁰⁷ The tetrahedral Ag_{20} structure was found to be the lowest in energy using the B3LYP, TPSS, and M06 functionals with the aug-cc-pVDZ-PP basis set. They then employed B3LYP, M06, ω B97XD, and PW91 functionals with the LANL2DZ basis set to calculate normalized atomization energies for silver clusters with up to 100 atoms. They found that the PW91, ω B97XD, and M06 functionals provide normalized atomization energies in good agreement with coupled cluster results for small systems.

Taherkhani et al. examined the energies of TO Ag_{38} , Ag_{38} with a vacancy and an adatom, and Ag_{37} clusters corresponding to TO Ag_{38} with a vacancy using PBE.²⁰⁸ They also calculated the barriers between structures and used these values as inputs to a kinetic Monte Carlo simulation. They found that the barriers to vacancy formation and adatom diffusion were much smaller than corresponding bulk systems, which was attributed to the size of the system.

2.2.2.2. Optical Properties. Some studies have examined the optical absorption spectra of highly symmetric silver clusters as models for larger nanoparticles. In 2008, Aikens et al. presented a TDDFT study of tetrahedral Ag_n ($n = 10, 20, 35, 56, 84, 120$) using the BP86/DZ level of theory.²⁰⁹ They found that filled electronic shells typically lead to the appearance of sharp spectra analogous to the plasmon resonance of larger clusters. The plasmon energies had a $1/L$ dependence on the cluster edge length, and the extrapolated energies agreed with classical electrodynamics modeling. Mayer et al. later used BP86/DZ TDDFT calculations on tetrahedral Ag_{20} , Ag_{84} , and Ag_{120} to parametrize a charge-dipole interaction model for calculating the frequency-dependent polarizability of silver clusters.²¹⁰ In 2011, Khan et al. calculated hyperpolarizabilities for tetrahedral Ag_n ($n = 10, 20, 35, 56$) using TDDFT at the BP86/DZ level of theory.²¹¹ They found that the hyperpolarizability increases with increasing particle size. They predicted a β_0 value of 12.3×10^{-30} esu with the right order of magnitude as their experimental β_0 value of 25.8×10^{-30} esu.

In 2008, Yan and Gao examined the optical absorption spectrum of silver chains up to 18 atoms long.²¹² They employed real-time TDLDA calculations and determined that the longitudinal excitation of the silver chains is not strongly affected by the presence of d electrons in the system, whereas the transverse plasmon modes are suppressed and mixed by the d electrons. Guidez and Aikens investigated excitation of these atomic wires as well as Ag_{20} and Ag_{40} .¹⁷⁰ Using SAOP and LB94 calculations, they demonstrated that the longitudinal peak arises primarily from a HOMO \rightarrow LUMO transition, whereas the transverse excitation originates from a mixture of occupied–unoccupied orbital transitions. The longitudinal peak wavelength was found to vary linearly with the length of the nanowire. The d-band was observable in the absorption spectrum, but was found to be of low intensity as compared to similar gold nanowires.

Johnson and Aikens examined a series of small pentagonal nanorods Ag_n ($n = 13, 19, 25, 31, 37, 43, 49, 55, 61$, and 67) in various charge states with a 6-atom cross section using BP86, LB94, and SAOP with a DZ basis set.²¹³ They found that the strong excited states arose from a linear combination of occupied–unoccupied orbital transitions and determined the reason why the sharp longitudinal excitation has a wavelength that is linearly dependent on the length of the nanorod. Liao et al. then investigated cigar-shaped and pentagonal nanorods with n up to 121 using the BP86/DZP level of theory.²¹⁴ They found that the absorption spectra of smaller rods exhibit multiple peaks, whereas the spectra of larger rods display a single plasmon-like absorption. Silver nanorods with an 11-atom star-shaped cross section Ag_n ($n = 18, 29, 40, 51, 62, 73$) and a 16-atom pentagonal cross section Ag_n ($n = 23, 39, 55, 71, 87$) were calculated at the LB94/DZ level of theory by Guidez and Aikens.²¹⁵ They found that the longitudinal peak was easier to identify as the aspect ratio of the particles became bigger. They determined that the longitudinal peak wavelengths shifted linearly to the red as the nanorod length increased. In addition, they noted that the strong peaks arose from a linear combination of several occupied–unoccupied orbital transitions.

In 2011, Weissker and Mottet investigated the optical absorption spectra of icosahedral and truncated octahedral clusters including Ag_{13} , Ag_{38} , Ag_{55} , Ag_{140} , and Ag_{147} using real-time TDDFT with a GGA exchange-correlation potential.¹⁶⁷ They found that the geometry of the cluster affects the

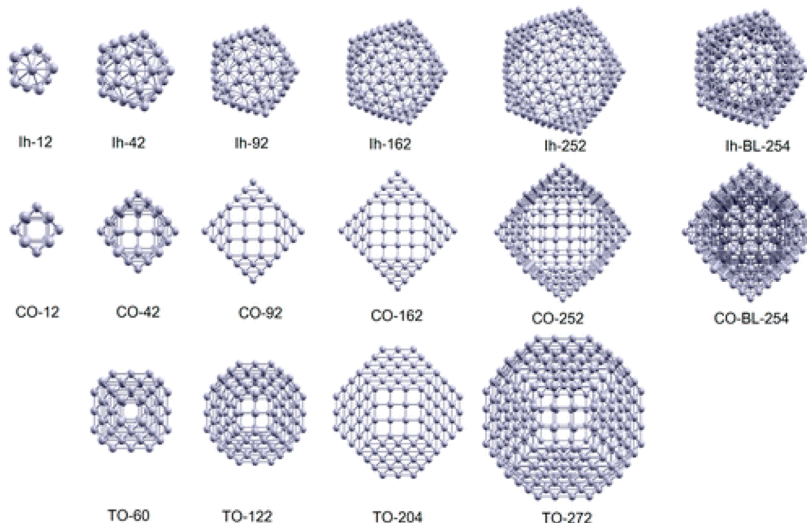


Figure 8. Structures of icosahedral (Ih), cubooctahedral (CO), and truncated octahedral (TO) silver nanocages with the number of atoms shown. Bilayer (BL) cages are also displayed. Reprinted with permission from ref 219. Copyright 2014 American Chemical Society.

absorption spectrum, which shows that calculations with explicit nuclei are necessary for accurate absorption spectra. They observed an overall blue-shift of the absorption spectra with decreasing size, although this blue-shift was hard to quantify due to the complexity of the resulting spectra. Shortly thereafter, Bae and Aikens examined the optical absorption spectra of silver octahedra Ag_n ($n = 6, 19, 44, 85$), truncated octahedra Ag_n ($n = 13, 38, 55, 79$), and icosahedra Ag_n ($n = 13, 43, 55$) with various charge states using the LB94 and SAOP potentials.²¹⁶ They likewise observed a blue-shift with decreasing size, although the shift was not as linear as those discussed above for tetrahedra and nanorods. They noted that the sharp peaks in the absorption spectra arise from a constructive interaction of several occupied–unoccupied orbital transitions.

He and Zeng studied icosahedra up to Ag_{561} and truncated octahedra up to Ag_{586} using LDA with a DZP basis set.²¹⁷ They approximated the optical absorption of these systems by calculating dipolar transition matrix elements between occupied and unoccupied single-particle states; however, they did not consider the coupling between the different single-particle transitions, so collective effects were not accounted for. All electronic transitions were shifted up in energy by 1.28 eV. Their results were fit to a Lorentz model to obtain a unified expression for the intraband ϵ_2 of silver nanoparticles of various sizes.

Weissker et al. examined the optical absorption of icosahedral hollow-shell structures using TDDFT with PBE.²¹⁸ They found that the first strong peak for the Ag_{92} nanoshell is red-shifted as compared to that for the solid Ag_{147} icosahedron. They found that the absorption intensity on a per-atom basis increases for nanoshells as compared to the solid structures. Barcaro et al. also investigated silver nanoshells of up to 272 atoms with icosahedral, octahedral, and truncated octahedral symmetries using the LB94/DZ level of theory (Figure 8).²¹⁹ They found that the absorption spectra progress from complex molecular-like spectra for the smallest systems to a single broad peak for larger systems. They established a linear relationship between the maximum excitation energy and the inverse of the nanoshell radius. They also observed that the spectrum for a nanoshell

such as Ag_{92}^{2+} is shifted by 0.8 eV as compared to that for the solid Ag_{147}^{-} system.

Some researchers have examined the optical absorption spectra of silver nanoparticle dimers. In 2009, Vincenot and Aikens employed TDDFT calculations at the BP86/DZ level of theory to investigate how the absorption spectra of pentagonal silver nanorods Ag_{19}^{+1} , Ag_{25}^{+1} , and Ag_{31}^{+1} that were arranged either in an end-to-end or side-by-side fashion varied with decreasing interparticle distance.²²⁰ In the end-to-end orientation, the longitudinal peak positions slightly red-shifted as the interparticle distance decreased, whereas the transverse peak location remained essentially constant. In the side-by-side orientation, the longitudinal peak slightly blue-shifted with decreasing interparticle distance, while the transverse peak split due to decreasing symmetry. These authors also found that additional low energy peaks attributed to charge-transfer plasmons arose when the interparticle distance became very small. Bae and Aikens later considered the interparticle distance dependence of the absorption spectra of dimers of Ag_4^{2+} , Ag_8 , and Ag_{20} tetrahedra using CIS and TDDFT.²²¹ They found that additional low energy peaks arose in SAOP/DZ calculations in addition to a red-shift of the longitudinal peak with decreasing interparticle distance, whereas CAM-B3LYP/SBKJC and CIS/SBKJC calculations exhibited the red-shift of the longitudinal peak without the appearance of additional low energy peaks. This suggested that some of the additional peaks may be charge-transfer artifacts from standard TDDFT; however, charge-transfer plasmons are known, and the exact relationship between these peaks has not yet been established.

In 2010, Silverstein and Jensen examined the optical absorption spectrum for Ag_{20} and smaller silver clusters using density functionals including PBE, PBE0, and LC-PBE.²²² They found that these functionals placed the strong absorption peak at 3.51, 3.78, and 3.97 eV, respectively, as compared to the experimental peak at 3.70 eV. For smaller clusters, LC-PBE performed the best. The long-range corrected functionals were found to reduce the number of spurious states in the optical absorption spectra. In 2013, Rabilloud presented a benchmarking study for the optical absorption spectra of silver clusters with sizes up to Ag_{20} and Ag_{22} .²²³ He found that long-range corrected functionals lead to a strong reduction of the number

of calculated excited states due to the removal of spurious charge-transfer states. He found that the long-range corrected functionals typically lead to spectra that are blue-shifted as compared to experiment; the best functionals for Ag_{20} were found to be CAM-B3LYP and ωB97x , which were only blue-shifted by about 0.2 eV.

2.2.2.3. Electron Transfer. In 2011, Chen et al. introduced an approach to examine photoinduced electron transfer (PIET) using constrained real-time time-dependent DFT.²²⁴ They modeled electron transfer rates in a (Ag_{20} –Ag)⁺ complex consisting of a tetrahedral Ag_{20} cluster and a silver atom. They found that PIET is a very small component of the overall light absorption process. It was found to be very inefficient for this model silver system, which was attributed to the strong damping known for plasmonic systems. These researchers later extended their theoretical method to a hybrid quantum mechanics/classical mechanics model so that they could incorporate the effect of aqueous solvation on PIET.²²⁵ They found that explicit solvation via classical water molecules led to larger reorganization energies, and thus a smaller ground-state electron transfer rate.

2.2.2.4. Adsorbate Binding. Cluster models of silver have often been employed to model adsorbate binding to surfaces; although many of these employ only few atom clusters, some of these involve large systems. In 2002, Tielens et al. employed a Ag_{23} cluster as a model of the (100) surface of bulk silver.²²⁶ They performed calculations at the B3PW91/LANL2DZ and BP86/TZP levels of theory. Vibrational frequencies of SCN[−] adsorbed in possible adsorption geometries such as hollow and atop sites were calculated. They found that adsorption via the sulfur atom at the atop site is preferred. From the frequency calculations, they found that the frequency shifts were also in agreement with binding via the sulfur atom in a direction orthogonal to the surface. Tobita and Yasuda utilized a Ag_{22} cluster as a model of the (111) surface; this model included a 19-atom hexagonal top layer with a second layer of three atoms.²²⁷ Using BPW91 with a LANL2DZ basis for silver atoms and 6-31+G(d,p) for other atoms, they showed that the vibrational frequencies of N–H stretching and wagging modes can be used to distinguish between neutral and cationic amines. They assigned current as well as previous experimental spectra, and predicted that cationic amines will display greater frequency shifts upon binding to a silver surface than neutral amines will.

Even though the ground-state structure of Ag_{20} is currently thought to have an icosahedral core, the fcc-like tetrahedral structure has been of interest as a model for adsorbate binding to the (111) surface of bulk silver. In 2006, Zhao et al. examined surface-enhanced Raman scattering (SERS) of pyridine binding both to the face (representing the (111) surface) and to a vertex atom (representing an adatom) of tetrahedral Ag_{20} using the BP86/TZP level of theory.²²⁸ They calculated the electronic polarizability both on and off resonance by incorporating a finite lifetime parameter into the TDDFT calculations. They found that the adsorption of pyridine on the silver cluster leads to an enhancement of the Raman intensity by about a factor of 10 for chemical enhancement effects obtainable from static Raman calculations, with an additional 5 orders of magnitude when electromagnetic enhancement effects are included. Jensen et al. then investigated the dependence of the SERS enhancement due to silver cluster size and counterintuitively found that the enhancement was larger for Ag_2 than Ag_{20} , which was attributed

to the shorter distance of the molecule to the center of the cluster.²²⁹ Later, Morton and Jensen studied *meta*- and *para*-substituted pyridines interacting with Ag_{20} and found that the chemical enhancement effects are governed by the energy difference between the highest occupied energy level of the metal cluster and the lowest unoccupied energy level of the molecule.²³⁰ The degree of ground-state charge transfer between the molecule and the metal cluster was not found to affect the SERS enhancements. Moore et al. then showed that long-range corrected density functionals provide an improved description of chemical enhancement effects due to improved HOMO–LUMO gaps and charge-transfer excitations for substituted pyridine– Ag_{20} complexes.²³¹ They found that long-range corrected functionals provide smaller enhancement factors for a variety of small molecules and substituted pyridines on silver clusters.

Gaff and Franzen studied the Raman enhancements of pyridine on a variety of silver clusters including tetrahedral Ag_{20} using a time-correlator formalism.²³² Their calculations suggest that coupling exists between the vibrations of pyridine and absorptive transitions in the silver clusters. They attributed the large SERS effects observed to resonance Raman scattering.

Valley et al. calculated hyper-Raman spectra for gas-phase pyridine and pyridine adsorbed on a tetrahedral Ag_{20} cluster.²³³ Hyperpolarizabilities were calculated using the SAOP model potential, and hyper-Raman intensities were calculated as derivatives of hyperpolarizabilities with respect to PW91/TZP normal coordinates. They found that the calculated hyper-Raman spectra were in reasonable agreement with experimental hyper-Raman spectra for gas-phase pyridine and pyridine on roughened silver electrode surfaces.

In addition to pyridine, other molecules have been studied with the tetrahedral Ag_{20} model cluster. In 2006, Zhao et al. examined SERS of pyrazine in the junction between two Ag_{20} clusters.²³⁴ They found enhancement factors of the order of 10^6 for the overall system, but an enhancement of 10^5 was attributed to chemical enhancement effects. The electromagnetic effects for the system were found to be only a factor of 5 rather than several orders of magnitude commonly observed for closely spaced nanoparticles, so the authors concluded that the junction between the two Ag_{20} clusters does not provide an electromagnetic “hot spot” unlike junctions between larger nanoparticles. Wang and co-workers investigated pyrazine on a face of Ag_{20} .²³⁵ They computed the chemical enhancement effects and the locations of excited states but could not calculate the magnitude of the electromagnetic enhancement effects. They determined the location of charge-transfer excitations using the B3LYP, B3PW91, and CAM-B3LYP functionals. Wang and co-workers also examined pyrimidine adsorbed to a face of Ag_{20} .²³⁶ They found several strong excitations around 350 nm that they assigned as charge-transfer excitations.

Lombardi, Burke, and co-workers experimentally and theoretically investigated regular and time-resolved SERS of 3-hydroxyflavone on silver.²³⁷ Using the B3LYP functional, they calculated the geometries and vibrational frequencies of 3-hydroxyflavone bound to tetrahedral Ag_{20} via a face or a vertex site. They found that both structures have nearly the same energy (within 0.01 eV). On the basis of changes in vibrational intensities upon binding to silver, they suggested that binding of 3-hydroxyflavone to an adatom site with the plane of the molecule tilted at 53° to the surface is a possible surface structure.

In 2009, Jensen presented the first simulations of surface-enhanced Raman optical activity (SEROA).²³⁸ The Ag₂₀ cluster geometry used in this work was not the T_d structure but rather a compact C_s structure that had been found to be the global minimum using a Sutton–Chen potential. Numerical polarizability derivatives were computed at the BP86/TZP level of theory. Adenine was found to bind through N7. UV-vis absorption, CD, SERS, and SEROA spectra were calculated for the adenine–Ag₂₀ complex. The total enhancement was determined to be of the order of 104 for SERS and SEROA, but this study predicted that the chemical enhancement is larger for SEROA than SERS. Lang et al. later examined SERS of adenine and 2'-deoxyadenosine 5'-monophosphate (dAMP) interacting with tetrahedral Ag₂₀ using B3LYP/LANL2DZ.²³⁹ They chose several isomers to examine because experimental observations had suggested that adenine is bound via various nitrogen atoms of the two rings. On the basis of frequency shifts, they predicted that adenine is bound to silver via N3 in an end-on orientation and dAMP via N7 in an end-on orientation. The authors also examined adenine between two Ag₂₀ clusters and determined that chemical enhancement effects for this arrangement are a factor of about 100.

Brewer and Aikens examined SERS of HCN and CN[−] on tetrahedral Ag₂₀ using the BP86/TZP level of theory both in the gas phase and in a continuum water solvent.²⁴⁰ They found that chemical enhancement effects for these systems were approximately 1–2 orders of magnitude. Electromagnetic enhancement effects were predicted to be 1–6 orders of magnitude for CN[−] and 4–5 orders of magnitude for HCN depending on the binding orientation. Binding to a vertex (adatom) site was predicted to be the most energetically preferable. However, on the basis of SERS intensities, the authors suggested that both vertex-bonded and edge-bonded structures may be present experimentally.

Zhuang et al. studied SERS of *trans*-1,2-bis(4-pyridyl)-ethylene (t-BPE) adsorbed to a vertex atom of tetrahedral Ag₂₀ as well as to smaller silver clusters using BP86/TZP.²⁴¹ They calculated Raman spectra excited at 514.5, 633, 785, and 1064 nm. They found that the Ag₂₀–t-BPE complex matches the experimental SERS spectrum at 514.5 nm excitation better than a Ag₆–t-BPE complex; however, for 633 nm excitation, the Ag₆–t-BPE complex was found to provide Raman spectra closer to experimental SERS.

Sánchez-González et al. examined nonradiative decay rates for a Ag₂₀–NI–Ag₂₀ (NI = 4-aminomethyl-naphthalimide) complex and compared the rates calculated with full quantum mechanical TDDFT calculations to those with a hybrid quantum/continuum model.²⁴² They found that the nonradiative decay is additive for small nanoparticle arrays, which suggests that single-particle systems can be effectively studied, at least for nanoparticles whose plasmons do not couple strongly.

Bokareva and Kühn optimized the geometries of [Ir(ppy)₂(bpy)]⁺ (bpy = bipyridine; ppy = phenylpyridyl) and bipyridine bound to silver clusters including Ag₂₀ and Ag₉₂ using the PBE/def2-SV(P) level of theory.²⁴³ C₆ coefficients were calculated using MP2 (and RPA for smaller silver clusters). Dissociation curves were calculated at the MP2, PBE-D3, PBE-D2, PBE-D2*, PBE-D2**, and PBE levels of theory for the Ag₂₀–[Ir(ppy)₂(bpy)]⁺ system, where the PBE-D2* and PBE-D2** theories use C₆ coefficients determined in their current work. The authors concluded that their new

coefficients are likely to give good results for silver clusters interacting with systems containing ppy and bpy ligands.

Thiol binding to silver clusters has also been of interest for many years. In 2006, Xie et al. examined the binding of up to four SCH₃ adsorbates on a Ag₂₀ cluster using B3LYP with LANL1MB and LANL2DZ for silver and 6-31G(d) for the other atoms.²⁴⁴ The silver cluster used in this work included 13 silver atoms in an upper layer and seven silver atoms in a second layer to represent the bulk surface; silver distances were fixed to the bulk Ag–Ag distance of 2.890 Å and were not optimized. From the charge densities, they found that SCH₃ has a charge of about −0.65 electrons when adsorbed on silver. El-Khoury and Hess computed Raman spectra for 1,3-propanedithiol tethered to the face and to the vertex of tetrahedral Ag₂₀ as well as for this molecule bridging between two Ag₂₀ units.²⁴⁵ They computed nonresonant SERS spectra using B3LYP/Def2-TZVP. They found low energy excited states with significant charge-transfer character. They examined the effects of the molecular orientation on the computed Raman intensities and found that the Raman spectra are very sensitive to orientation. In addition, the Raman spectra for molecules bound to face versus vertex sites are very different. Hidalgo and Noguez examined SCH₃ bound to different sites of an icosahedral Ag₅₅ cluster using PBE/DZP.²⁴⁶ They found that the resulting complexes may or may not be chiral depending on the adsorption geometry. They showed that the lowest energy structure is chiral. CD spectra were calculated for chiral configurations, and were found to strongly depend on the final structure of the molecule–metal complex.

2.2.3. Copper. Copper clusters are also of interest because copper has many interesting electronic properties. In addition, its optical properties and electronic structure have intriguing similarities to and differences from related silver and gold compounds. The bonding behavior of atomic oxygen to Cu (100) and Ag (100) surfaces has been investigated by Ricart et al.²⁴⁷ with ab initio HF combined with pseudopotentials. Cluster models consisting of up to 41 atoms of copper and silver were used in the investigation. The authors used orbital projection techniques and dipole moment curves to propose a similar type of bonding mechanism on the surfaces of both copper and silver that can be described as largely ionic. It has been found that around 20% of the total interaction energy has metal d electron participation.

Wang and co-workers²⁴⁸ investigated structures and electronic properties of Cu₂₀, Ag₂₀, and Au₂₀ with DFT. The silver and gold clusters are discussed in their respective sections. Initial geometries were obtained with genetic algorithm, and the PW91 exchange correlation functional was used in the density functional calculations. It was found that Cu₂₀ has a compact C_s symmetry, whereas silver and gold clusters have high symmetry tetrahedral structures. As compared to the gold and silver clusters, the HOMO–LUMO gap was small for Cu₂₀ tetrahedral clusters.

Fernández et al.²⁴⁹ presented a systematic study of the electronic and geometrical properties of noble metal clusters X_n^ν (X = Cu, Ag, and Au; ν = −1, 0, +1; n ≤ 13 and n = 20). They employed the PBE exchange correlation functional without spin polarization. Standard norm-conserving scalar-relativistic pseudopotentials were used in their fully nonlocal form with a numerical atomic basis set. Results for gold and silver have been previously discussed above. For X₂₀, the authors reported a T_d symmetric structure for Au and a C_1 compact structure for Ag and Cu. This is in partial agreement

with previous calculations by Wang and co-workers where they reported a T_d symmetric structure also for Ag_{20} clusters.

A density functional theory study of Cu_n , Al_n ($n = 4\text{--}31$), and copper-doped aluminum clusters was performed by Lacaze-Dufaure et al.²⁵⁰ Theoretical calculations were based on the B3PW91 exchange correlation functional combined with LANL2DZ for metal atoms. They calculated the atomization energies, work functions, and bond energies for Al and Cu clusters. They also studied the substitution of an Al atom by Cu. The authors demonstrated that electron transfer from the Al cluster to a Cu atom located at the surface is large, whereas it is negligible when Cu is inserted in the Al_n cluster. They also compared chemisorption energies of atomic oxygen on Al_{31} , Cu_{31} , and Al_{30}Cu clusters and showed that the energy decreases in the bimetallic systems as compared to the pure aluminum cluster.

A systematic study of geometric and electronic structures of Na, Cu, and Ag clusters was reported by Itoh et al.²⁵¹ They studied clusters ranging from 2 to 75 metal atoms using the PW91 exchange correlation functional combined with ultrasoft pseudopotentials. For all of the structures studied with these three metals, the shape was found to change in the order of linear, planar, open, and closed structures with increasing n . The most stable structures are the same for the three metal atoms for around one-half of the cluster sizes considered in this study. An interesting similarity was observed for the n dependence of cluster energy for the most stable geometric structures.

Yang and co-workers²⁵² calculated the electron removal energies for Cu_n^- clusters where $n = 9\text{--}20$. The computed energies were then compared to the corresponding experimental PES values. These calculations were carried out by using the scheme proposed by Jellinek and Acioli²⁵³ that uses DFT orbital energies using a correction based on DFT total energies. All DFT calculations were performed with the PBE functional. The pattern of calculated electron removal energies was found to be isomer specific for the size range they considered. They identified the isomers responsible for PES by matching the computed electron removal energies.

First-principles calculations using time-dependent density functional theory in the adiabatic local density approximation have been used to obtain optical absorption spectra for Cu_n , $n = 2\text{--}20$ by Baishya and co-workers.²⁵⁴ DFT calculations were carried out with the PBE exchange correlation functional with an all-electron basis set of 20 Gaussians contracted to 7s5p4d on each atom. The authors indicated that Cu d electrons affect the optical spectra by quenching the oscillator strengths and becoming directly involved in excitations at energies as low as 2 eV. These effects are most prominent in Cu_n clusters as compared to previous silver and gold cluster studies by the same authors. The authors also predicted large Mie resonances in extremely prolate or oblate Cu nanoparticles, but these are absent for the case of moderately ellipsoidal or spherical particles.

Jiang and co-workers²⁵⁵ employed a “basin-hopping” algorithm and the PBE/def-SVP level of theory to investigate the lowest energy isomers of Cu_n for $n = 20\text{--}30$. The lowest energy isomers in this size range were dominated by a 13-atom icosahedral core and a 19-atom double icosahedral core. A transition from icosahedral structure to double icosahedron core was predicted over $n = 21\text{--}23$. The authors noted that these clusters tend to create quasi-planar structures where additional atoms add in a way to form roughly planar structures

with surface atoms altering the cluster shape. The calculated IPs, vertical detachment energies, and HOMO–LUMO gaps are in good agreement with the experimental results.

By utilizing ab initio calculations, Ziashahabi et al.²⁵⁶ studied the stability and structural properties of copper clusters that affect the localized surface plasmon resonance properties. These clusters consisted of 14, 38, 62, and 116 atoms. They used B3LYP together with CEP-4G and LANL2DZ basis sets for their calculations. The authors concluded that larger clusters are more stable than the smaller ones by analyzing the formation energies. The authors suggested that copper clusters below 2 nm are not metallic and thus could not have a localized plasmon resonance. The authors noted a difference of surface charge density as compared to gold nanoclusters; copper clusters exhibit a reduction of surface charge that might cause the vanishing of the localized plasmon resonance for copper clusters below 2 nm.

Calaminici et al.²⁵⁷ investigated lowest energy isomers for Cu_n ($n = 12, 14, 16, 18, 20$) clusters using the PBE/TZVP level of theory. Initial structures were taken from Born–Oppenheimer molecular dynamics trajectories recorded at 2000 K. The calculated vertical ionization potentials and vertical electron affinities are in good agreement with the reported experimental values. A new ground-state structure was reported for the Cu_{16} cluster. The ground-state structure for Cu_{20} was similar to the one previously predicted by Itoh et al.

Anak et al.²⁵⁸ performed TDDFT calculations of the optical spectra of group 11 element clusters Cu_n , Ag_n , Au_n with $n = 2\text{--}9$ and 20. These gold and silver results have been previously described in their respective sections. These calculations were conducted with two long-range corrected exchange correlation functionals, LC-M06L and CAM-B3LYP. Copper and gold metals show a high density of peaks resulting in broadening and damping of the optical response, whereas silver shows a few well-separated strong peaks. A plasmon-like band was observed in the range of 3.5–4.0 eV for $n = 20$ clusters for the three metals. A few transitions were found below the plasmon, and a large band is found beyond 4.5–5.0 eV for both Cu_{20} and Au_{20} clusters, whereas no transition was found for Ag_{20} .

Pacchioni and Bagus²⁵⁹ studied the vibrational shift of CO coadsorbed with K on Cu(100) surface. They considered two K atoms and a CO molecule adsorbed on two cluster models of Cu_{12} and Cu_{32} . These early theoretical calculations were performed with the HF method. Effective core potentials were used to reduce the computational cost. It has been known that the alkali atoms influence the electronic structure of the CO molecule; in particular, they decrease the C–O vibrational frequency. This large decrease of vibrational frequency has been suggested to be dependent on two terms: the electrostatic interaction between the surface electric field and the improved back-donation into CO $2\pi^*$ molecular orbitals. The authors found no trace of direct K–CO charge-transfer reactions. The authors later reported another study of ionic and covalent electronic states of K-adsorbed Cu_5 and Cu_{25} cluster models.²⁶⁰ They employed the same theoretical method as before and found that all of the considered electronic states of $\text{Cu}_{25}\text{-K}$ are largely ionic in character. Different bonding characters were found for the lowest electronic states of $\text{Cu}_5\text{-K}$ ranging from dominantly ionic to dominantly covalent. The authors suggested that such behavior is related to the small size of the cluster.

Gomes et al.²⁶¹ reported a theoretical study of adsorption of dioxymethylene on the copper (111) surface. They used two

cluster models: Cu₇ to represent a small metal cluster and a Cu₃₀ metal cluster used as a model of the infinite surface. They performed theoretical calculations with the B3LYP exchange correlation functional combined with the LANL2DZ basis set for metal atoms and 6-31G** for nonmetallic atoms. Two adsorption sites were considered, and it was found that the cross-bridge conformation stabilizes dioxymethylene more than the aligned-bridge site. The oxygen to surface distance and the ionic bonding character remained the same for both conformations. Interestingly, they reported by comparing the adsorption energy of dioxymethylene and atomic oxygen with free formaldehyde that the H₂CO₂(ads) is more energetically favorable than the adsorbed O(ads) and H₂CO(g).

Domíngues-Ariza and co-workers²⁶² investigated the effect of surface models that can be used to describe the chemisorption of atomic hydrogen on the Cu (001) surface. They used cluster models consisting of up to 77 Cu atoms. Different theoretical approaches were taken including HF, MP2, PW91, and hybrid B3LYP with LANL2DZ for metal atoms and cc-pVQZ for hydrogen. Two different periodic calculations were also employed with GGA and LDA functionals. It was pointed out that convergence of a structure with adsorption at the 4-fold site is not achieved even for very large clusters. The authors suggested that the reason for such a scenario is the inability of the cluster model to accurately reproduce the charge density and electrostatic potential of the crystalline surface. The authors pointed out that the problem of atomic H on this kind of metallic surface does not relate to the level of theory but is intrinsic to the lack of an electronic core in atomic H.

Illas and Fernández-García et al.²⁶³ reported a study of the interaction of CO and NO with PdCu(111) surfaces. They employed ab initio HF wave function and DFT/B3LYP exchange correlation functional calculations combined with relativistic core potentials from Hay and Wadt³⁰ with LANL2DZ for metal atoms and 6-31G* for other atoms. Clusters up to Pd₄₀Cu₆₀ were investigated. The authors reported that the nature of CO bonding is covalent, whereas for NO it varies from nearly covalent for pure Pd to a mixture of covalent and ionic character for copper-rich alloys. The authors observed that the interaction energy decreases with the copper content of the alloy. They plotted the interaction energy with Pd-core level (4s) shifts and found that it has a descending linear correlation. This is in agreement with the previous trend reported by Rodriguez and Goodman.²⁶⁴ The predominance of the correlation contribution was used to rationalize the insensitivity of the C–O stretching frequency to the composition of the alloy. Later, these groups investigated the bonding nature of the PdCu(111) surface.²⁶⁵ Cluster models of Pd₈Cu₉₂ and Pd₄₀Cu₆₀ were used with BLYP and BPW91 functionals. It was found that an adjacent Cu produces an internal Pd d to sp rehybridization larger than that of pure metallic Pd. Introduction of Cu to the solid induces a higher polarization in Pd as a prerequisite for bonding. They also observed a charge-transfer process from Cu(4sp) to Pd(5sp) that makes the surface of Pd atom negatively charged. The authors also indicated that the sign and magnitude of the binding energy shift is not a valid parameter to measure the amount of charge transfer in these PdCu alloy systems.

2.2.4. Thiolate-Protected Gold Nanoparticles. Gold nanoparticles, including thiolate-stabilized gold nanoparticles, have many applications in biotagging, catalysis, sensing, electronics, and a variety of other applications. Although large, these systems provide excellent potential for theory–

experiment comparison, so a significant amount of theoretical work has been performed on these and related nanoparticles.

2.2.4.1. Initial Work. Early density functional theory studies of gold–thiolate nanoparticles focused on the Au₃₈(SR)₂₄ nanoparticle, because this system could be envisioned as a truncated-octahedral Au₃₈ core passivated by 24 thiolate ligands bridging the edges of the six fcc(100) facets.²⁶⁶ Häkkinen et al. employed the local density approximation (LDA) with methylthiolate ligands and found a local minimum structure that exhibited charge transfer from the outermost Au atoms to the S atoms.²⁶⁶ Shortly thereafter, Garzón and co-workers showed that a low symmetry disordered structure with an amorphous Au₃₈ core and irregular adsorption sites was energetically preferred as compared to the truncated octahedron form.²⁶⁷ In 2006, Häkkinen et al. used the PBE functional to revisit the truncated octahedral structure and determined that optimization using this functional led to a novel “divide-and-protect” structure in which six cyclic (AuSCH₃)₄ units protect a central Au₁₄ core.²⁶⁸ This study marked the first time when gold atoms were considered to be in the ligand layer (in gold–thiolate units) in addition to comprising the core of the nanoparticle. The CD spectrum of this system was later computed,²⁶⁹ and lattices of this nanoparticle have been investigated.²⁷⁰ Although the structure of the Au₃₈(SR)₂₄ nanoparticle has been revisited and a new structure has been determined (as discussed below), the “divide-and-protect” motif proposed theoretically was instrumental in aiding the X-ray crystal structure interpretation of the Au₁₀₂(SR)₄₄ (SR = *p*-mercaptopbenzoic acid) nanoparticle, which determined that gold–thiolate “staple” units SR–Au–SR on the surface of the nanoparticle protect a smaller interior gold core.²⁷¹ This crystal structure led to tremendous interest in the field. A few smaller reviews with a theoretical focus have been published previously.^{112,272–278}

2.2.4.2. Au₂₅(SR)₁₈. One of the most stable and most studied gold–thiolate nanoparticles (and one that has garnered significant theoretical interest) is the Au₂₅(SR)₁₈ system. Early work on Au₂₅(SR)₁₈⁺ proposed a Au₇ core surrounded by an (AuSR)₁₂ oligomer and two (AuSR)₃ rings.²⁷⁹ as well as face-centered cubic (fcc) and vertex-sharing icosahedral structures.²⁸⁰ In 2008, based on the core-staple arrangement known for Au₁₀₂, Akola et al. proposed a structure in which Au₂₅(SR)₁₈ (R = CH₃) in the anionic, neutral, and cationic charge states has an approximately icosahedral Au₁₃ core protected by six V-shaped oligomeric –SR–Au–SR–Au–SR– units (Figure 9).²⁸¹ This structure was determined by two simultaneous X-

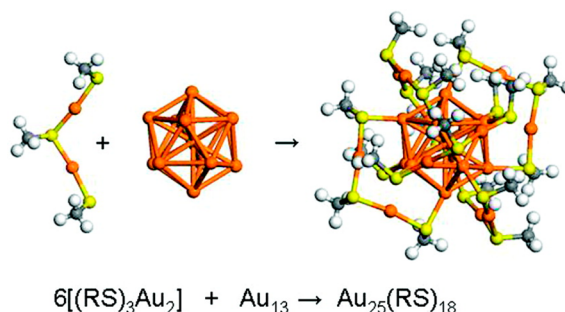


Figure 9. Structure of Au₂₅(SR)₁₈ consisting of an approximately icosahedral Au₁₃ core protected by six V-shaped Au₂(SR)₃ units. Reprinted with permission from ref 281. Copyright 2008 American Chemical Society.

ray crystal structures on the anion^{282,283} and a later crystal structure of the neutral system.²⁸⁴ The anionic $\text{Au}_{25}(\text{SR})_{18}^-$ nanoparticle has 8 superatomic electrons, so it has a closed shell associated with special stability.²⁸¹

One of the first properties of the $\text{Au}_{25}(\text{SR})_{18}^-$ system to be examined theoretically was linear optical absorption. Aikens and co-workers used time-dependent density functional theory (TDDFT) to assign the Kohn–Sham orbital contributions responsible for each absorption peak observed experimentally.^{284,285} They found that the first peak arises primarily from the HOMO → LUMO transition; the second peak is formed from a combination of HOMO → LUMO+1, HOMO → LUMO+2, and HOMO−2 → LUMO transitions; and the third peak is generated primarily from the HOMO−5 → LUMO transition. As shown by Akola et al. using a projected density of states approach²⁸¹ and by Aikens using Kohn–Sham orbitals,²⁸⁵ the HOMO of $\text{Au}_{25}(\text{SR})_{18}^-$ is a superatom P orbital (i.e., the orbital has symmetry similar to an atomic p orbital, but is delocalized throughout the entire nanoparticle core; for further information, see ref 10), the LUMO and LUMO+1 represent 2-fold and 3-fold degenerate sets of D orbitals, respectively, and the LUMO+2 is a 2S orbital. Orbitals just below the HOMO are generated primarily from 2p orbitals of the sulfur atoms and 5d orbitals of the Au atoms in the staple units.

Later work by Aikens showed that the optical absorption spectrum is very sensitive to the geometry of the nanoparticle, which is affected by the level of theory employed in the geometry optimization.²⁸⁶ Generalized gradient approximation (GGA), hybrid, and meta-GGA functionals as well as Hartree–Fock theory and MP2 theory were found to overestimate core Au–Au distances by 0.05 Å (less for PBE0 and TPSS), whereas LDA functionals underestimated these distances by <0.01 Å. TDDFT calculations using the SAOP/TZP level of theory at these geometries determined that a decrease in core Au–Au distance of 0.05 Å could lead to a blue-shift of the first excitation peak by 0.1 eV and a red-shift of the second excitation peak by about 0.05 eV, for an overall effect of 0.15 eV on the splitting between these two peaks; geometries closer to the experimental structure led to splittings that were also close to experiment. Aikens also examined changing the level of theory employed in the TDDFT calculations and found that LB94 was a good approximation to SAOP for the $\text{Au}_{25}(\text{SH})_{18}^-$ nanoparticle, whereas BP86 and PBE were slightly red-shifted. The effect of a continuum solvent on the geometry and optical absorption spectrum of this system was determined to be negligible. However, changing the ligand was suggested to lead to small but noticeable changes in the optical absorption spectrum.²⁸⁶

In 2010, Day et al. calculated both one- and two-photon absorption spectra for $\text{Au}_{25}(\text{SH})_{18}^-$ using a variety of density functional methods.²⁸⁷ They agreed that a $X\alpha$ geometry provided better results than a BP86 geometry. They found that B3LYP/SDD and mCAM/SDD energies give excellent agreement with experiment for the one-photon absorption spectra. For two-photon absorption (TPA) spectra, a wide variation in peak cross sections was obtained, which the authors believe is due to the high density of states and resonance effects. In consequence, they could qualitatively but not quantitatively predict TPA.

In 2010, Parker et al. performed a combined theory–experiment study to examine the effects of exchanging ligands on the HOMO, LUMO, and HOMO–LUMO gap energies.²⁸⁸

Using the PBE functional, simple electron-withdrawing SCH_2Cl model ligands were used to replace SCH_3 ligands. They found that the redox potentials shift nearly linearly with the number of ligands exchanged, in agreement with experimental results using substituted SPhp-X ($X = \text{Br}, \text{NO}_2$) ligands. In addition, they determined that no significant changes to the charge occur within the Au_{13} core even after complete exchange; all of the charge is transferred within the $-\text{SR}-\text{Au}-\text{SR}-\text{Au}-\text{SR}-$ oligomers.²⁸⁸ Related work by Aikens on $\text{Au}_{25}(\text{SPhX})_{18}^-$ ($X = \text{H}, \text{F}, \text{Cl}, \text{Br}, \text{CH}_3, \text{OCH}_3$) suggested that the lowest energy structure for this system has idealized S_6 symmetry with six sets of three π -stacked phenyl groups.²⁸⁹ Using LB94/DZ, the orbital energy shifts in the HOMO, LUMO, and HOMO–LUMO gap follow those expected from Hammett substituent constants with the exception of OCH_3 ,²⁸⁹ which was in agreement with previous experimental results from Murray and co-workers.²⁹⁰ This study showed that all of the P orbitals of the $\text{Au}_{25}(\text{SPh})_{18}^-$ nanoparticle are not perfectly degenerate; the P_z orbital was found to be slightly higher in energy than the essentially degenerate P_x and P_y , which led to an optical absorption spectrum with a split first peak unlike the previous calculated spectra for $\text{Au}_{25}(\text{SH})_{18}^-$ and $\text{Au}_{25}(\text{SCH}_3)_{18}^-$. Similar work by Häkkinen and co-workers showed that the optical absorption spectrum of the full $\text{Au}_{25}(\text{SCH}_2\text{CH}_2\text{Ph})_{18}^-$ nanoparticle exhibits a split first peak in agreement with the experimental UV–vis spectrum of this system.²⁹¹

Jung et al. examined the stability of the $\text{Au}_{25}(\text{SR})_{18}^-$ ($R = \text{CH}_3, \text{C}_6\text{H}_{13}, \text{CH}_2\text{CH}_2\text{Ph}, \text{Ph}, \text{PhF}$, and PhCOOH) nanoparticle using PW91; geometries were optimized with a numerical double- ζ basis set, and single point energies were computed with a numerical double- ζ plus polarization basis set.²⁹² The authors found that aliphatic thiols led to higher VIP-VEA (vertical ionization potential minus vertical electron affinity) values, defined as their measure of electrochemical stability, and reaction energies to separated gold and thiyl (SR) species, defined as their measure of thermodynamic stability. They proposed that of the ligands examined in their work, $\text{SCH}_2\text{CH}_2\text{Ph}$ leads to the greatest stability among aliphatic thiols, whereas SPhCOOH (*p*-MBA) leads to the greatest stability among aromatic thiols.

With chiral ligands, the $\text{Au}_{25}(\text{SR})_{18}^-$ system can potentially exhibit chiroptical activity, as shown experimentally by Schaaff and Whetten.²⁹³ Garzón and co-workers used the Rosenfeld equation within DFT to calculate rotational strengths for $\text{Au}_{25}(\text{SR})_{18}^-$ ($R = \text{H}, \text{CH}_3$, cysteine) and determined that the circular dichroism spectrum is sensitive to the exact arrangement of ligands; an achiral cluster gives a null CD spectrum, whereas structures that are not perfectly symmetric provide nonzero CD spectra.²⁹⁴

Tlahuice-Flores et al. examined the influence of ligands on structure and optical properties.²⁹⁵ Using PBE as implemented in the SIESTA code, they found that certain ligands such as phenylthiolate prefer to form C_1 symmetric nanoparticles rather than maintaining C_i symmetry as in the crystal structure of $\text{Au}_{25}(\text{SCH}_2\text{CH}_2\text{Ph})_{18}^-$.^{282,283} They also calculated real-time TDDFT optical absorption spectra for a variety of ligands.

Core level shifts (CLS) were reported by Grönbeck for the $\text{Au}_{25}(\text{SCH}_3)_{18}^-$ nanoparticle using the PBE exchange correlation functional with scalar-relativistic pseudopotentials generated with an electron hole in the Au 4f-shell.²⁹⁶ He found that atoms in the icosahedral shell of the nanoparticle have negative shifts of −0.47 eV relative to the central atom, whereas atoms in the $\text{Au}_2(\text{SCH}_3)_3$ units have positive shifts of +0.13 to +0.33 eV.

This indicates that atoms in the protecting units have a different chemical state than atoms in the surface layer.

Several researchers have studied the vibrational properties of the $\text{Au}_{25}(\text{SR})_{18}^-$ nanoparticle. Akola et al. calculated the vibrational density of states for this system and found radial breathing modes of the Au_{13} core around 110 cm^{-1} and of the ligand shell around 300 cm^{-1} , which correspond well to the experimental Raman peaks at 110 and 290 cm^{-1} .²⁹¹ In addition, these researchers found Au–Au stretching modes in the core at 150 – 180 cm^{-1} and S–Au–S bending modes at 205 and 230 cm^{-1} . Similar vibrational frequencies were also observed in later studies.^{297,298} In addition, the Au–S stretching modes were classified as “tangential” or “radial” with respect to their directionality relative to the core of the cluster. Tlahuicel-Flores et al. found that the tangential vibrations are those of the shorter, stronger bonds within the staple units, which occur at higher frequencies than the radial vibrational modes.²⁹⁸

Born–Oppenheimer molecular dynamics of the $\text{Au}_{25}(\text{SH})_{18}^-$ nanoparticle at temperatures ranging from 300 to 600 K using the PBE functional were performed to determine how the structure changes with time.²⁹⁹ As a result of their simulation, Mäkinen and Häkkinen suggested that the Au–S bonds at the core–thiolate interface are the weakest ones in this nanoparticle. They determined that the interface does not change greatly at the temperatures studied, although the gold–gold bond lengths are affected by the thermal fluctuations. The gold atoms in the core prefer to vibrate tangentially rather than radially.

Mass spectrometric experiments have reported fragments of the $\text{Au}_{25}(\text{SR})_{18}^-$ nanoparticle with compositions of $\text{Au}_{21}(\text{SR})_{14}^-$ and $\text{Au}_4(\text{SR})_4$. Using PBE, Lopez-Acevedo and Häkkinen examined the atomic configurations and energetics for the loss of a AuSR fragment from $\text{Au}_{25}(\text{SR})_{18}^-$.³⁰⁰ They found that a dramatic cluster core rearrangement takes place after four AuSR units are removed, which relieves the stress on the core that arises when a long $\text{Au}_2(\text{SR})_3$ staple unit becomes the shorter $\text{Au}(\text{SR})_2$ staple unit. This leads to the fully protected superatomic clusters $\text{Au}_{21}(\text{SR})_{14}^-$ and $\text{Au}_{19}(\text{SR})_{12}^-$. Later, Pei and co-workers proposed lower energy isomers for the $\text{Au}_{21}(\text{SR})_{14}^-$ system using PBE/DND in Dmol.³⁰¹ They employed a combination of structure minimizations and Born–Oppenheimer molecular dynamics using DFT to propose a pathway for the loss of the $\text{Au}_4(\text{SR})_4$ unit from the $\text{Au}_{25}(\text{SR})_{18}^-$ system. In addition, they proposed a similar pathway for a second loss of $\text{Au}_4(\text{SR})_4$ to yield $\text{Au}_{17}(\text{SR})_{10}^-$, which is a fragment observed in recent mass spectrometric experiments.³⁰¹

Catalysis on small gold nanoparticles is of significant interest, so several researchers have examined catalysis on the $\text{Au}_{25}(\text{SR})_{18}^-$ system using theoretical methods. Because the $\text{Au}_{25}(\text{SR})_{18}^-$ nanoparticle has 8 superatomic electrons and is thus a stable, closed-shell species that would be unlikely to bind CO or O_2 , Lopez-Acevedo et al. considered “activating” this nanoparticle via removal of two $\text{Au}_2(\text{SR})_3$ units, which makes the resulting $\text{Au}_{21}(\text{SR})_{12}$ species a 10 -electron system.³⁰² They examined the CO oxidation reaction on this system and showed that the $\text{Au}_{21}(\text{SR})_{12}$ species is reactive toward oxygen adsorption. In 2012, Kauffman et al. presented a combined theory–experiment study of the reduction of CO_2 on $\text{Au}_{25}(\text{SR})_{18}^-$ and found that the adsorption of carbon dioxide induces a rearrangement of the charge within the nanoparticle; they found that $\text{Au}_{25}(\text{SR})_{18}^-$ led to rates that were a factor of 10 – 100 times faster than the best currently available CO_2

reduction catalyst.³⁰³ In 2013, Pei and co-workers examined the mechanism for the oxidation of styrene to benzaldehyde using a *tert*-butyl hydroperoxide (TBHP) initiator, which is a process achieved experimentally with very high selectivity.³⁰¹ These authors found that the Au(I) atoms in the staples react with the TBHP initiator and potentially O_2 to form Au(III) species. Jiang, Jin, and co-workers examined the Sonogashira cross-coupling reaction of phenylacetylene and iodobenzene on $\text{Au}_{25}(\text{SR})_{18}^-$ in a combined theory–experiment paper.³⁰⁴ In this work, the authors used PBE in combination with the D2 dispersion method of Grimme to examine how the adsorbates react on a model $\text{Au}_{25}(\text{SCH}_3)_{18}^-$ system. They found that phenylacetylene and iodobenzene could bind to one of the 3 -fold facets of the $\text{Au}_{25}(\text{SCH}_3)_{18}^-$ nanoparticle with binding energies of -0.40 and -0.48 eV , respectively. In these adsorbed structures, the phenyl rings each interact with one of the Au(I) atoms in the staple motifs. Wu et al. also performed a combined theory–experiment investigation of CO oxidation on $\text{Au}_{25}(\text{SR})_{18}^-$.³⁰⁵ Using PBE0/def2-SV(P), they found that the adsorption energy of CO on $\text{Au}_{25}(\text{SCH}_3)_{18}^-$ is only -0.08 eV , which agreed with experimental results that CO does not adsorb. When they removed three thiyl/thiolate ligands (corresponding to thermal activation of the clusters) and relaxed the resulting $\text{Au}_{25}(\text{SCH}_3)_{15}$ system (a 10 -electron system for the neutral charge state), CO was found to have an adsorption energy of -1.12 eV .

A number of researchers have been interested in using dithiol ligands with the $\text{Au}_{25}(\text{SR})_{18}^-$ nanoparticle, which can potentially lead to the formation of aggregates. In 2010, Akola et al. examined two methylthiolate-passivated Au_{25} nanoparticles bridged by a benzenedithiolate (BDT) linker using PBE.²⁹¹ They found that the BDT linker does not disturb the electronic structure of the two individual nanoparticles, which can continue to be thought of as two separate 8 -electron superatoms. In 2011, Jupally et al. considered ligand exchange on the $\text{Au}_{25}(\text{SR})_{18}^-$ nanoparticle with a series of flexible ethane, propane, butane, pentane, and hexane dithiols.³⁰⁶ Using a combination of B3LYP/6-311+G** and TPSS/def2-SV(P) calculations, these researchers found that intrastaple binding is unlikely until the dithiol is at least 1,6-hexanedithiol; shorter dithiols appear to prefer interstaple coupling. Aggregates were not considered computationally.

Recently, Mathew et al. performed a combined theory–experiment study on a $\text{Au}_{25}(\text{SPh}-t\text{Bu})_{18}^-$ ($\text{SPh}-t\text{Bu} = 4$ -*tert*-butylbenzenethiolate) nanoparticle.³⁰⁷ These researchers found that up to four cyclodextrin molecules could bind to the nanoparticle in a supramolecular fashion. They calculated that the cyclodextrin binds to the *tBu* group with energies of -14.11 kcal/mol at its narrow rim or -12.12 kcal/mol at its wide rim.

Although most theoretical (and experimental) studies have focused on the anionic system, a number of investigations have also examined the neutral or cationic systems. In 2009, Zhu et al. calculated the electron paramagnetic resonance (EPR) *g* values, isotropic hyperfine constants, and spin density distribution for a model $\text{Au}_{25}(\text{SH})_{18}$ nanoparticle using spin-orbit coupled LB94/TZP calculations.³⁰⁸ Agreement with experiment was found to be excellent. The researchers interpreted the anisotropic EPR signal observed experimentally as arising from an electron that occupies a superatom P orbital, which is unpaired because the neutral system possesses only 7 superatomic electrons.

In 2011, Venzo et al. examined the NMR spectrum of $\text{Au}_{25}(\text{SCH}_2\text{CH}_2\text{Ph})_{18}^0$.³⁰⁹ They performed geometry optimiza-

tions from the crystal structure coordinates²⁸⁴ using B3LYP with the LACVP basis set for Au and 6-31G* for other atoms. They then undertook NMR calculations using B3LYP with the LANL2DZ basis set for Au and 6-31G* for other atoms. NMR calculations were performed in vacuum and were referenced to tetramethylsilane (TMS). A broad range of ¹³C and ¹H values were found for the various α -CH₂ and β -CH₂ groups in the nanoparticle.³⁰⁹

In 2013, Antonello et al. calculated the electronic structure and TDDFT spectra of the neutral and cationic Au₂₅(SCH₃)₁₈ systems at the S-VWN/def2-TZVP level of theory (def2-ecp for Au atoms).³¹⁰ In agreement with previous electronic structure studies of the related Au₂₅(SH)₁₈ nanoparticle,³⁰⁸ they found that there is an increased splitting of the three highest occupied a_u (P) orbitals as compared to the anionic system. They suggested that this is responsible for an effective increase in the HOMO–LUMO gap measured from UV–vis absorption data. They also determined that the splitting of these orbitals is even greater in the Au₂₅(SCH₃)₁₈⁺ nanoparticle and ascertained via both experiment and theory that the ground state of this nanoparticle is a singlet rather than the previously proposed triplet state.³¹⁰

Dainese et al. computed the hyperfine and quadrupole tensors for the neutral Au₂₅(SCH₂CH₃)₁₈ nanoparticle to compare with experimental electron nuclear double resonance (ENDOR) spectra.³¹¹ Geometries were again optimized at the S-VWN/def2-TZVP level of theory (def2-ecp for Au atoms) with starting geometries from an X-ray crystal structure determination of Au₂₅(SCH₂CH₃)₁₈, and then hyperfine constants and quadrupole tensors were calculated using unrestricted BP86 with a TZVP basis for Au atoms and a DZP basis set for all other atoms. The authors found that the Au₂₅(SCH₂CH₃)₁₈ nanoparticle possesses several different types of gold atom sites with electronic environments that are distinguishable by the sensitive ENDOR technique. In addition, they determined that the calculated ENDOR spectra of methylthiolate- and ethylthiolate-passivated nanoparticles are sufficiently different that ligand substitution is not appropriate for ENDOR spectral comparisons with experiment.³¹¹

2.2.4.3. Doped Au₂₅(SR)₁₈. In 2009, experimental mass spectrometry investigations showed that the Au₂₅(SCH₂CH₂Ph)₁₈⁻ nanoparticle can be alternatively prepared with a single Pd atom to yield Au₂₄Pd-(SCH₂CH₂Ph)₁₈⁻,³¹² which led to significant interest in doping of the Au₂₅(SR)₁₈ nanoparticle. Jiang and Dai investigated a series of M@Au₂₄(SCH₃)₁₈^q compounds, where M is a dopant atom from various groups of the periodic table positioned at the center of the Au₁₃ icosahedral core.³¹³ They chose charges of $q = -2, -1, 0, 1, 2$ to maintain the 8-electron superatom character of the original cluster and found that 16 elements generated reasonable structures. However, the position of the dopant atom has been debated, and is now thought to depend on the identity of the dopant. Kacprzak et al. using PBE and TPSS³¹⁴ and Walter and Moseler using PBE³¹⁵ found that the central position is the most energetically favorable place for a Pd atom in Au₂₄Pd(SR)₁₈ regardless of charge state. However, Kacprzak et al. suggested on the basis of comparison with experimental electronic and electrochemical properties that the Pd atom may actually be located on the surface of the core or in the metal–thiolate units.³¹⁴ A combined theory–experiment investigation by Negishi et al. showed that the preferred charge state of Au₂₄Pd(SR)₁₈ is neutral, so only six delocalized electrons are present in this system.³¹⁶ Using B3LYP geometry

optimizations, calculated XRD patterns, and LR-TDDFT calculations of the absorption spectra, they predicted that the Pd atom is located in the center of the icosahedral core.³¹⁶ Akola et al. considered a [PdAu₂₄(SCH₃)₁₇-BDT-(SCH₃)₁₇Au₂₅]⁻ (BDT = 1,4-benzenedithiolate) dimer using PBE and found that this system acts as a six-electron superatom on one side interacting with an eight-electron superatom on the other; the two holes in the superatomic P-shell are localized in the PdAu₂₄ part of the system.²⁹¹ Similar to Pd, Pt has also recently been predicted using PBE/def2-TZVP geometry optimizations and B3LYP/def2-SV(P) LR-TDDFT excitation calculations to preferentially occupy the central position in the PtAu₂₄(SR)₁₈ nanoparticle.³¹⁷

Several groups have been interested in magnetic doping of the Au₂₅(SR)₁₈ system. In 2009, Ulises Reveles et al. and Jiang and Whetten examined doping with magnetic atoms in the central position.^{318,319} Dimers of thiolate-stabilized MnAu₂₄ nanoparticles separated by BDT are predicted using PBE to maintain most of the electronic structure of a single MnAu₂₄(SR)₁₈ system and are calculated to be ferromagnetic.²⁹¹ Zhou et al. later showed using the PBE functional that Mn atoms are energetically preferred to be at the surface of the core rather than in the central position.³²⁰ Zhou et al. also calculated equilibrium spin-dependent conductance spectra for this system using nonequilibrium Green's functions and suggested that these types of clusters may be useful as spin filters.³²⁰ The preference of Mn for surface sites was also confirmed in a later study by Chen et al.³²¹ In addition, Chen et al. found that the magnetic MnAu₂₄(SR)₁₈ nanoparticle is electronically isolated from metal surface supports due to the thiolate ligand layer.³²¹

One of the most important types of doping of the Au₂₅(SR)₁₈⁻ nanoparticle is doping with silver atoms. The first study to consider doping of this nanoparticle examined substitution of silver within the core and/or within the ligand layer; using the SAOP/TZP level of theory, Aikens predicted that doping of silver within the core would lead to a sharp optical absorption spectrum.²⁸⁵ In 2009, Walter and Moseler showed using PBE that substitution of a single Ag atom occurs preferentially on the surface of the core.³¹⁵ Experimental evidence that multiple silver atoms could be doped in this system³²² provided support for the surface site doping. Later work from Guidez et al. also supported doping on the surface of the core and predicted using several levels of theory that the various Ag_nAu_{25-n}(SH)₁₈⁻ ($n = 1, 2, 4, 6, 8, 10, 12$) isomers with a given number of silver atom dopants would lie close in energy; this study examined Boltzmann-averaged excitation spectra.³²³ In 2013, Tlahuice-Flores reported a related study on Ag_nAu_{25-n}(SCH₃)₁₈⁻ ($n = 2, 4, 6, 8, 10, 12, 13, 25$) using PBE/LANL2DZ and found that the ligand did not greatly affect HOMO–LUMO gaps unless the central atom was substituted with silver.³²⁴ Tlahuice-Flores then calculated normal modes for Au₂₅(SCH₃)₁₈⁻, Ag₁₂Au₁₃(SCH₃)₁₈⁻, and Ag₂₅(SCH₃)₁₈⁻ clusters and proposed that their calculated infrared spectra would enable differentiation of these clusters.²⁹⁷ Kauffman et al. examined the doping of three silver atoms into the nanoparticle and also predicted that the silver atoms preferentially occupy sites on the surface of the core.³²⁵ Recently, a crystal structure was determined for Ag₆Au_{25-n}(SCH₂CH₂Ph)₁₈⁻, which showed on average approximately six silver atoms at surface sites in the system; absorption spectra for two representative Ag₆Au₁₉(SCH₂CH₂Ph)₁₈⁻ nanoparticles were calculated using LR-TDDFT at the LB94/DZ level of theory, and it was found

that the HOMO P orbital typically points toward the silver atoms.³²⁶

In 2012, Negishi et al. synthesized copper-doped $\text{Cu}_n\text{Au}_{25-n}(\text{SCH}_2\text{CH}_2\text{Ph})_{18}^-$ nanoparticles with $n \leq 5$.³²⁷ Using PBE0 calculations with a polarized double- ζ basis set, they predicted that the lowest energy structure for a single copper atom occurs if Cu is substituted for a Au atom on the surface of the core; sites in the metal–thiolate motifs and at the center of the nanoparticle were calculated to lie 0.13 and 0.40 eV higher in energy, respectively. However, they found that the predicted decreases in HOMO–LUMO gaps and in TDDFT absorption peak energies agreed best with doping at the center of the nanoparticle.

2.2.4.4. $\text{Au}_{25}(\text{XR})_{18}$. In addition to thiolate ligands, the Au_{25} nanoparticle has also been synthesized with selenolate ligands using a modified synthesis procedure.³²⁸ PBE0 calculations with a polarized double- ζ basis set indicate that the optimized structure for $\text{Au}_{25}(\text{SeCH}_3)_{18}^-$ is very similar to the structure of $\text{Au}_{25}(\text{SCH}_3)_{18}^-$, although the Au–Se bonds are naturally longer due to the larger atomic radius of Se as compared to S. The LR-TDDFT absorption spectra are also quite similar, although the second major peak is predicted to be shifted to slightly lower energies. They found experimentally that the selenolate-stabilized nanoparticles were more stable against degradation in solution at elevated temperature than the corresponding thiolate-stabilized nanoparticles, which they attributed to higher covalency of the Au–Se bond. In a later study, these authors found that more copper (up to $n = 9$) could be doped into $\text{Cu}_n\text{Au}_{25-n}(\text{SeCH}_2\text{CH}_2\text{Ph})_{18}^-$ nanoparticles than in the corresponding thiolate-stabilized nanoparticles.³²⁹ Using the same level of theory, they again calculated that copper doping at the center of the particle leads to red-shifts in the absorption peaks, so they predicted that the first copper atom is located in the center of the particle. In 2014, Kurashige et al. synthesized Au_{25} nanoparticles covered by telluroate ligands.³³⁰ They optimized the structure of $\text{Au}_{25}(\text{TeCH}_3)_{18}^-$ using PBE0 with a polarized double- ζ basis set and found that the bond lengths between Au atoms in the core and Au atoms in the $\text{Au}_2(\text{TeCH}_3)_3$ units increased by an average of 0.22 Å; the Au–Au bond lengths in the core also increased by 0.01 Å with the larger chalcogenate ligand.

2.2.4.5. $\text{Au}_{38}(\text{SR})_{24}$. As discussed above, many of the early studies on gold–thiolate nanoparticle structure focused on the $\text{Au}_{38}(\text{SR})_{24}$ nanoparticle due to the number of atoms in its core. Inspired by the Au_{102} crystal structure, in 2008 Jiang et al. re-examined the structure of $\text{Au}_{38}(\text{SCH}_3)_{24}$ using DFT-based molecular dynamics and suggested it to be a disordered core surrounded by six short and four long motifs³³¹ and later revised the structure to be passivated by three short and four long motifs.³³² Simultaneously, Pei et al. proposed a face-shared bi-icosahedral Au_{23} core surrounded by three short and six long motifs using PBE/DND.³³³ In 2010, Lopez-Acevedo et al. used both Xα and PBE to determine a lower energy structure that possesses a face-shared bi-icosahedral Au_{23} core surrounded by three $\text{Au}(\text{SR})_2$ and six $\text{Au}_2(\text{SR})_3$ staple units in a D_3 symmetric arrangement.³³⁴ This structure matched the experimental X-ray diffraction (XRD) pattern. These authors found that the electronic structure and optical absorption spectrum could be interpreted in terms of a particle-in-a-cylinder model. Even though the nanoparticle has 14 superatomic electrons, which is not a spherical magic number, this particle was found to have a large HOMO–LUMO gap due to its elongated structure. Furthermore, the authors calculated the CD spectrum for the

D_3 system and found it to be a close match with prior experimental work.²⁹³ Shortly thereafter, the D_3 structure of the nanoparticle was confirmed by an X-ray crystal structure investigation.³³⁵

Jung et al. examined the stability of the $\text{Au}_{38}(\text{SR})_{24}$ ($\text{R} = \text{CH}_3, \text{C}_6\text{H}_{13}, \text{CH}_2\text{CH}_2\text{Ph}, \text{Ph}, \text{PhF}$, and PhCOOH) nanoparticle using PW91.²⁹² As for $\text{Au}_{25}(\text{SR})_{18}^-$, the authors found that aliphatic thiols led to larger VIP–VEA values and reaction energies to separated gold and thiyil species.

Negishi et al. performed a combined theory–experiment investigation on Pd doping in $\text{Au}_{38}(\text{SR})_{24}$ and determined that up to two Pd atoms could be doped in this system.³³⁶ Using the B3LYP functional with a polarized double- ζ basis set, they optimized the geometry of the $\text{Pd}_2\text{Au}_{36}(\text{SCH}_3)_{24}$ nanoparticle with the Pd atoms in the centers of the two icosahedra in the core.

In 2013, Molina et al. examined ligand exchange of *R*-1,1'-binaphthyl-2,2'-dithiol (*R*-BINAS) on the anticlockwise (*A*)- $\text{Au}_{38}(\text{SCH}_3)_{24}$ nanoparticle.³³⁷ Using PBE/TZP, they found that *R*-BINAS thermodynamically favors binding between two dimer motifs; intrastaple binding was calculated to lie 1.05 eV higher in energy. The CD spectra of the various isomers were found to be quite sensitive to the structure; however, the two lowest energy isomers were similar to *A*- $\text{Au}_{38}(\text{SCH}_3)_{24}$.

2.2.4.6. $\text{Au}_{102}(\text{SR})_{44}$. As the first nanoparticle whose crystal structure was established, the $\text{Au}_{102}(\text{SR})_{44}$ nanoparticle immediately attracted significant theoretical interest. Three groups published studies of its electronic structure within the first year.^{10,338,339} Walter et al. proposed that the $\text{Au}_{102}(\text{SR})_{44}$ ($\text{R} = p\text{-MBA}$) nanoparticle could be thought of as a Au_{79} core surrounded by 19 RS–Au–SR units and 2 $\text{Au}_2(\text{SR})_3$ units.¹⁰ They calculated the electronic density of states and determined the HOMO–LUMO gap to be 0.5 eV using PBE. Using the angular momentum projected density of states, they showed that the orbitals near the HOMO have G character, whereas those near the LUMO have H character; a cut-plane visualization of the LUMO also showed nodal characteristics of an H orbital. These authors proposed that gold–thiolate nanoparticles can be understood via a superatom model in which the number of delocalized electrons in the core of the nanoparticle is calculated by subtracting the number of electrons localized by the thiolate ligands from the total number of valence gold electrons; the nanoparticle thus has 58 delocalized electrons, which corresponds to a shell filling in the jellium model, which is responsible for creating a large HOMO–LUMO gap.¹⁰ Although the core appears in this way to act as a formal Au_{79}^{21+} system, the authors found that the gold–thiolate bonds at the surface are only weakly polarized, so Bader charge analysis predicts a total charge in the core of only +2.2 electrons.¹⁰

Using PW91/DNP, Gao et al. calculated the HOMO–LUMO gap of $\text{Au}_{102}(\text{SCH}_3)_{44}$ to be 0.54–0.56 eV.³³⁸ They also calculated HOMO–LUMO gaps for related hypothetical clusters $\text{Au}_{102}(\text{SCH}_3)_{42}$ (56 delocalized electrons) and $\text{Au}_{104}(\text{SCH}_3)_{46}$ (58 electrons), and found HOMO–LUMO gaps of 0 and 0.51 eV, respectively, suggesting that the 58 electron shell closing of spherical jellium is important for creating a large gap. Using a Hirshfeld charge analysis, these authors predicted a total charge transfer of 2.87 electrons from Au to S. Similar to Walter et al., Li et al. employed a PBE exchange correlation functional to examine the $\text{Au}_{102}(\text{S } p\text{-MBA})_{44}$ nanoparticle and found a HOMO–LUMO gap of about 0.5 eV.³³⁹ They found that the DFT optimized

coordinates were in good agreement with the experimental values from the crystal structure. They calculated the average adsorption energy to be 1.96 eV per MBA radical.

In 2010, Reimers et al. questioned the need to consider superatomic electron shell fillings and instead suggested that the stability of clusters is due to binding strength and surface coverage.³⁴⁰ Similar to previous work, they found very small charge transfer between gold and sulfur atoms, with a charge of +0.16 electrons for gold atoms in the linear Au(SR)₂ motifs. Although the formal charge of gold atoms in small gold–thiolate molecules with related linear motifs is Au(I), these authors argued that they should be considered to be Au(0) in the nanoparticles.³⁴⁰ It should be noted that although the formal charge of these atoms is considered to be Au(I), the Au–S bonding is well-established to be quite covalent with relatively little charge transfer due to similar electronegativities of gold and sulfur. Later work showed (using PBE with Bader charge analysis) that gold atoms in the core have average charges of 0.00–0.06 electrons, while gold atoms in the outermost sulfur-containing layer have average charges of 0.13 electrons.³⁴¹ Core-level shifts (CLS) for Au₁₀₂(SCH₃)₄₄ using PBE with scalar-relativistic pseudopotentials generated with an electron hole in the Au 4f-shell show that atoms in the core of the nanoparticle have CLS values ranging from +0.2 to −0.2 eV, while the gold atoms in the gold–thiolate units lead to a peak centered at +0.5 eV, suggesting that the gold atoms are in significantly different environments.²⁹⁶

Heinecke et al. presented a combined theory–experiment study of ligand exchange on the Au₁₀₂(SR)₄₄ nanoparticle.³⁴² PBE calculations using the R = H ligand examined the mechanism for the ligand exchange of an incoming thiol (in this case, methanethiol) with the nanoparticle. The authors found an intermediate in the reaction that was formed by insertion of methylthiol into one of the HS–Au–SH motifs, leading to formation of a hydrogen bond between the S–H group of the incoming methylthiol and the sulfur atom that remained attached to the nanoparticle. Using a series of constrained optimizations, they estimated a barrier height of 23 kcal/mol for the ligand exchange process.

In 2012, Jung et al. examined the stability of the Au₁₀₂(SR)₄₄ (R = CH₃, C₆H₁₃, CH₂CH₂Ph, Ph, PhF, and PhCOOH) nanoparticle using PW91.²⁹² Geometries were optimized with a numerical double- ζ basis set, and single point energies were computed with a numerical double- ζ plus polarization basis set. As for Au₂₅(SR)₁₈[−] and Au₃₈(SR)₂₄, the authors found that aliphatic thiols led to higher VIP–VEA values and reaction energies to separated gold and thiyil species, and were thus predicted to lead to more stable nanoparticles.

Later, Gao studied the energetics of substitution of one *p*-BBT (*para*-bromobenzene thiol) for one *p*-MBA ligand in nine distinct sites on the Au₁₀₂(*p*-MBA)₄₄ nanoparticle using PBE with a Grimme dispersion correction and basis set superposition error corrections.³⁴³ The substitution energy at one site (denoted site 2) was found to be −5.68 kcal/mol, which was substantially lower than the others;³⁴³ this site was one of those determined in the previous crystal structure.³⁴² However, site 1, which was also exchanged in the experimental crystal structure study, was found to have a substitution energy of only −0.50 kcal/mol for the Au₁₀₂(*p*-MBA)₄₄ monomer, which was the least favorable site in the theoretical calculations. Gao explained this initially surprising result by considering the dimer, which in the crystal structure possesses π – π interactions between two ligands at site 1 on each monomer. He then

considered substitution of 14 groups in the *para* position on the benzenethiols and suggested that N(CH₃)₂ and NH₂ substitution may potentially enhance the aggregation and thus crystal formation of Au₁₀₂(SR)₄₄.

In 2011, linear response TDDFT calculations were utilized to study the optical absorption spectrum of Au₁₀₂(*p*-MBA)₄₄ using the PBE level of theory.³⁴⁴ Both experimental mid-IR measurements and theory indicated a band gap near 0.5 eV. The theoretical analysis of the electronic excitation spectrum indicated that the lowest energy transitions have primarily Au(6sp) to Au(6sp) character, and interband (Au(5d) to Au(6sp)) transitions have an onset around 1.7 eV.

Recently, the two chiral enantiomers of Au₁₀₂(SR)₄₄ were partially resolved experimentally using a chiral phase transfer agent.³⁴⁵ The CD spectrum of the left-handed A-Au₁₀₂(SH)₄₄ was calculated using LR-TDDFT with an LDA functional. The peaks above 600 nm were calculated to have the same sign as experiment, although the peak below 600 nm had the opposite sign. The authors attributed the differences to the use of the model ligand and to the omission of solvent effects.

2.2.4.7. Au₁₄₄(SR)₆₀. In 2009, Lopez-Acevedo et al. proposed a structure for the commonly observed Au₁₄₄(SR)₆₀ nanoparticle using the PBE exchange correlation functional with R = CH₃.³⁴⁶ The proposed structure has icosahedral symmetry with an interior core of 12 atoms and a second layer with 42 atoms, each with Mackay icosahedral packing, and a third shell with 60 symmetry-equivalent atoms. Finally, 30 Au(SCH₃)₂ units are arranged on the surface of the core in a chiral fashion. The authors found that the calculated XRD pattern of this predicted structure is in good agreement with experiment.

In 2011, Malola and Häkkinen predicted using PBE that silver atoms could substitute for gold atoms in the third shell of 60 atoms within the core of the Au₁₄₄(SH)₆₀ nanoparticle.³⁴⁷ This provided a logical explanation for the experimental observation that up to 60 silver atoms could be doped into Au₁₄₄(SR)₆₀.³⁴⁸ Koivisto et al. in a combined theory–experiment investigation studied the optical gap of both the pure gold Au₁₄₄(SR)₆₀ and the silver-doped (Au/Ag)₁₄₄(SR)₆₀ nanoparticles.³⁴⁹ Because the experimental alloys do not have an exact composition, LR-TDDFT calculations at the PBE level of theory were performed for Au₁₄₄(SH)₆₀, Au₁₁₄Ag₃₀(SH)₆₀, Au₈₆Ag₅₈(SH)₆₀, and Au₈₄Ag₆₀(SH)₆₀, where the silver atoms are located in the third shell of the core. The optical gap for Au₁₄₄(SR)₆₀ was found to be 0.19 eV in experiment and 0.32 eV theoretically, which are in reasonable agreement considering that thermal effects, which would widen the transitions by about 0.1 eV, were not treated in the calculations. For alloys, the optical gap was found to be 0.12–0.26 eV experimentally, and was predicted to be 0.16–0.36 eV computationally. Although the onset of the absorption appeared to stay the same regardless of silver content, the strength of the first peak increased with increasing silver content. Recently, Malola et al. examined the Au₁₄₄(SH)₆₀ and Au₈₄Ag₆₀(SH)₆₀ nanoparticles and found a collective intraband dipolar response that was particularly strong for the silver-doped system.³⁵⁰ They also predicted very strong CD signals due to the intrinsically chiral interface between the gold core and the S–Au–S units on the surface.

Grönbeck calculated core-level shifts (CLS) for the gold atoms in Au₁₄₄(SCH₃)₆₀ using PBE with scalar-relativistic pseudopotentials generated with an electron hole in the Au 4f-shell.²⁹⁶ His calculations suggested that the CLS for Au atoms in the third layer of the core may overlap with those in the first

two layers of the core in a range of -0.2 to 0.2 eV, although all of the shifts in the 0.1 – 0.2 eV range are predicted to come from the third (outer) core–shell. A clear positive shift of Au 4f binding energies in the $\text{Au}(\text{SR})_2$ units was predicted, which agreed with previous interpretation of experimental results.³⁵¹

In 2013, Bahena et al. revisited the original Lopez-Acevedo et al. model [ref 346] for the $\text{Au}_{144}(\text{SCH}_3)_{60}$ nanoparticle to create a structure with *I* (chiral icosahedral) symmetry.³⁵² This model has the same core structure and the same connectivity of the S–Au–S units at the surface; the difference in the two models lies in the orientation of the methyl groups. The structure was optimized with PBE and PW91, and the calculated STEM diffraction images were determined to be in good agreement with experiment. This model was then employed in real-time TDDFT calculations using the PBE functional to calculate the optical absorption spectrum of $\text{Au}_{144}(\text{SCH}_3)_{60}$, which was compared to low-temperature experimental measurements on $\text{Au}_{144}(\text{SCH}_2\text{CH}_2\text{Ph})_{60}$ to show that significant structure (and thus information about quantum confinement in this system) is present in its optical absorption spectrum.³⁵³

2.2.4.8. Recent Crystal Structures. Recently, several other crystal structures of nanoparticles with different stoichiometries have been determined, and theoretical studies on these systems have been performed. In 2012, Zeng et al. published a crystal structure determination of the $\text{Au}_{36}(\text{SPh}-t\text{Bu})_{24}$ ($\text{SPh}-t\text{Bu} = 4$ -*tert*-butylbenzenethiolate), which was the first nanoparticle to exhibit a face-centered cubic (fcc) core.³⁵⁴ This structure was initially interpreted as containing four $\text{Au}_2(\text{SR})_3$ staples and 12 bridging thiolates. DFT optimizations were performed for the experimentally determined atomic coordinates and for the nanoparticle with SH ligands. They calculated a large HOMO–LUMO gap of 1.5 – 1.8 eV, which was in good agreement with the experimental optical gap of 1.7 eV. They demonstrated that this large gap arises from crystal field splitting of the superatomic D orbitals, and that the nanoparticle has two filled and three unfilled D orbitals. LB94/TZP TDDFT calculations on PBE/TZP optimized structures were later employed with SCH_3 ligands to analyze the origin of the low-energy transitions, which primarily occur out of the HOMO.³⁵⁵

In 2013, Zeng et al. published the crystal structure of the $\text{Au}_{28}(\text{SPh}-t\text{Bu})_{20}$ nanoparticle and interpreted the structure as consisting of an Au_{20} core of two interpenetrating cuboctahedra with fcc symmetry protected by four $\text{Au}_2(\text{SR})_3$ units and eight bridging thiolates; the structure is chiral, and the researchers were able to separate the enantiomers and collect CD spectra for each.³⁵⁶ Knoppe et al. then used DFT with the PBE functional to study the electronic structure of the related $\text{Au}_{28}(\text{SCH}_3)_{20}$ nanoparticle.³⁵⁷ Using a Bader charge analysis, they reinterpreted the structure of the nanoparticle as a Au_{14} core protected by two $\text{Au}_3(\text{SR})_4$ trimer units as well as four $\text{Au}_2(\text{SR})_3$ dimer units. Of note, the six gold atoms in the trimer units were calculated to be the most oxidized in the nanoparticle. Using LR-TDDFT, they calculated both the optical absorption and the CD spectra of the $\text{Au}_{28}(\text{SCH}_3)_{20}$ system and found excellent agreement for spectra of the clockwise enantiomer with experimental enantiomer 2. Furthermore, they computed the electronic structure of the system and found that the 1S and 1P superatomic orbitals lie below the band arising from the 5d orbitals of Au and thus are not the frontier orbitals; the 1D orbitals do comprise the five lowest unoccupied orbitals, however. They attributed this finding to the nonspherical geometry of the Au_{14}^{6+} core.

In 2013, Das et al. solved the crystal structure of a $\text{Au}_{23}(\text{SC}_6\text{H}_{11})_{16}^-$ nanocluster and analyzed the structure as arising from a Au_{15} core, consisting of a Au_{13} cuboctahedron with two capping gold atoms, protected by two trimeric $\text{Au}_3(\text{SR})_4$ motifs, two dimeric $\text{Au}_2(\text{SR})_3$ units, and two bridging thiolates.³⁵⁸ They employed PBE0 calculations with a polarized double- ζ basis set and determined that, although the cluster has 8 delocalized electrons, the HOMO does not have P-like symmetry.

In 2014, Das et al. determined the crystal structure of the $\text{Au}_{24}(\text{SCH}_2\text{Ph}-t\text{Bu})_{20}$ nanoparticle and found that the system has a bitetrahedral Au_8 core protected by four $\text{Au}_4(\text{SR})_5$ units.³⁵⁹ They calculated the TDDFT optical absorption spectrum of this system using the B3LYP functional with a polarized double- ζ basis set and found that the optical absorption spectrum slightly overestimates the experimental excitation energies, but the overall shape is in good agreement. It should be noted that the crystal structure of this system differs from that of the related $\text{Au}_{24}(\text{SeC}_6\text{H}_5)_{20}$ nanoparticle³⁶⁰ and that the optical absorption spectrum differs from that of the previously reported $\text{Au}_{24}(\text{SCH}_2\text{CH}_2\text{Ph})_{18}$ nanoparticle,³⁶¹ so there is a possibility that several structures can exist for this stoichiometry.

Also in 2014, Crasto et al. published the first crystal structure of a gold nanoparticle containing bulky thiolate ligands and showed that $\text{Au}_{30}\text{S}(\text{S}-t\text{-Bu})_{18}$ possesses a combination of two monomeric $\text{Au}(\text{SR})_2$ and two trimeric $\text{Au}_3(\text{SR})_4$ units, several bridging thiolates, and a single sulfide in a novel μ_3 -coordinating position.³⁶² Using LDA geometry optimizations and PBE TDDFT calculations, they analyzed the Bader charges for the system and observed charges that ranged from -0.02 to $+0.12$ electrons for the gold atoms. They calculated optical absorption spectra for the $\text{Au}_{30}\text{S}(\text{S}-t\text{-Bu})_{18}$ nanoparticle as well as a related $\text{Au}_{30}(\text{S}-t\text{-Bu})_{18}$ system and determined that the spectrum of $\text{Au}_{30}(\text{S}-t\text{-Bu})_{18}$ was in good agreement with the available experimental spectrum of this system. CD spectra were also computed for both enantiomers.

2.2.4.9. Catenane Structures. Gold–thiolate clusters with the stoichiometry $(\text{AuSR})_n$ have been of interest for many years due to applications in antiarthritic and antitumor drugs.³⁶³–³⁶⁵ Most studies have examined clusters with fewer than 10 metal atoms, but several recent theoretical investigations have examined $(\text{AuSR})_n$ with $n \geq 10$. In 2009, Shao et al. proposed helical and catenane (interlocked ring) structures for systems with $n = 6$ – 12 .³⁶⁶ Kacprzak et al. investigated these systems in 2010 and found that crown structures were lower in energy than helical structures for $n = 6$ – 9 but agreed that catenane structures are favorable for $n = 10$ – 12 .³⁶⁷ They also found that silver–thiolate clusters have the smallest binding energies.

2.2.4.10. Other Proposed Nanocluster Structures. In 2009, Jiang et al. employed the TPSS/def2-TZVP level of theory and proposed structural models for nanoparticles including $\text{Au}_{10}(\text{SCH}_3)_8$, $\text{Au}_{12}(\text{SCH}_3)_9^+$, and $\text{Au}_{20}(\text{SCH}_3)_{16}^-$.^{368,369} The structure proposed for $\text{Au}_{12}(\text{SCH}_3)_9^+$ was an octahedral core surrounded by six $\text{Au}_2(\text{SCH}_3)_3$ units, which would possess two delocalized electrons within a symmetric gold core.³⁶⁸ The structures proposed for $\text{Au}_{10}(\text{SCH}_3)_8$, and $\text{Au}_{20}(\text{SCH}_3)_{16}^-$ involved a newly proposed $\text{Au}_3(\text{SCH}_3)_4$ trimer unit, which was postulated to cover portions of nanoparticles with a very small radius of curvature, such as the tetrahedral Au_4 core (covered by 2 trimer units) and elongated Au_8 core (covered by 4 trimer units) proposed for these nanoparticles.³⁶⁹ Simultaneously, using a basin-hopping approach followed by PBE/

DND and PBE/TZP calculations, Pei et al. proposed several low energy isomers of $\text{Au}_{20}(\text{SCH}_3)_{16}$ that also possess an elongated Au_8 core surrounded by four $\text{Au}_3(\text{SCH}_3)_4$ trimer units.³⁷⁰ They calculated the optical absorption spectra of this nanoparticle using TDDFT calculations and found that their third-lowest energy isomer yielded a spectrum in very good agreement with experiment.³⁷⁰ These trimer units have since been confirmed experimentally in other crystal structures.

In 2012, Tlahuice and Garzón using PBE/LANL2DZ proposed a related structure for the $\text{Au}_{18}(\text{SCH}_3)_{14}$ cluster with an elongated Au_8 core protected by two dimer and two trimer units.³⁷¹ They then offered a hypothetical series of nanoclusters based on replacing one to four of the trimer units of $\text{Au}_{20}(\text{SCH}_3)_{16}$ with dimer units, yielding $\text{Au}_{19}(\text{SCH}_3)_{15}$, $\text{Au}_{18}(\text{SCH}_3)_{14}$, $\text{Au}_{17}(\text{SCH}_3)_{13}$, and $\text{Au}_{16}(\text{SCH}_3)_{12}$.³⁷² In addition, they suggested structures for systems built by replacing dimer units of $\text{Au}_{12}(\text{SCH}_3)_9^+$ with trimer units, yielding $\text{Au}_{13}(\text{SCH}_3)_{10}^+$, $\text{Au}_{14}(\text{SCH}_3)_{11}^+$, and $\text{Au}_{15}(\text{SCH}_3)_{12}^+$.³⁷²

In 2011, Jiang developed a “Staple Fitness” model that suggested that the enormous variety of possible cores of nanoparticles could be refined by considering the “total pair distance”, or the sum of the interatomic pair distances, for the various ways of pairing up a certain number of gold atoms on the surface of the core.³⁷³ After establishing that this approach worked for the structures of $\text{Au}_{25}(\text{SR})_{18}$ and $\text{Au}_{38}(\text{SR})_{24}$, he employed this model to predict that the lowest energy structure of $\text{Au}_{19}(\text{SCH}_3)_{13}$ consists of an Au_{11} core that is a defective, centered icosahedron with C_2 symmetry, surrounded by two $\text{Au}(\text{SCH}_3)_2$ and three $\text{Au}_2(\text{SCH}_3)_3$ units. The PBE/def2-TZVP calculated XRD pattern for the lowest energy isomer agreed well with experiment.³⁷³

For structures with a high ratio of thiolates to gold, catenane-like structures have been proposed for several systems. In 2012, Pei et al. used a basin-hopping approach followed by PBE/DND and PBE/TZP calculations to propose a structure for the $\text{Au}_{24}(\text{SR})_{20}$ nanocluster, which has one less gold atom but two more thiolate ligands than the $\text{Au}_{25}(\text{SR})_{18}$ nanoparticle.³⁷⁴ They suggested a structure with an elongated Au_8 core protected by two $\text{Au}_3(\text{SR})_4$ and two $\text{Au}_5(\text{SR})_6$ motifs that are interlocked. The optical absorption spectrum for this structure was calculated with TDDFT and was found to be in reasonable agreement with experiment. Although the crystal structure of the $\text{Au}_{24}(\text{SCH}_2\text{Ph}-t\text{Bu})_{20}$ nanocluster was later found to be passivated by tetramer motifs,³⁵⁹ the selenolate version (i.e., $\text{Au}_{24}(\text{SeC}_6\text{H}_5)_{20}$)³⁶⁰ was found to have a two trimer and two pentamer passivated structure similar to that proposed by Pei et al. In addition, this study was instrumental in suggesting structures that could potentially arise from catenane structures. Jiang et al. then proposed a structure for $\text{Au}_{15}(\text{SR})_{13}$ that could also be envisioned as arising from reduction of a catenane-like species; this geometry has a tetrahedral Au_4 core protected by two trimer units surrounded by an $\text{Au}_5(\text{SR})_5$ ring and determined its optical absorption spectrum using TDDFT.³⁷⁵ Shortly thereafter, Tlahuice-Flores et al. proposed a related structure for $\text{Au}_{15}(\text{SR})_{13}$ with a tetrahedral Au_4 core covered by one tetramer $\text{Au}_4(\text{SR})_5$ motif and one heptamer $\text{Au}_7(\text{SR})_8$ motif; the optical absorption and CD spectra for this system were calculated, and the CD spectra were found to be in better agreement with experiment than the original proposed structure.³⁷⁶

Tlahuice-Flores et al. examined the vibrational normal modes for nanoparticles with less than 25 gold atoms whose structures had been proposed up to that time.²⁹⁸ They found that the

calculated Raman spectra show distinctive patterns for each cluster size, and that no size-dependent trends are apparent. Computed IR spectra have some intense peaks that can be attributed to Au–S asymmetric stretching modes of dimer and trimer motifs.

Recently, Yu et al. suggested a structure for the highly luminescent $\text{Au}_{22}(\text{SR})_{18}$ nanoparticle that contained an Au_8 core, two trimeric ($\text{Au}_3(\text{SR})_4$), and two tetrameric ($\text{Au}_4(\text{SR})_5$).³⁷⁷ By comparing hypothetical reaction energies using TPSS/def2-SV(P), they found that this cluster is somewhat more stable than the proposed $\text{Au}_{18}(\text{SR})_{14}$ and $\text{Au}_{20}(\text{SR})_{16}$ structures but slightly less stable than the $\text{Au}_{24}(\text{SR})_{20}$ structure suggested by Pei et al. in ref 374. TDDFT calculations of the most stable $\text{Au}_{22}(\text{SR})_{18}$ nanoparticle yielded a reasonable optical gap as compared to experiment, but the shape of the overall spectrum was found to be different.³⁷⁷

Some larger nanoparticle structures have also been proposed using density functional theory. In 2010, Jiang, Walter, and Akola used PBE in a variety of electronic structure codes (CPMD, VASP, Turbomole, and GPAW) to suggest that the structure of $\text{Au}_{44}(\text{SR})_{28}^{2-}$ has a fcc Au_{28} core surrounded by 3 monomer and 6 dimer units.³⁷⁸ Although the agreement with experimental optical absorption spectra and XRD pattern data was only moderate, fcc cores have since been found in experimental X-ray crystal structures of $\text{Au}_{36}(\text{SPh}-t\text{Bu})_{24}$ and later nanoparticles, so this motif may be further explored in the future.

In 2013, Pei et al. proposed a different structure based on an fcc core for a neutral $\text{Au}_{44}(\text{SR})_{28}$ nanoparticle.³⁷⁹ Motivated by related fcc crystal structures, they suggested a 26-atom core protected by 2 monomer and 8 dimer units in a chiral fashion. A similar structure was simultaneously proposed by Zeng et al., although no computations on this system were performed.³⁸⁰ At the PBE/TZP level of theory, Pei et al. found that this structure is more stable by 2.4 or 1.02 eV than the structure proposed by Jiang et al.³⁷⁸ for $\text{Au}_{44}(\text{SR})_{28}^{2-}$. They also found close agreement between the TDDFT and experimental optical absorption spectra for this system. In addition, they computed CD spectra of both enantiomers for future experiment–theory comparison.

In 2012, Malola et al. proposed using PBE that the $\text{Au}_{40}(\text{SR})_{24}$ nanoparticle, which had been found experimentally in close connection with $\text{Au}_{38}(\text{SR})_{24}$, has a core that consists of two Au_{13} icosahedra that do not share any atoms (in contrast to the face-shared biicosahedral Au_{23} core of Au_{38}) covered by 6 monomer and 4 dimer units.³⁸¹ This work was later extended to predict structures using LDA for $\text{Au}_{57}(\text{SH})_{32}^-$, $\text{Au}_{74}(\text{SH})_{40}$, and $\text{Au}_{108}(\text{SH})_{56}$ based on the idea of multimers (dimers, trimers, tetramers, and pentamers, respectively) of Au_{13} icosahedra connected by an appropriate number of monomer and dimer gold–thiolate units.³⁸² Using LR-TDDFT, Malola et al. calculated optical absorption and CD spectra for $\text{Au}_{40}(\text{SR})_{24}$ that were found to be in good agreement with experimental data.³⁸¹ Using the staple fitness model, Jiang suggested that a different low-symmetry structure for the $\text{Au}_{40}(\text{SR})_{24}$ nanoparticle with two extra Au atoms at the “waist” of a 23-atom biicosahedral core, which is covered by 3 monomer and 6 dimer units, is essentially isoenergetic at the PBE/def2-TZVP level of theory but is about 0.5 eV more stable at the TPSS/def2-TZVP level of theory.²⁷⁸

Two structures have also been proposed for the $\text{Au}_{54}(\text{SR})_{30}$ nanoparticle. Jiang suggested a truncated-octahedral Au_{38} core

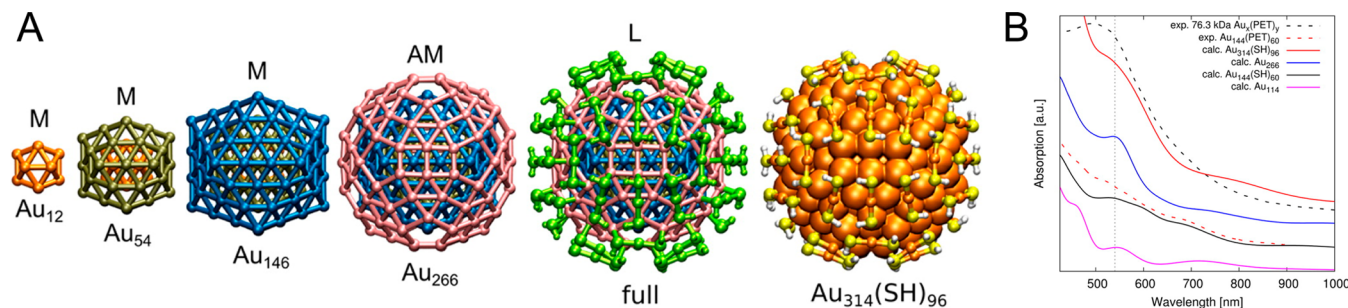


Figure 10. (A) Structure of $\text{Au}_{314}(\text{SH})_{96}$ showing Mackay (M) and anti-Mackay (AM) layers surrounded by 48 $\text{Au}(\text{SH})_2$ ligand units (L); (B) calculated optical absorption spectrum for $\text{Au}_{314}(\text{SH})_{96}$ and other nanoparticles. Adapted with permission from ref 385. Copyright 2013 American Chemical Society.

surrounded by 12 monomer and 4 dimer units for this system.²⁷⁸ Using PBE, the HOMO–LUMO gap for this nanoparticle was predicted to be 0.4 eV. In contrast, Malola et al. proposed a structure with a core consisting of a Au_{13} icosahedron in edge-contact with a Au_{23} biicosahedron; this cluster would be protected by 6 monomer and 6 dimer units.³⁸² They computed optical absorption spectra in reasonable agreement with experiment with a first, weak calculated transition at 0.3 eV.

A number of structures have been proposed that employ decahedral, particularly Marks decahedral, cores. For the $\text{Au}_{33}(\text{SR})_{22}$ nanoparticle, a structure has been proposed that consists of a 19-atom biicosahedral core covered with 2 monomer and 6 dimer units.²⁷⁸ PBE calculations predict a HOMO–LUMO gap of 0.60 eV for this system. For the $\text{Au}_{67}(\text{SR})_{35}$ nanoparticle, a combined theory–experiment investigation suggests a 47-atom decahedral core capped by 20 monomer units (10 on each end of the core) and 5 dimer units (linking the two ends of the core).³⁸³ PBE calculations were performed to predict the projected densities of states, XRD pattern, and large (0.75 eV) HOMO–LUMO gap for this system. For $\text{Au}_{130}(\text{SH})_{50}$ PBE optimizations have been performed on a system consisting of a 75-atom Marks decahedral core capped by two 15-atom rings; the resulting Au_{105} core is passivated by 25 $\text{Au}(\text{SH})_2$ units.³⁸⁴ Simulated high-angle annular dark field scanning/transmission electron microscopy (HAADF-STEM) images were found to be in good agreement with experiment. The optical absorption spectrum of this system was calculated using real-time TDDFT using TDLDAs with the Perdew–Zunger exchange-correlation functional and was found to be in moderate agreement with experiment.

The largest nanoparticle for which atomistic quantum mechanical calculations have been performed is the $\text{Au}_{314}(\text{SH})_{96}$ nanoparticle (Figure 10), which was built from Mackay icosahedral shells with an anti-Mackay shell at the core surface in analogy to the proposed $\text{Au}_{144}(\text{SH})_{60}$ structure, surrounded by 48 $\text{Au}(\text{SH})_2$ units.³⁸⁵ The geometry of this system was optimized using LDA, and the optical absorption of this system was calculated using LR-TDDFT with the PBE functional. The optical absorption spectrum of this system was analyzed using time-dependent density functional perturbation theory (TD-DFPT). These researchers found that a localized surface plasmon resonance (LSPR) peak arises at 540 nm in this system.³⁸⁵

2.2.5. Halogen-Stabilized Gold Nanoparticles. Very few theoretical studies have been performed for gold nanoparticles entirely passivated by halide ligands. Two studies^{386,387} have

examined gold–halide clusters that are in direct analogy to gold–thiolate structures, but which have slightly higher symmetry due to lack of an organic group. Jiang and Walter examined $\text{Au}_{25}\text{X}_{18}^-$ ($\text{X} = \text{F}, \text{Cl}, \text{Br}$, or I) with T_h symmetry using PBE/def2-TZVP.³⁸⁶ They found that I^- most closely reproduces SCH_3^- in terms of charge transfer, so $\text{Au}–\text{I}$ bonds were determined to be mostly covalent, whereas F^- leads to $\text{F}–\text{Au}–\text{F}$ angles that are the closest to $\text{S}–\text{Au}–\text{S}$ angles. Overall, they decided that $\text{Au}_{25}\text{Cl}_{18}^-$ is the closest structural analogue to $\text{Au}_{25}(\text{SCH}_3)_{18}^-$, which they attributed to similar covalent radii of the Cl and S atoms; the HOMO–LUMO gap of these nanoparticles is also essentially the same (within 0.01 eV). They suggest that the $\text{Au}_{25}\text{Cl}_{18}^-$ containing a 13-atom gold core and six Au_2Cl_3 units is a very stable local minimum, if not the global minimum, for this cluster.

In 2013, Thahuice-Flores et al.³⁸⁷ predicted a $\text{Au}_{144}\text{Cl}_{60}^z$ ($z = 0, 2+, 4+$) nanoparticle with I symmetry in analogy to their recent prediction³⁵² of the structure of $\text{Au}_{144}(\text{SR})_{60}$. They find a slight (within 0.13 Å) distortion from perfect I symmetry for the $z = 0$ system, which they attribute to a Jahn–Teller mechanism arising from partial occupancy of degenerate superatomic orbitals; the $z = 2+$ and $4+$ systems maintain I symmetry to within a tolerance of 0.03 Å.

2.2.6. Phosphine-Passivated Gold Nanoparticles. Gold nanoclusters stabilized with phosphine ligands (which also typically possess electron-withdrawing ligands such as halides and/or thiolates) have been studied experimentally since the 1960s,³⁸⁸ and represent some of the earliest systems investigated theoretically. Although a number of initial theoretical studies focused on systems with a small number of gold atoms (see refs 36 and 389, and references therein), in this Review we focus on investigations with at least 10 gold atoms.

2.2.6.1. Au_{11} . The undecagold compound has been one of the most studied phosphine-stabilized systems, and several crystal structures of $\text{Au}_{11}(\text{PR}_3)_7\text{X}_3$ ($\text{X} = \text{SCN}, \text{I}, \text{S}-4-\text{NC}_5\text{H}_4$; $\text{R} = \text{Ph}$),^{388,390,391} $\text{Au}_{11}(\text{PPh}_3)_8\text{Cl}_2^{+}$,³⁹² and $\text{Au}_{11}(\text{PMePh}_2)_{10}^{3+}$ [ref 393] are available. All ligands are bonded radially to the gold atoms; no bridging motifs are found for chloride or thiolate ligands for these systems. The very earliest theoretical work on this system was completed by Mingos, who performed extended Hückel calculations and showed that the gold 6s orbitals combine to form four bonding and seven antibonding molecular orbitals,³⁹⁴ which correspond to the delocalized superatomic orbitals discussed in recent work. In 2008, Walter et al. examined the $\text{Au}_{11}(\text{PH}_3)_7(\text{SCH}_3)_3$ and $\text{Au}_{11}(\text{PH}_3)_7\text{Cl}_3$ systems using PBE and found that both systems have HOMO

orbitals of P symmetry and LUMO orbitals with D symmetry, with HOMO–LUMO gaps of 1.5 and 2.1 eV, respectively.¹⁰

Early theoretical work on ligand-protected undecagold clusters by Spivey et al. examined the interactions of 1–4 thiolate ligands with a bare Au₁₁ cluster and determined that the lowest energy structure of the system is three-dimensional when ligands are attached.³⁹⁵ In a later study in 2014, Dufour et al. used several levels of theory (including B3LYP, CAM-B3LYP, wB97X, and MP2) to examine the structures of neutral and tricationic Au₁₁ and the binding of phosphine, thiol, thiolate, chlorine, and chloride ligands to these cores; similar to the study by Spivey et al.,³⁹⁵ they found that the adsorption of multiple ligands leads to large rearrangement of the metal core.³⁹⁶

Provorse and Aikens examined the structure of the Au₁₁(PH₂C₂H₂PH₂)₄X₂⁺ (X = Cl, Br) compound using Xα/TZP geometry optimizations and determined that the bidentate phosphine ligands lead to a C₂-symmetric gold cluster, which has higher symmetry than the C₁-symmetric crystal structures of Au₁₁ compounds with monodentate phosphines.³⁹⁷ They calculated SAOP/TZP optical absorption and CD spectra of these clusters and found spectra in good agreement with experiment. They determined that the peaks in the visible region of the spectra arose from transitions between the 6s p orbitals of gold (specifically P → D transitions); however, the CD signals were only apparent when the cluster core was in the presence of a ligand field.

Thiolate-for-thiolate ligand exchange on an Au₁₁(SR')₃(PH₃)₇ complex with several incoming thiols HSR'' (R' = H, CH₃; R'' = H, CH₃, CH₂CH₃, CH₂CH₂CH₃, CH₂CH(NH₂)COOH) was studied by Hadley and Aikens.³⁹⁸ They found that longer organic chains on the incoming thiol increase the reaction energy by up to 0.8 kJ/mol. The reaction of cysteine was found to be more exothermic than other ligands. The reaction was found to proceed through an associative mechanism involving breakage of an Au–S bond.

Lopez-Acevedo et al. studied CO oxidation on an Au₁₁(PH₃)₇Cl₃ compound that had been “activated” via removal of a Cl ligand to leave a nanoparticle with 9 superatomic electrons.³⁹⁹ They examined both the Langmuir–Hinshelwood and the Eley–Rideal reaction mechanisms and found them to be energetically competitive.

Chen and Häkkinen later studied O₂ adsorption on a calixarene-stabilized Au₁₁ cluster.⁴⁰⁰ They first computed the structure of Au₁₁L₅ and Au₁₁L₅(2NT)₃ complexes (L = diphosphine calix[4]arene; 2NT = 2-naphthalenethiolate) using PBE. They predicted 11 and 8 delocalized electrons for the two systems, respectively. The Au₁₁ core is protected by two bidentate bound ligands and three monodentate bound ligands, and the 2NT molecules cause no major rearrangement of the calixarene ligands. The Au¹¹L⁵ cluster without 2NT was found to readily adsorb O₂ and transfer one electron to one of the 2π* orbitals of O₂; the O–O bond length was observed to stretch upon O₂ activation.

2.2.6.2. Au₁₃. The Au₁₃(PM₂Ph)₁₀Cl₂³⁺ cluster structure has also been experimentally characterized and possesses an icosahedral core.⁴⁰¹ Early work by Mungos using an extended Hückel model showed that this compound is expected to have four bonding and nine antibonding orbitals arising from the 6s electrons;³⁹⁴ PBE calculations by Walter et al. showed that the HOMO and LUMO orbitals have P and D symmetry, respectively, with a 1.8 eV HOMO–LUMO gap.¹⁰

Li and Wang examined the geometry of the Au₁₃(PM₂Ph)₁₀Cl₂³⁺ cluster using HF, B3LYP, BP86, and VWN approaches after testing various DFT functionals against MP2, and CC2 approaches for smaller systems.⁴⁰² They found that VWN provided the best agreement with the experimental structure. They examined the effects of PH₃ and Cl[−] ligands on the orbitals and orbital energies of the Au₁₃(PH₃)₁₀Cl₂³⁺ cluster. They also investigated the effects of changing the PR₃ ligands (R₃ = (CH₃)₂Ph, (CH₃)₃, H₃, I₃, Br₃, Cl₃, F₃) and showed that electron-donating ligands shorten the Au–Au bond lengths.

Fresch et al. examined Au₁₃(PH₃)₁₀^z (z = 0, 3, 5) species using the CAM-B3LYP functional and found that bilayer and flake geometries are the most stable for the z = 0 and 3 systems, whereas an icosahedral core is the most stable geometry for the z = 5 species.⁴⁰³ They compared the stabilities of the bare cores using geometry optimizations using MP2 as well as other DFT functionals including B3LYP, BP86, and wB97X and found that CAM-B3LYP provided results in agreement with MP2, BP86, and wB97X.

In 2013, Yang et al. characterized three Au₁₃Cu_x (x = 2, 4, 8) nanoclusters protected by mixed thiolate (SPy or SC₆H₄-tert-C₄H₉) and phosphine (PPH₃ or PPh₂Py) ligands (Py = 2-pyridyl) via X-ray crystallography.⁴⁰⁴ They determined that each of these systems has an Au₁₃ core; the copper atoms are part of the ligand shell and bind to sulfur and nitrogen atoms. DFT analysis shows that the cationic systems are 8-electron superatoms. However, it was noted that the P orbitals in many cases lie close in energy to and are partially mixed with hybridized Cu⁺/ligand states. The HOMO–LUMO gaps were calculated to be 1–1.3 eV. These researchers also calculated LR-TDDFT absorption spectra and found them to be in good agreement with experiment.

2.2.6.3. Au₂₀. Initial work^{181,182} on phosphine-stabilized T_d Au₂₀ has been discussed in section 2.2.1.5. In 2014, Knoppe et al. analyzed the electronic structure of a recently crystallized Au₂₀(PP₃)₄⁴⁺ (PP₃ = tris(2-(diphenylphosphino)ethyl)-phosphine) nanoparticle.⁴⁰⁵ They found a superatomic electron configuration of 1S²1P⁶1D⁶2S². The splitting of the D orbitals into three occupied and two unoccupied orbitals was attributed to its nonspherical core, which could be described as a 7-atom chiral fan-like structure on top of a 13-atom icosahedral core. The HOMO–LUMO gap was calculated to be 1.30 eV with the PBE functional, in excellent agreement with the experimental optical gap of 1.33 eV. Moderate agreement between the TDDFT optical absorption spectrum and the experimental optical absorption spectrum of Au₂₀(PP₃)₄Cl₄ was achieved. Knoppe et al. also calculated the CD spectrum of this system and determined that the effect of the chiral ligands was not as large as for the Au₂(SR)₃ units of Au₃₈(SR)₂₄.

2.2.6.4. Au₂₅ and Related Nanoparticles. In 2007, Shichibu et al. published the crystal structure of a vertex-sharing biicosahedral Au₂₅(PPh₃)₁₀(SC_nH_{2n+1})₅Cl₂²⁺ (n = 2, 8, 10, 12, 14, 16, 18),⁴⁰⁶ which was in close analogy to a mixed metal (Ph₃P)₁₂Au₁₃Ag₁₂Cl₆^{m+} structure reported previously by Teo and Keating.⁴⁰⁷ The thiolates in this case bridge two metal atoms and do not form staple motifs. Shortly thereafter, Nobusada and Iwasa employed the B3LYP and PBE functionals with a polarized double-ζ basis set to optimize the geometry and calculate the TDDFT absorption spectrum of Au₂₅(PH₃)₁₀(SCH₃)₅Cl₂²⁺.⁴⁰⁸ They calculated a HOMO–LUMO gap of 2.13 eV and found that their theoretical absorption spectrum was in excellent agreement with experiment. Because the system contains 16 delocalized electrons,

they interpreted this structure as two interacting superatoms. They then proposed a larger $\text{Au}_{37}(\text{PH}_3)_{10}(\text{SCH}_3)_{10}\text{Cl}_2^+$ cluster consisting of three vertex-shared icosahedral cores in a linear arrangement. The HOMO–LUMO gap for this system is predicted to be 1.36 eV. Two longer wavelength peaks were calculated in the optical absorption spectrum of this compound.

Iwasa et al. later examined doping of the $\text{Au}_{25}(\text{PH}_3)_{10}(\text{SCH}_3)_5\text{Cl}_2^{2+}$ system with two metal atoms to form $\text{PtHgAu}_{23}(\text{PH}_3)_{10}(\text{SCH}_3)_5\text{Cl}_2^{2+}$ using the B3LYP level of theory.⁴⁰⁹ As in the pure gold system, the doped system possesses 16 delocalized electrons. Using projected density of states, they showed that the HOMO of this system has P-like character and the LUMO has D-like character within each icosahedron. The HOMO–LUMO gap of this cluster was calculated to decrease to 1.68 eV, and the dipole moment of this cluster was predicted to be 7.64 D.

In 2012, Das et al. presented the crystal structure of $\text{Au}_{24}(\text{PPh}_3)_{10}(\text{SCH}_2\text{CH}_2\text{Ph})_5\text{X}_2^+$ ($\text{X} = \text{Cl}, \text{Br}$), which is similar to $\text{Au}_{25}(\text{PPh}_3)_{10}(\text{SC}_n\text{H}_{2n+1})_5\text{Cl}_2^{2+}$ with the exception of a missing central Au atom.³⁸⁹ This leads to a slight shortening of the length of the nanoparticle by about 0.13 Å (−4.2%). DFT calculations on $\text{Au}_{24}(\text{PH}_3)_{10}(\text{SCH}_3)_5\text{X}_2^+$ agree with experimental results that the first peak in the absorption spectrum is blue-shifted as compared to the $\text{Au}_{25}(\text{PPh}_3)_{10}(\text{SCH}_2\text{CH}_2\text{Ph})_5\text{X}_2^{2+}$ version of the cluster. The authors predicted that this peak arises from a HOMO–1 to LUMO+2 transition rather than a HOMO to LUMO transition, but in both cases the transitions are caused by interactions between the two units.

Goh et al. then considered the geometry and the optical absorption spectrum for the full $\text{Au}_{24}(\text{PPh}_3)_{10}(\text{SCH}_2\text{CH}_2\text{Ph})_5\text{Cl}_2^+$ compound with 457 atoms.⁴¹⁰ They examined TDDFT calculations for optical absorption and CD spectra using PBE at an LDA geometry and also considered PBE and TPSS geometries. They found absorption spectra that were in qualitative agreement with the previously calculated and experimentally measured spectra. Their angular momentum analysis agreed with the idea that this system could be considered to be a dimer of two 8-electron superatoms.

2.2.6.5. Au_{39} . In 1992, Teo et al. published a crystal structure of a $\text{Au}_{39}(\text{PPh}_3)_{14}\text{Cl}_6^{2+}$ nanoparticle.⁴¹¹ In 2006, Häkkinen et al. optimized the structure of $\text{Au}_{39}(\text{PH}_3)_{14}\text{Cl}_6^-$ in which the anionic state was chosen to avoid effects of unpaired electrons.⁴¹² They found that PBE reproduced the experimental bond lengths within 0.1 Å. This structure was predicted to have a HOMO–LUMO gap of 0.8 eV and an s-electron count of 40. A later study by Häkkinen and co-workers revised the number of delocalized electrons to 34 (to account for the six localized Au–Cl bonds); this was in agreement with an angular momentum projected density of states analysis that demonstrated that the HOMO has F-like symmetry and the LUMO has G-like symmetry.¹⁰

2.2.6.6. Au_{55} and Related Nanoparticles. In 1981, Schmid identified a nanoparticle with the nominal structure $\text{Au}_{55}(\text{PPh}_3)_{12}\text{Cl}_6$.^{413,414} However, the composition and structure of this compound have since been debated. In 2009, Periyasamy and Remacle optimized bare Au_{55} , $\text{Au}_{55}(\text{PH}_3)_{12}$, $\text{Au}_{55}(\text{PH}_3)_{12}\text{Cl}_6$, and $\text{Au}_{55}(\text{PH}_3)_{12}\text{Cl}_6$ solvated with 54 H_2O molecules using unrestricted DFT with the B3LYP functional and LANL2MB for the gold atoms and 6-31G(d) for the ligands.⁴¹⁵ Their initial starting structures were icosahedral and cuboctahedral, and they found that optimization led to a distorted icosahedral geometry. The PH_3 ligands were found to

bind to the face edge atoms, whereas the six Cl ligands were predicted to asymmetrically coordinate to face-centered gold atoms. The singly occupied molecular orbital was predicted to have significant 6s contribution from the face edge atoms as well as 5d contribution from the face-centered atoms. They found that the charging energy of the cluster decreases in the presence of water molecules to 0.99 eV, which is still higher than the experimental value of 0.3–0.5 eV.

A similar study by Genest et al. also found that the structure based on an icosahedral core was lower in energy than the octahedral core.⁴¹⁶ They considered various positions for the Cl groups, which could exhibit some configurational disorder. They evaluated bridging Cl ligands in addition to radially bound Cl.

The following year, Pei et al. performed optimization of 49 isomers of $\text{Au}_{55}(\text{PH}_3)_{12}\text{Cl}_6$ using PBE/DNP.⁴¹⁷ They then optimized the structure of the full $\text{Au}_{55}(\text{PPh}_3)_{12}\text{Cl}_6$ compound and, in agreement with previous results, found that a quasi-icosahedral structure was lowest in energy. This structure has the triphenylphosphines at the vertexes of the icosahedron. They also found a decahedral structure that was only 0.02 eV higher in energy. For both structures, the Cl groups could potentially be arranged in a variety of ways, with <0.2 eV energy differences between different ligand arrangements. They found that bare Au_{55} is inert toward O_2 activation. The triangle faces of the quasi-icosahedral structure were found to have more charge transfer to oxygen than other sites.

In 2011, Walter et al. suggested that because the $\text{Au}_{55}(\text{PPh}_3)_{12}\text{Cl}_6$ system is a radical without a closed superatomic shell and because the original stoichiometric assignment of the nanoparticle was motivated by geometric considerations rather than mass spectrometry experiments, this model should be revisited.⁴¹⁸ They proposed that a somewhat larger $\text{Au}_{69}(\text{PH}_3)_{20}\text{Cl}_{12}^-$ structure would have a 58 electron shell closing and could be responsible for a $\text{Au}_{67}(\text{PPh}_3)_{14}\text{Cl}_8$ fragment observed in a previous mass spectrometry experiment.⁴¹⁹ They found that the stabilization energy (designed to compare the energy of the structure to fcc bulk gold and gas-phase PH_3 and Cl_2 ligands) per gold atom was 0.2 eV greater than the model from Pei et al. They predicted a HOMO–LUMO gap of 0.60 eV at the PBE level of theory, which was larger than the predicted gap for $\text{Au}_{55}(\text{PH}_3)_{12}\text{Cl}_6$.

Shortly thereafter, Burgess and Keast performed real-time TDDFT calculations of two bare Au_{55} clusters, two clusters, a bare Au_{69} cluster, and the recently proposed $\text{Au}_{69}(\text{PR}_3)_{20}\text{Cl}_{12}$ cluster using the Ceperly and Alder LDA.¹⁶⁸ They first optimized the geometries of the systems and found negligible movement (<0.05 Å) of the gold atoms. They found that the ligated particles have optical absorption spectra that have fewer features than the bare clusters. However, all absorption spectra were found to be very similar and did not provide a way to distinguish the clusters present experimentally.

2.2.7. Iron–Carbonyl Ligands on Gold Nanoparticles. In 2009, Lopez-Acevedo et al. presented a combined theoretical–experimental analysis of recently characterized carbonyl-protected Au–Fe particles such as $\text{Au}_{22}[\text{Fe}(\text{CO})_4]_{12}^-$.⁴²⁰ Using PBE and LB94 calculations, they found that these nanoparticles have HOMO–LUMO gaps on the order of 0.77–0.96 eV. Using LR-TDDFT calculations, they computed optical absorption spectra for clusters with various charge states and suggested that the true charge state in solution is less than the formal charge of −6.

2.2.8. Thiolate-Protected Silver and Copper Nanoparticles. The first silver–thiolate nanoparticle involving staple-like motifs was performed by Aikens and co-workers, who examined a $\text{Ag}_{25}(\text{SH})_{18}^-$ model nanoparticle analogous to the recently solved $\text{Au}_{25}(\text{SR})_{18}^-$ nanoparticle.^{285,421} From this model, the researchers determined that superatom orbitals split by ligand-field splitting could be the source of the multiple discrete absorption peaks observed experimentally. However, the lack of close agreement between the LR-TDDFT calculations and the experimental UV–vis spectrum suggested that the synthesized nanoparticle had a different structure and/or stoichiometry. The stoichiometry of this particle was later established to be $\text{Ag}_{44}(\text{SR})_{30}^{4-}$, and several years later two groups succeeded in solving the X-ray crystal structure of this nanoparticle.^{422,423} Very electron-withdrawing thiolates were employed including SPhF_4 ,⁴²² SPhF_2 ,⁴²² SPhCF_3 ,⁴²² and *p*-MBA.⁴²³ The nanoparticle was determined to have an inner icosahedral core of 12 atoms, surrounded by a 20-atom decahedral outer core; finally, the core is capped with six $\text{Ag}_2(\text{SR})_5$ motifs. Both sets of researchers employed DFT calculations with angular momentum projected densities of states and determined that the HOMO orbital corresponds to a 1D superatomic orbital, the LUMO is the 2S orbital, and the LUMO+1 is a 1F orbital, as expected for 18 delocalized electrons.^{422,423} LR-TDDFT calculations were employed to compute the optical absorption spectrum of $\text{Ag}_{44}(\text{SR})_{30}^{4-}$, and TD-DFPT was utilized to analyze the transitions.⁴²² The two lowest-energy transitions were found to be predominantly 1D → 1F type transitions, whereas higher-energy peaks also had contributions from excitations out of ligand (i.e., $\text{Ag}_2(\text{SR})_5$)-based orbitals.

Yang et al. also determined X-ray crystal structures for gold-doped nanoparticles $\text{Au}_{12}\text{Ag}_{32}(\text{SR})_{30}^{4-}$.⁴²² They found that the gold atoms are located in the inner core, whereas silver atoms occupy the outer core; this pattern was previously calculated for systems such Ag -doped $\text{Au}_{25}(\text{SR})_{18}^-$ and $\text{Au}_{144}(\text{SR})_{60}^-$ as described above. DFT analysis again shows that the HOMO orbital corresponds to a 1D superatomic orbital, the LUMO is a 2S orbital, and the LUMO+1 is a 1F orbital, in direct comparison with $\text{Ag}_{44}(\text{SR})_{30}^{4-}$. For $\text{Au}_{12}\text{Ag}_{32}(\text{SR})_{30}^{4-}$, the lower energy 1D orbitals were merged into the upper ligand states.

Yang et al. recently determined X-ray crystal structures for gold–copper alloy nanoparticles that are closely analogous to $\text{Au}_{12}\text{Ag}_{32}(\text{SR})_{30}^{4-}$.⁴²⁴ These nanoparticles have the chemical formula $\text{Au}_{12+n}\text{Cu}_{32}(\text{SR})_{30+n}^{4-}$ ($n = 0, 2, 4, 6$). The $n = 0$ compound is exactly analogous to $\text{Au}_{12}\text{Ag}_{32}(\text{SR})_{30}^{4-}$, with a 12-atom Au inner core and a 20-atom dodecahedral Cu shell surrounded by six $\text{Cu}_2(\text{SR})_5$ motifs. For $n > 0$, n Au(SR) units are inserted in a corresponding number of $\text{Cu}_2(\text{SR})_5$ units. Yang et al. calculated HOMO–LUMO gaps, electronic structures, and optical properties for these systems. They found that the lowest-energy absorption peak is caused primarily by the 1D → 1F transition, whereas higher-energy peaks also had contributions from ligand-based orbitals.

In 2012 prior to the crystal structure determination of $\text{Ag}_{44}(\text{SR})_{30}^{4-}$, Chakraborty et al. performed a combined theory–experiment study on a 25 kDa thiolate-stabilized silver nanoparticle.⁴²⁵ They proposed a core–shell model for this system consisting of a 92-atom core (a hollow 20-atom decahedron with 12 pentagonal faces each capped by a Ag atom, encapsulated by a second shell comprised of a 60-atom snub-dodecahedron) protected by 60 Ag atoms and 60 thiolates

(arranged into 20 sets of triangular $(\text{AgSR})_3$ units); the overall stoichiometry of the system was proposed to be $\text{Ag}_{152}(\text{SR})_{60}^{2+}$ (Figure 11). They employed PBE and analyzed the angular

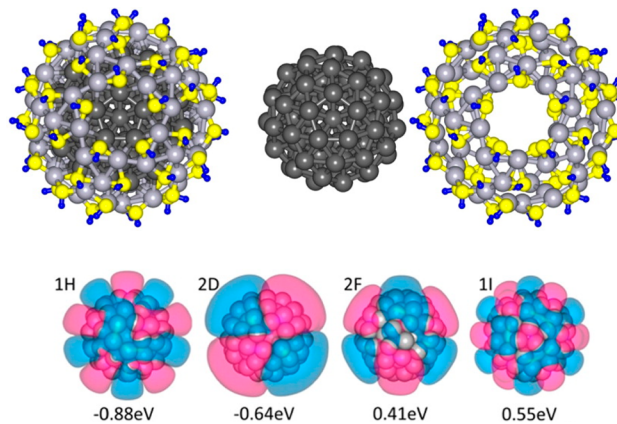


Figure 11. Calculated structure of $\text{Ag}_{152}(\text{SH})_{60}^{2+}$ and four representative delocalized Kohn–Sham orbitals. Adapted with permission from ref 425. Copyright 2012 American Chemical Society.

momentum projected density of states to determine a HOMO–LUMO gap of 0.73 eV. The gap was predicted to occur at 90 delocalized electrons; the HOMO and LUMO were calculated to have H and I symmetry, respectively.

Bertorelle et al. undertook a combined theory–experiment investigation of $\text{Ag}_{31}(\text{SG})_{19}$ and $\text{Ag}_{15}(\text{SG})_{11}$ nanoparticles (SG = glutathione).⁴²⁶ After initial structural searches with AM1, they employed B3LYP and CAM-B3LYP calculations with a TZVP basis set to predict structures and optical properties of these systems. They computed a structure for $\text{Ag}_{15}(\text{SR})_{11}$ ($\text{R} = \text{CH}_3$) that contained a Ag_8 core protected by two SR–Ag–SR units, one SR–Ag–SR–Ag–SR unit, and one SR–Ag–SR–Ag–SR–Ag–SR unit. For $\text{Ag}_{31}(\text{SR})_{19}$, they predicted a structure with a Ag_{21} core with eight SR–Ag–SR units and one SR–Ag–SR–Ag–SR unit. Their TDDFT computed spectrum for $\text{Ag}_{31}(\text{SR})_{19}$ exhibited a strong peak at 510 nm, which was in good agreement with the experimental spectrum that displayed only a single strong peak around 490 nm.

2.3. Group 12

The group 12 metals often occur naturally in oxide ores. In addition, chalcogenide compounds of these metals have also received significant attention due to their numerous applications. Theoretical studies on the oxide and chalcogenide compounds of group 12 elements are presented in sections 4.10 and 5.1. Zn and Cd are not typically used in applications as pure metals, although they can be components in alloys. On the other hand, metallic Hg has found numerous uses in thermometers, barometers, etc., because it is a liquid at room temperature. Overall, theoretical studies of group 12 elements are much rarer than those of group 10 and 11 elements.

2.3.1. Zn Clusters. The history of the theoretical investigations on Zn clusters is relatively recent. In the early 2000s, Michaelian et al. performed investigations based on global searches with the n -body Gupta potential followed by further relaxation with GGA and LDA density functionals.⁴²⁷ The generally geometrically closed-shell magic sizes of 13, 38, 55, 75, and 147 atom zinc clusters were found to have very low symmetry or to be disordered except for fcc-truncated octahedral Zn_{38} . They observed that icosahedral Zn_n ($n = 13$,

55, 147) structures and the Marks decahedral structure at 75 atoms are unstable or not viable with zinc.

First-principles calculations on the structural and electronic properties of Zn clusters containing up to 20 atoms were performed by Wang et al. using the PW91/DND level of theory.⁴²⁸ They observed a transition from covalent to metallic bonds around Zn_{17} , and in comparison with Cd and Hg clusters, zinc showed a more rapid transition toward bulk metallicity. The binding energies, second-order differences of binding energy, fragment energies ($\Delta E(n) = E(n) - E(n-1)$), and ionization potentials showed that the clusters having 10, 14, 18, and 20 atoms are more stable than their neighbors. Later, Iokibe et al. carried out a similar investigation employing several different levels of theory.⁴²⁹ To evaluate the clusters having up to 16 atoms, they used MP2/LANL2DZ and MP2/6-311+G(d) levels of theory. For Zn_n ($n = 10-32$) cluster systems, the DFT approach was used with the LANL2DZ basis set and the LSDA, B3LYP, and PW91 exchange correlation functionals. The binding energy was found to increase slightly with increasing cluster size. The authors identified that the natural population of 4p electrons of the Zn atoms plays an important role in clustering.

Johansson and Pykkö examined tetrahedral Zn clusters with up to 56 atoms.⁴³⁰ Using PBE/TZVPP calculations, they found that these symmetric structures were significantly higher in energy than lower symmetry structures originally optimized with a Gupta potential, and this energy difference increased as the cluster size increased.

Sun et al. performed a global optimization of Zn_{13} using the taboo search in descriptor space (TSDS) and energy evaluation with the LANL2DZ basis set and the LSD or PBE exchange correlation functional.⁶⁵ They found an open prolate structure for Zn_{13} . The PAW/PBE calculations predicted a similar disordered structure for the 13-atom zinc cluster.⁴³¹ Gustev et al. carried out PW91/6-311+G* calculations and found structures that resemble those reported earlier for Zn_{12} and Zn_{13} .⁴³² Both attachment and detachment of an electron to/from the neutral species induced a considerable rearrangement of its ground-state structure except for Zn_{13}^- .

2.3.2. Cd Clusters. Zhao carried out DFT calculations at the PW91/DND level of theory to study the lowest energy structures and electronic properties of Cd_n clusters having up to 21 atoms.⁴³³ He found an icosahedral growth pattern from $n = 13-17$ and then a close-packed multicage structure for the rest of the sizes. Cadmium clusters with closed electronic shells at $n = 10, 15, 17$, and 20 were found to be the magic clusters. He reported that Cd_n clusters containing about 20 atoms might already have some metallic-like features.

Johansson and Pykkö investigated tetrahedral Cd clusters with up to 56 atoms.⁴³⁰ At the PBE/TZVPP level of theory, they determined that tetrahedral clusters with 10 or 20 atoms were lower in energy than low symmetry structures from a Gupta potential, unlike corresponding Zn tetrahedra. However, tetrahedral clusters with 35 and 56 atoms were found to lie higher in energy than lower symmetry structures.

2.3.3. Hg Clusters. In the early 2000s, Dolg and co-workers performed calculations on small and medium-sized mercury clusters using a hybrid model (HM). The HM method includes valence electron correlation effects by adding a simple pair potential to the HF energies and core-valence correlation effects by a core-polarization potential (CPP).^{434,435} An icosahedral growth behavior was found to be more stable up to Hg_{55} , and the calculated vertical ionization potentials were in

good agreement with experiment.⁴³⁴ In contrast in their subsequent study, capped trigonal prism structures were found to be more stable for Hg_n clusters in the range of $n = 10-14$.⁴³⁵ Gaston and Schwerdtfeger performed calculations on mercury clusters having up to 14 atoms with DFT (LDA, PW91) methods.⁴³⁶ Both Lennard-Jones and alternative isomers⁴³⁵ were considered as candidate structures.⁴³⁶ However, they observed that DFT had difficulties in modeling mercury clusters and proposed an alternative HF plus two-body correlation approach.

2.4. Other 3d Transition Metal Clusters

For the transition metals in groups 3–9, both pure metal and metal oxide clusters are of wide interest. (Metal oxide clusters for groups 3–9 are discussed in sections 4.1–4.7.) For the metal clusters, most of the applications focus on magnetic properties because these systems potentially have several unpaired d electrons and are of interest in a variety of magnetic applications. Most theoretical work has focused on first-row transition metals due in part to the computational requirements. However, some theoretical work has also been performed on the 4d and 5d transition metals, as discussed in sections 2.5 and 2.6.

2.4.1. Sc Clusters. Although several experiments have been done over the years, theoretical investigations on Sc_n ($n > 10$) clusters are not very common. Zhang and co-workers performed the first DFT study on Sc_n ($n = 2-16$) clusters to determine their binding energies, ground-state structures, electronic structures, and magnetic properties using the BPW/DNP level of theory.⁴³⁷ The ground-state structures adopted closed compact arrangements, and the Sc_{13} was a perfect icosahedron with a huge magnetic moment (19 μ_B). The clusters with 10 and 13 atoms showed a higher stability than the neighboring clusters. Moreover, these authors obtained the general trend of the magnetic moment variation as a function of cluster size, which agrees well with the experimental results.

Li et al. explored the static polarizabilities of Sc_n ($n \leq 15$) clusters using the DFT formalism.⁴³⁸ The geometry optimization and vibrational frequency calculations have been performed within the BP86/CEP-121G level, while the finite field approach has been used to calculate the dipole moment and static electric polarizability. In agreement with the previous study,⁴³⁷ Li et al. also reported the preference of these clusters for compact structures and the higher stability of Sc_{10} and Sc_{13} .⁴³⁸ These authors mentioned that these stabilities are related to the polarizability properties. The calculated dipole moments have been found to associate with the electronic structure, where a large HOMO–LUMO gap contributes to a large dipole moment. The increasing cluster size led to a slow reduction of the static polarizability per atom. The polarizabilities of clusters have been found to depend on the HOMO–LUMO gap and the geometrical characteristics. Piotrowski et al. found an ideal icosahedral structure for the Sc_{13} cluster using the PBE level of theory.⁴³¹

The structural, electronic, and magnetic properties of scandium clusters containing up to 18 atoms have been studied using the PBE/DND level of theory.⁴³⁹ Wang proposed that other than Sc_{10} and Sc_{13} , Sc_{16} also shows high stability, which can be partly attributed to the high-symmetry and the electronic stability as predicted by the elliptical spherical jellium model. The size-dependent average magnetic moment per atom exhibited the highest value at $n = 13$, which is 1.5 μ_B .

Wang found that the clusters with $n = 15\text{--}17$ favor the ferrimagnetic/antiferromagnetic coupling, whereas the two types of coupling compete with each other at the size range of $n = 9\text{--}14$. Wang and co-workers performed a subsequent investigation to study the structure and magnetism of atomic oxygen adsorbed Sc_n ($n = 2\text{--}14$) clusters using the same theoretical approach.⁴⁴⁰ The oxygen atom has been found to adsorb at the hollow site in all of the ground-state structures and at the bridge site in some metastable structures of Sc_nO clusters. The large adsorption energies of O to the scandium clusters have been attributed to the strong hybridization between O-2p and Sc-3d electrons. The size-dependent adsorption energy curve showed peaks at $n = 10$ and 12 and a bottom at $n = 13$ correlating the stability of Sc_n clusters. The O atom considerably affected the magnetic properties of the parent clusters, inducing a magnetic reduction at $n = 12, 13$, and 14 and a magnetic enhancement at $n = 11$, which are associated with the increased or decreased local magnetic moments on the Sc atoms.

Wu et al. studied the adsorption properties of a single CO molecule on scandium clusters having up to 13 atoms using PBE/DND level of theory.⁴⁴¹ It has been found that the CO molecule binds to the hollow site at $n = 11$ and 12, whereas it binds to the bridge site at $n = 10$ and 13, accompanied by Sc-Sc bond lengthening. A very low adsorption energy has been reported for Sc_{13}CO , which might be due to the high stability of Sc_{13} . The magnetic moment of clusters with $n = 12$ and 13 has been reduced significantly upon CO adsorption, which can be attributed to the ferrimagnetic alignment and the decreased local atomic moments of Sc. Further, CO adsorption energies on Sc_{12} and Sc_{13} have been found to be significantly larger than the adsorption energies on other transition metal atoms reported in literature. An extended study performed by Wang et al. explored the changes in chemical activity and the magnetic properties of Sc_n and Sc_nO ($n = 2\text{--}13$) clusters toward CO molecule adsorption using the PBE/DND approach.⁴⁴² Sc_nO ($10 \leq n \leq 13$) clusters have been found to favor the bridge site adsorption of CO. The chemical activity toward CO molecule adsorption has been found to be better for Sc_nO than Sc_n at $n = 11$ and 12, but similar for both clusters at $n = 13$. The size-dependent variations of C–O bond lengths, adsorption energies, and net charges on CO proposed that the interaction between CO and the transition metal oxide clusters predominantly depends on charge transfer from nearby Sc atoms. Interestingly, the magnetic moment of Sc_{13}O increased significantly upon CO adsorption, although it was reduced in the pure Sc_{13} cluster.

The electronic and geometrical structures of Sc_{12} and Sc_{13} clusters along with their singly negatively and positively charged clusters were studied by means of the BPW91/6-311+G* level of theory.⁴³² Following the previous theoretical results, it has been found that the lowest-energy structure of Sc_{13} is an icosahedron with a total spin magnetic moment of $19 \mu_{\text{B}}$, which is very far from the experimental value of $6.0 \pm 0.02 \mu_{\text{B}}$. The Sc_{12} cluster has been found to possess a slightly distorted icosahedral geometry with a $16 \mu_{\text{B}}$ magnetic moment. The geometries of the singly charged ions did not change significantly from their neutral counterparts. Gutsev et al. obtained ionization energies of neutrals and vertical detachment energies of the anions and reported that these values agree fairly well with the experimental values.

The PW91/DND level of theory has been used to study the geometries, stabilities, and size-dependent electronic and

magnetic properties of Sc_nAl ($n = 1\text{--}14$) clusters.⁴⁴³ Wang et al. observed that in all of the clusters having more than 10 atoms, the Al atom takes up the center position in the Sc cage. The analysis of the average binding energy and the second-order energy differences revealed that the Al atom enhances the stability of the Sc clusters, and the Sc_nAl clusters with $n = 10$ and 12 are more stable. Moreover, it has been found that the doping of the Al atom decreases the magnetic moment of the host cluster, except for Sc_{15} (at $n = 14$), and the total magnetic moment is quenched at $n = 11$.

The structural and magnetic properties of charged Sc_{13} and doped XSc_{12} ($\text{X} = \text{Na}, \text{Mg}, \text{Al}, \text{Si}, \text{P}$) clusters have been studied using the PBE/DND level of theory.⁴⁴⁴ The center-doped icosahedron has been found as the ground-state geometry of XSc_{12} ($\text{X} = \text{Al}, \text{Si}$), whereas the surface substituting icosahedral configuration has been the lowest energy isomer when $\text{X} = \text{Na}, \text{Mg}$, and P. Both charging and doping enhanced the stability of Sc_{13} , while the doping reduced the magnetic moment.

2.4.2. Ti Clusters. Although the geometric structures and electronic properties of transition metal clusters have been studied extensively during the past couple of decades, theoretical investigations on titanium clusters have not been done too frequently. Zhao et al. performed the first DFT investigation on Ti_n ($n = 2\text{--}14, 19, 55$) clusters to study their structural and electronic properties using the PW91 exchange correlation function and the plane wave basis.⁴⁴⁵ The Ti clusters have been found to follow a pentagonal growth behavior favoring close-packed structures. The icosahedral Ti_{13} in particular showed a higher stability than its neighbors, in agreement with experiment. The electronic DOS of even smaller clusters showed some similarity to the bulk DOS. The authors attributed these results to the participation of 4s and 3d valence orbitals in bonding and to the considerable delocalization of valence electrons.

LYP/DNP calculations performed on Ti_n ($n = 2\text{--}15$) clusters suggested that Ti_{13} with an icosahedral geometry and Ti_{15} that has both pentagonal and hexagonal symmetries with a closed-shell icosahedron-like configuration are particularly stable.⁴⁴⁶ It has been reported that the stability of Ti_n clusters strongly depends on the geometry and the charge state of the clusters. Villanueva et al. observed a relatively small HOMO–LUMO gap for the titanium clusters except for $n = 13$ and 15 and its approach to the bulk value at $n > 8$. Another study has been carried out to explore the mechanical stability of the Ti_{13} cluster.⁴⁴⁷ The applied strain on the cluster induced a point symmetry change from I_h to D_{5d} and it has been found that the Ti_{13} cluster tolerates more load in compression than in tension.

Castro et al. also studied the structural and electronic properties of Ti_{13} and its anion using the PW86/DZVP2 level of theory and found that the ground-state structures are distorted icosahedra.⁴⁴⁸ The calculated DOS spectrum and the calculated electron affinities have been found to conform to the experimental PES data. The authors observed a zero magnetic moment for Ti_{13} and concluded that the magnetic moments approach the bulk at small sizes. Wang et al. performed BPW/DNP calculations to study the structural stability of neutral and singly charged icosahedral Ti_{13} clusters.⁴⁴⁹ However, it has been found that due to Jahn–Teller distortions the Ti_{13} , Ti_{13}^{-1} , and Ti_{13}^{+1} clusters favor D_{3d} structures, and these small distortions from the icosahedral geometry have been found to be in conformity with the experimental results. Subsequently, they studied the icosahedral Ti_n ($n = 13, 19, 43, 55$) clusters by means of binding energies, bond lengths, HOMO and LUMO

states, DOS, and magnetism with the same level of theory as in the previous study.⁴⁵⁰ They also considered the hcp structures at $n = 13$ and 19 and the fcc structures at $n = 13, 19, 43$, and 55 for comparison. The icosahedral geometry has been found to be the lowest-energy structure in most of the cases except for Ti_{43} , which favors the fcc close-packed structure. The DOS of icosahedral Ti_{55} has been found to be very close to that of bulk Ti. The weak magnetism in icosahedral Ti_{13} , Ti_{19} , and fcc- Ti_{43} and quenched atomic magnetic moments in icosahedral Ti_{55} have been attributed to the strong s, p-d hybridization states in all of these clusters.

Lee and Lee carried out a comparative study of Ti clusters having 13–19 atoms using the PBE level of theory with PAW.⁴⁵¹ They found a distorted icosahedron as the lowest energy isomer of Ti_{13} in agreement with the studies of Castro et al.⁴⁴⁸ and Wang et al.^{449,450} It has been found that the distortions evolve with the increasing cluster size, where atoms are added onto the cluster surface.⁴⁵¹ The shell effect of 3d electrons has been found to play a key role in the formation of directional bonds.

The structural, energetic, and magnetic properties of small Ti clusters have been studied using DFT, applying two different exchange-correlation functionals (PBE and BLYP), and the results have been compared.⁴⁵² The calculated equilibrium bond lengths and the binding energies have shown that the properties of titanium clusters having up to 13 atoms are significantly different from the bulk titanium properties. It has been found that the Ti_{13} cluster has a distorted icosahedral geometry. The theoretically found, size-dependent dissociation energies agreed well with the experimental results, and it has been found that both of the functionals are good in describing the energetics of these Ti clusters. Medina et al. concluded that the structural distortions have no effect on the magnetism of the Ti_{13} cluster. In contrast to the results of Castro et al., a magnetic moment of $0.46 \mu_B/\text{atom}$ has been obtained for Ti_{13} .

Piotrowski et al. found a distorted icosahedral structure for the Ti_{13} cluster using the PBE level of theory with PAW.⁴³¹ The electronic and geometrical structures of Ti_{12} and Ti_{13} clusters along with their singly negatively and positively charged clusters have been studied by means of the BPW91/6-311+G* level of theory.⁴³² Following the previous theoretical results, it has been found that the lowest-energy structure of Ti_{13} is a slightly distorted icosahedron with a total spin magnetic moment of $6 \mu_B$, which is in agreement with that of Medina et al.⁴⁵² The lowest energy structures of Ti_{13}^+ and Ti_{13}^- have been found to possess strongly distorted icosahedral geometries with large variations in the local spin magnetic moments.

Quite a few of the theoretical investigations have taken doped titanium clusters into consideration. Wang et al. studied the structural stability of neutral and charged icosahedral Ti_{12}X clusters ($\text{X} = \text{B}, \text{C}, \text{N}, \text{Al}, \text{Si}, \text{P}, \text{V}, \text{Cr}, \text{Mn}, \text{Fe}, \text{Co}$, and Ni) using the BPW/DN level of theory.⁴⁵³ The closed-shell systems with larger HOMO–LUMO gaps, $\text{Ti}_{12}\text{Fe}^{2-}$, $\text{Ti}_{12}\text{Co}^{1-}$, and Ti_{12}Ni , have been found to have lower binding energies as compared to the corresponding values of icosahedral Ti_{13} . Except for the $\text{Ti}_{12}\text{Fe}^{2-}$, $\text{Ti}_{12}\text{Co}^{1-}$, and Ti_{12}Ni systems, all of the other clusters showed weak magnetism. It has been reported that these three clusters are highly structurally and chemically stable and could be good candidates to design cluster-assembled materials.

Xiang et al. explored the equilibrium geometries, stabilities, and electronic properties of Ti_nAl ($n = 1$ –13) clusters.⁴⁵⁴ The stable structures optimized with the PW91 level of theory have

been reoptimized with the discrete variational method (DVM). The Al atom was encapsulated in the Ti cage for clusters with $n > 10$, while evolving toward the icosahedral-like clusters. Meanwhile, the Al atom exhibited a transformation from monovalent to trivalent. The strong ionic Ti–Ti bonds have been found to change to metallic-like Ti–Al bonds. A similar investigation has been carried out to study boron-substituted titanium clusters having up to 15 atoms.⁴⁵⁵ Du et al. used the PW91/DNP level of theory for their calculations. Except for Ti_{12}B , the substitution of B on the surface was energetically favorable. The increased binding energies and HOMO–LUMO gaps suggested that the B-doping enhances the stabilities of the host clusters. This can be attributed to electron transfer mechanisms taking place from 4s to 3d and 2s to 2p orbitals in bonding Ti and B atoms. It has been reported that the magnetic moments of the host clusters can be reduced due to the B-doping.

Similarly, Wang et al. used the PW91 level of theory to study the geometric, energetic, electronic, and magnetic properties of phosphorus-doped Ti clusters, Ti_nP ($n = 1$ –12).⁴⁵⁶ As in the case of B-doped clusters,⁴⁵⁵ Ti_{10}P , Ti_{11}P , and Ti_{12}P have been found to have P-encapsulated Ti cages.⁴⁵⁶ P-doping increased the stabilities of Ti clusters while imposing a special stability to the Ti_{12}P cluster. The magnetic moments of Ti_nP clusters showed an odd–even staggering pattern, whereas these clusters did not show the quenching of the magnetic moments. It has been observed that the magnetic moments are predominantly due to the 3d electrons of Ti.

The adsorption geometries and binding affinities of Ti_{13} nanoparticle onto carbon nanotubes (CNTs) have been investigated using both GGA and LDA functionals and a plane wave basis set.⁶⁹ It has been found that the Ti_{13} cluster has an icosahedral geometric structure with D_{3d} symmetry. The strong binding of the Ti_{13} cluster to the CNT surface has been attributed to the open d shells in the Ti electronic structure. These strongly adsorbed metal nanoparticles have been found to induce a strong distortion in the π electronic structure of the CNT.

Verkhovtsev et al. performed DFT calculations based on the PW91/DGDZVP2 level of theory to study geometric structures, stability, and electronic properties of pure and Ni-doped titanium clusters containing up to 15 atoms.⁴⁵⁷ The geometric structures of the most stable Ti_n clusters have been found to be analogous to that from the previous theoretical studies.^{448,455} In contrast to the boron-doped titanium clusters,⁴⁵⁵ the stability of the titanium clusters has not been affected by the doping of a Ni atom.⁴⁵⁷ However, the Ni atom preferred to be located on the surface in the most favorable geometries in agreement with the boron-doped clusters. Ti_{n-1}Ni clusters exhibited lower magnetic moments as compared to that of Ti_n where both showed oscillatory behaviors.

2.4.3. V Clusters. The geometries and the magnetic properties of vanadium clusters have been explored for several decades. In the early 1980s, Salahub and Messmer performed spin-polarized SCF-X α -SW calculations and identified that the V_{15} cluster is large enough to exhibit the magnetic order of bulk vanadium.⁴⁵⁸ About a decade later, the self-consistent-field linear combination of atomic orbitals method was used to investigate the electronic structure, density of states, and total energies of V_n ($n = 9, 15, 27, 51$) clusters in the bcc geometry and in linear chains.⁴⁵⁹ Liu et al. established the significance of the size and dimensionality of vanadium clusters on their

magnetic behavior. It has been observed that the reduced size and dimensionality as well as the increased atomic spacing mean that vanadium clusters are capable of exhibiting magnetic behavior. Following Salahub and Messmer, it has been reported that the total magnetic moment per atom of the V_{15} cluster is virtually zero.⁴⁵⁹

Lee and Callaway carried out a theoretical study using a Gaussian orbital basis and the local spin density approximation and have found that the DOS of the bcc- V_{15} cluster simulates the bulk DOS reasonably well, which is in agreement with the previous theoretical studies.⁴⁶⁰ The authors performed a subsequent investigation using the same theoretical method to explore all possible magnetic states of V_{15} from the fixed moment total energy curves.⁴⁶¹

Alvarado et al. performed unrestricted Hartree–Fock calculations with a d-band Hubbard-like Hamiltonian to calculate the local moments, magnetic order, and average magnetization of V_n clusters as a function of the intraatomic exchange integral J .⁴⁶² Ferromagnetic and antiferromagnetic ordering were found for fcc- V_{13} and ico- V_{13} clusters, respectively. PBE calculations have been performed on the experimentally characterized $K_6[V_{15}As_6O_{42}(H_2O)]$ unit to study the magnetic properties of the V_{15} cluster, where the lowest energy spin configuration has been found to be $S = 1/2$.⁴⁶³

Ratsch et al. performed a combined experimental–theoretical work to calculate the ground-state energy and vibrational spectra of cationic vanadium clusters having up to 15 atoms.⁴⁶⁴ The vibrational spectra obtained with PBE have been compared to the experimental spectra to assume the geometric structures present in the experiment. The energetically favored V_{11}^+ , V_{12}^+ , and V_{13}^+ clusters showed a similarity by having an icosahedral-like structure. However, the clusters with 13 or more atoms have shown signals corresponding to higher vibrational frequencies, which are associated with the strongly bound central atom rather than the surface atoms. As the cluster size increases, Ratsch et al. found it difficult to deduce the atomic structure clearly. It was concluded that for the larger clusters, a mixture of isomers can be present in the experiment and also that theory can miss important structures. To avoid missing the relevant structures, a large number of isomers should be tested with different spin states and various distortions.

Piotrowski et al. found a distorted icosahedral structure for the V_{13} cluster using the PBE level of theory.⁴³¹ The BPW91/6-311+G* calculations predicted a bell-shaped geometrical structure for all neutral and charged V_{12} clusters,⁴³² in contrast to the icosahedron-like structure found previously. For V_{13} , a strongly distorted icosahedral geometry with a doublet lowest total energy state has been found. Nevertheless, eight other doublet and quartet states were found for V_{13} , which are very close in energy to the lowest-energy structure.

Recently, Wu et al. used the PBE/DNP level of theory to explore the interacting behaviors of V clusters having up to 13 atoms with different adsorbates such as N_2 and NO.⁴⁶⁵ Dissociative adsorption has been found on V_n clusters with $n = 12$ for N_2 molecules and $n = 10–12$ for NO molecules, respectively, whereas on the rest of the clusters N_2 and NO adsorb molecularly. The magnetic moments of N_2 adsorbed clusters showed odd–even oscillations between 0 and $1 \mu_B$, while the adsorption of NO raised the magnetic moments of V_n at $n = 10$ and 12 and lowered them at $n = 11$ and 13. The chemical reactivity of V_n clusters has been found to depend on

cluster size, geometry, adsorption sites, and the adsorbate species.

2.4.4. Cr Clusters. Chromium is an interesting metal with a body-centered-cubic (bcc) crystal structure that shows antiferromagnetic properties in the bulk regime. Salahub and Messmer were the first to carry out theoretical investigations on chromium clusters.⁴⁵⁸ They performed SCF-X α -SW molecular orbital method calculations to study the magnetic order of chromium clusters and found that antiferromagnetic properties are exhibited even by the 15-atom bcc-cluster. This antiferromagnetism was identified by the higher stability of minority-spin levels, which is unusual for nonmagnetic or ferromagnetic systems.

Lee and Callaway studied the electronic structure and magnetism of bcc- Cr_{15} cluster using LSDA and a Gaussian orbital basis.⁴⁶⁰ The average magnetic moment of chromium clusters was found to decrease with increasing cluster size and agree well with the experimental results. Furthermore, a good agreement between the DOS of the Cr_{15} cluster and the bulk was found. The same authors performed a subsequent study to investigate the possibility of the existence of several magnetic states in the bcc- Cr_{15} cluster.⁴⁶¹ The same theoretical procedure was used, and the typical low and high spin moments ($0.40 \mu_B$ and $0.80 \mu_B$ per atom) for Cr_{15} were identified. LSDA has been used with the VWN/DNP level of theory to study growth behavior and antiferromagnetic ordering of chromium clusters having up to 15 atoms.⁴⁶⁶ Cheng and Wang observed a dimer-growth pattern until Cr_{11} that gives rise to odd–even variations to dissociation energies, electronic structure, net moment, etc. A structural transition occurred at $n = 11$ from dimer-growth to bcc-like structures. All of the clusters showed antiferromagnetic ordering resembling the bulk.

Sometime later, Reddy et al. studied the equilibrium geometry, electronic structure, and magnetic properties of the Cr_{13} cluster within the LSDA-VWN level of theory.⁴⁶⁷ As proposed by Cheng and Wang,⁴⁶⁶ the ground state of Cr_{13} corresponds to a fragment of the bulk bcc structure that has a $14.0 \mu_B$ net magnetic moment.⁴⁶⁷ An icosahedron with a magnetic moment of $2.0 \mu_B$ was also found, which lies 0.24 eV higher in energy. These nearly degenerate isomers and their magnetic moments were comparable to the experimental results. The HOMO–LUMO gap of Cr_{13} was found to be 0.15 eV . DFT calculations performed at the PBE/PAW⁴³¹ and BPW91/6-311+G*⁴³² levels of theory have suggested a distorted icosahedron as the lowest-energy antiferromagnetic singlet state of Cr_{13} .^{431,432} Furthermore, Gutsev et al. found that Cr_{12} and its ions have bell-type geometric structures with $4 \mu_B$ and $3 \mu_B$ magnetic moments, respectively.⁴³² They also found nearly degenerate singlet, triplet, and nonet states for the neutral Cr_{12} cluster.

2.4.5. Mn Clusters. Mn with a $3d^54s^2$ electronic configuration shows weak bonding and high magnetic moments in small clusters. Nayak et al. performed DFT calculations using the BPW91/DNP level of theory to study different isomers of the Mn_{13} cluster and their magnetic orders.⁴⁶⁸ Out of the icosahedral, hcp, and cuboctahedral isomers considered, the ferrimagnetic icosahedral Mn_{13} with a total magnetic moment of $33 \mu_B$ was found to be the lowest in energy.

Briere et al. studied the atomic structures and magnetic properties of Mn_n ($n = 13, 15, 19, 23$) clusters using a plane wave method and the GGA exchange-correlation potential.⁴⁶⁹ The 15-atom cluster was found to be body-centered cubic with

antiferromagnetic coupling, whereas the 13-, 19-, and 23- atom clusters were icosahedral having ordered spin configurations. The blocks of ferromagnetically coupled spins were found to couple antiferromagnetically with each other in the icosahedral clusters. In contrast to the previous study,⁴⁶⁸ Briere et al. found small net magnetic moments.⁴⁶⁹ The PBE calculations performed by Bobadova-Parvanova et al. obtained an icosahedral structure for Mn₁₃ and a net spin of 3 μ_B ,⁴⁷⁰ in agreement with Briere et al.⁴⁶⁹ In a subsequent study, Bobadova-Parvanova et al. found a strong preference for antiferromagnetic ordering for Mn_n ($n \geq 10$) clusters at the PBE/GTO level of theory.⁴⁷¹ A ferromagnetic order of atomic magnetic moments was also found in small groups within the larger clusters. These observations were attributed to the bonding in the clusters, which is governed by the transfer of electrons from antibonding 4s levels to minority 3d levels.

Kabir et al. performed a systematic investigation of the structural, electronic, and magnetic properties of Mn_n clusters having up to 20 atoms using the PAW method along with a plane wave basis and the PBE functional.⁴⁷² They found that the clusters having 11–20 atoms prefer to adopt an icosahedral growth pattern with a ferrimagnetic ground state. In contrast to Nayak et al.⁴⁶⁸ but similar to Bobadova-Parvanova et al.,⁴⁷⁰ the magnetic moment of icosahedral Mn₁₃ was found to be 0.23 μ_B /atom in this work.⁴⁷² The bcc structure found by Briere et al.⁴⁶⁹ for the ground state of Mn₁₅ was found to lie 0.28 eV higher in energy in the current study.⁴⁷² The binding energy increased monotonically as a function of cluster size, and the authors credited this to the increase in the s–d hybridization. Kabir et al. were able to reproduce the sudden fall of the magnetic moment of Mn₁₃ and Mn₁₉ observed in the experiment, and they attributed it to their closed icosahedral structures.⁴⁷² Furthermore, the authors reported that no nonmetal to metal transition was exhibited by the clusters in this studied size range.

Xie and Blackman performed calculations within the PW91/DNP level of theory to study the collinear and noncollinear magnetism in manganese clusters.⁴⁷³ The results reported for collinear spin arrangements were similar to Briere et al. However, a zero net moment was found for Mn₁₂, which is drastically different from 1 μ_B /atom in the study of Bobadova-Parvanova et al.⁴⁷¹ For the smaller clusters having up to 23 atoms, the energy of the lowest energy structure was further reduced at the noncollinear regime.

Gutsev et al. performed a combined experimental–theoretical study to explore the electronic and geometrical properties of neutral and charged Mn₁₃ clusters. The DFT calculations employed the BPW91/6-311+G* level of theory.⁴⁷⁴ In agreement with previous studies,^{469,471,472} the authors obtained a similar spin multiplicity and excess spin density pattern for the ground state of Mn₁₃.⁴⁷⁴ They also found the vertical detachment energy and the adiabatic electron affinity to agree well with the experimental results. However, the calculated ionization potential (IP)⁴⁷⁴ was in good agreement with the larger experimental IP value while not giving any clue about the smaller experimental IP. A subsequent study performed by Longo et al. with the PBE/TZ2P level of theory was able to account for the smaller IP that could not be found in the earlier study.⁴⁷⁵ Longo et al. concluded that lower vertical IP corresponds to the ionization of the icosahedral Mn₁₃, whereas the larger value corresponds to the ionization of an excited spin isomer of Mn₁₃.

Piotrowski et al. performed PBE calculations and, in accord with previous studies, found a slightly distorted icosahedral geometry with a 3 μ_B magnetic moment for the Mn₁₃ cluster.⁴³¹ The PW91/6-311+G* calculations performed by Gutsev et al. reported the same results for the neutral species, whereas 2 and 4 μ_B magnetic moments were determined for the ground-state icosahedral structures of Mn₁₃⁺ and Mn₁₃⁻, respectively.⁴³² The authors found the assignment of the ground state of neutral and charged Mn₁₂ clusters challenging. They calculated a magnetic moment of 8 μ_B for the ground state of Mn₁₂, where 12 μ_B ⁴⁷¹ and 16 μ_B ⁴⁷² magnetic moments were reported earlier.

With the intention of producing large magnetic moments, Datta et al. studied the pure Mn₁₃ and the doped clusters Mn₁₂X (X = Ti, V, Cr, Fe, Co, Ni) by means of the PBE level of theory.⁴⁷⁶ Following the results of Briere et al.,⁴⁶⁹ the current authors reported ferromagnetically aligned atoms in the two pentagonal rings of an icosahedral Mn₁₃ cluster, while the two pentagonal rings coupled antiferromagnetically with each other. Substitutional doping of Ti and V yielded substantial gains in binding energy and a stable ferromagnetic alignment of atomic spins resulting in a higher magnetic moment.

2.4.6. Fe Clusters. Small iron nanoparticles often show unusual magnetic properties as compared to those of the bulk. The properties of Fe_n clusters have been investigated both experimentally and theoretically during the past two to three decades. Dunlap used the all-electron linear-combination-of-Gaussian-type-orbital (LCGTO) method with the PZ local density functional to investigate isomers of the pure Fe₁₃ cluster and found that the ground state is icosahedral.⁴⁷⁷ The highest magnetic moment was also found for the icosahedral cluster, which was attributed to the enhanced symmetry-required orbital degeneracy for electrons of different spins.⁴⁷⁷ About a decade later, Diéguéz et al. performed DFT calculations to study structures, binding energies, and magnetic moments of Fe_n clusters having up to 17 atoms.⁴⁷⁸ They employed LSDA and a triple ζ basis with double ζ polarization functions. An icosahedral growth behavior was found for clusters with $n = 11$, 12, and 13, whereas nonicosahedral C_{2v} and D_{6h} symmetries were predicted for Fe₁₄ and Fe₁₅, respectively. A growth pattern based on the geometry of Fe₁₅ was found for Fe₁₆ and Fe₁₇ as well. The peaks at $n = 10$, 13, and 15 in the second finite difference of the total finite energy ($\Delta_2 E(n) = E(n+1) + E(n-1) - 2E(n)$) curve suggested that these are the magic numbers for neutral Fe_n clusters.

A two-step computational procedure was used by Bobadova-Parvanova et al. to explore the geometric and magnetic properties of Fe₁₃.⁴⁷⁹ Initially, a combined density functional-based tight-binding (DFTB) and single parent genetic algorithm technique was used to identify the lowest-lying isomers, and then the geometry optimizations were performed with PBE. As in previous studies, the icosahedral geometry was found to be the lowest in energy with two metastable spin states. The global minimum has a total spin of 44 μ_B and corresponds to a ferromagnetic ordering of individual atomic moments, whereas the low-spin state of 34 μ_B has the central atom antiferromagnetically ordered with respect to the surface atoms.

LSDA calculations performed by Duan and Zheng on 13- and 55-atom Fe clusters suggested that the magnetic moments depend not only on the cluster symmetry, but also on the size of the cluster.⁴⁸⁰ They found that contrary to Fe₁₃, the total magnetic moment of the Fe₅₅ cluster with icosahedral symmetry is lower than that with octahedral symmetry.

Furthermore, a strong surface enhancement of the magnetic moment was found for the Fe₅₅ cluster. Aguilera-Granja et al. performed calculations with the PBE/DZP level of theory on Fe₃₄ and Fe₄₀ clusters.⁴⁸¹ For Fe₃₄, they found a high spin (3 μ_B /atom) isomer with ferromagnetic order and a low spin (3 μ_B /atom) isomer whose atoms are antiferromagnetically coupled to their neighbors.

Postnikov et al. performed LDA/DZP calculations to study the electronic structure, relaxation, and magnetic moments of bcc-related (Fe₃₅, Fe₅₉) and fcc-related (Fe₃₈, Fe₄₃, Fe₅₅, Fe₆₂) larger iron nanoparticles.⁴⁸² They found a larger inward relaxation of outer shells in all cases, associated with an enhancement of the local magnetic moments on the surface to beyond 3 μ_B . Basically, the proportion between surface-layer atoms and their deep bulk-like counterparts was found to govern the overall magnetic properties of these larger nanoparticles. Furthermore, they concluded that the relaxation and magnetic properties are relatively independent of morphology, magnetic ordering, and size of these clusters. DFTB calculations were performed by Köhler et al. to investigate the structural and magnetic properties of iron clusters having up to 32 atoms and compared⁴⁸³ against the LSDA calculations of Diéguez et al. up to $n = 17$.⁴⁷⁸ The geometric and electronic structures were found to be in good agreement between the two studies.^{478,483} The current authors observed changes in the structural growth pattern at Fe₂₀ and Fe₃₀. An apparent change in the magnetic moment was observed at Fe₁₃, whereas the clusters' average spin magnetic moments were found to decrease smoothly for the larger sizes.

Sipr et al. investigated the electronic and magnetic properties of Fe clusters of 10 to 89 atoms within the LSDA-VWN level of theory and compared these to the results of crystal surfaces.⁴⁸⁴ They observed that both μ_{spin} and μ_{orb} are higher for atoms close to the cluster surface in free spherical bcc-structured Fe clusters. Spin magnetic moments μ_{spin} in clusters and at crystal surfaces depend linearly on the effective coordination number and on the valence charge. The DOS for an 89-atom cluster was found to be substantially different from the bulk DOS. The calculations based on the PW91 level of theory performed by Rollmann et al. considered the structural Jahn–Teller-like distortion and competing noncollinear and collinear magnetic moments of the Fe _{n} ($n \leq 15$) clusters simultaneously.⁴⁸⁵ In agreement with Bobadova-Parvanova et al.,⁴⁷⁹ the authors found a distorted icosahedron for Fe₁₃ with two different magnetic alignments.⁴⁸⁵ They also reported that the geometries of small iron clusters are distorted with collinear ferromagnetic arrangement of the magnetic moments. In a subsequent study, these authors performed PBE calculations and found that the bcc isomers are the lowest in energy when the clusters contain more than about 100 atoms.⁴⁸⁶ Additionally, another stable conformation was found for magic-number clusters, which is close in energy to the bcc isomers. The new structure is comprised of a close-packed particle core and an icosahedral surface and the partially transformed intermediate shells along the Mackay path between icosahedral and cuboctahedral geometry. The ground state of Fe₅₅ was found to be a shellwise Mackay-transformed morphology.

The structures, binding energies, and magnetic moments of Fe _{n} ($n = 10–13, 15, 19$) clusters were studied using the BLYP/DNP level of theory.⁴⁸⁷ Ma et al. identified that the Jahn–Teller effect plays an important role in determining the ground state of Fe _{n} clusters in this size range. They found the mean binding energy to decrease monotonically with the increasing

cluster size, whereas the magnetic moment per atom varied slightly around 3.0 μ_B /atom. PBE/TZDP calculations were performed on Fe₁₃ and Fe₂₃ clusters to study their electronic and structural properties.⁴⁴ Aguilera-Granja et al. found icosahedral and poly icosahedral ground-state structures for Fe₁₃ and Fe₂₃, respectively, out of the several different compact and open arrangements considered. They reported that the magnetism in iron clusters plays a role in favoring compact structures. Piotrowski et al.⁴³¹ and Gutsev et al.⁴³² also suggested a distorted icosahedral geometry for Fe₁₃. The Fe₁₃⁺ cluster was found to have T_h symmetry in its ground state and a magnetic moment lowered by 9 μ_B from that of the neutral 13-atom cluster.⁴³²

Gutsev et al. explored the electronic and geometrical properties of neutral, anionic, and cationic clusters of Fe _{n} ($n = 10–20$) using the BPW91/6-311+G* level of theory.⁴⁸⁸ They found that the geometrical configurations of anionic and cationic clusters are the same as their neutral counterparts except for Fe₁₀⁻, Fe₁₀⁺, Fe₁₅⁻, and Fe₁₉⁺. In agreement with their previous study, a -9 μ_B magnetic moment change was observed for Fe₁₃⁺, which is related to its high T_h symmetry. A subsequent study by Wu et al. reported that the remarkably low magnetic moment of Fe₁₃⁺ is not due to antiferromagnetic coupling between the spins of the core and surface atoms but due to the quenching of the magnetic moment of the central atom.⁴⁸⁹ These authors used three different GGA functionals and different basis sets to examine the sensitivity of the results to the choice of the level of theory. All three approaches (PBE/ plane wave basis, PW91/DNP, and BPW91/6-311+G*) produced similar geometric structures.

Sahoo et al. performed calculations at the PW91 level of theory to study the spin and orbital magnetic moments and magnetic anisotropy energies (MAE) of Fe₁₃ and Fe₁₃Pt _{n} ($n = 3, 4, 5, 20$) clusters.⁴⁹⁰ For Fe₁₃, both Jahn–Teller (JT) and Mackay transformations (MT) were considered, and the MAE for JT distorted Fe₁₃ was found to be larger than the MT clusters. Additionally, they showed that the Pt capping further enhance the MAE. Wang and Johnson predicted core–shell preferences of 132 transition metal binary alloy nanoparticles using the PAW/PW91 approach.⁵² They proposed that the Fe core with Ag, Cu, Au, Pt, and Pd shells are the preferred combinations for binary alloys.

2.4.7. Co Clusters. Because of their interesting magnetic properties, Co clusters have been studied over the past couple of decades. Most of the theoretical investigations focussed on the electronic structure and magnetic properties of the 13-atom cobalt cluster. Li and Gu studied the electronic and magnetic properties of small cobalt clusters having up to 19 atoms using the spin polarized DVM within the local density functional theory.⁴⁹¹ They found that the icosahedral Co₁₃ isomer has the highest magnetic moment and it converges to that of the bulk value. It was reported that the cluster size and interatomic spacing affect the magnetic moment. The cluster symmetry was also found to play a significant role in determining the moment by splitting the d orbitals into different subsets. A subsequent study was performed by Miura et al. on the icosahedral (I_h) Co₁₃ using the discrete variational Xα cluster method.⁴⁹² They found a high-spin and a low-spin state with 2.23 μ_B and 1.77 μ_B average magnetic moments, respectively. The DVM calculations within LSDA performed by Duan and Zheng reported that the icosahedral Co₁₃ and Co₅₅ can be characterized by their higher magnetic moments as compared to the octahedral ones.⁴⁸⁰

Ma et al. studied the lowest energy geometric structures and their corresponding magnetic moments of small Co clusters containing up to 13 atoms.^{493,494} The BLYP/DNP level of theory was used in the calculations, and it was apparent that the Jahn–Teller effect plays an important role due to the existence of several structures near the ground state of cobalt clusters in this size range. They observed an icosahedral growth pattern, and, in agreement with Li and Gu,⁴⁹¹ the magnetic moment was found to be more sensitive to the cluster symmetry than to interatomic spacing. The formation energy and the second derivative of the binding energy showed that the 10- and 12-atom clusters are magic clusters. Subsequently, Datta et al. performed PBE calculations on Co_n ($n = 10\text{--}20$) clusters to study their structural, electronic, and magnetic properties.⁴⁹⁵ They observed an unusual hexagonal growth pattern in contrast to the previous theoretical studies. The hexagonal Co_{13} was found to possess a magnetic moment of $25 \mu_B$ ($1.9 \mu_B/\text{atom}$), which is in good agreement with the experimental results. The ferromagnetically ordered cobalt atoms produced magnetic moments higher than that of the corresponding hcp bulk value.

Dong and Gong studied the atomic and electronic structures of Co_n ($13 \leq n \leq 23$) clusters using the PW91/PAW formalism.⁴⁹⁶ The clusters in this size range exhibited layer-like structures with hcp or fcc stacking rather than geometries based on icosahedra. Basically, these structures could be considered as small fragments of the bulk. The authors found bilayer structures up to $n = 16$ and then trilayer structures from $n = 17\text{--}23$. They concluded that the stabilities of the layer-like structures are facilitated by the magnetism of the Co clusters.

In agreement with the above study, recent theoretical studies suggested that the hexagonal bilayer (HBL) structure is the most stable isomer for Co_{13} within several different levels of DFT.^{431,432,497} The PBE calculations of Piotrowski et al. found a magnetic moment of $27 \mu_B$ for this HBL Co_{13} .⁴³¹ These authors carried out another study to investigate the role of self-interaction error in the determination of the ground state of Co_{13} using the PAW method with PBE, PBE+U, and HSE functionals.⁴⁹⁷ They found the HBL structure to remain as the lowest energy configuration in the range $U_{\text{eff}} = 0\text{--}1.0 \text{ eV}$ and $\alpha_{\text{HF}} = 0\text{--}0.05$. Gutsev et al. performed PW91/6-311+G* calculations on charged and neutral cobalt clusters containing 12 and 13 atoms.⁴³² The HBL structures were found to dominate the lowest energy isomers. In contrast, the LDA+U calculations of Tereshchuk found an icosahedral growth behavior for cobalt clusters in the range of $n = 10\text{--}19$.⁴⁹⁸

Aguilera-Granja et al. performed calculations using the PBE exchange correlation potential and a plane wave basis to study the magnetic properties of Co_n ($n = 10\text{--}21$) clusters.⁴⁹⁹ They observed a smoothly decreasing average magnetic moment with increasing cluster size. Subsequently these authors studied the 13- and 23-atom cobalt clusters using the PBE/DZP level of theory and found that the hcp structures of Co_{13} and Co_{23} are favored with about $2 \mu_B/\text{atom}$ magnetic moment.⁴⁴ These authors carried out another study with the same theoretical method where they considered high spin ($\text{HS} = 2 \mu_B/\text{atom}$) and low spin ($\text{LS} = 1 \mu_B/\text{atom}$) magnetic configurations of Co_{23} .⁴⁸¹ All of the HS isomers showed ferromagnetic order, whereas the LS isomers were found to have partial antiferromagnetic order. The barrier between the HS and LS magnetic states of Co_{34} was found to be larger than that of Co_{23} .

Jinlong et al. were the first to perform calculations on doped cobalt clusters. The DV-LSD method was used to study the stability, electronic properties, reactivity (toward H_2 , N_2 , and

CO), and magnetic properties of icosahedral MCo_{12} ($\text{M} = \text{Ti}, \text{V}, \text{Cr}, \text{Mn}, \text{Fe}, \text{Co}$, and Ni) clusters.⁵⁰⁰ They found that all of the doped clusters except for NiCo_{12} are energetically more stable than Co_{13} and that CrCo_{12} is the most stable one. The electronic structures of these clusters revealed that these clusters have metallic character. The clusters with $\text{M} = \text{Ti}, \text{Mn}$, or Co were found to have closed electronic shells, while the others have open electronic shells and are expected to undergo further Jahn–Teller distortions. The doping decreased the magnetic moment of the pure cobalt cluster, and the central M atom exhibited a strong influence on the reactivity of the clusters toward H_2 , N_2 , and CO . The structural and magnetic properties of Co_{12}Y ($\text{Y} = \text{Fe}, \text{Co}, \text{Ni}, \text{Ru}, \text{Rh}, \text{Pd}, \text{Pt}$) were studied by means of the PBE/DZ2P level of theory.⁵⁵ Some distortions took place in the hcp structure of Co_{12}Y . The magnetic moment of Co_{12}Fe was reported to be $28 \mu_B$, which is larger than Co_{13} ($27 \mu_B$), whereas the moments of all of the other Co_{12}Y are in the range of $24 \mu_B\text{--}26 \mu_B$. Lv et al. performed calculations using the PW91/DNP level of theory to study the structural, electronic, and magnetic properties of $\text{Co}_{13-n}\text{M}_n$ ($n = 1, 2$; $\text{M} = \text{Mn}, \text{V}, \text{Al}$).⁵⁰¹ All Co_{12}M and Co_{11}M_2 clusters were found to favor the icosahedral geometry in the ground state, where Mn and Al atoms prefer surface positions while V prefers the central position. The total magnetic moment was found to be enhanced with Mn doping of the Co clusters and to be reduced with V or Al doping.

Calculations of spin and orbital magnetic moments as well as MAE of Co_{13} and $\text{Co}_{13}\text{Pt}_n$ ($n = 3, 4, 5, 20$) were performed with the PW91 level of theory.⁴⁹⁰ The icosahedral Co_{13} was found to possess a magnetic moment of $31 \mu_B$,⁴⁹⁰ which differs from the $25 \mu_B$ magnetic moment found by Ma et al.^{493,494} for the icosahedral Co_{13} . For all investigated compositions of $\text{Co}_{13}\text{Pt}_n$ clusters, Sahoo et al. found a ferromagnetic ground state.⁴⁹⁰ Recently, Piotrowski et al. also studied the structural and electronic properties of $\text{Pt}_n\text{Co}_{55-n}$ ($n = 0\text{--}55$) clusters using PBE calculations.⁵⁰² For a wide range of Pt compositions, the $\text{Pt}_n\text{Co}_{55-n}$ clusters were stable, which was apparent by the negative relative energy stability with respect to the $n = 0$ and $n = 55$ states. The core–shell icosahedron-like configuration at $n = 42$ was slightly more stable. This was attributed to the larger release of strain energy due to the smaller atomic size of the Co atoms. The PW91 calculations of Wang and Johnson predicted that having a cobalt core and a Ag, Cu, Au, Pd, Ni, Rh, Pt, Ru, Ir, or Os shell is preferred.⁶⁴ Recently, Islam and Khanna performed PBE calculations to study the enhancement of MAE by doping cobalt clusters with group IV elements (C and Si).⁵⁰³ This significantly increasing anisotropy was attributed mainly to controlled mixing between cobalt d-states and the C p-states.

2.5. Other 4d Transition Metal Clusters

During the past two decades, 4d transition metal clusters were studied extensively due to their applications in developing new magnetic materials and heterogeneous catalysis. Investigations on metal clusters of Rh, Ru, Pd, and Ag were the most popular both experimentally and theoretically. In the mid-1990s, Kaiming et al. performed discrete variational local spin density functional method calculations on M_{13} ($\text{M} = \text{Y}, \text{Zr}, \text{Nb}, \text{Mo}, \text{Tc}$) clusters of three possible high-symmetry geometries (O_h , I_h , D_{3h}) to explore their magnetic properties.⁵⁰⁴ Except for Mo_{13} and Tc_{13} that prefer the cuboctahedral (O_h) structure, all of the other 13 atom metal clusters studied here were most stable in the icosahedral structure. The ground states of all of the clusters

were found to be magnetic, but the magnetic moments were not large.

Subsequently, Kumar and Kawazoe performed electronic structure calculations of Nb_n clusters containing up to 23 atoms using a GGA exchange correlation functional and a plane wave basis set.⁵⁰⁵ They found a distorted body centered cubic structure for $n = 15$ and high coordination structures with hexagonal antiprisms for all of the other clusters with $n > 13$. In contrast to the results of Kaiming et al.,⁵⁰⁴ the current study reported that the icosahedral Nb_{13} is not even a local minimum.⁵⁰⁵ The magic clusters that showed larger HOMO–LUMO gaps were $n = 10, 12$, and 16.

DFT calculations performed by Chang and Chou using the PW91 exchange correlation potential suggested a new buckled biplanar (BBP) structure with C_{2v} symmetry to be a low-lying isomer in addition to icosahedral, cuboctahedral, and decahedral structures.⁶⁰ The ground states of Y_{13} and Zr_{13} were found to be icosahedral structures with small distortions, and Nb_{13} and Mo_{13} were also found to favor the icosahedron with significant distortions. The other 13-atom 4d transition metal clusters showed a preference toward the new BBP structure, which in turn suggested that this BBP structure is favored by the late transition metals having more than half filled d shells. The authors identified that the BBP structure is stabilized by enhanced s–d hybridization. The magnetic moments of this new ground-state structure were found to be smaller than the icosahedral structures and agreed well with experimental results.

PBE/DZP calculations performed by Aguilera-Granja et al. on late 4d transition metals (Ru, Rh, and Pd) reported that the number of localized d electrons relative to the delocalized sp ones is larger in 4d clusters.⁴⁴ Open, cubic structures were favored by the late 4d transition metals because more d electrons with fewer sp electrons favored more covalent directional bonding of the cubic structures. Sun et al. performed DFT calculations based on the LSDA or PBE/LANL2DZ level of theory to identify periodic trends in the geometric structures of 13-atom 4d transition metal clusters.^{65,66} They found that the geometric structures evolve from icosahedral (Y, Zr), to distorted compact structures (Nb, Mo), to fcc or simple cubic crystal fragments (Tc, Ru, Rh), and return to icosahedral (Pd) again in going from left to right in the 4d series.⁶⁶ These structural trends were attributed to the increasingly localized nature of molecular orbitals in going from left to right and to the importance of d-type bonding in the middle of the series. The clusters with the lowest density of states near the Fermi level and with the lowest spin magnetic moment were found to be the lowest energy geometric structures.

2.5.1. Ru Clusters. Ru is nonmagnetic in bulk. However, it has an open 4d shell unlike Pd with a magnetic moment of 4 μ_{B} . Reddy et al. were the first to study the atomic structures and electronic properties of ruthenium. They used LCGTO calculations with PZ and VWN exchange correlation contributions to study electronic and magnetic properties of octahedral and icosahedral Ru_{13} .⁵⁶ The icosahedral Ru_{13} with a large magnetic moment of 1.02 μ_{B} /atom for the surface atoms was found to be more stable than the fcc octahedral one. A few years later, Jennison and co-workers studied the total energies and the relaxed geometries of Ru_n ($n = 55, 135, 140$) clusters using the LDA-PZ level of theory.⁷¹ As in the case of the 13-atom cluster above, these authors observed that the icosahedral geometries are more stable than the fcc geometries for small clusters, whereas a transition is likely to occur between 120 and

140 atoms. The PW91/plane wave basis calculations performed by Kumar and Kawazoe also predicted an icosahedral (*i*) growth behavior for ruthenium clusters.⁵⁰⁶ The magnetic moments of *i*- Ru_{13} and *i*- Ru_{55} were found to be 12 μ_{B} and 14 μ_{B} , respectively.⁵⁰⁶ However, a cubic isomer of Ru_{13} with a magnetic moment of 10 μ_{B} was found to lie significantly lower in energy. At $n = 147$, the icosahedral cluster with a magnetic moment of 16 μ_{B} was found to lie 0.115 eV lower in energy than the nonmagnetic state.

In contrast to the previous results, the PW91 calculations performed by Chang and Chou predicted a new buckled biplanar structure with C_{2v} symmetry as the lowest energy of Ru_{13} .⁶⁰ It was found to have a magnetic moment of 0.46 μ_{B} /atom, which is smaller than that of the icosahedral structure, but closer to the experimental value. Zhang et al. performed DFT calculations using the PW91 functional and a plane wave basis set to study ruthenium clusters having up to 64 atoms and found that the simple cubic structures are more favorable up to 40 atoms.⁵⁰⁷ The analysis suggested that the icosahedron is the most stable structure for clusters of 40–147 atoms, and the cuboctahedron, that is, the bulk structure, dominates the clusters of more than 147 atoms. All of the ruthenium clusters were found to be ferromagnetic with large magnetic moments, and they were found to have small HOMO–LUMO gaps.

Li et al. performed PW91 calculations on ruthenium clusters containing up to 14 atoms and were able to obtain a ground-state structure for Ru_{13} that has never been reported previously.⁵⁰⁸ An amorphous-like arrangement with C_s symmetry that has an average magnetic moment of 0.15 μ_{B} /atom was found, which lies lower in energy than the isomers found by Zhang et al.⁵⁰⁷ and Chang and Chou.⁶⁰ The stabilities of the clusters were found to oscillate in an odd–even fashion with the cluster size, and this was attributed to the novel electronic structure and bonding environment in Ru_n clusters.⁵⁰⁸ Sun et al. performed global optimization of Ru_{13} using TSDS and energy evaluation with the LANL2DZ basis set and the LSDA or PBE exchange correlation functional.⁶⁵ They found the same lowest energy isomer as Li et al.⁵⁰⁸ The preference for the low symmetry and cubic structures of ruthenium was attributed to localized d bonds.⁶⁶ The lowest and the second lowest energy isomers found by Aguilera-Granja et al. using the PBE/DZP level of theory⁴⁴ were consistent with the results of Li et al.,⁵⁰⁸ and the corresponding magnetic moments of the two isomers were 0.15 μ_{B} and 0.31 μ_{B} , respectively.⁴⁴ Piotrowski et al. also performed PBE calculations on Ru_{13} and obtained an open structure as the lowest energy isomer,⁴³¹ which is similar to previous theoretical investigations.^{44,65,66,508}

Aguilera-Granja et al. studied the structural and magnetic properties of Ru_{12}Y (Y = Fe, Co, Ni, Ru, Rh, Pd, Pt) by means of the PBE/DZ2P level of theory.⁵⁵ The structure of the most stable Ru_{13} was found to be retained with minor to more substantial distortions. The antiparallel couplings within the Ru_{12} subcluster were less in Ru_{12}Ni . Hence, the net magnetic moment of the Ru_{12} subcluster was found to be larger in Ru_{12}Ni than in Ru_{12}Fe and Ru_{12}Co . Wang and Johnson performed PAW/PW91 calculations on binary metal clusters containing 55 atoms and predicted that a ruthenium core with a Ag, Cu, Au, Pd, Rh, Ir, or Pt shell is preferred.⁵²

2.5.2. Rh Clusters. Rhodium is a nonmagnetic element that lies just below a magnetic element (Co) in the periodic table. Both experimental and theoretical investigations have taken place since the early 1990s to study the structural, electronic,

and magnetic properties of rhodium clusters. Reddy et al. studied the 13-atom Rh cluster using LCGTO calculations with PZ and VWN exchange correlation contributions.⁵⁶ They observed the icosahedral Rh₁₃ to be more stable than the fcc octahedral one. The ground state of Rh₁₃ was found to have 21 unpaired electrons and hence a magnetic moment of 21 μ_B , unlike the bulk. This magnetic moment is a result of the reduced dimensionality and the enhanced electronic degeneracy due to the symmetry of the cluster. Subsequently, Jinlong et al. performed DV-LSD method calculations and found the ground state of Rh₁₃ is a distorted icosahedron with a magnetic moment of 15 μ_B .⁵⁰⁹ The solution obtained by Reddy et al. (21 μ_B) was found to be a local minimum here.

Reddy and co-workers then carried out a systematic investigation to study the ground-state geometries, electronic structure, binding energies, ionization potentials, and magnetic moments of Rh_n clusters containing up to 13 atoms using the LANL2DZ basis set with either the VWN or the PW91 exchange correlation functionals.⁵¹⁰ The Rh clusters having 10–13 atoms evolved toward icosahedral-based geometries, and their binding energy per atom changed monotonically with size. The ferromagnetic Rh₁₃ was found to have a higher moment per atom than its neighbors, and the authors showed that the changing of geometry and interparticle spacing results in different multiplicities. The PW91/plane wave basis calculations performed by Kumar and Kawazoe also predicted an icosahedral growth behavior to be generally the most favorable for rhodium clusters.⁵⁰⁶ Large magnetic moments were obtained for small clusters, but the values decreased rapidly to very small numbers or even zero at around 147 atoms. In agreement with Reddy et al.,⁵⁶ a magnetic moment of 21 μ_B was obtained for Rh₁₃, and two nearly degenerate states having 17 μ_B and 15 μ_B moments were found to lie about 0.044 eV higher in energy. The icosahedral Rh₅₅ and Rh₁₄₇ clusters exhibited 25 μ_B and 5 μ_B magnetic moments, respectively.

Unlike the previous studies, Bae et al. found a nonicosahedral growth pattern for small Rh clusters.^{511,512} The calculations were performed using a plane wave basis and GGA for the exchange correlation energy.⁵¹¹ Relatively open structures were observed with no central atom up to $n = 13$. Although an atom resides at the center for $n = 14$ and 15, the lowest energy structures are not the closest packed. These observations were attributed to some covalent character in bonding. Furthermore, a magnetic moment of 17 μ_B was found for the Rh₁₃ cluster. A subsequent study performed by these authors using the same theoretical procedure predicted a simple cubic growth for rhodium clusters up to $n \approx 27$.⁵¹² Lower magnetic moments were reported for these simple cubic clusters, which is in better agreement with the available experimental data. With increasing size, cuboctahedral, decahedral, and icosahedral isomers were preferred for Rh_n ($n = 10$ –64). A bilayer structure was also reported during the same time period for Rh₁₃ that has a magnetic moment of 1.31 μ_B /atom and is 0.13 eV lower in energy than the icosahedron.⁶⁰

Futschek et al. performed calculations using the PZ level of theory with PAW to study Rh_n ($n = 10$ –13) clusters and found that the ground-state structures can be considered as fragments of the fcc crystal structure of the bulk.⁶² The magnetic moments of these most stable isomers were found to be around 1 μ_B /atom. The PBE/plane wave basis calculations were performed on noncompact structures of Rh_n ($n = 10$ –21) clusters to study their magnetic properties.⁴⁹⁹ They considered different growth sequences based on the atomic capping of

small half-octahedral and tetrahedral units. These growth patterns were identified as precursors for the lowest energy configurations reported by Chang and Chou⁶⁰ and also by Bae and co-workers.⁵¹¹ The average magnetization of rhodium clusters at this size range decreased in a complex oscillatory manner.⁴⁹⁹

Wang and Johnson carried out DFT calculations at the PW91 level of theory to study the structure of the Rh₁₃ cluster.⁶⁴ In agreement with Bae et al.,⁵¹² the lowest energy isomer of Rh₁₃ was found to be a cubic structure with a maximum number of simple cubes and a magnetic moment of 0.69 μ_B /atom. They found some cubic isomers having even lower magnetic moments than the experimental value of 0.48 μ_B /atom.⁵¹³ The PBE/DZP calculations performed by Aguilera-Granja on 13- and 23- atom 4d clusters also proposed the preference of Rh clusters toward cubic structures.⁴⁴ It was found that the number of localized d electrons with respect to the delocalized sp ones is larger in 4d clusters, and more d electrons with fewer sp electrons favors the more covalent directional bonding in cubic structures.

During the past few years, several theoretical investigations were performed on the 13-atom rhodium cluster.^{65,66,431,497} Sun et al. performed global optimization of Rh₁₃ using TSDS and energy evaluation with the LANL2DZ basis set and the LSDA or PBE exchange correlation functional.⁶⁵ The lowest energy isomer of Rh₁₃ was found to be consistent with the structure found by Bae et al.,⁵¹² and with this same equilibrium structure many spin states were found to be close in energy.⁶⁵ However, they observed a structural change in the lowest energy isomer from cubic to a biplanar fcc fragment upon changing the exchange correlation functional to B3LYP. In a similar subsequent study, the above authors reported that the experimental magnetic moment value can be an ensemble average of several isomers having different moments.⁶⁶

The PBE calculations of Piotrowski et al. also found the double simple cubic structure for Rh₁₃ in agreement with the previous studies.⁴³¹ These authors performed further investigations using the PAW method with PBE, PBE+U, and HSE functionals.⁴⁹⁷ In the range $U_{\text{eff}} = 0$ –2.5 eV and $\alpha_{\text{HF}} = 0$ –0.17, the lowest energy structure of Rh₁₃ was found to change from double simple cubic (DSC) to icosahedral structure. This result suggested that the choice of the functional such as PBE+U or HSE can affect the ground-state structure of rhodium, and favor compact structures versus open structures. This change in stability is mainly driven by a decrease in the sd hybridization of the DSC configuration. Hence, it was pointed out that the description of sd hybridization is essential in determining the ground-state structures and properties of transition metal clusters.

Aguilera-Granja et al. studied the structural and magnetic properties of Rh₁₂Y (Y = Fe, Co, Ni, Ru, Rh, Pd, Pt) by means of the PBE/DZ2P level of theory.⁵⁵ The DSC structure of Rh₁₃ was retained with minor to more noticeable distortions upon doping. A reduction in the magnetic moment by 1 μ_B in every step of the sequence Rh₁₂Fe–Rh₁₂Co–Rh₁₂Ni was observed due to the successive increase of one electron in the d-band when replacing Fe by cobalt and then by Ni. Recently, Piotrowski et al. studied the structural and electronic properties of Pt_nRh_{55-n} ($n = 0$ –55) clusters using PBE calculations.⁵⁰² At $n = 0$, the Rh₅₅ cluster was found to be an icosahedron and the core–shell icosahedral Pt₄₂Rh₁₃ had the highest stability. The PtRh nanoalloys were found to have enhanced magnetic moments by a few times as compared to their separated 55-

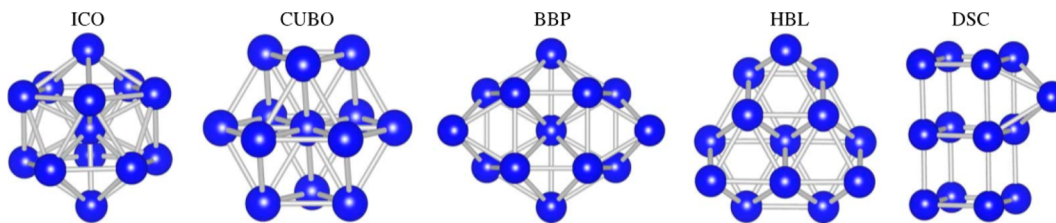


Figure 12. Configurations calculated for 13-atom transition metal clusters. Reprinted with permission from ref 431. Copyright 2010 American Physical Society.

atom counterparts. The PW91 calculations of Wang and Johnson predicted that a rhodium core and a Ag, Cu, Au, Pd, or Pt shell is preferred.⁵²

2.6. Other 5d Transition Metal Clusters

Even though numerous theoretical investigations have been performed on nanoclusters of Pt and Au, studies on other 5d transition metal clusters are very limited. Zhang et al. performed PW91/plane wave basis calculations on Ir clusters having 12 and 13 atoms and some other precious metals (Ru, Rh, Pd, Os, Pt).⁵¹⁴ Simple cubic structures were favored by the iridium clusters as well as by Ru, Rh, and Pt. This trend was found to be stronger from right to left across a period and top to bottom in the group. For the formation of icosahedra or cuboctahedra, this trend was found to be opposite.

Sun et al. performed DFT calculations based on the LSDA or PBE/LANL2DZ level of theory to identify the geometric structures of 13-atom 5d transition metal clusters (Ta, W, Re, Os, and Ir).⁶⁵ The ground-state structures of these clusters are almost the same as the 4d transition metal clusters Nb, Mo, Tc, Ru, and Rh that lie just above in the periodic table. PBE calculations on the 13-atom 5d transition metal clusters by Piotrowski et al. suggested a slightly different structure for W (Figure 12).⁴³¹ In agreement with the previous study, an ideal hexagonal bilayer (HBL) structure that has C_{3v} symmetry was reported for Re_{13} . Furthermore, it was observed that the HBL and buckled biplanar (BBP) structure of W_{13} and Hg_{13} are almost degenerate. The authors found a decreasing total magnetic moment for the first four elements in the 5d series, which starts from $13 \mu_B$ for Lu_{13} and decreases to $0 \mu_B$ for W_{13} . For the first four elements going from left to right, the magnetic interaction changed from ferromagnetic to antiferromagnetic with increasing atomic number. It then increased to $5 \mu_B$ for ferrimagnetic Re_{13} and again decreased gradually to $0 \mu_B$ for Hg_{13} .

Piotrowski et al. performed PBE calculations on the 13-atom transition metal clusters⁴³¹ and observed a quite good agreement with the results of Sun et al.⁶⁵ However, the new equilibrium geometries of Pd_{13} were found to be lower in energy than those of Sun et al.⁶⁵ They compared the metal clusters of the 3d, 4d, and 5d series and concluded that the localization of d states favors compact structures.

3. MAIN GROUP METAL CLUSTERS

3.1. Group 13

3.1.1. Al Clusters. In the early 1990s, theoretical studies on the geometry and electronic structure of Al_n clusters became necessary to account for the available experimental data such as selective reactivity of aluminum clusters with oxygen, which supports the “spherical jellium model” and measurements of static polarizabilities and ionization potentials that cannot be explained by this model.^{515,516}

DFT calculations performed with the LDA- X_α exchange correlation function to determine the electronic structures, binding energies, ionization energies, electron affinities, energy spectra, and DOS of Al_{13} , Al_{43} , and Al_{55} suggest that Al_{13} is most stable in a slightly distorted icosahedral geometry, whereas the fcc cuboctahedron is slightly lower in energy than the icosahedron for Al_{55} .⁵¹⁶ The calculated ionization potentials (IP) and electron affinities (EA) have been found to agree well with the experimental results, and the inconsistencies of the experimental IP curve have been effectively attributed to crystal-field splitting. A subsequent study suggests several inequivalent, yet almost isoenergetic structures for fully annealed Al_{55} , which are notably different from icosahedron or cuboctahedron.⁵¹⁷ This is due to very similar local topologies with minor changes in the positions of the surface atoms of these structures. However, the short range of interactions among Al atoms is apparent by the nearly degenerate energies calculated with the ab initio Car–Parrinello method and LDA along with the plane wave basis set. Another earlier study that used the same calculation method plus the dynamical simulated annealing predicted that Al_{13} is most stable in a quasi-icosahedral geometry unlike its neighbors Na, Mg, and Si.⁵¹⁸

Manninen and co-workers used the BO-LSD-MD method to study structure, electronic structure, and ionization potential of aluminum clusters having 2–23 atoms and have observed that the calculated and experimental IP curves match remarkably well.⁵¹⁹ It has been found that Al_{13} has a jellium-type shell structure because it has 39 electrons, which is close to a magic number of spherical jellium. Furthermore, they found that the simultaneous existence of icosahedral, decahedral, and fcc-based structures of aluminum clusters with 12–23 atoms causes the strong fluctuations in the experimental IP curve. A similar study performed by Duque et al. using DFT with the VWN exchange correlation function has considered both neutral and charged aluminum clusters with atoms less than 22.⁵²⁰ They also found IP values comparable with experiments but slightly overestimated binding energies, which are proportional to the inverse of the cluster size. The s–p hybridization has been found to start at Al_8 for both neutral and charged clusters, and the occupation of the p band increases by one electron with each Al atom added to the cluster.

Akola et al. performed contiguous investigations on anionic aluminum clusters to study their geometries, electronic structure, temperature-dependent photoelectron spectra, and dynamical properties by using the BO-LSD-MD method.^{521–523} The calculated PES of Al_n^- , where $12 \leq n \leq 15$ ⁵²¹ and $n = 19–102$,⁵²² have been found to agree well with the experimentally obtained PES spectra, which also paves the way to determine the structures and temperatures of these clusters theoretically. It has been difficult to correlate the experimental and theoretical PES spectra of anionic clusters having 36 atoms or more due to the complex nature of the multidimensional

energy surface. Comparable to the earlier theoretical studies, the structural patterns of Al clusters changed from the icosahedral motif to the less strained decahedral and fcc-based motifs around $n = 20$. The behavior of Al_{13}^- and Al_{14} was found to be considerably different during heating, and it was observed that Al_{13}^- remains in a “soft solid” phase even after the melting temperature of the bulk Al (933 K).⁵²³

PW91/LANL2DZ calculations have been performed to obtain the ground-state geometries and electronic structure of neutral, cationic, and anionic Al_n clusters up to $n = 15$.⁵²⁴ The size-dependent evolution of binding energy, relative stability, magnetic properties, ionization potential, vertical and adiabatic electron affinities, and fragmentation channels of the clusters have been studied. Despite the monotonic variation of the binding energy with cluster size, the peaks at Al_{11}^- and Al_{13}^- show greater stability due to the electronic shell closure. The neutral and charged Al_n clusters preferentially undergo fragmentation through removal of a single atom. As expected, the odd-atom clusters have a magnetic moment of $1 \mu_B$, and the clusters with an even number of atoms greater than 10 have a value of $0 \mu_B$. Rao and Jena also observed a strong peak for Al_{13}^- in the adiabatic electron affinity curve.⁵²⁴ The geometry of the neutral clusters was not affected considerably upon attaching or removing an electron. Sometime later, Fournier carried out an analogous study using a TSDS algorithm with the same level of theory as above to do global optimization of clusters and compared the results to available experimental and theoretical data.⁵²⁵ He found significantly different global minima (GM) for Al_n , Al_n^- , and Al_n^+ from previous work;⁵²⁴ 24 instances constitute an improved structure, while the calculated properties differ only slightly.⁵²⁵ However, the properties calculated in the previous work⁵²⁴ agree with the experimental results better than do Fournier’s.

Recently, Candido et al. performed both quantum Monte Carlo simulations and PBE/GEN calculations to find out the total energies of the relaxed and unrelaxed neutral, cationic, and anionic aluminum clusters up to $n = 13$.⁵²⁶ The two different theoretical frameworks produced total energies, ionization potentials, and electron detachment energies, which were comparable with previous theoretical and experimental results. They found that the difference of the results between the two methods is only a few tenths of electronvolt.

Ho and co-workers performed a genetic algorithm search together with a tight-binding interatomic potential to locate the lowest-energy structures of Al_n , $2 \leq n \leq 23$.⁵²⁷ They observed size-dependent growth behavior of aluminum clusters and found that the clusters start to form an icosahedral-like motif from $n = 11$ to 13, cap extra atoms on the icosahedron of Al_{13} from $n = 14$ to 18, and undergo additional alterations for $n \geq 19$. The energetics revealed that clusters with $n = 13$, 20, and 22 have extra stability. In a later study,⁵²⁸ these authors have considered aluminum clusters with $n = 27$ –30 to figure out the lowest energy structures by using the same procedure. Further optimization of these structures with the PBE/DND level of theory showed that Al_{27} – Al_{30} clusters favor a double-tetrahedron motif as well as that Al_{28} and Al_{30} have higher stability than Al_{27} and Al_{29} . The geometries of Al_n^- ($n = 27$ –30) are almost the same, suggesting that the larger cluster size with the stronger degree of metallic bonding is weakly affected by the extra electron.⁵²⁸

Neutral and singly charged aluminum clusters containing up to 34 atoms have been studied using PBE/DZP to locate their global minima.^{529,530} Aguado and Lopez have shown that

neutral aluminum clusters with 13–21 atoms tend to adopt icosahedral structures, whereas larger clusters compete to be decahedral, bulklike fcc, or hexagonal prismatic structures.⁵²⁹ They have also pointed out that the global minimum structure strongly depends on the charge of the cluster for any given number of atoms. A set of new lower energy structures was located for $n = 19, 22, 24, 25, 26, 29$, and 30 clusters.⁵²⁹ Drebov and Ahlrichs employed genetic algorithm and basin hopping procedures to locate global minimum structures and obtained results⁵³⁰ similar to those of Aguado and Lopez for clusters up to $n = 21$,⁵²⁹ which in turn are identical to those of Chuang et al. for $n < 19$.⁵²⁷ Additionally, they found new global minima for $n = 23$ –31 and 33, which have been calculated with the PBE/def2-TZVP level of theory and are about 0.27 eV lower in energy than previous ones.⁵³⁰ The GM of Al_{23} and triplet state of Al_{28} have high symmetries. The global minima of anions with $n = 24$ –27, 29, 30, 31 and cations with 24–27, 33 are also different⁵³⁰ from the ones calculated by Aguado and Lopez.⁵²⁹ A similar investigation has been performed by Aguado and Lopez to study the structures and stabilities of Al_n^+ ($n = 46$ –62). The clusters with $n = 51, 57$, and 61 have extra stability, whereas significant structural changes occur between Al_{55}^+ and Al_{56}^+ . Most clusters with $n \geq 48$ tend to adopt fragments of the fcc lattice with significant distortions. They also pointed out the importance of a better parametrized potential to model the atomic interactions in Al clusters to obtain realistic structural trends other than using first-principles methods.⁵³¹

Lopez and co-workers have performed another theoretical analysis to understand the correlation between the latent heats and cohesive energies of Al_n^+ ($n = 25$ –83).⁵³² They mentioned that the size-dependent variations of the cohesive energies are merely due to the size-dependent variations in the latent heats. The global minimum structures of the clusters can be grouped into four categories: distorted decahedral fragments, fcc fragments, fcc fragments with stacking faults, and “disordered”. The geometric and electronic shell effects cause variations in the cohesive energies. The higher cohesive energy and the latent heat of Al_{37} are due to an electronic shell closing, whereas that of Al_{44} is due to a structural shell closing.⁵³²

A combined experimental–theoretical work has been done to study the heat capacities of the aluminum clusters with $n = 31$ –48.⁵³³ The heat capacities have been measured on cationic clusters, whereas calculations have been performed on neutral ones. However, the authors stated that the charge of the cluster would not affect the results of the cluster at this size range. Because of the decreasing surface-to-volume ratio, it was expected to see a decrease in the melting temperature with decreasing particle size. Nevertheless, they observed the reverse: increasing melting temperature with decreasing cluster size. The authors correlated geometric features identified by analyzing the nature of the ground state with the heat capacity curve. The broad heat capacity curves were attributed to open structures and defects in the clusters, whereas high melting temperatures have been associated with strong core–surface interactions.⁵³³

A novel route to investigate the most stable structures of Al clusters up to 13 atoms has been explored.⁵³⁴ Pushpa et al. have performed ab initio DFT calculations where exchange correlation effects were described using the LDA and a plane wave basis was used to find total energy and vibrational modes of each cluster. To determine stable, low-energy structures of clusters, they started with different high symmetry structures and distorted them according to their unstable vibrational

modes. The icosahedral Al_{13} does not have unstable vibrations, yet can be relaxed to obtain a distorted lower energy structure.⁵³⁴ A DFT investigation based on the LSDA and the PBE/LANL2DZ level of theory predicts a decahedron for the lowest-energy Al_{13} ,⁶⁵ which agrees with some of the previous theoretical studies.^{519,525}

VWN/TZVP calculations have been carried out to understand the reactivity and the bonding of a hydrogen atom to an Al_{13} cluster.⁵³⁵ Mananes et al. have also used reactivity indexes (Fukui functions) to predict the reactivity of atomic species with metallic clusters.⁵³⁵ Al_{13}H is particularly stable because it has a closed-shell electronic structure and a calculated HOMO–LUMO gap of 1.77 eV. Al_{13} is a slightly oblate icosahedron, while the H atom resides on top of one of the two faces of the icosahedron closer to the center (hollow site) with a binding energy of 3.36 eV. The preference for hollow site locations has been supported by the Fukui indexes as well.⁵³⁵

Chen and co-workers investigated the adsorption of molecular water on $\text{Al}_{17}^{\pm q}$ ($q = 0\text{--}3$) with the BP/DNP level of theory.⁵³⁶ The bare $\text{Al}_{17}^{\pm q}$ ($q = 0\text{--}3$) were studied and compared to learn that the Al_{17}^- anion has the lowest energy. They then studied the adsorption complexes ($\text{Al}_{17}\text{H}_2\text{O}$) $^{\pm q}$ ($q = 0\text{--}3$) and found that anionic clusters favor the H-affinity adsorptions, whereas cationic and neutral ones favor O-affinity adsorptions. Regardless of the nature of the charge, the adsorption energies increase with increasing cluster charge values. They classified H-affinity adsorptions as physisorptions and O-affinity adsorptions as chemisorptions on the basis of geometrical and electronic structures and population analyses.⁵³⁶

The transition state structures and reaction mechanisms for the dissociative chemisorption of HI , I_2 , and CH_3I on the magic cluster Al_{13}^- were investigated.⁵³⁷ Kim et al. used the PBE0/6-31G(d,p) level of theory for all of the calculations. These molecules approached the aluminum cluster anion with the end-on orientation due to the effective overlap of Al_{13}^- HOMO with the antibonding σ^* LUMOs of the small molecules. The chemisorption of I_2 molecule and physisorption of HI and CH_3I molecules on Al_{13}^- was observed. Because of the low mobility of CH_3 on Al_{13}^- and the high activation barrier for the $\text{S}_{\text{N}}2$ -type reaction, the reaction between CH_3I and Al_{13}^- was found to be unlikely to take place. Recently, Reber et al. performed PBE investigations to understand the size-selective reactivity of Al_n^- ($n = 10\text{--}20, 23, 25, 27$) clusters with methanol and the reaction energetics including reaction barriers.⁵³⁸ The O–H bond was cleaved by complementary Lewis acid and Lewis base active sites that can be found at precise locations on the geometry of the small clusters. However, the aluminum cluster anions having more than 20 atoms were found to react rapidly with ROH species due to the accumulation of complementary pairs on edges. Recently, Abreu et al. performed PBE calculations on $\text{Al}_{13}\text{I}_n^-$ ($n = 0\text{--}4$) and $\text{Al}_{14}\text{I}_n^-$ ($n = 0\text{--}5$) clusters to study how the clusters with closed electronic shells can break O–H bonds through repositioning of I atoms to induce active sites.⁵³⁹ The closed geometric shell of Al_{13}^- was activated by two adjacent ligands on it, whereas in $\text{Al}_{14}\text{I}_3^-$, iodine induced an active site on the adatom, making the cluster reactive.

Even though most of the theoretical work on Al clusters has been restricted to bare clusters, Häkkinen and co-workers have paid attention to ligand-stabilized Al clusters.⁵⁴⁰ It has been shown that the ligand-stabilized aluminum clusters similar to

$\text{Al}_{50}\text{Cp}^{*12}$ have a superatom-like electronic shell structure with shell closures at 8, 20, 40, etc.⁵⁴⁰

Doping of pure metal clusters influences their physical and chemical properties. One can create novel materials by changing the cluster size or the composition of these doped clusters. Doping of Al clusters with a variety of dopants has been popular both experimentally and theoretically because it generates magic clusters.

The Al_{13} cluster can satisfy the electronic shell closure criteria when it interacts with an alkali metal. Ab initio molecular dynamics simulations on Al_{14} and Al_{13}Na clusters have been performed with the local density functional theory and a plane wave basis set, and the lowest-energy isomer of Al_{14} has been found to be a capped icosahedron.⁵⁴¹ As a result, the 3s electrons of the capping Al atom behave more like core electrons, giving rise to an electronic shell closure of 40 electrons similar to Al_{13}Na , and hence both become magic clusters. The HOMO–LUMO gap of Al_{14} has been found to be lower than that of Al_{13} indicating a lower stability, whereas the higher HOMO–LUMO gap of Al_{13}Na as compared to Al_{13} suggests higher stability for Al_{13}Na . These findings completely agree with the observation of a lower IP for Al_{14} and higher IP for Al_{13}Na .

Several theoretical studies have been done to study the global minima, binding energies, HOMO–LUMO gaps, ionization potentials, dipole polarizability, and first hyperpolarizabilities of Al_{13}X clusters where X is an alkali metal.^{542–544} Jena and co-workers studied the interactions of the Al_{13} cluster having nearly degenerate Jahn–Teller distorted icosahedral and decahedral structures with all of the alkali metals up to Cs.⁵⁴² The calculations were performed with both the BPW/LANL2DZ level of theory in the Gaussian 94 code and the PBE exchange correlation function in the NRMOL code. Except for the case of Cs, the distortions in bare cluster structures are no longer present for all of the other alkali metals. The bonding nature of the alkali metal to the Al_{13} cluster changes from Li to Cs to vary from more covalent to more ionic, respectively. The binding energy of X to Al_{13} decreases as X goes from Li to Cs, suggesting that the size of the atom is dominant over its ionization potential. The same group performed another DFT investigation with the PBE exchange correlation functional to study both neutral and anionic Al_n and Al_nX ($n = 12\text{--}14$, X = Li, Na, K) clusters.⁵⁴³ The addition of alkali atoms caused apparent rearrangements in the structure of the Al_{12} cluster, while the alkali atoms bound to faces without distorting the structure much for larger sizes. The “magic” nature of Al_{13}X is noticeable by its large ionization potential, large HOMO–LUMO gap, and smallest adiabatic electron affinity. The ionic nature of bonding between Al_{13} and X is established by their very little electron-density overlap and by the increasing dipole moment values of Al_{13}X for X going from Li to K.

The bonding, dipole polarizabilities, and hyperpolarizabilities of $\text{Al}_{13}\text{X}^{0/1-}$ clusters with X = Li, Na, and K have been investigated using the HF, BHandHLYP, and CAM-B3LYP/6-311+G(3d2f) levels of theory.⁵⁴⁴ The dipole polarizabilities of Al_{13}X species have been found to be larger than that of Al_{13} and smaller than Al_{13}^- , the species that has the same number of valence electrons. Otero et al. found that the nonlinear polarizabilities of these species depend on the electron-donating nature of Al_{13} in the excited state and the electron-withdrawing ability of the alkali metal. They observed a significant difference in hyperpolarizabilities between neutral

and charged species, which in turn indicates that charging these species with one electron results in a considerable increase in the first hyperpolarizability.

Pure Al₁₃, Al₁₉, and Al₂₃ clusters and these clusters doped with a Si impurity have been studied with LDA-CA/plane wave basis to determine their most stable structures and physical properties.⁵⁴⁵ The geometries of the pure clusters are a Jahn-Teller distorted icosahedron, a double icosahedron, and a decahedron, respectively. Out of the three doped clusters studied here, the icosahedral Al₁₂Si has the highest stability. The differently capped icosahedrons have almost degenerate energies for Al₁₈Si, whereas the cuboctahedral structure is only a local minimum. For Al₂₂Si, the decahedral isomer is stable with a relatively substantial HOMO–LUMO gap (0.82 eV). The doping of these pure Al clusters has given them electronic shell closures and increased binding energies. The binding energy has decreased with the increasing cluster size. Lu et al. performed DFT calculations on Si@Al₁₂H_n ($n = 1$ –14) clusters using the PBE/DNP level of theory to explore their structures and stability.⁵⁴⁶ Si@Al₁₂H_n clusters showed enhanced stability, even for large numbers of H atoms. These clusters were characterized by their large binding energies, HOMO–LUMO gaps, and high ionization potentials.

PBE calculations have been performed to find geometries, electronic structures, and energetics of Al_nCu ($n = 11, 12, 13, 14$).⁵⁴⁷ In contrast to the alkali atom doped aluminum clusters of the same size, the Cu atom tends to reside inside the aluminum cluster. The high ionization potential of Cu, its comparable size to Al, and strong AlCu bond strength cause the Cu atom to occupy an interior site, where mixing of electronic states of Cu and Al takes place. Both geometric and electronic shell closures are vital for the relative stability of these species. Al₁₂Cu has a geometric shell closure, whereas an electronic shell closure occurs for Al₁₃Cu. The calculated adiabatic electron affinities in this study have been in very good agreement with experiment. Roach et al. performed PBE calculations to measure the relative reactivity of CuAl_n[−] ($n = 11$ –34) clusters with O₂.⁵⁴⁸ They found the CuAl₂₂[−] cluster to be a magic cluster and resistant to oxygen etching. The large HOMO–LUMO gap observed for the CuAl₂₂[−] cluster was not due to a spherical electronic subshell closure but can be due to its distorted shape and hence the crystal field splitting of the jellium orbitals.

The ground-state geometries, binding energies, vertical ionization potentials, and vertical electron affinities of Al₁₃, Al₁₂M, and Al₁₃M (M = Cu, Ag, Au) have been obtained using the B3LYP/LANL2DZ level of theory.⁵⁴⁹ Zope et al. found the decahedral Al₁₃ to be the lowest in energy. As discussed earlier, the coinage metal atom resides in the center of the aluminum cluster in Al₁₃M, but for Al₁₂M it is on the surface. As in an alkali doped Al₁₃ cluster, Al₁₂M has ionic type bonding nature, whereas Al₁₃M has covalent type bonding. The electronic shell closure of Al₁₃M is apparent by the large values of adsorption energies, HOMO–LUMO gaps, and low electron affinities.

Wang and co-workers have studied the growth behavior and electronic properties of NiAl_n ($n = 1$ –14) by using the PW91/DNP level of theory.⁵⁵⁰ In the ground-state structures, the Ni atom moves from a convex, to a surface, to an interior site with an increasing number of Al atoms in the cluster. Doping the aluminum clusters with one Ni atom enhanced their stability. It has been found that NiAl₁₃ has a higher stability than its neighbors. The HOMO–LUMO orbitals of these clusters are composed of sp–d hybridized orbitals in Ni atom and in Al

atoms, and this phenomenon is responsible for the variation of the HOMO–LUMO gap with the cluster size. They found that there is only a little effect on the spin state of pure aluminum clusters by the addition of the Ni atom.

The RI-PBE/def-SV(P) level of theory was used to study the geometric, electronic, and optical properties of B₂Al₂₁[−].⁵⁵¹ The basin-hopping method was used to find the lowest-energy isomer, which is an aluminum cage encapsulating two boron atoms endohedrally. This isomer is different from the Al₂₃[−] structure found by Aguado and Lopez,⁵²⁹ and the smaller size of B than Al can be the cause for this distinction. The projected density of states (PDOS) predicts the electronic structure of B₂Al₂₁[−] to be 1S, 1P, 1D+2S, 1F+2P, 2D+1G+3S with unoccupied orbitals of 1H+2F. The same group has used the same level of theory to perform an equivalent study on X@Al₁₂ (X = B, Al, Si, P) clusters and their assemblies.⁵⁵² It has been found that the geometries of all X@Al₁₂^{+/-} clusters except for Al₁₃⁺ are icosahedral structures. The sides of the monomer have been kept in a staggered fashion to obtain the optimized structures of dimers X@Al₁₂–Y@Al₁₂ (X–Y = Si–Si, B–P, Al–P). These dimers have shown unusual hybridizations such as SD, PF, and SDG orbitals.

3.1.2. Ga Clusters. Ga is an interesting metal in group IIIA in the periodic table, having a relatively low melting point (303 K) as compared to its neighbors Al (934 K) and In (430 K) in the same group. However, it has been found that the Ga_n clusters have higher melting temperatures,^{553,554} which has been attributed mainly to the covalent bonding in these clusters, in contrast to the covalent–metallic bonding in the bulk.⁵⁵⁴ Theoretical investigations on Ga_n clusters have been performed during the past three decades to identify their lowest-energy structures and electronic properties.^{515,555–557} However, most of the studies on larger clusters ($n > 10$) have been done in recent years, and these studies have additionally focused on binding energies, ionization potentials, and electron affinities of the clusters.^{558–560}

Song and Cao were the first to carry out DFT calculations to study structural and electronic evolutions of Ga_n clusters up to $n = 26$ with the PW91/DNP level of theory.⁵⁵⁸ Herein, the lowest-energy structures and their electronic properties including the HOMO–LUMO gap, IP, and EA have been calculated to compare with the available literature. Gallium clusters tend to attain more compact structures with increasing cluster size. The size-dependent binding energies suggest a particularly high stability for clusters with $n = 8, 14$, and 20. A similar study done by Ahlrichs and co-workers to investigate structures and properties of neutral gallium clusters predicts comparable as well as contrasting viewpoints about structures and stability of Ga_n clusters using the meta-GGA functional TPSS and the TZVP basis.⁵⁵⁹ They looked at cohesive energies and second-order differences (a general SOD equation takes the form of $x_{t+2} = f(t, x_t, x_{t+1})$, and two starting values, x_0 and x_1 , are needed) of the gallium clusters and observed from SODs that Ga₇, Ga₁₄, and Ga₂₀ have a higher stability, whereas Ga₈ and others were found to have higher stability in the earlier study. Additionally, this group has seen structural discrepancies for clusters with $n = 14, 15$, and 21–24,⁵⁵⁹ from those reported by Song and Cao.⁵⁵⁸ Recently, Sai et al. studied medium-sized gallium clusters with 20–40 atoms and reported the same lowest energy configurations for Ga₂₀–Ga₂₂⁵⁶⁰ as in Song and Cao's previous study. They observed that the growth of core–shell structures becomes dominant from Ga₃₁. Furthermore, it has been found that Ga₂₃ and Ga₃₆ have high point group

symmetries and Ga_{36} is the most stable structure with a large HOMO–LUMO gap.

Aside from the bare gallium cluster studies, a PBE investigation with PAW has been performed to analyze the electronic structures and to verify the existence of superatom cores with closed electron shells in three of the previously synthesized ligand-protected gallium clusters and their model derivatives.⁵⁶¹ Corresponding to a magic number in the spherical jellium model, these three clusters, $\text{Ga}_{23}\text{N}(\text{SiMe}_3)_2\}$ ₁₁, $[\text{Ga}_{22}\text{N}(\text{SiMe}_3)_2]_{10}]^{2-}$, and $\text{Ga}_{22}\text{Si}(\text{SiMe}_3)_3\}$ ₈, have been found to have 58 delocalized valence electrons.^{562–564} Comparing the electron DOS of the model derivatives and the original clusters has shown that the covalent gallium–ligand bonds and a closed electron shell play important roles in widening the HOMO–LUMO gaps, hence enhancing the chemical stability. A subsequent study from the same group that used the same level of theory has identified a close relation between the cage-like icosahedral Ga_{12} center and the α phase of gallium.⁵⁶⁵ They also suggested that the electronic structure of Ga_{12} center bridged by six phosphorus ligands most closely resembles δ - Ga and there are no well-defined superatom orbitals.

There has been a particular interest in Ga_{13} clusters because it is the smallest cluster having almost a closed-shell magic electronic configuration. Previous ab initio molecular dynamics (MD) simulation studies have predicted inconsistent ideas regarding the lowest energy structure of Ga_{13} . The MD simulation that used the PZ exchange-correlation functional suggests that the Ga_{13} could be an icosahedron,⁵⁶⁶ whereas a distorted decahedron is found in the Car–Parrinello method-based calculations with the CA exchange-correlation functional.⁵⁶⁷

Doping of these gallium clusters Ga_{12}X ($\text{X} = \text{B}, \text{C}, \text{N}, \text{Al}, \text{Si}, \text{P}, \text{Ge}, \text{Al}$) has been studied with the PBE0/6-311G(d) level of theory, and it has been found that the stability increases relative to Ga_{13} .⁵⁶⁸ Icosahedral endo- Ga_{12}C has been found to be the most stable cluster that exhibits the most jellium-like orbital structure. Moreover, it has been observed that the hydrogen adsorption on these doped clusters is energetically favorable, but adsorption energies vary significantly with valence electron count and the adsorption site.⁵⁶⁹ The structures, stabilities, and electronic properties of lithium-doped gallium clusters, Ga_nLi ($n = 1–13$), have been investigated by means of the B3LYP/LANL2DZ level of theory as well as the dissociation energies, second-order energy differences, and HOMO–LUMO energy gaps.⁵⁷⁰ It has been reported that the impurity lithium enhances the stability of the clusters and also affects the geometrical structure. Guo has also used the B3LYP/LANL2DZ level of theory and has reported that the ground-state geometric structures of Ga_nAl ($n = 1–15$) clusters have frameworks similar to those of the most stable Ga_{n+1} clusters except for $n = 8$ and 13.⁵⁷¹ Furthermore, Guo has pointed out that the Al atom prefers to substitute for a surface Ga atom until $n = 12$, and then it lies in the center of the Ga frame. Recently, Guo has investigated the growth behavior of $(\text{GaAl})_n$ ($n = 1–12$) clusters and chemisorption of H_2 on these systems using the same level of theory as of the previous study.⁵⁷² The magic numbers of the calculated $(\text{GaAl})_n$ clusters have been found to be $n = 4$ and 6, whereas those of the $(\text{GaAl})_n\text{H}_m$ clusters are $n = 10, 11$ and $m = 2$.

3.2. Group 14

3.2.1. Sn Clusters. Tin is typically used experimentally in metal alloys rather than as a pure metal. A few theoretical

investigations have been carried out to study pure and doped tin clusters during the past decade. A systematic study of structures and dynamical properties of Sn_n clusters having up to 13 atoms was carried out by means of the Car–Parrinello ab initio molecular dynamics method with the CA exchange correlation potential, and Lu et al. observed compact structures for Sn_n clusters.⁵⁷³ Majumder et al. performed GGA/plane wave basis calculations on Sn_n ($n \leq 20$) to study their atomic structures, energetics, and fragmentation behavior.⁵⁷⁴ The prolate structures of Sn_n ($n > 10$) clusters had a bonding nature different from that of the bulk fragments, and the binding energies were within about 11% of the calculated bulk value. The authors identified this as the reason for higher melting temperatures of the tin clusters as compared to the bulk.

Pushpa et al. studied the symmetries and vibrational instabilities of the 13-atom Sn cluster using a plane wave basis and the LDA exchange correlation functional.⁵³⁴ They found a lower energy structure for Sn_{13} than that previously reported.⁵⁷⁴ The authors used a computationally efficient, simple procedure to find the low-energy structures of clusters.⁵³⁴ They examined the unstable modes obtained using density functional perturbation theory calculations and improved the structures from high-symmetry to low-symmetry structures by following the vibrational instabilities.

A combined experimental-theoretical investigation was carried out by Schäfer et al. to study the structures and electronic properties of neutral Sn_n clusters with up to 20 atoms.⁵⁷⁵ They used the B3P86 functional and extended Stuttgart valence basis set for their calculations and obtained more stable structures for $\text{Sn}_{11–13}$. The calculated stacked structures of $\text{Sn}_{14–16,18}$ were similar to those reported by Majumder et al.,⁵⁷⁴ whereas Sn_{17} reported here is more stable by 0.22 eV.⁵⁷⁵ For Sn_n ($n = 12–20$) clusters, the predicted dipole moments from theory were significantly larger than the experimental values because the tin clusters at this size range were too flexible to be treated as rigid rotors even at a nozzle temperature of 40 K and hence the electric dipole moments were quenched.

Few theoretical studies have been performed on doped stannaspherenes (Sn_{12}^{2-}). Matxain et al. studied structural and electronic properties of the neutral Mn@Sn_{12} cluster and its dimer using the hybrid meta GGA functional MPWB1K combined with the SKBJ basis set.⁵⁷⁶ The endohedral Mn@Sn_{12} was found to have I_h symmetry, and the inner manganese atom was found to lose two valence electrons to the cage upon encapsulation. The adiabatic ionization energy of Mn@Sn_{12} was close to 7 eV, indicating its higher stability. It was reported that the icosahedral geometry was retained upon dimerization of Mn@Sn_{12} . Kandalam et al. also studied Mn@Sn_{12} using the PW91 level of theory⁵⁷⁷ and reported results similar to those of Matxain et al.⁵⁷⁶ The magnetic coupling between the Mn@Sn_{12} cages was found to depend on their relative orientation. Chen et al. performed BLYP/DND calculations on M@Sn_{12} ($\text{M} = \text{Ti}, \text{V}, \text{Cr}, \text{Mn}, \text{Fe}, \text{Co}, \text{Ni}$) clusters to study their geometric, optical, and magnetic properties.⁵⁷⁸ The ground-state structures were found to be slightly distorted icosahedrons, and the authors called them the pseudoicosahedrons. In agreement with Matxain et al.,⁵⁷⁶ Mn@Sn_{12} showed the smallest distortion and was hence found to have essentially I_h symmetry.⁵⁷⁸ The optical gaps of the doped clusters were found to be red-shifted as compared to Sn_{12}^{2-} . With all of the dopants studied here, the

M@Sn₁₂ clusters were found to be magnetic, and the magnetic moment was found to vary between 2–5 μ_B .

3.2.2. Pb Clusters. Bulk lead solid is metallic, whereas silicon and germanium are semiconductor crystals while being in the same group of the periodic table. Lead is also used as weights and in lead-acid batteries, so it has a variety of uses in its pure form. Ab initio theoretical methods have been used to study Pb clusters extensively during the past three decades. Iniguez et al. performed the first LDA calculations to study lead clusters having up to 20 atoms.⁵⁷⁹ They attributed the stability of Pb₁₃ and Pb₁₉ to the sphere packing of an icosahedron and a capped icosahedron, respectively, whereas the stability of Pb₁₀ and Pb₁₇ was explained by the closing of the 2p and 2d electronic shells. Later, Rubio et al. used the jellium model and the density functional approach to study neutral and charged Pb clusters.⁵⁸⁰ Alonso and co-workers reported their work on Pb_n ($n = 3–14$) clusters using a Car–Parrinello-like scheme for energy minimization.⁵⁸¹ They used the PZ exchange correlation functional and a plane wave basis. An icosahedral-like packing scheme was found for the ground-state geometries of larger clusters starting from $n = 7$. Enhanced HOMO–LUMO gaps were observed for Pb₁₀ and Pb₁₃, which suggest that the abundance of Pb₁₀ and Pb₁₃ clusters in the experimental mass spectra is an electronic effect.

Wang et al. performed a DFT investigation on Pb_n clusters having up to 22 atoms and discussed their geometric structures, binding energies, and size-dependent electronic properties.⁵⁸² The BLYP/DND level of theory predicted that the close-packed icosahedral structures are not the lowest energy structures for Pb₁₂ and Pb₁₃, but a strongly distorted icosahedral cage and a face-capped icosahedral cage, respectively. However, the layered stacking structures predominate in the $n = 13–18$ region. The binding energies, second-order differences in energy, and the HOMO–LUMO gaps indicated that the clusters with $n = 10, 12, 16, 18, 21$ have higher stability than their neighbors. It was reported that the relative stability of lead clusters is mostly related to the electron effect rather than the geometry packing effect. The covalent-to-metallic transition seems to start at an early stage as of $n = 11$, but Pb₂₀ has a finite gap of about 1 eV, suggesting that it is still a semimetallic cluster with covalent bonding.

Rajesh et al. performed ab initio molecular dynamic simulations within the DFT formalism to study the geometric and electronic structure of Pb_n clusters ($n = 2–15$).⁵⁸³ The relative stability of GGA/PAW optimized geometries was verified by more accurate methods based on hybrid energy functionals and also the MP2 level of theory under the LCAO-MO method. In contrast to the results of Wang et al.,⁵⁸² Rajesh et al. obtained a slightly distorted Pb atom encapsulated icosahedron for Pb₁₃.⁵⁸³ Further, it was mentioned that the compact spherical structures are formed for Pb at an earlier stage than the other group IV clusters. This trend was attributed to the respective bulk structures (diamond-like for Si, Ge, and Sn and fcc for Pb) and to the higher compressibility of lead. Rajesh et al. found that the clusters with $n = 10$ and 13 have higher stability over their neighbors,⁵⁸³ which was $n = 10$ and 12 for Wang et al.⁵⁸² Later, Rajesh et al. performed a similar investigation using the same theoretical procedure to study charged Pb_n clusters in the same size range and to compare with the corresponding neutral clusters.⁵⁸⁴ In accord with the neutral clusters in the previous study, Pb_n⁺ clusters exhibited a compact growth pattern with a small relaxation of the ground-state geometry after removing an electron.

Moreover, the average binding energy, second-order difference in energy, and the fragmentation energy predicted that Pb₁₀ and Pb₁₃ are more stable, whereas the analysis of HOMO–LUMO gap and the ionization potential suggest a lower stability for Pb₁₃. This suggests that, although Pb₁₃ is thermodynamically more stable, it is chemically not the most stable, which means it is more reactive due to the lowering of the energy gap.⁵⁸⁴

Li et al. performed global structural optimizations of neutral Pb_n clusters having up to 20 atoms using a genetic algorithm coupled with a tight-binding potential and then have further optimized these clusters with the DFT-PBE level of theory.⁵⁸⁵ The lowest-energy structures of Pb_n clusters ($n = 2–15$) agreed remarkably well with those previously reported⁵⁸³ except for Pb₁₄. The second lowest-energy isomer that was reported for Pb₁₃ is similar to the lowest-energy isomer reported by Wang et al.⁵⁸² The most stable isomer of Pb₁₅ is consistent with both of the previous studies. The relative stability of the lead clusters was evaluated, and it was found that the 10-, 13-, 15-, and 17-atom clusters are more stable than their neighbors, which is in good agreement with the experimental data. It was also concluded that the Pb_n clusters with $10 < n \leq 20$ can be easily dissociated into smaller stable lead clusters.

Lately, Lei et al. explored the geometric structures and dipole moments of Pb_n ($n = 13–18$) clusters.⁵⁸⁶ They used the basin-hopping method glue potential to obtain the initial structures and then performed further optimizations with the MP2/LANL2DZ level of theory. The lowest-energy structures of Pb₁₃ and Pb₁₄ are consistent with the previous theoretical results.⁵⁸³ They found a new lowest-energy isomer for Pb₁₅, which is a distorted decahedron structure with O_h symmetry.⁵⁸⁶ An overall conclusion was made about the lowest-energy structures of Pb_n ($n = 13–18$) clusters: they prefer compact structures. Lei et al. found that Pb₁₅ has extra stability as compared to its neighbors, while Pb₁₄ and Pb₁₈ possess large dipole moments, which is in agreement with the experiment.

Several theoretical studies have been performed on doped lead clusters during the past decade. Rajesh and Majumder introduced C, Al, and Mg atom impurities into Pb₁₂ clusters to study their influence on the stability of Pb₁₃ cluster.⁵⁸⁷ The ground-state geometries and energetics of MPb₁₂ were calculated within the GGA level of theory. All of the lowest-energy isomers were found to be icosahedrons with the impurity atom at the center. In terms of binding energy, CPb₁₂ has the highest stability, whereas the incorporation of an Mg atom enhances the HOMO–LUMO gap to the most (2.30 eV) that has ever been reported for any metal cluster. Rajesh and Majumder observed an extraordinary increase in interaction energy for Mg at Pb₁₂, while the interaction energy of C, Pb, and Al atoms with Pb_n was found to increase linearly with the cluster size. The higher interaction energy of Mg with Pb₁₂ and the largest HOMO–LUMO gap of MgPb₁₂ were attributed to the 50 electron rule for icosahedral structures. The authors carried out a subsequent theoretical investigation on Pb_nM (M = C, Al, In, Mg, Sr, Ba, and Pb; $n = 8, 10, 12$, and 14) clusters with the same level of theory and found that the structure and stability of these clusters strongly depend on the atomic size of the impurity atom and its interaction energy with Pb_n.⁵⁸⁸ When the impurity atom is small, it occupies the endohedral position, whereas larger impurity atoms prefer the capped positions. The energetics suggested that the p–p interaction dominates over the s–p interaction and the smaller atoms interact more strongly. The substitution of C or Al enhanced the stability of the host cluster, whereas Mg lowered the stability. However, it

was observed that the HOMO–LUMO energy gap is widened only by Mg, while all of the other impurities reduce the gap.

Chen et al. used the B3LYP/aug-cc-pVDZ(-PP) level of theory to study AlPb_n and AlPb_n^+ clusters up to $n = 12$.⁵⁸⁹ The Al-encapsulated structures were favored by both neutral and charged clusters for $n = 9\text{--}12$. The enhanced HOMO–LUMO gaps suggest higher stability for AlPb_9^+ , AlPb_{10}^+ , and AlPb_{12}^+ . The higher stability of AlPb_{12}^+ has been attributed to the 50-electron principle with highly symmetric icosahedral structure. A combined experimental–theoretical work has been done to study Pb_{10}^{2-} , Pb_{12}^{2-} , and M@Pb_{10}^{2-} ($\text{M} = \text{Ni, Pd, Pt}$), and the DFT calculations predicted structural data that agree remarkably well with the experimental values.⁵⁹⁰ Wang and co-workers investigated the geometric and magnetic properties of endohedral M@Pb_{12} clusters ($\text{M} = \text{Sc, Ti, V, Cr, Mn, Fe, Co, Ni}$) by means of PW91/DND.⁵⁹¹ The ground-state geometric structures of these clusters were found to be pseudoicosahedrons. It was found that the encapsulated metal atom donates a small amount of charge to the surrounding Pb_{12} shell. It was observed that the magnetic properties of M@Pb_{12} can be adjusted by varying the transition metal atom involved. These clusters have higher HOMO–LUMO gaps that remain unchanged even with a higher electric field supplied.

Recently, Bai et al. calculated the structures, stabilities, and electronic properties of FePb_n ($n = 1\text{--}14$) clusters by means of the PW91/DND level of theory.⁵⁹² In the ground-state structures, the Fe atom resides completely in the Pb cage beginning from $n = 10$. The highest symmetrical icosahedral structure made FePb_{12} the most stable cluster. It was mentioned that Fe doping partially improves the stability of pure lead clusters, because the average binding energies increase while HOMO–LUMO gaps decrease upon doping. The atomic orbital hybridization gave rise to the smaller energy gaps of Fe-doped lead clusters. It was found that the magnetic moments of the doped clusters are mainly on the Fe-atom sites.

4. TRANSITION METAL OXIDES

4.1. Group 3 Oxides

4.1.1. Scandium Oxides. Scandium oxides occur naturally, although they have few commercial uses at present. There are very few investigations reported on scandium oxide clusters, and these studies are relatively recent. Scandium monoxides are briefly discussed in section 2.4.1. Charkin and co-workers⁵⁹³ performed a theoretical study of polyoxide clusters of $\text{Sc}_{20}\text{O}_{30}$, $\text{P}_{20}\text{O}_{50}$, $\text{Ti}_{20}\text{O}_{30}\text{F}_{20}$, and $\text{V}_{20}\text{O}_{30}\text{F}_{20}$. They used the B3LYP/6-31G* level of theory to calculate structural, electronic, and vibrational characteristics and energies of these isolated clusters. For $\text{Sc}_{20}\text{O}_{30}$, a puck-shaped isomer was found to be the lowest energy isomer. They also found a dodecahedron that is predicted to lie 170–200 kcal mol⁻¹ higher in energy than the puck-shaped isomer. Solvation of these clusters with ammonia strongly decreased the energy gap between these isomers, yet the dodecahedron remained the higher energy isomer under all circumstances. The corresponding Ti and V clusters will be discussed in their sections.

In a theoretical study of transition metal oxide clusters that possess an oxygen-centered radical character, Zhao et al.⁵⁹⁴ determined stable structures of Sc_4O_6^+ , Sc_6O_9^+ , Sc_5O_8 , Sc_4O_7^- , and $\text{Sc}_6\text{O}_{10}^-$. They found that Sc_4O_6^+ and Sc_6O_9^+ clusters are cage-like structures with 3-fold and 2-fold coordination on each scandium and oxygen, respectively. The unpaired electron is mainly localized over a single bridging oxygen atom in Sc_4O_6^+

and Sc_6O_9^+ clusters. A terminal radical oxygen is observed in the Sc_4O_7^- and Sc_5O_8 clusters, and a bridging radical oxygen was observed in the $\text{Sc}_6\text{O}_{10}^-$ cluster.

Wu and co-workers⁵⁹⁵ studied C–H bond activation by nanosized scandium oxide clusters both experimentally and theoretically. These scandium oxide clusters were prepared by laser ablation and reacted with *n*-butane in a fast flow reactor. Hydrogen atom abstraction was identified with two series of scandium oxide cluster cations: $(\text{Sc}_2\text{O}_3)_n^+$ ($n = 1\text{--}22$) and $(\text{Sc}_2\text{O}_3)_n\text{O}_4^+$ ($n = 4\text{--}22$). The authors observed from theoretical calculations that the C–H bond activation is facilitated by oxygen centered radicals that are bridge bonded in $(\text{Sc}_2\text{O}_3)_n^+$. These authors also suggested that the observed size-dependent reactivity may be explained on the basis of spin density distribution within clusters.

The study of scandium oxides changed direction when Stevenson et al.⁵⁹⁶ reported encapsulation of a tetrahedral scandium oxide cluster in an endohedral fullerene, $\text{Sc}_4(\mu_3\text{-O})_2@\text{I}_h\text{-C}_{80}$, and they also predicted the presence of a related species $\text{Sc}_4\text{O}_3\text{C}_{80}$ in two different configurations, $\text{Sc}_4(\mu_3\text{-O})_3@\text{I}_h\text{-C}_{80}$ with an addition of an oxygen atom as part of the internal cluster or $\text{Sc}_4(\mu_3\text{-O})_2@\text{I}_h\text{-C}_{80}\text{-O}$ with an epoxide unit on the fullerene exterior. They generated these endohedral fullerenes by introducing air into the arc discharge process. Later, Valencia and co-workers⁵⁹⁷ studied these two clusters theoretically. They employed the BP86 exchange and correlation functional with a triple- ζ polarization basis set. They observed that the formal transfer of six electrons from the cluster to the carbon cage forms these metallofullerenes. Atomic charges were computed according to the Mulliken partition scheme and multipole derived charge analysis. The fullerene encapsulating the Sc_4O_3 in $\text{Sc}_4(\mu_3\text{-O})_3@\text{I}_h\text{-C}_{80}$ cluster is computed to be 115 kcal mol⁻¹ more stable than the $\text{Sc}_4(\mu_3\text{-O})_2@\text{I}_h\text{-C}_{80}\text{-O}$ isomer with an external epoxide. All of the scandium atoms in the $\text{Sc}_4(\mu_3\text{-O})_3@\text{I}_h\text{-C}_{80}$ complex show a 3+ oxidation state, and Sc atoms exhibit a mixed valence state in the $\text{Sc}_4(\mu_3\text{-O})_2@\text{I}_h\text{-C}_{80}$ cluster. Theoretical electrochemical studies for $\text{Sc}_4(\mu_3\text{-O})_2@\text{I}_h\text{-C}_{80}$ suggest that it has a very small electrochemical gap, whereas $\text{Sc}_4(\mu_3\text{-O})_3@\text{I}_h\text{-C}_{80}$ is predicted to have a more conventional behavior with a large electrochemical gap.⁵⁹⁷ Mercado et al.⁵⁹⁸ later experimentally isolated this $\text{Sc}_4(\mu_3\text{-O})_3@\text{I}_h\text{-C}_{80}$ cluster, and bond lengths within the $(\text{Sc}_4(\mu_3\text{-O})_3)^{6+}$ unit were in agreement with the theoretical values computed by Valencia et al.⁵⁹⁷

Later, Popov et al.⁵⁹⁹ investigated the $\text{Sc}_4(\mu_3\text{-O})_2@\text{I}_h\text{-C}_{80}$ system with spectroscopic, voltammetric, electron spin resonance spectroscopy, and extended density functional theory calculations. The $\text{Sc}_4\text{O}_2@\text{C}_{80}$ compound was reported to exhibit two reversible reduction and oxidation steps with a small electrochemical gap of 1.10 V. They used experimental data and extended DFT and MD calculations to determine the isotropic constant $a(^{45}\text{Sc})$ values of two types of Sc in $\text{Sc}_4\text{O}_2@\text{C}_{80}$ cluster. Sc adopting a divalent state in the neutral $\text{Sc}_4\text{O}_2@\text{C}_{80}$ shows a remarkable large coupling constant of 150.4 G in the cationic radical, which is the record high $a(^{45}\text{Sc})$ value for Sc-based endohedral metallofullerenes.

4.1.2. Yttrium Oxides. Yttria or Y_2O_3 is most important as a ceramic material and has a wide range of applications in electronics, optics, and catalysis. Yttrium oxide exists in the cubic phase and has a band gap of 5.8 eV. Among the limited theoretical studies of these yttrium oxides, most of them are small clusters with less than four metal atoms.

The first theoretical study with at least four yttrium atoms was reported in the form of a monoxide. Dai et al.⁶⁰⁰ studied this Y_4O molecule in its neutral, anionic, and cationic stages. They performed DFT calculations with the B3LYP exchange correlation functional and used LANL2DZ as the basis set. Equilibrium geometries of Y_4O , Y_4O^- , and Y_4O^+ are trigonal bipyramids with C_{3v} , C_s , and C_s symmetries, and the ground states of these clusters have triplet, doublet, and doublet multiplicities, respectively.

Yang and Xiong⁶⁰¹ investigated structural, electronic, and magnetic properties of Y_nO ($n = 2–14$). They employed the generalized gradient approximation BPW/DNP level of theory. They observed that the equilibrium site of the oxygen atom gradually progresses from the outer site of the cluster toward the surface and finally to the interior of the structure as the number of Y atoms varies from 2 to 14 in ground-state structures. Starting from $n = 12$, the cluster forms a cage-like structure surrounding the oxygen. Relatively high stability was observed for $n = 2, 4, 8$, and 12 clusters. Calculated magnetic moments of Y_nO clusters were small except for Y_{12}O , and the magnetic moment was quenched when $n = 2, 6$, and 8. Later in 2010, these authors investigated the structural, electronic, and magnetic properties of Y_nO_2 and Y_nO_2^- clusters with $n = 1–8$.⁶⁰² For the theoretical calculations, they employed the B3LYP/LANL2DZ level of theory. They observed similar lowest energy isomers for neutral and anionic clusters except for $n = 2$. The magnetic moments of neutral clusters are larger than those of the corresponding anions for small clusters where $n \leq 3$. For larger clusters, the opposite trend was observed. For Y_4O_2 , Y_6O_2 , and YO_2^- clusters, the total magnetic moments are quenched.

In 2013, Rahane et al.⁶⁰³ reported an investigation of the structural and electronic properties of $(\text{Y}_2\text{O}_3)_n$ clusters with $n = 1–10$. They used the generalized gradient approximation with the PBE exchange correlation functional and the PAW pseudopotential method. Periodic calculations were also performed for bulk yttria with the same exchange and correlation functional. The bulk phase of yttrium oxide shows coordination numbers of 6 and 4 for Y and O, respectively. The lowest energy clusters were also shown to be derived from the bulk structure. The neutral clusters were observed to adopt singlet states, whereas ionic clusters preferred a doublet state. The HOMO–LUMO gap remained nearly the same for all of the cluster sizes they studied. For neutral clusters, this gap varies in the range around 2.04–2.88 eV, and for charged clusters it is 0–0.5 eV.

4.2. Group 4 Oxides

4.2.1. Titanium Oxides. Titanium dioxide (TiO_2) is among the most investigated transition metal oxides both in experiment as well as in theory. The main reason is because of the use of TiO_2 nanoparticles, bulk, and surfaces in a wide range of applications. Titanium oxide is used in heterogeneous catalysis, as a white pigment, as a gas sensor, and in various applications as a wide band gap semiconductor.⁶⁰⁴ Most importantly, TiO_2 has been investigated thoroughly over the past few decades as a photocatalyst that provides hydrogen as a clean and sustainable energy carrier from solar energy.^{605,606} This process was first discovered by Fujishima and Honda in 1972.⁶⁰⁷ The TiO_2 semiconductor has a large band gap of 3–3.2 eV, and it absorbs only the ultraviolet region of the solar emission. It can be tuned for absorption of visible light by doping it with other elements. Applications of TiO_2 have

become more important because it is inexpensive and both chemically and biologically inert. Bulk titanium dioxide exists as three natural phases at room temperature: rutile, anatase, and brookite. In these three phases, six oxygen atoms in a distorted octahedral configuration surround the Ti atoms, and three Ti atoms in trigonal planar configurations surround the O atoms. Rutile is the most common phase. However, if the particle size is small, it can have varied structures that may not resemble the bulk. These small clusters of titanium dioxide are interesting due to their astrophysical implications and quantum size effects on photophysics and substrate–particle interactions. Most of the theoretical studies with titanium dioxides are periodic calculations related to understanding the surface as a catalyst. There have also been many theoretical studies related to small titanium oxide clusters ($\text{TiO}_2)_n$, where $n = 1–3$ with different levels of theory, which are not the scope of this Review. Gong, Zhou, and Andrews⁶⁰⁸ have previously reviewed theoretical and spectroscopic studies of transition metal oxides and dioxygen complexes. These smaller TiO_2 clusters that have been examined up through 2009 have been discussed in that review. In 2010, Sun and co-workers⁶⁰⁹ reviewed theoretical studies of the interactions of water with different phases of TiO_2 .

Recent theoretical evidence of somewhat larger clusters with a total number of titanium atoms ≥ 4 has been reported by Jeong et al.⁶¹⁰ ($\text{TiO}_2)_n$ clusters up to $n = 6$ have been studied with the B3P86/6-31G(d) level of theory. A detailed discussion of equilibrium geometries, energetics, and vibrational analysis emphasizing atomization energies and harmonic vibrational wave numbers, which are crucial input data for the thermodynamic description of gas-phase nucleation processes, has been described. Some of their results were compared to previous ionic pair potential models by Yu and Freas,⁶¹¹ an ab initio HF/STO-4G* study by Hagfeldt et al.,⁶¹² and a small clusters ($n < 4$) study with the LSDA approach by Albaret et al.⁶¹³

It should also be noted that TiO_2 has been studied as a supporting material for VO_x . Mikheeva and co-workers⁶¹⁴ reported that vanadium could be stabilized on the anatase surface (001) both in tetrahedral and in octahedral coordination with the formation of monoxo- and dioxygenadyl structures. They used LDA with the VWN exchange correlation functional. $[\text{Ti}_3\text{O}_{11}\text{H}_9]^{-1}$, $[\text{Ti}_4\text{O}_{12}\text{H}_8]^0$, $[\text{Ti}_4\text{O}_{14}\text{H}_{11}]^{-1}$, and $[\text{Ti}_3\text{O}_{12}\text{H}_{11}]^{-1}$ clusters were used in this study.

Persson et al.⁶¹⁵ used the general bonding principle to predict the structure of defect-free nanocrystals in nanocrystalline materials with semi-ionic bonding. They used structures of titanium dioxide in anatase form. The effect of structural relaxation was investigated for larger clusters of $\text{Ti}_{16}\text{O}_{32}$ with PW86x-PW91c using large core potentials. There were large local relaxations, but the cluster maintained a charge-balanced structure with Ti–O bonds in the range of 1.7–2.3 Å. Densities of states of these clusters were investigated using the B3LYP hybrid method and the LANL2DZ basis set. For some of the larger clusters ($\text{TiO}_2)_n$ with $n = 18, 22, 34$, and 38, structural relaxation and its influence on electronic properties were estimated using a single- ζ (SZ) basis set. They observed a significant shift of absorption thresholds toward shorter wavelengths in relaxed structures.

Hammad et al.⁶¹⁶ reported a study of Ti_nO_{2n} clusters with $n = 1–15$ using different techniques of simulated annealing and Monte Carlo basin hopping simulations together with the genetic algorithm technique with the energy calculated by means of an interatomic potential. The stable structures were

then refined by density functional theory calculations. They observed similar results with DFT and methods based on interatomic potentials. Agreement was especially good for larger particles with $n = 9\text{--}15$ for both structure and energy. DFT calculations were first done with B3LYP with effective core potentials that remove 10 electrons from Ti and 2 electrons from O combined with a DZ basis set. These structures then were reoptimized with a polarized double- ζ basis set (DZVP). Finally, a more accurate basis set of 6-311G** was used to calculate the energy at the DZVP optimized geometries.

Qu and co-workers⁶¹⁷ investigated the electronic structure and stability of the neutral $(\text{TiO}_2)_n$ and charged $(\text{TiO}_2)_n^-$ and $(\text{TiO}_2)_n^+$ clusters ($n = 1\text{--}9$) with the B3LYP/LANL2DZ method. For all of the clusters they studied, global minima were always found in the singlet ground state with the triplet state being about 1.4–2.5 eV less stable. For increasing cluster sizes, compact structures with one or two terminal oxygen atoms have been shown to become energetically favored. In a different study by Qu and co-workers,⁶⁰⁴ larger clusters with $n = 10\text{--}16$ were investigated with the same level of theory with a focus on finding stable defect-free Ti=O structures. They reported the half-spherical $(\text{TiO}_2)_{15}$ cluster as the smallest defect-free rutile nanocrystal, which is slightly higher in energy than the spherical cluster with two defective Ti=O---Ti sites. Interestingly, they reported that even- n clusters tend to form compact structures of more covalent character that are more stable, with larger HOMO–LUMO gaps, vertical excitation energies, and ionization potentials, while odd- n clusters tend to form compact structures of more ionic nature that are less stable. Some of the smallest clusters with odd- n show small vertical excitation energies even smaller than the band gap of bulk TiO_2 . These authors suggest that if the material can be engineered with small odd- n values, they may tend to exhibit visible light photoactivity. It is well-known that the optical excitation band gap of semiconductor materials may change as the function of particle size because of quantum confinement effects. This basically causes a blue-shift (increase) of the band gap as compared to bulk. There has been a debate of such quantum confinement existing for TiO_2 nanoparticles. Previous studies by Qu and co-workers reported that the excitation gaps of the neutral TiO_2 clusters decrease with increasing cluster size. More reliable basis set calculations were used in a recent study⁶¹⁸ with B3LYP/6-31+G(d) to resolve this contradiction. They found vertical excitation gap values of neutral clusters with $n = 1\text{--}10$ showed a clear blue-shift relative to the bulk band gap.

Lundqvist and co-workers⁶¹⁹ studied structural and electronic properties of bare and dye-sensitized TiO_2 clusters and nanoparticles with sizes of ≤ 2 nm. Small clusters of $(\text{TiO}_2)_n$ with $n = 1\text{--}16$ and some larger clusters with $n = 16\text{--}68$ were studied. On every cluster model, two different DFT functional and basis set combinations were used. PW86 and PW91 were used with the Slater-type orbital valence single- ζ basis set and large frozen cores. Several other basis sets with the B3LYP functional were also used to test the properties, and they found that the degree of structural reorganization of bare TiO_2 nanocrystals, including formation of surface Ti=O bonds, is sensitive to the quality of the method used. The electronic structure of these 1–2 nm size nanoparticles has shown well-developed band structures with no electronic band gap defect states. Significant broadening of the band gap is observed due to the quantum size effect when the particle size is reduced

from 2 to 1 nm, but further band gap widening is limited by competing surface defect sites as the particle becomes smaller than ~ 1 nm. They also compared electronic coupling of pyridine anchored to TiO_2 with phosphonic and carboxylic acid anchor groups with published periodic calculations. Cluster calculations predict the same order of magnitude surface electron transfer rates with similar trends with respect to the influence of the anchor groups as the periodic calculations.

Jirkovsky and co-workers⁶²⁰ reported a B3LYP/BPW91-6-31G* study of Ti_yO_z and $\text{Li}_x\text{Ti}_y\text{O}_z$ systems. To interpret the experimental Raman spectra of nanocrystalline Li-Ti-O, optimized geometries of Ti_3O_7 , Ti_4O_8 , Ti_7O_{14} , and $\text{Li}_x\text{Ti}_y\text{O}_z^{2+}$ were used. Calculated geometries were used to predict the DOS diagrams and vibrational spectra with harmonic approximation. They successfully reproduced the main structural characteristics of the Ti_xO_y clusters, but $\text{Li}_x\text{Ti}_y\text{O}_z$ calculated and real structures were less satisfactory due to the smaller cluster size. They observed overestimates of the calculated band gap energies with respect to experimental values for the cubic Li-Ti-O oxides. The calculated values became closer to experimental values with increased cluster size. Raman spectra calculated under the harmonic approximation for the optimized structure reproduced all important features of experimental spectra.

First-principles thermochemistry for the production of TiO_2 from TiCl_4 clusters was reported by West and co-workers.⁶²¹ They calculated enthalpies of formation and thermochemical data for many intermediates in the early stage of the mechanism up to $\text{Ti}_5\text{O}_6\text{C}_{18}$. Three different DFT functionals were used: mPW-PW91, B3LYP, and B97-1 with the 6-311+G(d,p) basis set.

Calatayud, Maldonado, and Minot⁶²² investigated $(\text{TiO}_2)_n$ clusters up to $n = 10$ to analyze their reactivity as a function of electronic structure. Gas-phase acidity was probed by the interaction of H^+ with oxygen sites, and basicity was tested by the interaction of molecular NH_3 with titanium sites. They did not find any general rules for predicting cluster stability. The HOMO–LUMO gaps calculated were significantly dispersed for most of the system. The values calculated seem to oscillate in the range of 3.5–5.0 eV. The main trend is a decrease of HOMO–LUMO gap with $n = 1, 3$, and 10 being exceptions ($n = 1$ and 3 have lower values, whereas $n = 10$ has a higher value). There was no clear trend for acidic and basic reactivity with size. In general, correlation with HOMO and LUMO levels was a good criterion for reactivity, but it was not always observed. Two of these authors investigated the reactivity of TiO_2 compounds using atomic hydrogen adsorption as a probe in a later year.⁶²³ Spin polarized ab initio periodic calculations were performed with the PW91 exchange correlation functional to treat both aggregates and periodic systems. Ultrasoft pseudopotentials were used together with a plane wave basis set. Small clusters of $(\text{TiO}_2)_n$ with $n = 1\text{--}24$ were compared to infinite systems. For $n = 1\text{--}10$ clusters, the B3LYP/6-31+G(2d,p) level of theory was also employed. The binding energy for the most reactive clusters reached 3.5 eV, for the smallest one it was 2.8 eV, and for the most reactive surface (rutile (110)) it was 2.3 eV. Polymers of TiO_2 were made of rings bridged by oxygen atoms. Polymers were reactive due to the absence of a terminal oxygen atom. On the other hand, surfaces also deprived of terminal oxygen atoms are more reactive than the polymers due to the smaller size of their HOMO–LUMO gaps. Clusters remain the most reactive, and they surprisingly tended to have smaller gaps and their LUMOs

were found to have low energies; however, pure GGA functionals are known to underestimate energies for unoccupied orbitals. This electronic factor was not the sole reason for the reactivity; it seems flexibility of the structures matters most. Finally, they concluded that the titanium atoms on these clusters were 4-fold coordinated and that the solvent effect (hydration) may facilitate 6-fold coordination of the Ti atoms, which might modify the stability of the naked clusters.

Li and Dixon⁶²⁴ reported molecular structures and energetics of anions and neutral clusters of $(\text{TiO}_2)_n$, where n goes up to 4 atoms. They studied these systems with coupled cluster theory [CCSD(T)] and DFT. Electron detachment energies of the low-lying conformations of the anions and the first excitation energies of the corresponding neutral clusters were calculated and compared to data from photoelectron spectroscopy. The ground-state structures predicted by DFT with different functionals were the same as the CCSD(T) method except for the dimer and the tetramer. Recently, Chen and Dixon⁶²⁵ developed a hybrid tree growth-hybrid genetic algorithm (TG-HGA) and used it to study the neutral $(\text{TiO}_2)_n$, $n = 2-13$, nanoclusters. Initially, TG algorithm is used to grow clusters stepwise from small seeds to the size of interest. After each step, energies of the structures are evaluated, and the lowest energy structures are fed into the HGA to compute the global minima for each formula of interest. These lowest energy structures from the HGA are then optimized with DFT. It was found that these nanoclusters have the character of a TiO_2 bulk crystal with hexacoordinate Ti. The average clustering energy converged slowly to the bulk value. It was also found that $(\text{TiO}_2)_{12}$ is a quite stable cluster, whereas $(\text{TiO}_2)_{13}$ is much less stable.

The structural and electronic properties of anatase TiO_2 nanocrystals were investigated by Iacomino and co-workers.⁶²⁶ They employed GGA with the PW91 exchange correlation functional and ultrasoft pseudopotentials. The clusters represented in this study consist of 87 atoms with the chemical formula $(\text{TiO}_2)_{29}$. They used two different surface coverages, titanium atoms with OH and H, to identify the dependence of structural properties on the surface. The results for the hydrated nanocrystal showed the largest overlap with the experimental findings.

Zhang and co-workers⁶²⁷ showed that a dimer of the TiO_2 molecule, Ti_2O_4 , is qualified for serving as a basic building block of TiO_2 nanostructures. They studied two thin TiO_2 nanowires, $(\text{TiO}_2)_{12}$ and $(\text{TiO}_2)_{24}$, as prototypes of TiO_2 nanostructures. Theoretical calculations were performed with the PW91 exchange correlation functional with a double numerical basis set including p-polarization functions. They showed that the size and shape of these nanowires affect the structural stabilities and energy gaps. Later, they also proposed that heterofullerenes of titanium dioxides (up to $(\text{TiO}_2)_{60}$) possessing the same frameworks as carbon fullerenes can arise from Ti_2O_4 units.⁶²⁸ By using the previous level of theory together with ab initio molecular dynamics (AIMD) simulations, they showed the structural and thermal stabilities of TiO_2 heterofullerenes.

NO reduction with carbon monoxide catalyzed on reduced Ti_8O_{15} was investigated by Andreev and co-workers.⁶²⁹ They employed density functional theory with B3PW91/6-31G for lighter atoms and B3PW91/LANL2DZ for titanium atoms. Two NO molecules were simulated on two different types of oxygen vacancies. Adsorption resulted in formation of a stable adsorption complex with the bidentate $-\text{ONNO}-$ ligand. They proposed a new mechanism of NO adsorption via these four-

membered ligands on the oxygen vacancies. This proposed mechanism is consistent with experimental studies and does not suggest the generation of the electron–hole pair in the body of the cluster. In a later study by Andreev et al.,⁶³⁰ they used LANL2DZ for the titanium, 6-31G for the oxygen, and 6-31++G** for the hydrogen to study the reduction of the Ti_8O_{16} molecular cluster through interaction between atomic hydrogen and the resulting defect species with oxygen molecule adsorption. Results of the calculations show that atomic hydrogen reacts with each surface oxygen atom of the cluster and forms a stable OH species without a significant activation barrier. This allows formation of the reduced Ti^{3+} oxidation state. Molecular oxygen reacts with these reduced species to form O_2^- and oxidizes the titanium atoms back to the +4 oxidation state. Singly occupied orbitals of Ti 3d type with energies in the band gap of the cluster disappear with the formation of the O_2^- species. Following the study of the Ti_8O_{16} cluster, a very recent study by Andreev et al.⁶³¹ used a much larger cluster of $\text{Ti}_{15}\text{O}_{30}$. It was shown that both of these model systems provide qualitatively very similar results and are in good agreement with experimental studies. As in the previous system, they observed the appearance of reduced Ti^{3+} species with the corresponding band gap localized 3d-Ti states after H adsorption and their disappearance after O_2 adsorption with the formation of O_2^- species. These authors concluded that these cluster calculations provide results comparable with periodic calculations with respect to modeling chemical processes. They also suggested that the clusters with crystal-like structures are the most plausible models to further study both the dark and the photoinduced chemical reactions on the surfaces of TiO_2 subnanoparticles.

Interactions of carbon dioxide with titania nanoparticles with acetate groups were investigated theoretically and experimentally by Sui and co-workers.⁶³² They used two types of model clusters based on $[\text{Ti}_6(\text{C}_2\text{H}_3\text{O}_2)_6(\text{C}_3\text{H}_7\text{O})_6\text{O}_6]$: one replaces the isopropoxyl group with a hydroxyl group, and the other one is a dimer of two of these TiO_2 clusters bridged by Ti–O–Ti bonds. They employed plane-wave-based DFT with the PBE functional in conjunction with the PAW method. For comparison, a conventional basis set method was also used. For that they used the PBE/SD-RECP/DZVP level of theory. They concluded that Lewis acid–Lewis base-type interactions exist between CO_2 and metal acetate groups. They observed five possible binding modes of CO_2 , and among them the most preferential mode is the T-shaped configuration to the acetate ligand.

De Francesco and co-workers⁶³³ used TDDFT calculations to simulate the sulfur K-edge NEXAFS spectra of model systems for the adsorption of SO_2 on the TiO_2 (110) surface. They used the $\text{Ti}_{19}\text{O}_{32}$ cluster as the model TiO_2 system, and geometry optimizations were carried out with VWN with TZP, DZP, and SZ basis sets. The spectra calculated for the adsorbate models are compared to the spectrum of the free SO_2 to discuss the nature of the adsorbate–substrate interactions. The theoretical and experimental spectra were in agreement only at low temperatures.

Shelvin and Woodley⁶³⁴ calculated the geometric, electronic, and optical properties of bare and anion-doped $(\text{TiO}_2)_n$ clusters, where $n = 1-7$, 10, and 13 with the PBE functional. Initial structures were chosen from the evolutionary algorithm. They observed that with increasing particle size, the HOMO–LUMO transition energy saturates toward bulk values. For the C-, N-, and S-substitutional doped clusters, all dopant

formation energies were lower than those calculated for bulk rutile. Carbon and sulfur dopants gave transition energies that are closer to the peak in the solar spectrum. In particular, carbon was suggested as the optimum dopant for maximizing the photoactivity of subnanometer (TiO_2)_n nanoparticles.

Much larger clusters were used in recent years to determine the structures and properties of titanium dioxide. The (TiO_2)₂₆ cluster was used as the model system to study the photo-oxidation of water by Valdés et al.⁶⁰⁵ It was constructed from bulk rutile and exhibits a (110)-like surface. The B3LYP functional and the LANL2DZ ECP basis set were chosen, and the augmented LANL2DZdp was used for a better description of the surface species of the photo-oxidation process. This cluster has a calculated HOMO–LUMO gap of 3.05 eV and water adsorption energy of $-75.7 \text{ kJ mol}^{-1}$, which are in good agreement with the experimental values. With this model they were able to produce results similar to those published previously,⁶³⁵ as compared to the photo-oxidation of water on TiO_2 (110) surface using periodic DFT calculations. They concluded that illumination of the TiO_2 (110) surface with light provides enough overpotential for the photo-oxidation to proceed spontaneously.

Zhanpeisov⁶³⁶ investigated the selective oxidation of carbon monoxide on gold-supported titania. He used two cluster models, $\text{H}_{38}\text{O}_{53}\text{Ti}_{17}$ and $\text{H}_{34}\text{O}_{43}\text{Ti}_{13}$, with the B3LYP/LANL2DZ,6-31G* level of theory. Additional calculations were done with nonmetal doping (C and N) on TiO_2 with an aim to increase its photocatalytic functionality. He has shown that the strongly bound state of Au (+1 formal oxidation number) with these two vacancy-containing cluster models of titania (110) surface can be used to explain the selective oxidation of CO. Binding of O₂ with the vacancy site is energetically more favorable than adsorption on an Au site. Carbon doped at an interstitial position in the deep bulk is energetically more favorable while N replaces the protruded oxygen atom and forms a surface N–H bond.

The structural, electronic, and adsorption properties of single-walled TiO_2 anatase nanotubes were explored by Nunzi and De Angelis.⁶³⁷ They used (TiO_2)₇₂ and (TiO_2)₁₂₀ nanotube models. All of the geometry optimizations were carried out with VWN augmented with the BP86 exchange correlation functional combined with a double- ζ basis set. These nanotube models were formally obtained by rolling TiO_2 anatase monolayer around [101] and [010] directions, giving rise to (n,0) and (0,m) TiO_2 nanotubes. They observed that (n,0) tubes are lower in energy than the (0,m) tubes. The authors then investigated the adsorption of formic acid on the TiO_2 nanotube sidewalls and planar surfaces. They observed that the bidentate configuration is more stable for planar surfaces, while the monodentate configuration is more stable for curvature in TiO_2 nanotubes.

The hydrolysis reaction of titanium dioxides (TiO_2)_n with $n = 1\text{--}4$ was studied by Wang and co-workers.⁶⁰⁶ All of the geometry optimizations were carried out with the BP86/DZVP level of theory. The singlet and triplet energy gap was calculated to lie between 30–65 kcal mol⁻¹. The first H₂O adsorption energies for these titanium clusters range around -10 to $-35 \text{ kcal mol}^{-1}$ for the singlet state and -10 to $-50 \text{ kcal mol}^{-1}$ for the triplet state. They reported that both the singlet and the triplet states of the TiO_2 nanoclusters readily react with H₂O yielding reaction barriers of 5–16 kcal mol⁻¹ for the singlet state and 5–26 kcal mol⁻¹ for the triplet state for the first hydrolysis step. Overall, these results show that H₂O

can be readily split on TiO_2 clusters to form OH groups. These hydrolysis reactions are highly exothermic with fairly small barrier heights. Visible photon energy is not required for the hydrolysis step. However, water splitting to form H₂ and O₂ is an endothermic reaction by $\sim 116 \text{ kcal mol}^{-1}$. Approximately two 500 nm photons are needed to overcome this endothermic water splitting reaction. They concluded that if TiO_2 is first photoexcited to an excited state and then the hydrolysis follows, the photon energy required for the overall water splitting process can be expected to be much less than 116 kcal mol⁻¹, assuming this excited state should have a lower hydrolysis reaction energy as compared to the ground-state singlet.

De Angelis and co-workers⁶³⁸ reported a study of the absorption spectrum and the excited-state energy levels of the N719 Ru(II) sensitizer (N719 is a dye that is derived from N3 [(*cis*-(dithiocyanato)-Ru-bis(2,2'-bipyridine-4,4'-dicarboxylate)] by bonding of tetrabutylammonium (TBA) at two of the carboxyl sites of the N3 dye) adsorbed on a extended TiO_2 cluster. The authors considered a (TiO_2)₈₂ cluster model and employed the PBE exchange correlation functional together with a plane wave basis set and ultrasoft pseudopotentials. TDDFT calculations were performed with the B3LYP/3-21G* level of theory at DFT optimized geometries. The calculated spectrum was in good agreement with the experimental spectra over the explored energy range, with an absorption maximum deviation below 0.1 eV. The authors predicted an instantaneous electron injection mechanism on the basis of strong coupling and the matching of the visible absorption spectrum and density of TiO_2 unoccupied states. This corresponds to excitation from the dye ground state to an excited state largely delocalized within the semiconductor. Interestingly, this was found to give rise to the exactly same absorption profile as for the dye in solution. Sousa et al.⁶³⁹ recently reviewed these kinds of excited-state-related phenomena in oxide surfaces with great detail about various theoretical approaches and their limitations for such investigations.

Electronic and spectral properties and the size and shape dependency of small (TiO_2)_n ($n = 1, 2, 8, 18, 28, 38$) clusters were investigated by Auvinen and co-workers.⁶⁴⁰ They employed the projector augmented wave method with the PBE exchange and correlation functional. The photoabsorption spectra were calculated with TDDFT. The authors indicated evidence of structure-dependent band gap broadening about 0.1–0.74 eV in the case of three of the smallest particles. The other particles have a band gap smaller than that of the bulk anatase phase. The authors concluded that the spectral blue shifts and electronic structure in ultrasmall particles are strongly dependent on the shape and the structure of the cluster, whereas in symmetrical clusters absorption characteristics do not seem to depend on the studied size range of the clusters.

Syzgantseva and co-workers⁶⁴¹ studied H₂ adsorption on small-sized titania clusters for (TiO_2)_n with $n = 1\text{--}10$. The hybrid B3LYP functional was employed with all electron 6-31+G* basis sets for O and H, and the titanium atom was represented by the LANL2DZ pseudopotential with 12 valence electrons explicitly treated. Initial hydrogen atoms easily bind only to terminal oxygen sites. These adsorption energies are larger than 20 kcal mol⁻¹ for all hydrogenated clusters with two terminal hydroxyl groups. Adsorption energies for the second hydrogen atom were found to be poorly exothermic except on clusters of size $n = 1, 4$, and 8. The general trend is the decrease of the absolute energy with the increase of size of the cluster. This pattern was also observed for cluster sizes of $n = 1\text{--}6$ for

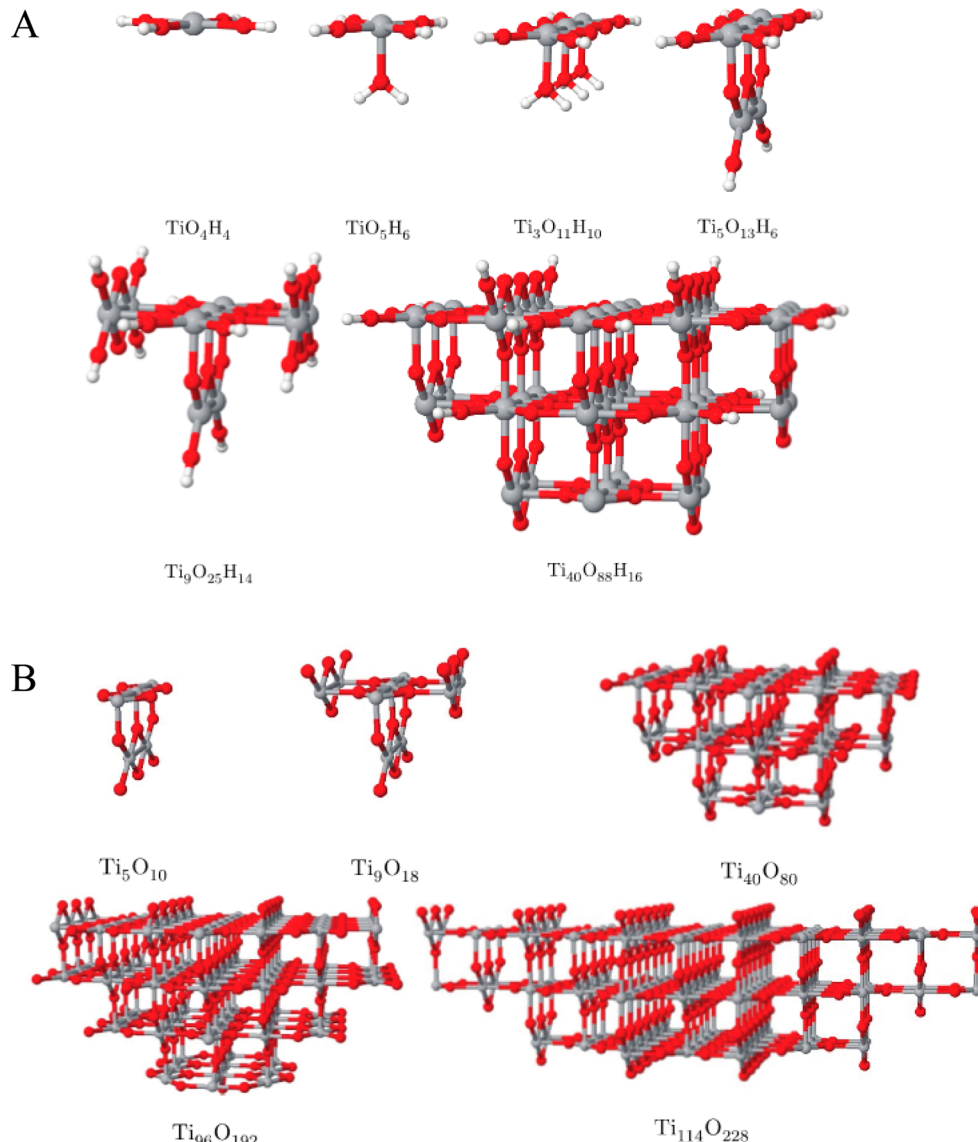


Figure 13. Geometric structures of (A) six hydrogen saturated clusters TiO_4H_4 , TiO_5H_6 , $\text{Ti}_3\text{O}_{11}\text{H}_{10}$, $\text{Ti}_5\text{O}_{13}\text{H}_6$, $\text{Ti}_9\text{O}_{25}\text{H}_{14}$, and $\text{Ti}_{40}\text{O}_{88}\text{H}_{16}$; and (B) five electrostatically embedded clusters Ti_5O_{10} , Ti_9O_{18} , $\text{Ti}_{40}\text{O}_{80}$, $\text{Ti}_{96}\text{O}_{192}$, and $\text{Ti}_{114}\text{O}_{228}$ (color code: gray, Ti; red, O; and white, H). Reprinted with permission from ref 642. Copyright 2012 AIP Publishing LLC.

the H_2 dissociation mechanism studied. They also observed that their hydrogenated cluster calculations lead to a triplet state in most cases.

Stadt and Hättig⁶⁴² used embedded cluster density functional and MP2 theory to study N_2 adsorption on the rutile (110) surface. Both hydrogen saturated clusters (TiO_4H_4 , TiO_5H_6 , $\text{Ti}_3\text{O}_{11}\text{H}_{10}$, $\text{Ti}_5\text{O}_{13}\text{H}_6$, $\text{Ti}_9\text{O}_{25}\text{H}_{14}$, and $\text{Ti}_{40}\text{O}_{88}\text{H}_{16}$) and electrostatically embedded clusters (Ti_5O_{10} , Ti_9O_{18} , $\text{Ti}_{40}\text{O}_{80}$, $\text{Ti}_{96}\text{O}_{192}$, and $\text{Ti}_{114}\text{O}_{228}$) were used as models (Figure 13). Of all the methods investigated such as HF, PBE, B3LYP, and MP2, only MP2 and B3LYP were able to correctly describe the adsorption of N_2 . After including the zero point energy correction, they were able to get adsorption energies closer to experimental values. Multiple basis sets were also used (SVP, TZVP, TZVPP, QZVP), and they reported that the basis set dependence is small as compared to the geometric relaxation of the surface.

The energetically favorable structures and characteristic IR and Raman peaks of Ti_nO_m ($n = 2-4$, $m \leq 2n$) clusters were

studied using the B3LYP/6-311G(d) method by Du et al.⁶⁴³ The Ti_nO_m ($n = 2-4$, $m < 2n$) clusters show strong IR peaks in the range of 600–1100 cm^{-1} and strong Raman peaks in the region of 300–800 cm^{-1} . Both the IR and the Raman spectrum peaks of the Ti_nO_m ($n = 2-4$, $m = 2n$) clusters are in the region of 700–1100 cm^{-1} . The main Raman peak of the Ti_nO_m ($m \neq 2n$) is at a frequency considerably lower than that of the IR spectrum. Similarly, as mentioned earlier in this Review, the presence of a larger number of unsaturated bonds of a cluster structure makes its reactivity significantly stronger than its bulk counterpart.

Iwaszuk and co-workers⁶⁴⁴ scrutinized the properties of nanoclusters of $(\text{TiO}_2)_n$ ($n = 5, 6, 8, 16, 30$) deposited on the TiO_2 (110) rutile surface. For the calculations, they used DFT and DFT+U corrected for onsite Coulomb interactions. The PW91 exchange correlation functional was used with PAW potentials. These novel heterostructures have been shown to function as visible light active photocatalysts. It was found that these clusters adsorb strongly on the rutile surface and are

thermodynamically stable toward aggregation to larger clusters or films. As compared to the unmodified surface, they observed a reduction in band gap in these heterostructures.

Lee and Aikens⁶⁴⁵ investigated Mn doping of $(\text{TiO}_2)_n$ ($n = 2-5$) complexes with the BP86/ATZP level of theory. They observed that Mn doping does not significantly alter the structure from its parent structure. However, some important changes occur with bond lengths and angles. Mn–O bonds are usually reported to be shorter in these complexes and the Ti–O bonds lengthen slightly. The angle centered on Mn was reported to increase significantly. The most stable structures have low-coordinated manganese atoms. It was also found that the HOMO–LUMO gap decreases significantly upon doping, and this decrease is not proportional to the number of doped Mn atoms.

In a recent paper, Oprea et al.⁶⁴⁶ studied a $\text{Ti}_{24}\text{O}_{50}\text{H}_4$ cluster with DFT for a metal-free dye, 5-(4-sulfophenylazo) salicylic acid disodium salt, known as Moderate Yellow 10 (MY-10), which is used as a sensitizer for TiO_2 dye-sensitized solar cells (DSSCs). The anatase form titanium cluster with the adsorbed dye was optimized with the B3LYP/3-21G(d) level of theory, and the dye itself with its singly and doubly deprotonated forms were optimized with the 6-31G(d) basis set. In agreement with other experimental reports, they found that the carboxyl groups tend to bind in a bidentate fashion. The salicylate uses both carboxyl and hydroxyl groups for either a tridentate binding to adjacent Ti^{4+} ions or a bidentate Ti–O binding together with an O–H–O binding. The sulfonic group prefers a tridentate binding. On the basis of their calculations, they concluded that DSSC performance decreases in the order of hydroxyl > carboxyl > sulfonate.

Recently in 2014, Berardo and co-workers⁶⁴⁷ investigated the suitability of TDDFT to describe vertical low-energy excitations in naked and hydrated titanium dioxide nanoparticles. Model clusters of $(\text{TiO}_2)_n$ up to $n = 13$ were used in this study. Geometry optimizations were carried out with the B3LYP/def2-TZVP level of theory. Clusters of $n = 9$ and 11–13 were obtained from recent structures of Chen and Dixon.⁶²⁵ The authors reported that B3LYP and CAM-B3LYP methods gave quantitative fits to excitation energies predicted by the more accurate and expensive EOM-CC method. Some significant subsets of structures gave qualitatively different results depending upon the exchange correlation potential used. These sets only yielded consistent results with EOM-CC theory when CAM-B3LYP and BHLYP levels of theory were used. The authors demonstrated that such discrepancies are due to the charge-transfer excitations, which are poorly described by functionals that do not use HF exchange.

4.2.2. Zirconium Oxides. Zirconia (ZrO_2) shows many desirable structural and electronic properties and has been used in many applications.^{648,649} It is an exceptionally stable transition metal oxide over a wide temperature range and is known to show strong resistance to poisoning. These properties make it good as both a catalyst and a catalyst support material. Bulk phase zirconia is used as an effective catalytic material for oxidation of CO and CH_4 and epoxidation of propylene.⁶⁴⁹ Zirconia is also used as a support material with copper and shows catalytic properties toward NO_x reduction by CO, CO_2 hydrogenation, water gas shift, and combustion.⁶⁴⁸

Isobe et al.⁶⁵⁰ reported an early study of a $(\text{M}\text{Zr}_{12}\text{O}_8)^{36+}$ ($\text{M} = \text{Zr}$, 3d transition metals, and alkali metals) cluster. They employed the LSDA approach to investigate the additive element effects on the electronic conductivity of oxide film

formed on Zr alloys. When alkali metals were added, the impurity levels that were formed increased the electronic conductivity, whereas with transition metals the conductivity was lowered due to widening of the energy gap.

In 2004, Foschini et al.⁶⁵¹ demonstrated an experimental and theoretical study of zirconia. They used the ab initio Hartree–Fock cluster method with a Huzinaga basis set to calculate the electronic structures of perfect monoclinic, tetragonal, and cubic geometries with a Zr_4O_8 model structure and an oxygen-vacancy $\text{Zr}_4\text{O}_7^{2+}$ model cluster. Theoretical calculations reproduced qualitative values for geometrical parameters (Zr–O bond lengths) taken from experiment. The energy gaps of zirconia polymorphic phases were also well reproduced in this study. The cubic structure of the oxygen-vacancy zirconia model was more stable than the corresponding monoclinic and tetragonal ones. They suggested that oxygen vacancies act as local stabilizing agents that generate the crystalline field and thus decrease the volume of these phases. This causes destabilization in the monoclinic phase resulting in the formation of cubic or tetragonal phases.

Formation of ring-like Si–O–Zr bonds at intergranular interfaces in silica-doped zirconia has been investigated by Chen and co-workers.⁶⁵² Cluster models with up to eight zirconium atoms were used with the B3LYP/LANL2DZ,6-31G(d) level of theory. These new clusters were validated by the reaction Gibbs free energies and calculated IR spectra. Analysis of the Mulliken charges demonstrated the reduced charge of oxygen atoms located at the interface and coordinated with the neighboring zirconium atoms. This accords well with the view⁶⁵³ that the reduction of the negative charge of oxygen atoms coordinated with Zr atoms increased the stability of tetragonal phase zirconia and caused the increase of the temperature and critical size for the tetragonal to monoclinic phase transformation.

Walther and co-workers⁶⁵⁴ reported an experimental and theoretical study of ligand dynamics of zirconium oxo clusters. They studied two clusters: $\text{Zr}_4\text{O}_2(\text{OMc})_{12}$ (OMc = methacrylate) and $\text{Zr}_6(\text{OH})_4\text{O}_4(\text{OOCR})_{12}$ (R = methacrylate, *endo* or *exo* 5-norbornene-2-carboxylate, formate). $\text{Zr}_4\text{O}_2(\text{OMc})_{12}$ was investigated with one- and two-dimensional NMR spectra both in solid state and in solution. An AIMD simulation was carried out for the $\text{Zr}_6(\text{OH})_4\text{O}_4(\text{OOCR})_{12}$ cluster. The authors employed LDA and GGA methods in their theoretical calculations. They observed rearrangement of three chelating ligands into bridging positions and conversion of a C_3 -symmetric cluster into an O_h -symmetric cluster. They also observed a dip in the energy barrier along the reaction coordinate that originated from changes in hydrogen bonds between the moving ligand and the neighboring OH groups.

Gas-phase cluster reactivity experiments done by Johnson et al.⁶⁴⁹ observed that a distinct series of zirconium oxide clusters $(\text{ZrO}_2)_n^+$ where $n = 1-4$ are active toward transferring an oxygen atom to CO, C_2H_4 , and C_2H_2 . They employed DFT with the hybrid B3LYP exchange correlation functional in combination with TZVP and the Stuttgart group 12 electron relativistic effective core potential (12e-RECP). Enhanced reactivity of these clusters was attributed to a radical oxygen center with an elongated zirconium–oxygen bond. The authors propose incorporation of zirconium oxides into cluster-assembled materials as a good candidate for improving industrially important CO, C_2H_4 , and C_2H_2 oxidation reactions. They further studied these radical oxygen centers with elongated Zr–O bonds in a paper published in early 2009⁶⁵⁵

using the same level of theory. A series of anionic clusters with radical oxygen centers having elongated Zr–O bonds were shown to oxidize CO, strongly associated C₂H₂, and weakly associated C₂H₄. The oxidation of C₂H₂ and C₂H₄ requires an energetically unfavorable hydrogen transfer step. This is in contrast with the previous study for cationic clusters, where all of the clusters oxidized these species. These authors also proposed that catalytic activity can be obtained by doping with a metal containing fewer electrons (Y,Sc) or with a metal containing one additional valence electron (Nb,V). An overview of these zirconium oxide radical centers toward oxidation of CO, C₂H₄, and C₂H₂ together with oxidation of carbon monoxide by gold clusters was given in a later paper published by Johnson et al.⁶⁵⁶

Herrera et al.⁶⁴⁸ investigated the impact of Cu atoms on the reactivity of (ZrO₂)_{*n*} (*n* = 1–5) and Cu/ZrO₂ clusters with the B3LYP/6-31G** level of theory along with LANL2DZ pseudopotentials on metallic centers. They reported that IP and EA are strongly dependent on the number of building blocks involved, and reactivity reaches a reasonably constant value at *n* = 5. The band gap obtained for an infinite number of units was in good agreement with the experimental bulk values and suggests that zirconia is not able to transfer electrons. The addition of a Cu atom decreases the band gap and increases the charge transferability. It was also found that charge transfer comes from Cu to zirconia. Copper creates dual active sites, where it acts as an electron donor and Zr atom next to Cu acts as an electron acceptor.

Molecular structures and energetics of the (ZrO₂)_{*n*} and (HfO₂)_{*n*} (*n* = 1–4) clusters have been explored by Li and Dixon.⁶⁵⁷ Optimized geometries and vibrational frequencies were calculated with the B3LYP and BP86 exchange correlation functionals. They used aug-cc-pVXZ for O and aug-cc-pVXX-PP for Zr and Hf. Monomers and dimers were also calculated with the CCSD(T) level of theory. Similar to titania, these clusters also have a number of low-lying isomeric structures. They observed a strong dependence of electron affinities with cluster sizes. Anion photoelectron spectra were calculated for the monomer and dimer and demonstrated the possibility of structure identification.

Stable and low energy structures for (ZrO₂)_{*n*} clusters where *n* = 1–12 have been predicted by Woodley, Hamad, and Catlow.⁶⁵⁸ They employed a data mining technique with an evolutionary algorithm to three different energy landscapes as defined by interatomic potentials to generate plausible structures for refinement using DFT at the PBEsol level of theory. The predicted global minimum and next local minima are in agreement with the previous structures found by Li et al.⁶⁵⁷ for smaller clusters, *n* = 1–4. These authors also mentioned similarities with previous titania and silica clusters, and they presented energies of local minima and their respective HOMO–LUMO gaps as a function of *n*.

Nößler et al.⁶⁵⁹ presented a theoretical study of Zr_{*n*–1}ScO_{2*n*} (*n* = 4–7) based on the hybrid B3LYP functional. They used the TZVP basis set combined with the Stuttgart group relativistic effective core potential for Zr and Sc. The scandium atom in the zirconium oxide clusters plays the role of mimicking the removal of one electron and represents the pure cationic stoichiometric clusters. It was found that these clusters with radical oxygen centers promote oxidation reactions of CO and C₂H₂.

Boulet et al.⁶⁶⁰ investigated the adsorption of CO₂ onto clusters of zirconia using various cluster models up to

Zr₅O₂₄H₂₈. The calculations were performed with the meta-GGA TPSS exchange correlation functional in combination with the TZVP basis set. They also used Grimme's empirical dispersion model to describe the weak interaction occurring between the surface and the adsorbates. They reported that adsorption onto two adjacent zirconium atoms leads to either dissociation or the adsorption of the molecule depending on the initial geometry of the structure. The energy released by either of these processes was found to be very high. A single unsaturated zirconium adsorbed CO₂ in an apical manner with an intermediate adsorption energy. Because they did not observe spontaneous formation of CO₃[–] species, they proposed that the formation of this adsorbate is an activated process.

Recently, Cerón et al.⁶⁶¹ studied the influence of monoclinic and tetragonal zirconia phases on the water gas shift reaction. They employed the MP2/6-31G level of theory with the LANL2DZ pseudopotential for the Zr atoms. They found that the most preferred surface is the tetragonal phase. In the tetragonal phase, adsorption is not facilitated but desorption is favored. The authors concluded that low charge-transfer values in the tetragonal phase generate less stable intermediates that later allow an easy desorption process. Stable intermediates were found in the monoclinic system, preventing the release of H₂ and CO₂.

Lousada and co-workers⁶⁶² explored the reactivity of Zr, Ti, and Y oxide clusters with hydrogen peroxide and water using different exchange and correlation functionals including B3LYP, B3LYP-D, B3LYP*, M06, M06-L, PBE0, PBE, and PWPW91. They employed a variety of small cluster models including clusters of Zr as large as (ZrO₂)₂₆. The LACVP*+ basis set was used, which is a combination of the 6-31+G(d) split valence basis set and the Los Alamos effective core potential for the Zr, Ti, and Y transition metals. Two types of interactions responsible for H₂O₂ adsorption onto the metal surface were examined: direct interaction between the O atoms of H₂O₂ and the exposed metal atoms and hydrogen bonding between surface OH groups and H₂O₂. With these cluster models, the best performance was observed with the M06 and PBE0 functionals. For the (ZrO₂)₈ monoclinic cluster, the M06 functional reproduced results in good agreement with experiment for the different oxides. PBE0 was found to be the most effective in terms of performance and computational cost.

4.3. Group 5 Oxides

4.3.1. Vanadium Oxides. Vanadium oxides have been studied over the past few decades as a catalyst for dehydrogenation of hydrocarbons and other organic compounds, mild oxidation, ammonoxidation, selective oxidation of hydrocarbons, removal of NO_x, and selective reduction.⁶⁶³ In addition to these applications, in recent years they have been researched as bolometric detectors, cathode materials in lithium batteries, and as ferromagnetic nanotubes.⁶⁶⁴ The early stages of vanadium oxide cluster studies were centered on locating the structurally different surface oxygen sites, which aid in understanding the selective reaction mechanisms of vanadia. There were a couple of arguments: some reports indicate terminal vanadyl oxygen (V=O) is removed from the surface to form a lattice vacancy, while other reports indicate that bridging oxygen (V–O–V or V–O–Me) may favor this more than the surface species.⁶⁶³ There were reports indicating that a mixture of these two may lead to the formation of vacancies. Increasing theoretical and experimental evidence suggested that after hydrogen adsorp-

tion, bridging oxygen could be removed more easily than the vanadyl oxygens.⁶⁶³

In 1997, Michalak, Witko, and Hermann⁶⁶⁵ used LSDA based on the VWN functional to study clusters as large as $V_{10}O_{31}H_{12}$ and $V_{16}O_{49}H_{18}$ to get information about the catalytic surface. Detailed analyses of the electronic structure were performed with Mulliken populations and Mayer bond order indices. They reported the ionic character of the catalyst by atomic populations and described the covalent nature with bond order results. They observed that the terminal vanadyl surface oxygen ($V=O$) has the least ionic character, $O^{-0.3}$, from the population analysis. One type of bridging surface oxygen becomes $O^{-0.6}$ and binds with two vanadium atoms by single bonds ($V-O-V$), and the other type of bridging oxygen becomes more negative, with $O^{-0.7}$, and forms four center bonds with three vanadium atoms. They showed increased local reactivity of bridging oxygen atoms with respect to electrophilic attack. Two years later, Hermann and co-workers⁶⁶³ studied the V_2O_5 (010) surface by embedded clusters where they employed clusters as large as $V_{20}O_{62}H_{24}$ representing one or two layers of the vanadia. LSDA based on the VWN functional as well as GGA-II functionals⁶⁶⁶ were used for this investigation. The results of local binding, charging, and density of states were used to help characterize the detailed electronic structure of the surface. Moreover, they also removed oxygen from specific surface sites of the catalyst and compared the energies, charging, and geometric relaxation and found that there is a pronounced variation between these different sites. Cluster calculations of hydrogen adsorption to these different surface oxygen sites forming OH and H_2O were also performed. These calculations suggest that oxygen removal from the surface occurs by the formation of H_2O , which is bound weakly enough to desorb, creating oxygen vacancies. Witko, Hermann, and Tokarz⁶⁶⁷ later studied cluster sizes up to $V_{38}O_{116}H_{42}$. Clusters of $V_2O_9H_8$, $V_{10}O_{31}H_{12}$, and $V_{16}O_{49}H_{18}$ were compared to DFT and semiempirical ZINDO-type methods. Both of these methods yield qualitatively similar results. The resulting outcome of hydrogen adsorption can be used as the first step to model the selective oxidation of hydrocarbons. The H/H^+ species always adsorbs at the V_2O_5 surface and forms stable surface hydroxyl groups. Generation of these surface hydroxyls leads to significant weakening of respective $V-O$ bonds. This weakening is strongest for $V-O-V$ bonds, where oxygen is bridging to two bare vanadium atoms. These oxygen sites were found to become mobile in the presence of H/H^+ adparticles, which suggests the fast oxygenation of hydrocarbons. Later, Hermann et al.^{668,669} studied $V_{10}O_{31}H_{12}$ and $V_{20}O_{62}H_{24}$ systems with LSDA and RPBE functionals. Similar to previous results, they concluded that the presence of hydrogen at the oxide surface facilitates oxygen removal and contributes to the generated oxygenated products near vanadia-based surfaces. Haras et al.⁶⁷⁰ later used different cluster sizes to model the vanadium dioxide (011) surface. This surface exhibits both unsaturated metallic and oxygen centers. Cationic and anionic species will react similarly because of this distribution. This resulted in low sensitivity to any surface reaction; thus, it is not interesting as a catalyst, which has been confirmed by experimental observations.⁶⁷¹ A study of oxygen stabilization at the surface of V_2O_3 (0001) has been reported by Czekaj, Hermann, and Witko et al.⁶⁷² They used large cluster models like $V_{11}O_{33}H_{33}$, $V_{11}O_{36}H_{33}$, $V_{14}O_{33}H_{24}$, $V_{14}O_{37}H_{26}$, and $V_{14}O_{41}H_{28}$ with the LSDA based on VWN as well as GGA with the RPBE approach and described in detail the geometric

and electronic properties of two intrinsic bulk terminations after the surface has adsorbed oxygen. Haber and Witko⁶⁷³ revisited the electronic theory of the V_2O_5 and V_2O_5/TiO_2 systems. The authors stated that interfacial electron transfer requires matching energy and symmetry of frontier orbitals; thus the energy levels of the reacting molecule must correspond to the region of high density of states of the solid. This can be achieved either by activation of the adsorbing molecule or through generation of defects, as well as introduction of dopants or deposition of the active phase on a support to form oxide-monolayer-type catalysts. Examples of the interaction of methane and V_2O_5 ($V_{10}O_{31}H_{12}$) with various defects have been discussed using previously used DFT methods. The authors reported that cleavage of the C–H bond in primary carbon atoms proceeds by transfer of two electrons to the empty V surface and formation of adsorbed alkoxy and surface hydroxyl species.

To understand the energetics of creation and annihilation of surface oxygen vacancies, Tokarz-Sobieraj, Witko, and Grybos⁶⁷⁴ used vanadia and molybdena cluster calculations. Catalytic activity of different surface species that contain oxygen was examined in this model with the RPBE functional and a polarized double- ζ basis set. Larger clusters of $Mo_{15}O_{55}H_{22}$ and $V_{10}O_{30}H_{12}$ were obtained by removing oxygen from structurally different positions of respective surfaces. It was found that prior hydrogen adsorption decreases the energy required for vacancy creation. Local point defects have been shown to exhibit a stronger nucleophilic character than respective surface oxygen. They also reported that surface vacancies may become reoxidized via gaseous oxygen or oxygen diffusion from the bulk. Adsorption of O_2 is an exothermic process and leads to molecular, weakly bonded, and active oxygen species. They also noted the aggregation of vacancies because of the electrostatic interactions. Kolczewski, Hermann, and co-workers⁶⁷⁵ used a $V_{21}O_{61}$ large cluster with RPBE/DZVP to determine polarization-dependent NEXAFS spectra to determine vanadyl termination of the V_2O_3 (0001) surface. They were able to theoretically support the experimentally suggested vanadyl surface termination. Cavalleri, Hermann, and co-workers⁶⁷⁶ investigated cluster models of silica-supported vanadia simulating monomer and different nonmonomeric species in pyramidal and umbrella configurations. They studied Si and V combined clusters as large as $V_2Si_{12}O_{23}H_{12}$. Ground and excited electronic states were calculated with the RPBE/DZVP/IGLO-III level of theory. The comparison of theoretical and experimental NEXAFS spectra provides clear evidence of nonmonomeric V_mO_n existing at the catalyst surface under in situ conditions. Hejduk, Witko, and Hermann⁶⁷⁷ used $V_{14}O_{45}H_{20}$, $V_{14}O_{44}H_{18}$, and $V_{21}O_{65}H_{25}$ clusters to represent the V_2O_5 (001) surface and $V_{12}O_{40}H_{20}$, $V_{14}O_{46}H_{22}$, and $V_{16}O_{52}H_{24}$ for the (100) surface with the RPBE functional to study the electronic structure of these surfaces. It was found that the charge on the oxygen centers scales with their coordination. The least negative charge was on the terminal oxygen atoms, whereas the doubly coordinated oxygen sites had charges that were twice as large. This shows that these oxygen sites are more nucleophilic than terminal vanadyl sites. The vanadium atom on these surfaces carries a positive charge, and these sites are important in determining the reactivity of these surfaces.

Vyboishchikov and Sauer⁶⁷⁸ reported a study of vanadium oxide anions, VO_n^- ($n = 1-4$), $V_2O_n^-$ ($n = 4, 6$, and 7), $V_3O_8^-$, $V_4O_{10}^-$, and $V_4O_{11}^-$ with a triple- ζ valence polarization basis set adopted with the B3LYP and BP86 functionals. Both

functionals yielded the same structures for these vanadium oxide systems. The authors were the first to characterize the structures and detachment energies of these smaller clusters. Two important trends in electron detachment energies were reported. First, energies increase strongly with an increasing metal oxidation state. Second, the electron detachment energies increase with a higher delocalization of the unpaired electron of the anion. Electron detachment energies of peroxy complexes are not higher than those of analogous complexes without an O₂ ligand. When the oxygen to vanadium ratio increases in the clusters, reaction energies have been shown to decrease. Later, these authors⁶⁷⁹ reported a gas-phase study of much larger clusters (V₂O₅)_n, where n = 1–12. The BP86 functional with DZVP and TZVP basis sets was used in cluster calculations. Gas-phase clusters were found to have very different geometries from the layered structure of the bulk. The crystal structure of the solid bulk has 6-fold coordination for vanadium, whereas gas-phase structures tend to form 4-fold coordination with one terminal V=O and three V–O bonds. Cluster structures that correspond to fragments cut out of the crystal structure were reported to be very high in energy.

Asmis, Sauer, and co-workers⁶⁸⁰ studied polyhedral cage cluster anion structures of (V₂O₅)_n[−] (n = 2,3,4). These clusters have been studied spectroscopically for the first time by infrared multiple photon dissociation (IRMPD) spectroscopy. They used measured IRMPD data to choose the best functional and reported that B3LYP has the right admixture of Hartree–Fock exchange to reproduce the size-dependent change from delocalized to localized d electron states in vanadium oxide cages. Later, Feyel, Sauer, and co-workers⁶⁸¹ studied the thermal activation of methane by [V₄O₁₀]⁺ species. They used the B3LYP/TZVP level of theory to propose a reaction pathway for the methane activation. The vanadium species was found to be highly reactive due to a radical cation nature.

The geometrical and electronic structures of V_mO_n⁺ and V_mO_n (m = 2–4, n = 2–10) clusters were investigated with the UHF/6-31G* and B3LYP/6-31G* level of theories by Calatayud et al.⁶⁸² They were able to obtain similar geometric structures and parameters for some of the structures previously studied by Vyboishchikov and Sauer.⁶⁷⁸

Najbar et al.⁶⁸³ studied competition between NO reduction and NO decomposition over the reduced V–W–O catalyst. Cluster models of V₁₀O₃₁H₂ (with V–V bonds) and V₉WO₃₁H₁₂ (with V–W bonds) were used to model vanadia and WO₃–V₂O₅. The B3LYP/LANL2DZ level of theory was used for the vanadium cluster calculations. It was found that NO tends to adsorb by W sites and electrons will be back-donated to these adsorbed molecules. This results in structural reorganization of the adsorbed NO species that is then followed by decomposition to form N₂. They concluded that formation of the tungsten nitrosyl complex is the reason for the high selectivity of NO decomposition to dinitrogen with the presence of ammonia.

Anstrom and co-workers⁶⁸⁴ used a V₄O₁₆H₁₂ cluster to study the mechanism of the selective catalytic reduction of NO with ammonia. Unlike the previous study by Najbar et al., this system does not contain W sites. B3LYP with the LACVP** basis set for V and 6-31G** for H, N, O was used in these cluster calculations. Direct interaction of NO with the surface of vanadia was found to be considerably weak. Nitric oxide was seen to react with adsorbed NH₄ species to form NH₃NHO and then further react to form NH₂NO. These intermediate species will be supported by hydrogen bonding with vanadium

moieties. NH₂NO then isomerizes and decomposes to form N₂, H₂O, and reduced vanadium oxide through a series of steps where hydrogen is transferred back and forth in a “push and pull” manner.

Justes et al.⁶⁸⁵ reported experimental and theoretical evidence for the selectivity of V_mO_n⁺ clusters in reaction with ethylene. Cluster sizes of up to V₄O₁₀⁺ were treated with the B3LYP/TZVP level of theory. The oxygen transfer reaction pathway was determined to be the most favorable for V₂O₅⁺ and V₄O₁₀⁺ species. This happened through a radical-cation mechanism, whereas reactions on V₂O₄⁺ and V₂O₆⁺ proceed through an association and replacement type reaction pathway. Formation of acetaldehyde and formaldehyde products is in agreement with experimental studies, and the authors concluded that the gas-phase vanadium oxide cluster and small hydrocarbon calculations are suitable for identification of reactive centers responsible for selectivity in heterogeneous catalysis.

Matsuda and Bernstein⁶⁸⁶ reported an experimental and theoretical study of small neutral vanadium oxide clusters. DFT calculations were performed at the BPW91/TZVP and BPW91/LANL2DZ/D95 levels of theory, and neutral clusters up to V₄O₉ were reported. Stable neutral clusters under saturated oxygen growth conditions are found to be of the form (VO₂)_x(V₂O₅)_y. They used these theoretical calculations to explain the fragmentation of these clusters by multiphoton ionization process. Later, Jakubikova and Bernstein⁶⁸⁷ investigated small vanadium oxide clusters. Structures of VO_n (n = 1–5), V₂O_n (n = 2–7), V₃O_n (n = 4–9), and V₄O_n (n = 7–12) have been computed with BPW91/LANL2DZ level of theory. Oxygen–oxygen bonds were seen in oxygen-rich clusters. Small clusters showed cyclic and cage-like geometries. Clusters with an odd number of vanadium atoms tend to have low spin ground states, while clusters with even number of vanadium atoms tend to have a variety of spin multiplicities for their ground state. VO₂, V₂O₅, V₃O₇, and V₄O₁₀ are the most stable clusters under the oxygen-saturated conditions.

De Francesco and Fronzoni et al.⁶⁸⁸ employed TDDFT calculations on a cluster model of V₂O₅ to compute core excitation spectra. The cluster models selected for this study were V₁₀O₃₁H₁₂, V₂₀O₆₂H₂₄, and V₃₀O₉₃H₃₆. They employed the LB94 exchange correlation potential in the Kohn–Sham equations and employed ALDA for the TDDFT calculations. A detailed analysis of the NEXAFS spectral features was performed with the help of partial density of the virtual states calculated for each hole considered. The comparison of the TDDFT spectra with the experimental one was successful except for the V L-edge, which was attributed to the lack of spin–orbit effects in the computational model. Recently, Fronzoni, De Francesco, and Stener⁶⁸⁹ investigated the L_{2,3} edge photoabsorption spectra of bulk V₂O₅. They employed the previous TDDFT method and used the V₁₀O₃₁H₁₂ cluster model. The analysis of the transitions showed that the spectral features can be described with the crystal field splitting of virtual molecular orbitals with mainly V 3d character as well as configuration mixing and spin–orbital coupling. The calculated spectrum was in good agreement with the experimental one.

The structural, electronic, and vibrational characteristics and the energies of the isolated polyoxide clusters B₂₀O₃₀, Al₂₀O₃₀, V₂₀O₅₀, Si₂₀O₃₀H₂₀, and Si₂₀O₃₀F₂₀ and their complexes with H[−] and NH₃ have been calculated by Charkin et al.⁶⁹⁰ They employed the B3LYP exchange correlation functional with different basis sets. It was shown that the I_h symmetric *clos*

structure with oxygen bridges located above the centers of the faces of an empty dodecahedron is more favorable for V and Si clusters, whereas for B the caged *closo* isomer is more favorable in energy. For Al, a set of puck shaped isomers was observed. The dodecahedral I_h structure for Al is 90 kcal mol⁻¹ higher in energy than puck shaped structures.

Ma et al.⁶⁹¹ reported an experimental and theoretical study of methane activation by $V_4O_{10}^{•+}$ and $V_3PO_{10}^{•+}$. DFT calculations show that the structures of $V_3PO_{10}^{•+}$, $V_4O_{10}^{•+}$, and $P_4O_{10}^{•+}$ are topologically similar and behave similarly toward methane activation. An oxygen centered radical was found to be the key species that plays the major role in methane activation. It was also found that O^{\bullet} radical can transfer within high symmetry clusters like $V_4O_{10}^{•+}$ and $P_4O_{10}^{•+}$ but is thermodynamically forbidden to transfer in $V_3PO_{10}^{•+}$. The methane molecule also helps to enhance the rate of intracluster spin density transfer. This intracluster spin density transfer was used as a tool to explain the experimentally observed reactivity difference in these clusters. These researchers later reported an experimental and theoretical study of reactions of vanadium oxide cluster cations with water.⁶⁹² The reaction mechanism of the $V_4O_{10}^{•+}$ cluster with H_2O was studied with the B3LYP/TZVP level of theory. They concluded with both experimental and theoretical results that H_2O is dissociatively adsorbed rather than molecularly adsorbed, and the terminal oxygen centered radical in $V_4O_{10}^{•+}$ may abstract hydrogen. Li et al.⁶⁹³ used an experimental and theoretical study of V–Ag bimetallic clusters ($V_xAg_yO_z^{•+}$; $x = 1–4$, $y = 1–4$, $z = 3–11$) to investigate the reaction mechanism with C_2H_6 . Hybrid B3LYP with the SDD basis set for silver and the TZVP basis set for other atoms was used. It was found that more silver atoms in the cluster may decrease the reactivity and that the V–Ag cluster can be well tuned for selectivity by changing the number of Ag atoms. This selectivity is remarkably enhanced as compared to that of homonuclear vanadium oxide clusters. This is due to the fact that terminal oxygen atoms are sterically protected by peripherally and bridge-bonded Ag atoms.

Ard, Dibble, Akin, and Duncan⁶⁹⁴ studied ligand-coated vanadium oxide clusters experimentally. Acetonitrile (ACN) and tetrahydrofuran (THF) were used as ligands. In parallel they performed BP86/TZVP and B3LYP/TZVP calculations to study some of these ligated structures including $V_4O_9(ACN)_2$, $V_5O_{12}(ACN)_3$, and $V_4O_7(THF)_2$. It was found that these clusters are minimally perturbed by the addition of ligands.

Saldias and co-workers⁶⁹⁵ investigated two hybrid manganese(II) vanadates experimentally and theoretically. These compounds have $C_{24}H_{16}MnN_4O_6V_2$ (compound 1) and $C_{23}H_{16}MnN_4O_{11}V_4$ (compound 2) empirical formulas. They performed theoretical calculations with the PBE exchange correlation functional using a polarized double- ζ numerical basis set. Compound 1 is a chain consisting of VO_3 units decorated with $[Mn(\text{phen})_2]^{2+}$ (phen = 1,10-phenanthroline) subunits, and compound 2 is a ladder-like structure consisting of two helical chains connected by the heterobinuclear $[\text{Mn}(\text{bipy})\text{VO}_4]$ (bipy = 2,2'-bipyridine) moieties, generating a double helical structure. Both structures show antiferromagnetic interactions mediated between the manganese(II) centers through oxovanadate bridge. DFT calculations also predicted the antiferromagnetic nature as observed experimentally.

4.3.2. Niobium Oxides. Niobium is most often used in alloys in its metallic form, but has found some use in its oxide form in electroceramics. Wang and co-workers⁶⁹⁶ reported a study of niobium monoxide Nb_nO clusters with $n = 3–10$

niobium atoms in 2013. They employed GGA with the Saunders “kick” method. The kick method runs at the B3LYP/3-21G level of theory for 500 iterations. They then rank the top 10–30 isomers according to their relative energies. Finally, these isomers are again optimized using a triple- ζ 6-311+G(2d) basis set for O and with the SDD basis set for Nb. They observed special stability for Nb_7O and Nb_9O clusters, while Nb_5O and Nb_8O clusters were weakly stable. On the basis of a natural population analysis, they concluded that an O atom attracts around 0.8 electrons of charge from its neighboring Nb atoms, and the additional charge occupies the 2p valence orbitals of the O atom. These authors observed that the magnetic moments of the clusters are mostly aided by the 4d orbitals of Nb, whereas contributions to the magnetic moments from O were very small.

4.4. Group 6 Oxides

4.4.1. Chromium Oxides. Chromium oxides occur naturally and have been used as anticorrosion agents. Compere et al.⁶⁹⁷ used ab initio calculations to investigate Cr_2O units as an initial model of chromium oxide clusters interacting with ions and molecules present in natural seawater. They used ROHF, MP2, B3LYP, and CASSCF level of theories to investigate Cr_2O_3 , Cr_4O_6 , and Cr_6O_9 clusters. The goal of this study was to understand the formation of conditioning film on stainless steel immersed in natural seawater. Most of the interactions with small molecules and ions were calculated for the Cr_2O_3 dimer, but in limited cases they used the Cr_4O_6 tetramer as well. They reported that alcohol groups, carboxyl groups, and magnesium cations are primarily important in formation of the conditioning film.

Wang and co-workers⁶⁹⁸ reported an experimental study of Cr_nO_m clusters $n = 3–50$, $m = 0,1,2$. These clusters were produced by a laser vaporization cluster source and later investigated by laser photoionization spectroscopy and photo-fragmentation spectroscopy together with mass spectrometry. Stability steps for Cr_nO_m clusters ($n = 3–50$, $m = 1,2$) correspond to icosahedral geometrical shell closings, which were insensitive to the oxygen content. Magic numbers were also found for $Cr_nO_m^{•+}$ clusters ($n = 3–50$, $m = 0,1,2$).

Bergeron et al.⁶⁹⁹ studied stable cluster motifs for nanoscale chromium oxide clusters. This joint experimental and theoretical study shows that two different classes of very stable and chemically inert Cr_nO_m clusters are possible: Cr_nO_{2n+2} and Cr_nO_{3n} . Each series has its own unique magnetic and electronic properties. Cr_nO_{2n+2} clusters were found to be ferromagnetic, whereas Cr_nO_{3n} are nonmagnetic. These clusters were also found to have higher electron affinities and thus can act as efficient electron scavengers. Both of these clusters do not have O–O bonds or Cr–Cr bonds. Because the energy to remove oxygen from Cr_nO_{3n} clusters is smaller, the authors suggested that these clusters can act as catalysts for CO oxidation.

Li and Dixon⁷⁰⁰ investigated structure and properties of the group 6 metal oxides $(MO_3)_n$ ($M=Cr$, Mo, W) where $n = 1–6$. They used different levels of theories within LDA and GGA. Equilibrium geometries and vibrational frequencies were obtained at local and nonlocal DFT levels. Energetics were calculated mainly with B88P86 and B3LYP functionals. Two types of conformations were observed: the ring and the chain, with the ring being more stable. Their calculations predict weak binding for $(CrO_3)_n$ ($n = 4–6$). For M_6O_{18} , two additional structures were reported: the cage and the inverted cage. The cage structure was the most stable for W, slightly higher in

energy than the ring for Mo, and the least stable for Cr. The normalized clustering energies (average binding energies per MO_3 unit) for the ring structures increase with the cluster size and appeared to be converging for only Cr, whereas differential clustering energies (binding energy per last unit) of the ring structures decrease as the size of the cluster increases and appeared to be converging for Mo and W. Overall, their calculation results show that these clusters can act as strong Lewis acids so they can easily accept a lone pair in catalytic processes, which is especially important because it is the first step in oxidative dehydrogenation of alcohols. Later, Zhai et al.⁷⁰¹ investigated the electronic and structural properties of $(\text{CrO}_3)_n^-$ and $(\text{CrO}_3)_n$ ($n = 1-5$) clusters with photoelectron spectroscopy and DFT calculations. They used the PW91 exchange correlation functional with the aug-cc-pVDZ basis set for O and the aug-cc-pVDZ-PP with corresponding ECP for Cr. In addition, energies were also calculated with the CCSD level. Similar to their previous report, they observed unique nonplanar cyclic rings for $(\text{CrO}_3)_n$ and $(\text{CrO}_3)_n^-$ ($n \geq 3$). The extra electron on $(\text{CrO}_3)_n^-$ in $n \geq 2$ is delocalized over all Cr centers. Li and co-workers⁷⁰² later presented a DFT and CCSD(T) study of group 6 metal hydroxides with up to 4 metal atoms. Two isomers were located that are similar to metal oxides: for $\text{M}_n\text{O}_{3n-1}(\text{OH})_2$ ($n = 2-4$), the chain isomer is more stable than the ring except for W for $n = 3, 4$. Bridging OH groups were found in some low energy isomers with the $\text{M}_2\text{O}_{6-m}(\text{OH})_{2m}$ ($m = 2, 3$) formula. The metal hydroxides were predicted to be strong Brønsted acids and weak to modest Brønsted bases and Lewis acids. The pK_a values were predicted to be as negative as -31 . The potential energy surface for the hydrolysis of M_nO_{3n} ($n = 1-4$) ($\text{M} = \text{Cr}, \text{Mo}, \text{W}$) clusters was calculated. The first hydrolysis step was exothermic; it became less negative as n increases and converged at $n = 3$. Further hydrolysis was an endothermic process especially for Cr. They benchmarked 55 exchange and correlation functionals as compared to CCSD(T) results, and no single functional worked for all processes and all three metals.

Recently, these authors investigated the structural and electronic properties of reduced M_4O_{10} and $\text{M}_4\text{O}_{10}^-$ ($\text{M} = \text{Cr}$ and W) metal clusters from photoelectron spectroscopy and quantum calculations.⁷⁰³ Geometries were optimized with the B3LYP and BP86 exchange correlation functionals, and aug-cc-pVDZ was used as the basis set. Additionally they performed CCSD(T) single point energy calculations for the DFT optimized geometries. The authors observed two different configurations for the Cr and W neutral and anionic clusters. Cr_4O_{10} and its anion have a tetrahedral configuration for metal centers, whereas W_4O_{10} and its anion have a butterfly shape with two metal centers. The authors predicted that the $\text{W}_4\text{O}_{10}^{2-}$ dianion is more stable than the $\text{W}_4\text{O}_{10}^-$ monoanion. For Cr at the BP86 level of theory, vertical detachment energies are in good agreement with the experimental values, but at the B3LYP and CCSD(T) levels, these values significantly deviated. For the W clusters, all three methods were in good agreement with the experimental values.

4.4.2. Molybdenum Oxides. Most of the molybdenum oxides have been studied as polyoxometalates. These can be found in the polyoxometalate section (section 4.11). Additional papers that are directly related to molybdenum oxides are discussed in this section.

Tokarz-Sobieraj, Hermann, and Witko et al.⁷⁰⁴ studied MoO_3 (010) surface with an ab initio density functional theory cluster model and ultraviolet photoemission experiments. They used

an embedded cluster model for a large $\text{Mo}_{15}\text{O}_{56}\text{H}_{22}$ cluster with the RPBE exchange correlation functional. In addition, different surface oxygen vacancies of the clusters were also studied. They reported mixed ionic and covalent nature of the oxide. Calculated vacancy energy values were rather large at 6.8–7.6 eV. This shows that oxygen is strongly bound to the substrate. Vacancy formation led to reduction of the neighboring Mo centers. This was observed with the increased metal d electron occupation and corresponding DOS contribution above the oxygen 2sp region. Tokarz-Sobieraj, Witko, and Grybos⁶⁷⁴ later investigated these oxygen vacancies in detail with molybdena and vanadia clusters. This has been explained in the previous vanadium oxide section.

As discussed in the chromium oxide section (section 4.4.1), Li and Dixon⁷⁰⁰ explored group 6 metal oxide clusters in detail, particularly $(\text{MO}_3)_n$ with $n = 1-6$. Later, they investigated the molecular structures and acid–base properties of metal hydroxides of group 6.⁷⁰² This investigation has been previously described in the chromium oxide section.

Wei and co-workers⁷⁰⁵ recently reported a theoretical design of organoimido-substituted hexamolybdates with different electron donors for dye-sensitized solar cells. On the basis of $[\text{Mo}_6\text{O}_{18}(\text{MBTH})]^{2-}$ (MBTH = *N*-methylbenzothiazole hydrazine), they designed six dyes by changing the electron donors with TT (thienothiophene) or EDOT (3,4-ethylenedioxythiophene) units. Geometry optimizations were carried out with the BP86 exchange correlation functional with a triple- ζ polarized basis set. The electronic structures, absorption spectra, and electron transition characteristics of designed systems were described with DFT and TDDFT calculations. It is found that incorporating a biTT unit can enhance the absorption in the visible region of the solar spectrum. This dye seems to show promising properties for a high performance solar cell material as it contains higher short circuit current density and higher light harvesting efficiency.

Very recently, Zhao and co-workers⁷⁰⁶ investigated a Mo–V–O type mixed metal oxide (MMO) cluster. They used PBE/PBE0 functionals combined with Stuttgart–Dresden effective core potential for V and Mo and 6-31G** for other atoms. These clusters have up to 4 molybdenum atoms and 2 vanadium atoms. With PBE0, reaction energies of the hydrogenation process over MMO system depend on the oxidation state of the V center and the number of layers in the cluster model. For this Mo–V–O system, it is suggested to include at least two layers.

4.4.3. Tungsten Oxides. Sun, Jena, and co-workers⁷⁰⁷ showed that even dimers of tungsten oxides $(\text{WO}_3)_2$ exhibit bulk-like features and that the clusters of small tungsten oxides up to four tungsten atoms bear the hallmarks of crystalline tungsten oxides. These $(\text{WO}_3)_n$ ($n = 1-4$) were optimized with the BPW91 exchange correlation functional using Stuttgart relativistic effective core potentials for W atoms and 6-311G* for other atoms. Among the neutral clusters studied, W_3O_9 is the most stable one, and W_2O_6^- is more stable than W_2O_9^- and $\text{W}_4\text{O}_{12}^-$. All of the bond lengths and angles of the W_4O_{12} cluster are nearly the same as in the bulk. The band gap of this cluster also agrees well with that of bulk.

Li and co-workers^{700,702,703} reported electronic structure and properties of group 6 metal oxides and hydroxides. These sections are discussed in the chromium oxide section (4.4.1).

David Jeba Singh and co-workers⁷⁰⁸ reported a study of closed cage tungsten oxide clusters. They observed several of these clusters when studying W–Se and W–S mixtures with

laser desorption ionization mass spectrometry. Three of these clusters, $\text{W}_6\text{O}_{19}^-$, $\text{W}_{13}\text{O}_{29}^-$, and $\text{W}_{14}\text{O}_{32}^-$, stand out from the peaks, which demonstrates the higher stability of these clusters. The geometries were optimized with the B3LYP/LANL2DZ level of theory. Calculated atomization energies are consistent with the experimental results revealing that these W_6 , W_{13} , and W_{14} structures are quite stable. The authors suggest these unique magic numbered clusters may be of importance, especially for their catalytic properties.

4.5. Group 7 Oxides

4.5.1. Manganese Oxides. Manganese oxides have gained a wide popularity with the structural discovery of the oxygen evolving complex (OEC) in photosystem II (PSII). The OEC is composed of CaMn_4O_5 , where the manganese, calcium, and oxygen atoms are arranged in a cubane shape. There have been many theoretical and experimental studies related to understanding the structural configurations and reaction mechanism of this complex because the oxygen evolution complex catalyzes the water oxidation process. Most of these studies employ QM/MM techniques. Over the past decade, there have been many crystal structures of the OEC resolved at different resolutions (sometimes these are known from the cities of origin): 3.8,⁷⁰⁹ 3.7 ("Hyogo"),⁷¹⁰ 3.5 ("London"),⁷¹¹ 3.0 ("Berlin"),⁷¹² and 2.9 ("Berlin") Å.⁷¹³ Recently, many aspects changed with the 1.9 Å resolution structure solved by Umena and Kawakami et al.⁷¹⁴ On the basis of the cubane structure, there have been many experimental and theoretical studies related to μ -oxo and hydroxo complexes synthesized or computed as model water splitting catalysts. Most of these systems are ligated mononuclear systems, dimers, or trimers. We should note that this current section on manganese oxides does not cover the entire history of OEC structure and mechanism evolution. We encourage readers interested in wider aspects of the experimental and theoretical background on manganese oxides and other complexes for water splitting to read the review and perspective articles written by McEvoy and Brudvig et al.,^{715,716} Mullins and Pecoraro,⁷¹⁷ Sproviero et al.,^{718–720} Yamazaki et al.,⁷²¹ Siegbahn,⁷²² Kusunoki,⁷²³ Williamson,⁷²⁴ Liu and Wang,⁷²⁵ Najafpour et al.,⁷²⁶ Vinyard et al.,⁷²⁷ Pokhrel and Brudvig,⁷²⁸ Hirahara et al.,⁷²⁹ and an early review by Rüttinger et al.,⁷³⁰ among others. In this section, we will include studies that match our criteria of this Review and some studies representing important aspects of this oxygen-evolving complex. In this section, we first describe early studies of manganese oxides, and then later we describe systems that are related to water splitting.

4.5.1.1. Manganese Oxide Clusters. Early work on manganese oxides clusters dates back to 1992, when Ziemann and Castleman⁷³¹ measured the mass spectra of $(\text{MnO})_n$ clusters for $n \leq 12$ and observed $n = 3, 6, 9$, and 12 to be unusually stable. They suggested that $(\text{MnO})_3$ is a hexagon and the other subsequent clusters are made from stacking $(\text{MnO})_3$ on top of each other. Later, Nayak and Jena⁷³² investigated these $(\text{MnO})_n$ clusters where $n \leq 9$ with density functional theory. The atomic functions forming the molecular orbitals are taken as double numerical basis with added polarization functions with BPW91 used as the exchange and correlation function. They concluded that these clusters are ferromagnetic and carry atomic-like magnetic moments ranging from 4 to 5 μ_{B} per MnO unit. They particularly noted that $(\text{MnO})_8$ has a nearly degenerate ferromagnetic and atypical antiferromagnetic solution with a ferromagnetic structure carrying a moment of

40 μ_{B} . These clusters also compete with the cubic and hexagonal forms for stability. MnO_2 and MnO_3 were found to be unusually stable, and thus the authors suggested that these clusters form the foundation for the growth of manganese oxides. They then reported a study of equilibrium geometries, binding energies, electronic structures, and magnetic properties of small MnO clusters with the same sizes as their earlier study.⁷³³ In their new calculations, they employed BPW91 with the 6-311G* basis set for manganese. Results obtained were similar to their previous report. They did not find any evidence to prove that the HOMO–LUMO gaps depend on the cluster size. There was no specific pattern to this band gap, and the authors suggested that this was due to the existence of multiple oxidation states of Mn. The charge transfer between manganese and oxygen as well as the average Mn–O bond distance were ascertained to be insensitive to the cluster size.

Han et al.⁷³⁴ demonstrated a relation between the cluster size and the magnetic configuration of $(\text{MnO})_n$ ($n = 6, 8, 9, 10, 12$, and 15) clusters. These calculations were carried out with LSDA by employing a linear combination of localized pseudoatomic orbitals method. GGA was also used to compare with the results of LSDA. Various spin configurations were tested mimicking different bulk phase orderings. The bulk-like [111] antiferromagnetic ordering was found to be energetically favored, while the other fully ordered ferromagnetic clusters were suggested not to exist. Because of the reduction of the coordination number and the bond length contractions, they showed that the spin configurations of nanoclusters can be different from that of the bulk. They observed that when the coordination number N decreases from 5 to 3, the width of the Mn 3d band became smaller, whereas the magnetic moment was enhanced.

The effect of molybdenum substitution on the electronic structure of manganese dioxides has been calculated by Kim et al.⁷³⁵ They employed the DV-Xα molecular orbital method. The cluster model of $\text{Mn}_{15}\text{O}_{56}^{52-}$ was used, and the Mo atom was substituted for the manganese atom located in the center site of this model. They observed a decrease in the HOMO–LUMO energy gap after this substitution. The bonds of both substituted and pure cluster models were composed of both ionic and partially covalent bonding character.

In 2013, Kanan and Carter⁷³⁶ reported a study of electron and hole transport in pure and doped MnO and $\text{MnO}: \text{ZnO}$ alloy. For pure manganese, they used clusters up to $[\text{Mn}_6\text{O}_{22}]^{31-}$, and for pure Zn up to $[\text{Zn}_{10}\text{O}_{28}]^{37-}$, with different combinations used for alloys. UHF calculations of the electrostatically embedded clusters were used to compute and compare relative electron/hole transfer barriers. The clusters used by the authors were calculated with ab initio wave function methods with an environment modeled as a finite array of point charges. The presence of Zn in the $\text{MnO}: \text{ZnO}$ alloy does not affect the hole transport pathway or barrier. $\text{MnO}: \text{ZnO}$ exhibits higher conductivity because of its smaller band gap. They reported that Ga, Sc, Ti, F, and Sb dopants create deep traps. Al, Y, Gd, and Li can be considered as dopants that increase the carrier concentration and are recommended for increasing the conductivity of the $\text{MnO}: \text{ZnO}$ and its effectiveness in solar energy conversion. Aluminum may only be doped in lower concentrations due to the mismatch of the ionic radii.

4.5.1.2. Oxygen Evolving Complex (OEC) and Related Systems. Other than the cubane shape geometries, a couple of other structures found experimentally have been shown to act as good water splitting catalysts; among them, linear,

adamantane, square, basket, butterfly, and dimer of dimers structures are popular geometries that consist of four manganese atoms.⁷¹⁷ Wu and co-workers⁷³⁷ explored a partial model of the photosynthetic water oxidation site, $Mn_4O_4L^1_6$ ($L^1 = Ph_2PO_2^-$) with a butterfly core, which was previously shown to undergo photodissociation and generate O_2 , phosphinate ion, and the core cation $Mn_4O_2L^{1+}_5$. They examined three cores, $Mn_4O_4^{7+}$, $Mn_4O_4^{6+}$, and $Mn_4O_3(OH)^{6+}$, with the BPW91/TZP,DZP level of theory. They suggested that the photodissociation yield increases upon reducing the core oxidation state by hydrogenation of a corner oxo, increasing the electron donation from the phosphinate ligand, and reducing the net charge from +1 to 0. On the basis of the observations of these systems, these authors also reported a similar path for water oxidation by PSII, where coupling of two bridging oxides releases O_2 . Kuznetsov et al.⁷³⁸ demonstrated that after the oxygen release from coupling of two bridged oxygens, the Mn centers of the core are reduced by one electron each. It should be noted that after the discovery of these butterfly complexes, similar cubane-like or butterfly clusters have been proposed by Christou and co-workers.^{739–741} These complexes do not accurately define the real OEC complex as they lack the role of Ca^{2+} , and phosphinate ligands are not likely to act as the ligands surrounding the real cubane complex. These butterfly complexes have not been yet been shown to act as efficient catalysts.

When the 3.5 Å resolution structure was published in 2004, Messinger⁷⁴² modified his early concepts of OEC structure and mechanism. He proposed two reaction mechanisms based on the dangling-Mn structure and favored the second pathway, which accounted for most of the experimental data observed at the time. In his first pathway, he suggested water oxidation involving nucleophilic attack of a Ca bound substrate water onto a $Mn(V)=O$ species in the S_4 state. The most favored second pathway follows through a ligand-centered oxidation in the S_2 to S_3 transition. Pantazis et al.⁷⁴³ reported 12 structural models for the S_2 state of OEC in terms of their magnetic properties. Out of these, 10 models include “fused twist” core geometries obtained from polarized EXAFS measurements⁷⁴⁴ and two models proposed by Siegbahn.^{745,746} They employed the BP86/TZVP level of theory for all of the geometry optimizations and calculated the hyperfine coupling constants with TPSSh, which has been identified as superior to hybrid or GGA functionals for magnetic spectroscopic properties of transition metal complexes. The authors suggested that the “fused twist” models need to be expanded to include other comparative “dangler” and “cubane” shape models. Ames, Pantazis, and Messinger et al.⁷⁴⁷ studied the new 1.9 Å structure with the BP86/def2-SVP,def2-TZVP level of theory. Their results suggested that one water molecule out of two proposed to coordinate the outer Mn of the cluster is deprotonated in the S_2 state. Deprotonation of the Ca^{2+} bound water molecule is strongly disfavored in the S_2 state. They have also found that upon geometry optimization in the S_2 state, the core relaxes to a less connected one than that suggested in crystallographic model. DFT calculations were performed by Cox and Messinger et al.⁷⁴⁸ to assess the effect of Ca^{2+}/Sr^{2+} substitution on all electronic structure models of the OEC to that point (London, Berlin, EXAFS cores, and Siegbahn). With experimental and theoretical studies combined, they reported that Sr substitution in the OEC does not significantly alter the Mn–Mn distances and the exchange coupling pathways of the Mn_4O_x complex. Recently in 2013,

Cox and Messinger⁷⁴⁹ published a review article summarizing all experimental findings regarding the substrate water binding to the Mn_4CaO_5 cluster. They strongly disfavored the nucleophilic attack mechanism between a Ca bound water and a terminal oxo on Mn, which was suggested by Brudvig and Batista. They emphasized that the O–O bond formation occurs between a hydroxo bound to Mn and the μ_3 -oxo bridge between Ca and two Mn ions in the cube.

Lundberg and Siegbahn⁷⁵⁰ reported a mechanism for the early version of the Mn_3CaMn cubane-like structure (based on 3.5 Å) for water splitting. Geometries were optimized with B3LYP/lacv3p* level of theory. They extensively investigated the position of the heavy atoms, oxidation states of manganese centers, and protonation states of the ligands and proposed transitions of $S_0-S_1-S_2-S_3-S_4$. At the time, oxidation to a higher-valent manganese–oxo species was not found to be energetically favorable without structural rearrangements to the cubane geometry. In 2006, Siegbahn proposed that an oxyl radical in the center of the OEC forms the O–O bond with a bridging oxo group.⁷⁵¹ He employed B3LYP with the lacv3p** basis set for geometries and cc-pVTZ(-f) for energies. This mechanism has been a popular mechanism so far even after the new high-resolution X-ray structure. Using this O–O bond formation mechanism as a starting point, he proposed structures and energies for all of the S states.^{745,752} The resting state of the OEC was obtained from the transition state of O–O bond formation by adding electrons and protons (later known as the Siegbahn model). Again in 2009, Siegbahn investigated the mechanism of water oxidation in PSII by using hybrid DFT calculations.⁷⁴⁶ Similar to previous studies, he used B3LYP with the lacvp* basis set for geometries and cc-pVTZ(-f) for energies. The best oxygen evolution mechanism was found to start with a reaction between oxygen radical and a μ -oxo ligand, as explained previously. The oxygen radical was found to be on a different manganese center. Previously, the proposed S_2 to S_3 transition was energetically favored by binding the water molecule to manganese in the Mn_3Ca cube instead of the outer manganese. The author also proposed a model for substrate water binding. Shortly thereafter, a communication paper by the same author reported the calculated total energies of different structural models of the OEC and proposed that total energy is a useful property for discriminating different structures and ruled out some models based on that criterion.⁷⁵³ The only model left was the one he proposed before using the cluster model (Siegbahn Model).^{746,752} Computational work in the decade before the 1.9 Å resolution crystal structure of the OEC of PSII was published was reviewed by Siegbahn in the middle of 2011.⁷²² Different structure models, proposed reaction mechanisms, and methods studied are summarized in this short review and will not be further reviewed here. Later in the same year, Siegbahn reviewed the procedure for fixing amino acid residues in cluster model calculations on enzymes.⁷⁵⁴ For this he used a model from the 1.9 Å resolution crystal structure of PSII and Mo, Cu-dependent CO dehydrogenase. The mechanism from this new high-resolution X-ray structure was also investigated and compared to the old theoretically suggested structure and mechanism. The author concluded that the mechanism remains the same with a similar barrier height, and only small structural changes were observed with respect to the position of an amino acid (Asp170) as compared to his previous model. He also reported that the different positions of Asp170 have only very small effects on the mechanism. With the new high-resolution

structure, more detailed studies were carried out to know more about the water oxidation process. Early in 2012, Siegbahn reported two final S-transitions of water oxidation.⁷⁵⁵ He reported that electron coupled proton transfers occur from the center of the OEC to Asp61. This is considered to be the start of the proton transfer chain through the protein to the luminal side. The new experimental structure is very similar to the one suggested five years ago; thus, it was suggested that O–O formation follows through same pathway. Energy diagrams of the full sequence of proton and electron release steps in the water oxidation of PSII were obtained and reported for the first time at the end of 2012 by Siegbahn.⁷⁵⁶ He used the same previous level of theory for his calculations. The author concluded that Mn centers are oxidized in the order of Mn3, Mn4, and Mn1, and that Mn2 is always Mn(IV). The oxygen on Mn1 is oxidized when the transition from S₃ to S₄ occurs. It was found that His337 has to be protonated to obtain a reasonable energy for the O₂ release step. Particularly, he found that a larger driving force is needed for the last two S-transitions than the first two. Support for his structures and reaction pathway was provided by EPR data, ENDOR data, and W-band ¹⁷O-ELDOR detected NMR spectroscopy. By the end of 2013, Siegbahn and Blomberg⁷⁵⁷ used theoretically and experimentally well-established energy diagrams for the water oxidation in PSII to benchmark several different density functionals. On the basis of benchmark tests, they concluded that only the B3LYP functional with 15% or 20% exchange is in good agreement with experiment. The other functionals tried show larger errors for some energy levels as large as 20–30 kcal mol⁻¹. The suggested reason for this is that the error for three consecutive oxidations of Mn(III) to Mn(IV) accumulates as the cluster is oxidized.

In 2006, Sproviero et al.⁷⁵⁸ developed structural models of OEC of PSII based on the 3.5 Å resolution crystal structure and a QM/MM method (UHF B3LYP/lacvp, 6-31G(2df), 6-31G:AMBER). With the QM/MM model, they were able to obtain results that were in good agreement with experimental data. The authors later explored the capabilities and limitations of the B3LYP method to calculate the properties of the mixed valent multinuclear oxomanganese complexes.⁷⁵⁹ They have shown that some overestimations of bond distances can be corrected by expanding the basis set of the ligands coordinated to the Mn ions with polarization functions. They have also shown that the hydrated CaMn₄O₄ structure (modeled from the 3.5 Å structure) ligated by OH⁻, Cl⁻, carboxylate, and imidazole ligands is a stable structure even without other amino acids. McEvoy and Brudvig⁷¹⁵ compared the theoretical work done on the OEC of PSII up to 2006 in a review paper. They explained the mechanism of O–O bond formation suggested by Yachandra and co-workers, Messinger and co-workers, Siegbahn and co-workers, and Dau and co-workers and compared it to their proposed reaction of the calcium bound water molecule with an oxo–Mn(V) species. Later, Sproviero et al. developed a refined (R)-QM/MM method, which was a structural refinement method based on simulations of isotropic and polarized EXAFS spectra.⁷⁶⁰ The resulting structures were in agreement with experimental data; however, this did not rule out other possibilities because they found a local solution relative to DFT-QM/MM. Later, they investigated the mechanism of water oxidation and suggested that there is formation of an oxyl radical in the S₃ to S₄ transition and a nucleophilic attack of the calcium bound substrate water on the electrophilic oxyl radical.⁷⁶¹ This oxyl radical formation was

also suggested by Siegbahn and Messinger, but the nucleophilic attack is significantly different because they proposed that oxyl radical reacts with the μ -oxo bridge instead of reacting with terminal calcium bound water. Luber et al.⁷⁶² then introduced a QM/MM model of the OEC in the S₁ Mn4 (IV,III,IV,III) state with a ligation scheme similar to the 1.9 Å XRD structure. These authors noted that their QM/MM structure is fully consistent with the high-resolution spectroscopic data and concluded that the XRD structure model corresponds to a mixture of oxidation states including species more reduced than those observed in the catalytic cycle. The authors also compared the bond distances of constituents of the cubane structure with previous R-QM/MM⁷⁶⁰ and 2006-QM/MM⁷⁴⁹ methods. Later in 2013, Pal et al.⁷⁶³ introduced a QM/MM model of the S₀ state consistent with the new experimental data. They reported a proton coupled electron transfer (PCET) process that occurs during the S₀ to S₁ transition where oxidation of Mn center and deprotonation of a μ -oxo bridge lead to a structural rearrangement. The structure of S₁ is given in Figure 14.

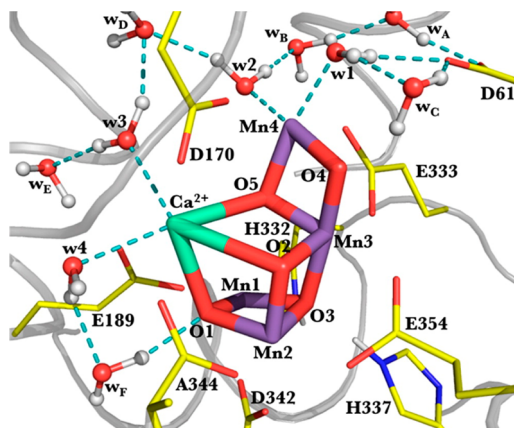


Figure 14. Quantum mechanics/molecular mechanics optimized S₁ structure of the OEC CaMn₄O₅ cluster (based on 1.9 Å structure). Four water molecules directly ligated to the core are numbered as W₁–W₄ and six other water molecules in the second sphere are numbered as W_A–W_F (color code: green, Ca; red, O; purple, Mn; and white, H). Reproduced with permission from ref 763. Copyright 2013 American Chemical Society.

Petrie et al.⁷⁶⁴ in 2010 explored the sequential hydration of several of the structures (“Hyogo”, “Berlin”-2.9 Å, and “London” structures) proposed across charges from -1 to +3 and all feasible magnetic coupling modes. With their BP/TZP calculations, they proposed that the “Hyogo” model is a more realistic model for the true PSII active site. In late 2010, these authors investigated the consequences of sequential hydration on a series of Mn₄Ca structure types with charge states of -1 to +3.⁷⁶⁵ They observed preferences for antiferromagnetic coupling with Mn(II) and Mn(III) atoms invariably adopting high spin configuration regardless of spin coupling. Energy differences between these structures were sufficiently small. Petrie and co-workers⁷⁶⁶ investigated the interaction of His337 with a Mn₄Ca cluster with VWN and nonlocal corrections of Becke and Perdew with the TZP basis set. They performed additional calculations with the B3LYP and PBE0 hybrid functionals. Calculations were performed on a minimal complex model and extended models in which a 13-peptide sequence was treated explicitly. From these calculations, they demon-

strated that while the 2.9 Å structure is best described by models in which the μ_3 -oxo bridge is neither protonated nor involved in significant H-bonding, the 1.9 Å XRD structure is best described by structures in which the μ_3 -oxo bridge undergoes hydrogen-bonding interactions with His337. Petrie et al.⁷⁶⁷ later in the same year presented a study of a set of model compounds based on the 1.9 Å structure using the same level of theory as before. In contrast to other theoretical studies addressing this structure, Petrie et al. reported that it is not necessary to invoke the photoreduction of the sample below the S₁ resting state. These authors stated that S₁ corresponds to a low oxidation state paradigm of either (MnIII)₄ or Mn(II)(MnIII)₂(MnIV) rather than the high oxidation states of S₁-Mn(III)₂Mn(IV)₂.

Kusunoki^{768,769} in 2007 reported a chemically complete model of the Mn₄Ca cluster based on the 3 Å structure. This author showed that two substrate water molecules are bound to asymmetric *cis* positions on the terminal Mn ion to the Mn₃CaO₃(OH) core. Later, this author reported an investigation of the isomeric properties of the S₁ state of OEC using a chemically truncated OEC-cluster model.⁷²³ This study employed the UB3LYP/lacvp** method and showed that the S₁ state of the OEC is in a thermal equilibrium between the two most stable states.

Extensive quantum chemical calculations using the B3LYP exchange correlation functional with LACVP for transition metal atoms and the 6-31G** basis set for other elements were performed by Galstyan et al.⁷⁷⁰ to study the protonation pattern and the oxidation states in the high-resolution crystal structure. They concluded that the experimental structure is not the S₁ state; rather, it is a mixture of states containing highly reduced forms with almost 60% contribution from the S₃ state, Mn(II,II,III,III).

In 2011, Saito et al.⁷⁷¹ examined symmetry breaking of a number of manganese oxide cluster models by doping with Ca²⁺ ion. They used the UB3LYP/def2-SVP level of theory and demonstrated that doping of Ca²⁺ ions into multinuclear Mn oxide induces symmetry breaking and introduces zwitterionic character for the O–O bond formation. They have also used spin polarized molecular orbital models to show the correspondence between magnetic coupling and the reaction mechanism for O₂ evolution. Overall, they concluded that reactions proceed through a continuous diradicaloid pathway without discrete free radical fragments or an electron pair transfer mechanism induced by symmetry breaking with Ca(II) in the pure low spin singlet state. The concepts of symmetry breaking together with multiple reaction mechanisms suggested for water splitting by OEC of photosystem II were already in the field, and there are multiple reports regarding this (e.g., Rüttinger et al.,⁷³⁰ Pecoraro et al.,⁷⁷² Iwata and Barber,⁷⁷³ Yachandra et al.,⁷⁷⁴ and others). Yamanaka et al.⁷⁷⁵ also used the 1.9 Å-refined structure with UB3LYP calculations to elucidate possible O–O bond formation mechanisms in the oxygen evolution reaction of PSII. After analyzing the natural orbitals to obtain LUMOs of labile chemical bonds, they concluded a possibility of a nucleophilic attack of hydroxide or water on calcium to nearby two electrophilic O sites. In a later paper published in the middle of 2011, these authors again emphasized the O–O formation from nucleophilic attack.⁷⁷⁶ Kanda et al.⁷⁷⁷ performed UB3LYP calculations on the 1.9 Å X-ray crystal structure. They constructed energy diagrams on eight different spin structures and analyzed them with a Heisenberg model that involves six effective integrals between

manganese atoms. The ground and excited states of these eight structures exhibit remarkable quasi-degenerate character within 9 kcal mol⁻¹. Ichino, Yamaguchi, and Yoshioka⁷⁷⁸ also examined the electronic structure of the OEC based on the 1.9 Å geometry. They used B3LYP with the Wachters DZ basis for Mn and the 6-31G* basis set for other atoms. They proposed the oxidation mechanism from S₀–S₃ states. These authors showed that optimizing geometries purifies the spin structures of the four manganese atoms, and thus it is easy to determine the oxidation states. It was also shown that one of the two water molecules is a substrate for the reaction. Isobe et al.⁷⁷⁹ revealed geometrical structures of several key intermediates from hybrid DFT calculations (B3LYP/LANL2DZ,6-31G(d)). A left-elongated structure with a uniform valence cuboidal core (444) was favorable in the high valent S₃ state. The authors concluded that, based on the different intermediates, many pathways have similar energy and are conceivable for water oxidation depending on the key intermediates in the S₀–S₃ states. In 2013, Yamaguchi et al.⁷⁸⁰ used several hybrid DFT methods for the full geometry optimization of CaMn₄O₄X(H₂O)₄ (X = OH⁻ or O²⁻). These bonds lengths were compared to previous XRD and EXAFS results together with the high-resolution XRD structure. These DFT results led them to reassign the Mn–Mn and Mn–Ca bond lengths by the EXAFS experiments, which became consistent with the high-resolution XRD structure. There was a remarkable difference between the UBHandHLYP and other hybrid DFT methods for the degree of symmetry breaking. They also reported a full geometry optimization of mixed valence cubane Mn(III)_{4-n}Mn(IV)_n cluster (*n* = 0–4) by UB3LYP to elucidate the Jahn–Teller effect for the Mn(III) ions. It is found that Ca doping in cubane structures suppressed the Jahn–Teller effect.⁷⁸¹

Lang and co-workers⁷⁸² used gas-phase ion trap experiments and first principle theoretical calculations of ligand free manganese oxide clusters with water to design a bioinspired water splitting molecular catalyst. Theoretical calculations were performed with Born–Oppenheimer spin density functional theory molecular dynamics simulations using GGA for electronic exchange and correlation. These simulations offered new insight into the mechanism of the water oxidation process and demonstrated the importance of water adsorption and dimensionality change of Mn₄O₄⁺.

Recently, Kurashige et al.⁷⁸³ computed the entangled valence many electron wave functions of the Mn₄CaO₅ cluster model with more than 10¹⁸ quantum degrees of freedom. This is the first treatment of PSII beyond the single-electron picture of DFT. They identified multiple low-lying energy surfaces associated with the structural distortions seen using X-ray crystallography. This suggests the multistate reactivity of the OEC of PSII.

4.6. Group 8 Oxides

4.6.1. Iron Oxides. Iron is the fourth most abundant element in the earth's crust. Naturally, iron tends to react with oxygen in the air and form various iron oxides. They have become the most plentiful transitional metal oxides on earth. Iron oxides have many phases including 16 pure phases (e.g., FeO, Fe₃O₄), five polymorphs (e.g., α -FeOOH, β -FeOOH), and four kinds of Fe₂O₃ (e.g., α -Fe₂O₃, γ -Fe₂O₃).⁷⁸⁴ These iron oxide clusters are of particular interest due to their unique physical and chemical properties. They are being used as heterogeneous catalysts, gas sensors, pigments, sorbents, and in

biomedical applications and magnetic recording devices. Recently, iron oxides gained more interest because of their remarkable ability to resist moisture and CO_2 in the environment while reacting as a catalyst, thus acting as a competitor to noble metal catalysts. These nanosized clusters have been shown to catalyze the oxidation of carbon monoxide and small organic molecules like methane and methanol.⁷⁸⁵

In 1996, Wang et al.⁷⁸⁶ experimentally studied iron clusters and oxygen-chemisorbed iron clusters. They examined photo-electron spectroscopy for Fe_n^- clusters where $n = 3\text{--}24$ and Fe_nO^- where $n = 1\text{--}16$. Experimentally, they observed sharp features for pure iron clusters in the whole size range they studied, but chemisorbed oxygen clusters only showed sharp features up to $n = 6$. At the time they published the paper, they calculated DFT structures only for iron oxide clusters up to $n = 6$. Later, they experimentally studied Fe_mO_n^- ($m = 1\text{--}4$, $n = 1\text{--}6$) clusters and observed sequential oxygen atom chemisorptions on the surfaces of small iron oxide clusters.⁷⁸⁷

Sun, Wang, and co-workers reported early experimental and theoretical studies of small iron oxide nanoparticles. Much interest was gained when Sakurai and Sun et al.⁷⁸⁸ reported the existence of magic cluster Fe_{13}O_8 . Wang and Sun et al.⁷⁸⁹ reported a first-principles study of this magic cluster with ab initio DFT used with pseudopotentials and a plane wave basis. The exchange correlation functional was adopted in the form of Ceperley and Alder as parametrized by Perdew and Zunger. They found that the equilibrium geometry has D_{4h} symmetry, and by comparing this magic cluster with Fe_{13}O_6 , Fe_{12}O_9 , and Fe_{14}O_7 , they found that the magic cluster has a closed electron configuration in the HOMO, a large HOMO–LUMO gap, and a large binding energy that suggests this cluster is stable as observed experimentally. Sun and Wang et al.⁷⁹⁰ later calculated vibrational properties and confirmed the intrinsic stability of the magic cluster. For this, they used a first-principles ab initio force constant approach by employing a supercell with periodic boundary conditions. Sun and Sakurai et al.⁷⁹¹ studied M_9O_6 magic oxide clusters where $\text{M} = \text{Fe}$, Co, and Ni. They performed DFT calculations with the above technique by using a plane-wave basis and ultrasoft pseudopotentials. From the calculations they determined that these clusters have C_{2v} symmetry. As compared to the M_{13}O_8 clusters, these M_9O_9 clusters have enhanced magnetic moments and reduced average binding energies.

Sun and co-workers⁷⁹² studied gold-coated iron nanoclusters to understand the magnetic properties of this core–shell structure. For small clusters of $\text{Fe}_2\text{--Au}_n$ ($n = 1\text{--}6$ and 18), they used the BPW91 exchange correlation functional with the LANL2DZ basis set for Au and 6-311G* basis set for Fe. For larger clusters Fe_mAu_n ($m = 1, 13$ and $n = 12, 42, 54, 134$), the plane wave basis set with the PAW method was used in supercell calculations. They reported that the magnetic moment of the Fe core was significantly higher than that of the bulk and that it is insensitive to the gold coating. They first calculated the interaction of Fe_{13} with O_2 and found that oxygen readily dissociates and binds with a binding energy of 8.04 eV. For the gold-coated Fe_{13} complex with O_2 , interaction energies for two different orientations were calculated as 0.143 and 0.251 eV. Later in 2007, they used the PW91 functional in supercell calculations to study the interaction of amino acids with gold-coated iron oxide particles.⁷⁹³ The iron oxide magic cluster (Fe_{13}O_8) was capped with 6, 18, and 50 gold atoms (Figure 15). These clusters were then studied for interactions with sulfur-containing amino acids: methionine, cysteine, and

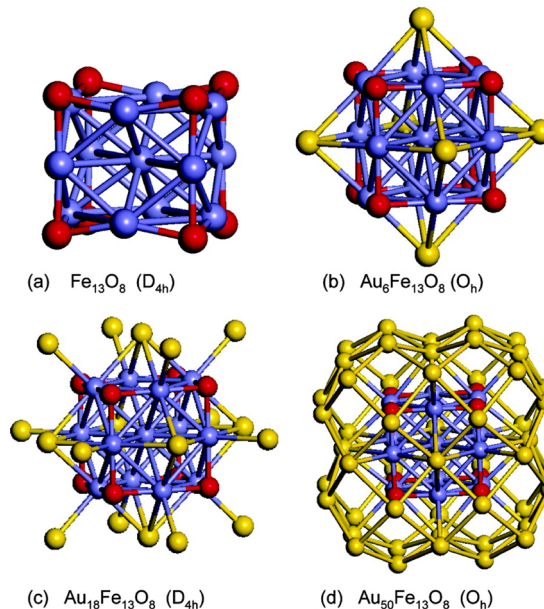


Figure 15. Structures of Fe_{13}O_8 clusters (a) uncoated, (b,c) partially coated, and (d) fully coated with gold (color code: yellow, Au; blue, Fe; and red, O). Reprinted with permission from ref 793. Copyright 2007 American Chemical Society.

taurine. They showed that the interaction of cysteine is stronger than methionine, whereas taurine does not bind with gold-coated iron oxide clusters. The authors suggest that this selectivity can be used for the separation of taurine from the other two sulfur-containing amino acids.

Later, Kortus and Pederson⁷⁹⁴ investigated the magnetic coupling between iron atoms in the Fe_{13}O_8 magic cluster by employing the PBE exchange correlation functional. They have shown that this cluster has complicated magnetic properties with several magnetically stable ferro-, ferri-, and antiferromagnetic states. The authors indicated four metastable ferromagnetic states with total magnetic moments of 20, 26, 32, and 34 μ_B . The lowest energy state is a ferromagnetic state with 32 μ_B per molecule. The 34 μ_B ferromagnetic state is found to be energetically nearly degenerate with the lowest energy state. The lowest energy isomer differs from a previously reported⁷⁸⁹ ferromagnetic state, which had a magnetic moment of 26 μ_B . They also calculated the IR and Raman intensities of these systems.

The structural and magnetic properties of the anion oxide clusters, Fe_3O_n^- ($n = 1\text{--}5$) and Fe_4O_n^- ($n = 1\text{--}6$), were investigated by means of first-principles molecular dynamics based on DFT by Shiroishi et al.⁷⁹⁵ Looking at the geometry, the first O atom favors a bridge site, and the second O atom occupies another bridge site in Fe_3O_2^- and the surface site in Fe_4O_2^- . Vertical detachment energies of Fe_3O_m^- are in good agreement except for the $n = 5$ structure, and for the Fe_4O_m^- cases these values were lower than the experimental values.

Jones et al.⁷⁹⁶ have shown that small Fe_nO_n clusters of $n = 2\text{--}5$ form open ring structures. Starting from $n = 6$, these highly stable rings begin to assemble into nano columnar structures to form towers. These towers can also be decorated by O atoms to lead to hollow drums. Readers should also note that these types of towers were previously speculated to form with manganese oxides (Mn_nO_n),⁷³¹ and later also reported to form with chromium oxides (Cr_nO_{3n}).⁶⁹⁹

Van Natter and co-workers⁷⁹⁷ demonstrated a simple two-step regenerative model for the kinetics of high temperature water–gas shift reaction. DFT with the B3LYP/TZV** level of theory was used in cluster models of the Fe₃O₄ {100}, {110}, and {111} surfaces. Clusters containing as many as 6 units of Fe₃O₄ were used to calculate energies of the oxygen adatom localization on octahedral cation sites. They found that computed energies of localization are linearly proportional to the number of missing oxygen anions from the normal octahedral coordination of the cation adsorption sites. The experimental enthalpy of localization was found to be closer to that of the {111} surface, suggesting that the active site may be a {111} surface. Van Natter et al.⁷⁹⁸ later investigated the effect of copper promotion upon iron oxide surface species for the water–gas shift reaction. Three models were used: an unpromoted catalyst, a catalyst where copper cations substituted for iron cations below the surface, and a catalyst where copper cations substitute in the surface. Binding energies of oxygen, carbon dioxide, dissociated water, and formic acid are all lowered by less than 20 kJ mol⁻¹ (bonding of these intermediates to the surface weakened only slightly) when copper is substituted below the surface. When the copper is substituted in the surface of the catalyst, the binding energies decrease by 60–80 kJ mol⁻¹. Overall, their results suggest that large differences between promoted and unpromoted clusters are due to copper substitution within the surface, but they do not rule out the possibility of aggregation of metallic copper.

Taguchi and co-workers⁷⁹⁹ reported an experimental and theoretical study of three new iron clusters: [Fe₆O₂(NO₃)₄(hmp)₈(H₂O)₂](NO₃)₂, [Fe₄(N₃)₆(hmp)₆], and Fe₈O₃(OMe)(pdm)₄(pdmH)₄(MeOH)₂][ClO₄]₅ (hmpH = 2-(hydroxymethyl)pyridine; pdmH₂ = 2,6-pyridinedimethanol). The B3LYP/LANL2DZ level of theory and semiempirical molecular orbital calculations were used in theoretical calculations. Both methods were in good agreement with overall conclusions of the analysis of the experimental data, in terms of ground state of the complex and the sign and relative magnitude of the constituent *J* values. The DFT method was able to provide reasonably accurate *J* values as compared to experimental values.

A study of structures, stability and bonding, and vibrational frequencies of cage and noncage structures of (Fe₂O₃)_{*n*}, *n* = 2–6 and 10, was reported by Ding et al.⁷⁸⁵ They used hybrid DFT methods B3LYP and BPW91 combined with three different basis sets (LANL2DZ, LAN6311G, and 6-311+G*) for their calculations. Most of the noncage structures were found to be more stable than the corresponding cage clusters. They concluded that oxidation of Fe₄O_{*n*} clusters is exothermic for *n* < 6 and endothermic for *n* ≥ 6. The authors also pointed out that the experimental observation of Fe₄O_{*n*}⁺ for *n* ≥ 6 is in qualitative agreement with their theoretical studies.

López et al.⁸⁰⁰ studied Fe_{*n*}O_{*m*} clusters having 33, 45, and 113 total atoms (Fe₁₇O₁₆, Fe₁₇O₂₈, and Fe₄₅O₆₈) using a GGA+U approach. They used PW91 for the exchange correlation functional. Initial geometries of the clusters were created by considering two different space groups: cubic *Fd*₃*m* and monoclinic *P*2/c. The calculated results suggest that the ground-state cohesive energy is smaller for the monoclinic phase than the cubic phase, suggesting that, at least for the larger clusters, the monoclinic phase is stable. Monoclinic clusters show an insulating band gap in agreement with experimental results.

Zueva and co-workers⁸⁰¹ investigated six [Fe₈(μ₄-O)₄(μ-4-R-pyrazolato)₁₂X₄] complexes (X = NCS, R = H and Cl), which possess identical Fe₈(μ₄-O)₄ cores, with an experimental and theoretical Mössbauer study. It was found that in each case, an inner μ₄-O bridged Fe^{III} cubane core is surrounded by four trigonal bipyramidal iron centers. Theoretical DFT calculations were performed with B3LYP in conjunction with a CP(PPP) basis set for Fe and TZVP for other atoms. From the results, the authors suggested that two quadrupole doublets from the structurally different iron centers form a nested rather than crossed pair in the all-ferric clusters. The larger quadrupole splitting corresponds to the 5-coordinated Fe atoms. They experimentally and theoretically observed changes to the Mössbauer parameters for 1-electron reduced species that are consistent with a redox event that is localized within the cubane core.

Ohshima et al.⁸⁰² used ion mobility mass spectrometry to analyze the geometric structure of iron oxide clusters. They observed a series of (FeO)_{*n*}⁺ and Fe_{*n*}O_{*n*+1}⁺ cluster cations. The arrival time distribution indicates that two structural isomers are possible for (FeO)_{*n*}⁺ clusters with *n* ≥ 5. Theoretical calculations were employed using the B3LYP/6-31+G(d) level of theory. They observed that two-dimensional ring and sheet-like structures are stable for (FeO)_{*n*}⁺ cations where *n* = 3–8, and in addition to these structures, three-dimensional structures are also stable for *n* ≥ 6. These authors concluded that for (FeO)_{*n*}⁺ cations with *n* = 6–8, two-dimensional sheet-like structures and three-dimensional tower or cube-like structures coexist.

4.6.2. Ruthenium Oxides. Ruthenium oxide has been found to be one of the most efficient cocatalysts in photocatalytic systems as compared to other transition metal oxides. In addition, it is of interest for other applications including superconductivity and high temperature ferromagnetism. Very recently, Dong and co-workers⁸⁰³ investigated the structural and electronic properties of small RuO₂ clusters (up to Ru₄O₈) as cocatalysts on TiO₂ surfaces. Ruthenium oxide clusters were calculated with the B3LYP/LANL2DZ, 6-31+G(d,p) level of theory, and the bulk TiO₂ and TiO₂-supported RuO₂ clusters were calculated by periodic calculations. These authors reported that the most energetically stable configuration for each cluster is formed by maximizing the number of interfacial bonds between the cluster and surface. It was shown that RuO₂ clusters have a stronger adsorbing ability on rutile than on anatase surface. Loading of RuO₂ clusters on rutile surface rather than anatase surface was found to favor electron and hole separation, which enhances photocatalytic activity.

4.7. Group 9 Oxides

4.7.1. Cobalt Oxides. Cobalt oxides have applications in pigments and in battery technology. In addition, cobalt oxide became the most popular transition metal oxide with the recent discovery of its remarkable catalytic activity toward water splitting. However, inorganic cobalt oxide salts as water oxidation catalysts have a long history dating back to the late 1970s.^{804–807} This early stage of cobalt catalysts suffered from a major problem, in which oxygen generation dropped rapidly in the presence of a chemical oxidant. The problem was that the active catalyst precipitated out of the solution to form particles, which then reduced the yield of the oxygen. Later, these particles were found to be cobalt oxides and hydroxides.⁸⁰⁸ A new catalyst discovered by Kanan and Nocera⁸⁰⁹ did not suffer from these problems. A couple of models have been proposed

for the cobalt oxide water oxidation catalyst. In 2009, Risch et al.⁸¹⁰ proposed a corner sharing cubane-like model of the catalyst. They studied a film of the catalyst shortly after it was removed from an oxidizing potential and suggested that the catalyst is composed of clusters of complete and incomplete vertex-sharing cobalt oxo cubanes. In 2010, Kanan et al.⁸¹¹ reported a molecular cobaltate cluster model (Figure 16) based

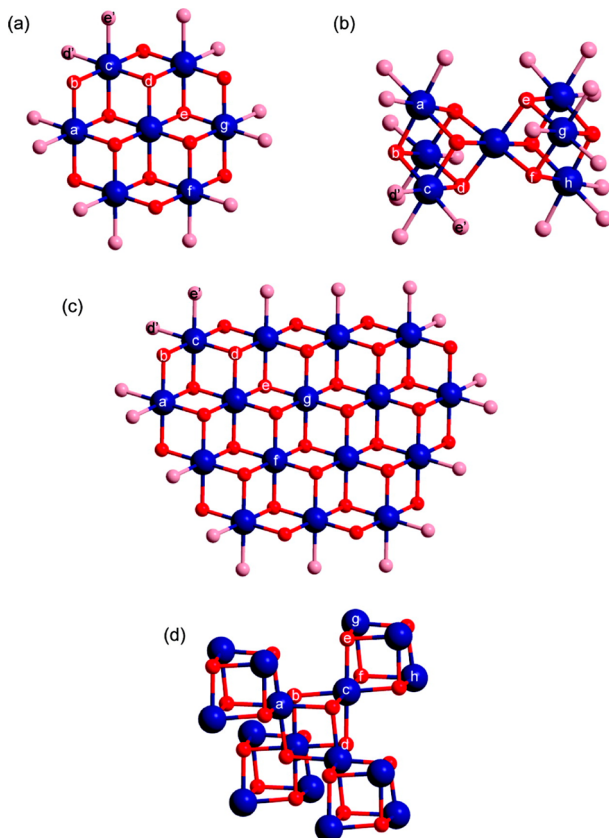


Figure 16. Structural model for the Co-Pi catalyst: (a) Edge-sharing molecular cobaltate cluster model for surface Co-Pi. (b) Corner-sharing cubane model for surface Co-Pi. (c) Edge-sharing molecular cobaltate cluster model for bulk Co-Pi. (d) Corner-sharing cubane model for bulk Co-Pi (color code: blue, Co; and red/pink, O). Reprinted with permission from ref 811. Copyright 2010 American Chemical Society.

on comparison of the EXAFS spectra to the spectrum of a cobaltate compound, $\text{CoO}(\text{OH})$. They measured the XAS spectrum *in situ* while the film was under potential and suggested a core of edge-sharing CoO_6 octahedra.

Surendranath et al.⁸¹² reported a mechanistic study of this catalyst based on electrokinetics and ^{18}O isotope experiments. They suggested a water splitting mechanism involving a rapid, one electron, one proton equilibrium between Co(III)-OH and Co(IV-O) . The phosphate group acts as the proton acceptor, and they also observed a chemical turnover-limiting process involving oxygen–oxygen bond coupling. To establish a foundation for theoretical papers published later, it is necessary to understand some of these experimental studies. However, a detailed description of these experimental studies is not targeted in this Review; readers interested in cobalt water oxidation catalysts are encouraged to read reviews published by Dau et al.,⁸¹³ Artero et al.,^{814,815} Du et al.,⁸⁰⁸ MacAlpin et al.,⁸¹⁶ Sartorel et al.,⁸¹⁷ and others. We should also note that McCool

and co-workers⁸¹⁸ scrutinized a cobalt oxide molecular catalyst that consists of $\text{Co}_4\text{O}_4(\text{C}_5\text{H}_5\text{N})_4(\text{CH}_3\text{CO}_2)_4$ cubane complex, which can be powered by a standard photochemical or electrochemical oxidation reaction.

Cobalt oxides are also used as promoters of catalytic reactions and play a major role in processes like formation of hydrocarbons from methane.⁸¹⁹ The reaction of neutral cobalt oxide clusters Co_mO_n ($m = 3–9$, $n = 3–13$) with CO, NO, C_2H_2 , and C_2H_4 was investigated by Xie et al.⁸²⁰ in a fast-flow reactor using time-of-flight mass spectrometry. They used the BPW91/TZVP level of theory to calculate reaction pathways for the Co_3O_4 cluster.

Yin and co-workers⁸²¹ described an experimental and theoretical study of oxygen-rich iron and cobalt oxide clusters. These oxygen-rich clusters of Fe_mO_n ($n/m \approx 3/2$) and Co_mO_n ($n/m \approx 4/3$) correspond, respectively, to bulk materials of Fe_2O_3 and Co_3O_4 where Fe and Co are in the highest possible oxidation states. DFT calculations were performed on $(\text{Fe}_2\text{O}_3)_m$ with $m = 2–6$ and $(\text{CoO})_m$ with $m = 2–4$, 6, 9, and 12. They used the B3LYP exchange correlation functional with the LANL2DZ basis set in their calculations. The tower or cage structures of Co_9O_9 and $\text{Co}_{12}\text{O}_{12}$ were found to be more stable than the bulk NaCl-like cubic structure. They observed a different and more complex behavior for Co_mO_n^+ clusters than Fe_mO_n^+ clusters. These authors noted that $\text{Co}_{11}\text{O}_{13}^+$ and $\text{Co}_{12}\text{O}_{13}^+$ clusters are missing from the cluster distribution. This indicates high stability for $\text{Co}_{11}\text{O}_{12}^+$ and $\text{Co}_{12}\text{O}_{12}^+$ clusters.

Mattioli and co-workers⁸²² reported AIMD simulations of the cobalt oxide water oxidation catalyst. For static calculations, they also employed GGA and GGA+U level of theories. They used three cluster models proposed previously for the Nocera catalyst (CoCat/Co-Pi WOC) together with LiCoO_2 cluster. This new CoCat is a black thin film, which was deposited on a surface of indium tin oxide (ITO). They used ITO as the working electrode in a three-electrode system containing 0.05 M Co(II) and inorganic phosphate (Pi) as the electrolyte. Lithiated cobalt oxide, LiCoO_2 , was examined because this material is now used extensively in Li-ion batteries. Their theoretical results presented bonds that were closely reproduced by XAS data. This supported the idea that CoCat is built by interconnecting defective and possibly complete cubane units. These authors also observed that oxygen atoms placed as $\mu_2\text{-O}$ bridges between Co(III) ions are likely to be protonated, whereas the μ_3 bridges are likely to be in a deprotonated state. Interestingly, they concluded that terminal oxygen atoms reported so far are likely to form low barrier hydrogen bonds. The authors also reported a study of reaction pathways promoted by the cobalt oxide catalyst.⁸²³ They used AIMD calculations together with static geometry optimization performed with Hubbard U corrected density functional theory. They proposed a Co(IV)-O species as the driving ingredient for the activation of the catalytic mechanism. This is followed by a geminal coupling of O atoms coordinated by the same Co atom. Nucleophilic attack of the water molecule from the solvent is discouraged due to the high activation barrier.

Wang and Van Voorhis⁸²⁴ reported a QM/MM study of the mechanism for water oxidation in a cobalt oxide cubane model compound. The quantum mechanics part consisted of the B3LYP exchange and correlation functional and the LANL2DZ basis set for cobalt and 6-31G* for all of the other atoms. They proposed a direct coupling pathway for the oxygen evolution reaction. This pathway does not include oxygen evolution from the metal oxide core of the catalyst suggested by experimental

studies. However, previous experimental evidence⁸¹¹ suggested the existence of multiple pathways for the oxygen evolution, as well as isotope labeling studies proposed a mechanism involving two coordinate μ -hydroxo moieties, which is not present in this study. It is also important to note that the direct coupling pathway occurs from Co(IV)–O moieties. They have also proposed that this pathway consists of proton coupled oxidation reaction steps. Very recently, Mavros et al.⁸²⁵ published a paper on examining the role of DFT in understanding the water-splitting reaction on clusters. They have shown that DFT-derived chemical descriptors of reactivity are good estimators for reactive trends in water splitting catalysts. They used a five centered Co–Pi model cluster with a direct coupling reaction pathway as a case study to represent that the solvent treatment is a crucial step for predicting accurate redox potentials as well as rate-limiting steps and electrochemical overpotential.

MacAlpin and co-workers⁸²⁶ reported an electronic description of a $\text{Co}(\text{III})_3\text{Co}(\text{IV})\text{O}_4$ cluster as a model for the paramagnetic intermediate in cobalt oxide water oxidation catalyst. The cluster they studied is a cobalt tetramer with a total spin of $S = 1/2$ and with III, III, III, and IV formal cobalt oxidation states, $[\text{Co}_4\text{O}_4(\text{C}_5\text{H}_5\text{N})_4(\text{CH}_3\text{CO}_2)_4]^+$. Their EPR studies indicated that the unpaired spin is delocalized equally across the eight core atoms. This is in agreement with density functional theory calculations they performed using the PW91 and PBE functionals with TZVP and SVP basis sets.

Hu and co-workers⁸²⁷ have exploited ab initio and classical atomistic simulation combined with metadynamics to build a statistically meaningful model for the Co-Pi nanoparticles. They also performed DFT calculations with the PBE exchange correlation functional using a periodic cubic super cell of 25 Å with ultrasoft pseudopotentials. They provided direct evidence of the formation of stable crystallites consisting of complete and incomplete cubane molecular units. Also, their calculations showed that these layered cobaltite structures coexist with corner- and face-sharing cubane motifs in the same crystallite. Their models also included crystallite edges with exposed Co ions and disordered phosphate groups at the nanoparticle surface.

Li and Siegbahn⁸²⁸ recently reported a study of the water oxidation mechanism for synthetic Co–oxides with small nuclearity. Hybrid DFT calculations were performed on these cobalt oxide clusters, and important aspects were compared to the Mn_4Ca structure in the photosystem II. One aspect found was that a M(IV)O radical species is the key precursor for O–O bond formation in both cases. Getting a M(IV) state is not enough; rather, it requires a M(V)=O state with two oxidations on one center from M(III). The cobalt oxide water oxidation catalyst follows through a much more complicated mechanism than the corresponding Mn catalyst. A favorable direct coupling pathway for manganese oxide cubane is not possible for cobalt oxides. For the McCool⁸¹⁸ complex, the best mechanism found was a water attack on a radical species. The calculated barrier was in good agreement with the measured one, 23.0 as compared to 20.0 kcal mol⁻¹. For the amorphous Nocera catalyst, a 31.6 kcal mol⁻¹ barrier was found as compared to the measured 21.8 kcal mol⁻¹. This is for a similar mechanism observed for the McCool et al. cluster. They employed a simple cubane model used by Wang et al. Additional calculations then were done with different models including three and five cobalt atoms and some larger clusters with more irregularities. A three Co atom model was

investigated in detail with small defect or edge effects, and it was found that the barrier is lowered to 27.3 kcal mol⁻¹. The authors suggested that larger clusters with more irregularities may reduce this barrier and the presence of other alkali atoms in the Co–Pi may act as dopants to reduce the barrier.

Kwapien, Piccinin, and Fabris⁸²⁹ investigated the amorphous cobalt catalyst using a simple cubane model. They used high-level coupled cluster theory quantum calculations on these clusters to benchmark the accuracy of popular exchange and correlation functionals used to study these systems. For their studies, they examined the nucleophilic attack of the water molecule to the Co–O species pathway. Hybrid B3LYP and PBE0 functionals were in fair agreement with the CC energies, whereas standard gradient corrected functional have shown important discrepancies. They found that inclusion of on-site electronic repulsion (DFT+U) improves the calculated electronic and structural properties but did not reproduce the coupled cluster results.

4.7.2. Rhodium Oxides. Experimentally, rhodium is primarily used in its elemental form, and it is highly resistant to corrosion. Mainardi and Balbuena⁸³⁰ reported a theoretical study of hydrogen and oxygen adsorption on Rh_n ($n = 1$ –6) clusters. They used the LANL2DZ basis set with the B3PW91 functional. Additional calculations were also performed with the B3LYP/LANL2DZ and MP2 levels of theory. They observed that bridged sites are preferred for O adsorption in small Rh_n clusters, whereas for H it was not conclusive. In Rh_n –O ($n = 1$ –6) clusters, charge transfer occurs from d orbitals of Rh atoms to p orbitals of O. The authors observed significant changes to the Rh_6 cluster upon O and H adsorption.

Harding et al.⁸³¹ investigated the experimental reactivities of small rhodium oxide clusters using DFT calculations. They performed all calculations with the PBE exchange correlation functional combined with aug-cc-pVQZ for O and N and the Stuttgart Dresden effective core potential and accompanying valence basis functions for Rh atoms. The structures of Rh_6O_m^+ ($m = 1$ –4) were used in these calculations. Oxygen atom adsorption favored the bridge sites on the monoxide and dioxide clusters, and high coordination sites were favored for trioxide and tetroxide clusters. High spin multiplicities were found to be less favored for oxides as compared to Rh metal clusters. The dissociation of nitric oxide on Rh_6O_4^+ was found to be unfavorable as compared to molecular adsorption. Later, Harding et al.⁸³² reported infrared vibrational spectra of the low energy isomers of rhodium oxide clusters Rh_6O_m^+ ($m = 1$ –4) using the same level of theory as in the previous study. They reported that oxygen-stretching frequencies are characteristic of the oxygen-binding mode. Each binding mode of oxygen can be attributed to a fingerprint range of frequency, which blue-shifts with an increasing number of adsorbed oxygen atoms. These authors also suggested that these vibrational frequencies will be a useful guide for future experimental measurements of infrared multi photon dissociation spectra (IRMPD).

4.7.3. Iridium Oxides. Iridium oxides have been studied as favorable cocatalysts in photocatalytic and photoelectrochemical water splitting. A number of experimental studies have been carried out to observe how oxygen evolution is affected by changing and mixing the composition of IrO_x with other compounds. Zhou, Yang, and Li⁸³³ investigated the structures, stability, and hydrolysis reaction of small iridium oxide nanoclusters. Neutral Ir_mO_n ($m = 1$ –5 and $n = 1$ –2 m) and ionic Ir_4O_n and Ir_5O_n clusters were investigated with the UB3LYP/LANL2DZ,6-31++G(d,p) level of theory. It was

found that the iridium monoxide clusters have great stability. Calculations of the hydrolysis reaction of $(\text{IrO}_2)_n^{0+}$ ($n = 1–5$) showed that overall the hydrolysis reactions are more favorable for the cationic than the neutral clusters. The authors also reported that the adsorption of water molecules on the cationic clusters is more favorable than on the neutral clusters.

4.8. Group 10 Oxides

4.8.1. Nickel Oxides. Nickel oxides have been widely used for electrochromic anodes. Nickel oxides give favorable coloration but are known to have some problems as well: lower charge capacity, dissolution in organic electrolytes, and dark residual coloration after electron beam deposition or sputtering.⁸³⁴ Most experimental applications of nickel focus on the pure metal rather than the oxide.

The largest theoretical nickel oxide cluster study we found (and the only one with over four nickel oxide units) was performed by Nagai and Morisaki.⁸³⁴ The optical properties of bulk or crystalline NiO can be represented by the $[\text{Ni}_6\text{O}_{19}]^{26-}$ cluster, which consists of six octahedral $[\text{NiO}_6]^{10-}$ units centered by oxygen.⁸³⁵ If a metal atom M substitutes one nickel atom, the partially substituted nickel oxide can be represented with the $[\text{Ni}_5\text{M}^{2+}\text{O}_{19}]^{(28-z)-}$ cluster model. They used the discrete variational $X\alpha$ method for the calculation of $[\text{Ni}_5\text{M}^{2+}\text{O}_{19}]^{(28-z)-}$, where M is a 3d, 4d, or 5d transitional metal. They observed overlapping of Ni 3d and M nd ($n = 3–5$) orbitals at the Fermi level. This suggests a competitive electrode reaction between NiO and the substituted metal oxide. They also found that when Co and Cu were selected as metal M, their optical gaps were approximately the same as that of the $[\text{Ni}_6\text{O}_{19}]^{26-}$ cluster. This study was reported as the first step to modify NiO electrodes by substitution with foreign atoms.

4.8.2. Palladium Oxides. Palladium is resistant to oxidation of the metal; nonetheless, oxidation of Pd is of interest because this metal is often used in catalysis. Lang and co-workers⁸³⁶ recently published an experimental and theoretical study of Pd_6O_4^+ clusters. The palladium oxide cluster was formed in an octopole ion trap under multicollision conditions. This cluster was formed as the sole product of reaction of bare palladium cluster Pd_6^+ with oxygen. This cluster was also identified as the catalytically active species in an oxygen-rich O_2/CO mixture and actively oxidizes CO to CO_2 . They employed the Born–Oppenheimer-spin density functional-molecular dynamics method (which is suitable for investigation of charged systems, as no periodic replication of the ionic system is used) with norm-conserving soft pseudopotentials and PBE as the exchange correlation functional. The palladium clusters and their oxygenated species were optimized with DFT calculations. On the basis of the theoretical calculations and the experimental reaction kinetic data, they proposed a catalytic reaction cycle for the oxidation of CO. Very recently, these authors published a study of a size-dependent self-limiting oxidation of free palladium clusters.⁸³⁷ Experimentally, they observed a strong size-dependent reactivity of Pd_n^+ ($n = 2–7$) in the reaction with molecular oxygen. Remarkable stability and resistance to further oxidation were observed for Pd_nO_4^+ clusters. The same computational methodology was used in these theoretical calculations, and the authors showed the size-dependent bonding of oxygen to small Pd clusters and the stability of Pd_nO_4^+ clusters and its oxidation resistance.

Kwon et al.⁸³⁸ reported a study of water oxidation in alkaline conditions using size-selected clusters of Pd. They reported

experimentally that the Pd_6 and Pd_{17} clusters are very reactive, whereas Pd_4 is catalytically inactive. Theoretically, they employed supercell calculations with PW91 and the PAW potential for energy calculations; the Birmingham cluster genetic algorithm was used in optimizations. They used Pd_4 , Pd_4O_4 , Pd_4O_3 , and Pd_6O_6 clusters to investigate the catalytic process. Pd_4O_4 and Pd_6O_6 represent the oxidation states of supported Pd_4 and Pd_6 clusters. These authors suggest that the key difference between Pd_4 and Pd_6 clusters may originate from the Pd–Pd bridging sites in Pd_6O_6 clusters, which may act as active sites for the oxygen evolution reaction.

4.8.3. Platinum Oxides. Like palladium, platinum is also resistant to corrosion. Again, the oxidation of Pt is of interest because it is widely used in a variety of oxidation catalysis. Hermes et al.⁸³⁹ investigated the IR-activated CO oxidation reaction on isolated platinum oxide cluster cations Pt_nO_m^+ ($n = 3–7$, $m = 2, 4$). These clusters decorated with CO have been subjected to multiple photon infrared excitations. The $\text{Pt}_n\text{O}_m\text{CO}^+$ clusters have been experimentally characterized. The authors undertook a theoretical study of $\text{Pt}_n\text{O}_2\text{CO}^+$ clusters and their plausible CO oxidation pathways. The TPSS functional with a def2-TZVP basis set was used for all atoms with def2-ecp representing the core electrons of Pt. These preliminary calculations identified transition states below the CO desorption energy consistent with the experimental findings.

Kerpel et al.⁸⁴⁰ investigated the structures of small gas-phase $\text{Pt}_n\text{O}_{2m}^+$ ($n = 1–6$, $m = 1, 2$) clusters with IRMPD spectroscopy and DFT calculations. They performed all calculations with the TPSS/def2-TZVP,def2-ecp level of theory. Significant structural changes were observed upon oxygen binding. This has been previously observed with bare Pt surfaces as well.⁸⁴¹ It was found that in most clusters oxygen is bound dissociatively with 2-fold bridge binding motifs, sometimes coordinated with singly coordinated terminal binding.

4.9. Group 11 Oxides

4.9.1. Copper Oxides. Copper oxides, especially Cu_2O , are used as catalysts to degrade organic pollutants^{842–847} and as semiconductor^{848,849} materials. They can also be used as colorants in glassmaking and ceramic glazes. When Cu_2O is doped with other oxides, a new composite material with good energy conversion efficiency can be obtained.^{850,851} Some studies have been reported on understanding the structure and properties of Cu_nO_m clusters, but these are primarily limited to small numbers of atoms, possibly due to the complexity of these clusters.

Onishi and co-workers⁸⁵² investigated the electronic states of copper oxides after hole-doping by hybrid UB2LYP calculations. They used three cluster models: Cu_2O , Cu_3O_2 , and Cu_4O_4 . The energy diagram of hole-doped states was explained by interaction between copper $3d_{x^2-y^2}$ and oxygen 2p orbitals and superexchange interaction between copper orbitals via closed oxygen orbitals.

Yang et al.⁸⁵³ reported a study of Cu_nO_m clusters with a total number of atoms ranging from 5 to 59 (Cu_4O , Cu_4O_2 , Cu_4O_5 , $\text{Cu}_{16}\text{O}_{15}$, $\text{Cu}_{28}\text{O}_{15}$, $\text{Cu}_{44}\text{O}_{15}$, and $\text{Cu}_{28}\text{O}_{27}$). They used GGA-PW91 and GGA+U levels of theory in their calculations. They found higher stabilities for oxygen-rich clusters with longer Cu–Cu average bond lengths such as Cu_4O_5 , $\text{Cu}_{16}\text{O}_{15}$, and $\text{Cu}_{28}\text{O}_{27}$. They observed higher probabilities of generating vacancies in these clusters. The oxygen-rich clusters (Cu_4O_5 , $\text{Cu}_{16}\text{O}_{15}$, and $\text{Cu}_{28}\text{O}_{27}$) were determined to be magnetic. With

GGA-PW91, a highest magnetic moment of $14 \mu_B$ was observed for the $\text{Cu}_{16}\text{O}_{15}$ cluster and GGA+U demonstrated a highest magnetic moment of $22 \mu_B$ for $\text{Cu}_{28}\text{O}_{27}$. When the clusters are hydrogenated, their magnetic moments can be reduced, and the stability of the clusters can be improved.

4.9.2. Silver Oxides. Silver oxide has some industrial uses. Ag_2O can be used as a positive electrode in watch batteries. There have also been many theoretical and experimental studies reported on understanding the mechanism of silver-catalyzed ethylene epoxidation. Fellah et al.⁸⁵⁴ reported a DFT study of epoxidation on a Ag_{14}O_9 cluster model representing the silver oxide (001) surface. They used the B3LYP exchange correlation functional with the LANL2DZ ECP for silver and the 6-31G(d,p) basis set for other atoms. It has been shown that the formation path of acetaldehyde and vinyl alcohol has a higher barrier than that of ethylene oxide formation. The activation barrier reported for the ethylene oxide formation is in good agreement with the experimental global activation energies for the formation of ethylene oxide on a bulk silver catalyst. The formation of an oxometallocycle is not a probable intermediate on this surface. The authors suggested that the reason is due to the lower basicity of the surface oxygen atom and the absence of a surface vacancy position to activate ethylene. Later, they studied the epoxidation reaction of propylene on the same cluster using the same level of theory.⁸⁵⁵ Propylene oxide, propanal, acetone, and Π -allyl radical formation reaction mechanisms were investigated. They observed that a Π -allyl formation path and two propylene adsorption pathways resulting in propylene oxide formation are competing reactions with comparable activation barriers. Their calculations also showed a higher spin density for surface oxygen atom as compared to that of oxygen adsorbed on silver, which indicated that oxygen atoms on a silver oxide cluster have more radical character.

Trushin and co-workers⁸⁵⁶ recently investigated small silver oxide clusters: Ag_2O , Ag_3O_2 , Ag_3O_2 , and $(\text{AgO})_n$ where $n = 1–4$, 6. They employed PW86x and PW91c exchange and correlation functionals together with a polarized triple- ζ basis set. Their results indicated anion-radical form of oxygen centers for small silver oxide clusters having AgO stoichiometry. It was found that spins on oxygen are ferromagnetically ordered for small clusters, while the antiferromagnetic state is more likely to be favorable for the larger clusters. The spin density and charge found on radical-like oxygen centers in the $(\text{AgO})_n$ clusters are larger than those in the Ag_2O cluster. The authors also noted that the anion radical oxygen has the same nature as the electrophilic atomic oxygen species that govern the silver-catalyzed ethylene epoxidation.

4.10. Group 12 Oxides

4.10.1. Zinc Oxides. Zn is primarily used to galvanize other corrosive metals. ZnO is the most important compound of Zn, and it was known before Zn metal because it is the byproduct of primitive brass production. ZnO is used on a large scale for many applications including batteries, pharmaceuticals, inks, soap, rubber and plastic products, cosmetics, etc.⁸⁵⁷ ZnO has also been investigated over the past decade in chemical and gas sensors, varistors, UV light emitters, electronic devices, and as piezoelectric transducers.⁸⁵⁸ ZnO crystallizes into hexagonal wurtzite and has a band gap of 3.37 eV. Catlow, Woodley, and co-workers have reviewed computational techniques along with the broad range of chemical and physical properties of zinc oxide nanoclusters in 2008 and in 2010.^{859,860}

Jiang Lai⁸⁶¹ reported an early study of a ZnO model as a $\text{ZnO}-\text{CuO}$ catalyst for activation of CO and H_2 for methanol synthesis in 1992. This author used self-consistent charge-discrete variation X_α quantum chemical calculations and found that the CO is terminally adsorbed with the C atom toward the Cu atom. The calculated DOS for the Zn_8O_8 cluster representing the (10 $\bar{1}$ 0) surface is in good agreement with the observed photoelectron spectrum. This indicates that the Zn_8O_8 cluster model provides a good representation of the electronic structure of the (10 $\bar{1}$ 0) surface.

Martins et al.⁸⁶² in 1995 used ab initio HF calculations on $(\text{ZnO})_n$ clusters with $n = 3–5$ representing (10 $\bar{1}$ 0) and (0001) surfaces. They used nonrelativistic ECPs (Hay and Wadt ECP for Zn and Stevens ECP for oxygen) and DZ basis sets and compared properties like net atomic charges, force constants, etc., with previous experimental and theoretical data. The ultraviolet photoelectron spectrum was shown to be dependent on the cluster model. They reported that use of Stevens ECP and DZ basis set for oxygen improved the results slightly, and there was a significant dependence on the valence DZ or minimal basis set used for the zinc atom.

The ground state of small clusters of Zn_nO_n where $n = 1–9$ was studied by Matxain, Fowler, and Ugalde.⁸⁶³ They found that clusters with $n = 2–7$ form ring-like structures and $n = 8$ and 9 form three-dimensional spheroid structures. Ring-like structures are formed due to the obtuse O–Zn–O angles, and spheroidal ones are stable due to the higher coordination. These three-dimensional structures can be viewed as being built from Zn_2O_2 rhombi and Zn_3O_3 hexagons. Three years later, Matxain et al.⁸⁶⁴ investigated the excitation energies of Zn_nO_n clusters ($n = 1–15$) using TDDFT with B3LYP and MPW1PW91 functionals with the SKBJ basis set. They found that nonbonding p orbitals, which are perpendicular to the rings and normal to the spheroid surface in 3D structures, cause the calculated excitations in both types of clusters. Ring-like structures of $n = 2–7$ are shown to have excitation energies larger than three-dimensional structures where $n \geq 8$.

Xin Lü and co-workers⁸⁶⁵ proposed three principles to describe the applicability of metal oxide models: the neutrality principle, the stoichiometry principle, and the coordination principle. They proposed that a stoichiometric cluster model is a good model in selecting a cluster to represent a surface that has a correct ratio of cations and anions and meets the requirement of neutrality. They also described how to cut a stoichiometric cluster with as few dangling bonds as possible. They reported RHF energies for neutral clusters of $(\text{ZnO})_n$ where $n = 3, 4, 5, 6, 10$, and 13.

Staemmler and co-workers⁸⁶⁶ demonstrated that adsorption of CO-like small molecules can be used as a probe to distinguish different microscopic models. They used advanced molecular beam techniques together with first-principles calculations and found significant differences between various models proposed. In particular, they found a modest chemisorption on a clean unreconstructed polar Zn–ZnO surface and a weak physisorption on a hypothetical O–ZnO surface. They also reported a significant adsorption energy for CO in the hydrogen saturated O–ZnO surface. They used ab initio embedded cluster calculations at HF and post-HF levels, where the multiconfiguration-coupled electrons approximation (MC-CEPA) was employed for the post-HF calculations, with a large extended TZ2P quality basis set.

The ONIOM method with three layers was used by Lopes Martins et al.⁸⁶⁷ to study the interaction of CO, H_2 , H_2O , NH_3 ,

and CO₂ molecules with the ZnO (1010) surface using a (ZnO)₃₄₈ cluster. The all electron calculations were performed with the 3-21G as well as 6-31+G** basis sets. The universal force field was used for the low level ONIOM layer, RHF/3-21G* was used for the medium layer, and CCSD theory was used for the high level. They employed (ZnO)₁ for the high level layer, (ZnO)₅ for the medium layer, and (ZnO)₃₄₂ for the lowest level layer. They found that binding energies, geometries, and orbital stabilization were comparable to experimental studies. A higher basis set of 6-31+G** yielded more accurate results. The partial charges calculated using the ChelpG method indicated better agreement with experimental acid–base properties for the layer treated with the highest level of theory.

Oxygen vacancies at the polar O terminated (000 $\bar{1}$) surface of ZnO were investigated as active sites in methanol synthesis by Fink.⁸⁶⁸ All of the calculations were performed in the form of an embedded cluster model. Electronic structure and adsorption properties of four different types of oxygen vacancies were investigated. The author found that CO₂ dissociates at electron-rich vacancies into CO and O. Near OH vacancies, CO₂ adsorbs in the form of CO₂⁻, while CO₂ adsorbs as a neutral linear molecule at the H₂O defect sites.

In 2006, Liu et al.⁸⁶⁹ studied large clusters of Zn₁₂O₁₂ doped with one or two Mn atoms to investigate their structural, electronic, and magnetic properties. They used the PW91/ECP level of theory and studied substitutional, exohedral, and endohedral dopings of manganese. For Zn₁₂O₁₂, they found that a cage-like structure is highly stable with a HOMO–LUMO gap of 2.47 eV. In the case of the monodoped structure, the substitutional isomer is the most favorable in energy. It was found that AFM and FM states are degenerate if the Mn–Mn distance is larger than 5 Å and the magnetic coupling is nearly negligible for the bidoped Zn₁₂O₁₂ clusters. The substitutional isomer and the exohedral isomer were found to be the most stable in bidoped clusters. They concluded that the cavity of the Zn₁₂O₁₂ cage can hold two Mn atoms even though the cage is greatly distorted.

Jain et al.⁸⁷⁰ reported an ab initio study of small clusters of (ZnO)_n, where $n \leq 6$. They used ultrasoft pseudopotentials with GGA and optimized several isomers for each size. They found that in all cases ring-like structures are most favorable. Structures of $n = 5$ and 6 show nonplanar configurations, suggesting covalent character of the bonds. They also reported a small HOMO–LUMO gap for small clusters defying the general trend of larger gaps for small clusters. Their bond angles and bond lengths were similar to the previous study by Matxain et al.⁸⁶³

A first-principles study of cobalt doped rings and cages of (ZnO)_n ($n \leq 21$) clusters was undertaken by Reber and co-workers.⁸⁷¹ They employed GGA calculations to investigate the magnetic properties of Zn oxide clusters doped with Co. This study was similar to that of Liu et al.,⁸⁶⁹ which used manganese doped ZnO clusters. They also reported, similar to Matxain et al.,⁸⁶³ that the structures of $n = 2$ –7 are all open ring structures. Zn₈O₈ was found to have a tower-like structure built from Zn₄O₄ units. From $n = 9$ on, towers begin to develop as a cage-like structure built from Zn₂O₂ and Zn₃O₃ rings. This is similar to the results of Liu et al.⁸⁶⁹ These authors also found a stable Zn₁₂O₁₂ cage containing 4 and 6 atom rings. This single cage starts to grow for $n = 13$, 14, 15, and 16. The lowest energy structure for Zn₂₁O₂₁ is built from a double cage of Zn₁₂O₁₂ sharing a Zn₃O₃ ring. For monodoped clusters, cobalt sites

show a spin moment of 3.0 μ_B , whereas bulk ZnO with Co impurities have been shown to have spin moments of 2.6 μ_B . When Co replaced two Zn atoms, the ferromagnetic arrangement was shown to be more stable. A later study by Reber et al.⁸⁷² investigated (ZnO)_n clusters with $n = 2$ –18, 21. With GGA calculations they showed results similar to the previous paper. Among the larger clusters, the most stable were oblong cages Zn₁₅O₁₅, Zn₁₈O₁₈, and Zn₂₁O₂₁, which were reminiscent of nanotubes.

Ralf Steudel and Yana Steudel⁸⁷³ used a highly symmetrical Zn₄O₄ cluster as a model to study the thermodynamics of the initial interactions of the vulcanization molecules. ZnO is added as an activator in rubber vulcanization process with sulfur. They found that the interaction energies of the Lewis bases with Zn₄O₄ increase in the following order: CO < S₆ < C₂H₄ < C₃H₆ < Me₂S₂ < 1,4-C₅H₈ < MeSH < Me₂O < Me₂S < Me₃N ≪ CH₃COO⁻. These molecules have binding energies ranging from -57 to -262 kJ mol⁻¹. Brønsted acid reactions are strongly exothermic, ranging from -121 kJ mol⁻¹ for C₃H₆ to -255 kJ mol⁻¹ for CH₃COOH. The Zn₄O₄ cluster reacts with mercaptobenzothiazole via proton transfer from the NH group to one of the oxygen atoms of ZnO resulting in a binding energy of -247 kJ mol⁻¹.

The structural and electronic properties of (ZnO)_n ($n = 2$ –18) clusters were studied by Wang et al.⁸⁷⁴ They employed PBE with density functional semicore pseudo potential (DSPP) fitted to all electron relativistic DFT and a double numerical basis set including d-polarization functions (DND). They also reported, similar to previous results, that $n = 2$ –7 forms ring structures, while cage and tube structures become dominant for $n = 9$ –18 and crossover from ring to cage/tube was found for $n = 8$. For clusters of $n = 12$, 15, 16, and 18, perfect tube and cage structures were found, which satisfy the six isolated rhomboidal ring rule. They concluded that the HOMO–LUMO gap and the charge transfer between Zn and O are not sensitive to cluster size but rather were dominated by the local coordination. Vibrational spectra were useful in identifying cages, tubes, rings, and bulk structures. They found a strong peak around 550–760 cm⁻¹ for ring structures and a strong peak around 570–590 cm⁻¹ for tube structures. Later, Wang et al.⁸⁷⁵ studied much larger clusters of (ZnO)_n, where $n = 24$, 28, 36, and 48, with the same techniques mentioned above. They demonstrated that cage and tube are the most favored structures of the (ZnO)_n clusters studied and they are similar to (BN)_n counterparts. The onion and bulk-like structures were progressively stable with increasing cluster size. They concluded that this new class of ZnO will be potentially suitable as building blocks in optoelectronic devices. First-principle calculations of zinc oxide clusters with n up to 96 were carried out with the PBE/DSPP/DND level of theory after mass spectroscopic evidence of a (ZnO)₆₀ magic number cluster in 2010 by Wang et al.⁸⁷⁶ Instead of the previously reported cage structure for (ZnO)₆₀, these authors reported a sodalite structure via a coalescence of (ZnO)₁₂ cages. It was also found that sodalite structures are more favorable in energy for (ZnO)₇₈ and (ZnO)₉₆.

Li and co-workers⁸⁷⁷ investigated the structures and properties of ZnO clusters with hexagonal prism configurations using the PBE functional with pseudopotentials. The initial structures were directly cut out from the ZnO wurtzite crystal, and they used clusters up to 96 atoms (Zn and O) with 8 layers. They performed the structural relaxation and found that the zinc atoms move toward the core of the cluster while the

oxygen atoms move outward. The HOMO–LUMO gap was found to decrease with an increasing number of atoms in the clusters while the binding energy increases with increasing cluster size, and both quantities reached the bulk values at the same size of cluster. The wide band gap arises from quantum confinement, and the lower binding energies in the smaller clusters indicate relatively unstable structures. After optimization they found that the initial Zn–O double layer merges into a single layer. This indicates a phase transition from four-coordinate wurtzite to the six-coordinate rocksalt structures in ZnO clusters of 48 atoms.

Zhao et al.⁸⁷⁸ reported a first-principles study of $(\text{ZnO})_n$ clusters for n ranging from 9 to 64 with a PBE level of theory. They found that the formation of bubble-like clusters (b-clusters) decreases with increasing cluster size. There was an approximate linear relationship to $1/n$ for $n > 16$. The b-clusters were found to be more energetically favored than the wurtzite derived w-clusters for $n < 26$. It was also found that the HOMO–LUMO gap of the w-clusters is narrower than that of the b-clusters.

Carrasco, Illas, and Bromley⁸⁷⁹ studied the electronic structure of Mg and Zn oxide clusters and their bulk phases with the PW91 exchange correlation functional. Similar to previous results by Reber et al.,^{871,872} they also found a $(\text{ZnO})_{12}$ cage-like structure as a stable structure. Furthermore, they also reported a second highest energy isomer, which is a distorted cage-like structure lying 0.11 eV above the ground state. This relative energy separation signifies the high probability of isolating cage-like structures in the gas phase. They also suggested that coalescence of these nanoclusters may lead to the formation of ultralow density nanocage-based metal oxide polymorphs.

The electronic and electrical properties of ZnO semiconductor nanotubes were investigated by Zhu and co-workers.⁸⁸⁰ They performed DFT and tight binding methods in their approach. They employed the local density approximation of Ceperley–Alder and the Perdew–Zunger parametrization to account for the exchange correlation to calculate the ZnO nanotubes. The fullerene-like ZnO clusters were calculated with the BLYP/DNP level of theory. Among the optimized geometries of single wall nanotubes, they examined zigzag (10,0) and armchair (10,10) geometries, and for fullerene-like structures of $(\text{ZnO})_n$, they investigated large clusters where $n = 12, 16, 28, 36, 48$, and 76. It was found that the band gaps between the valence band maximum and conduction band minimum of the nanotubes calculated by means of the two methods are similar but larger than that of the bulk ZnO. From the electrical conductivity calculations, the authors concluded that nondefect bulk and nanotubes of ZnO are insulators. With respect to fullerene-like structures, the authors observed that the cohesive energies decrease with the increasing size of the cluster and there was no clear dependency for the band gap energies.

Al-Sunaidi and co-workers⁸⁸¹ reported stable and low energy metastable structures of $(\text{ZnO})_n$, $n = 1–32$. They used an evolutionary algorithm with polarizable shell interatomic potentials. This was the first systematic search of nanoparticle structures above $n = 18$. It was found that when n increases, the ring-like structures become more bubble-like. Bulk-like wurtzite or multilayered clusters as well as the simple cuboid and related rock salt configurations were not found to be thermodynamically stable in the size range considered. Later, Sokol and co-workers⁸⁸² demonstrated a study of a data mining technique to

predict the structures of $(\text{MX})_{12}$ clusters. This technique includes cross-examination of geometric structures collected for ZnO, GaN, LiF, and AgI. They considered the energy landscape of $(\text{MX})_{12}$ clusters that have bulk phases, wurtzite or sphalerite including LiF, BeO, BN, AlN, SiC, CuF, ZnO, GaN, GeC, and AgI. The energy was calculated with the hybrid PBEsol0 functional for structures optimized at the PBEsol level. Woodley et al.⁸⁸³ recently used global optimization with data mining techniques to generate structures of Mg and Cd doped ZnO nanoclusters. The used three levels to calculate energies: interatomic potentials during the filtering stage, PBE during the refinement of structures, and hybrid PBE0 for final structure solutions used to predict the absorption spectra. With the exception of low temperature Mg doped $n = 4$ and 6 clusters, the authors reported a continuous series of stable clusters.

Cheng et al.⁸⁸⁴ studied $(\text{ZnO})_n$ clusters where $n = 1–12$ with the B3LYP/6-31G level of theory. They have found that ring structures are more stable for $n = 1–5$. This contradicted the previous results by Matxain et al.,⁸⁶³ Jain et al.,⁸⁷⁰ and Wang et al.,⁸⁷⁴ where they found $n = 6$ and 7 to be also ring-like. For $n > 5$, the three-dimensional structures were more stable than the ring ones. They were not able to obtain ring-like structures for $n \geq 9$. Similar to previous studies mentioned above, they also reported that with increasing n the 3D structures are more favorable in energy. Simulated IR spectra were found to be helpful to distinguish the ring structures from the cubic or hexagonal packing ones.

Chen and Wang⁸⁸⁵ investigated the structural, electronic, and magnetic properties of transition metal doped $(\text{ZnO})_{12}$ clusters. They used first row transition metals in doping (monodoped and bidoped) and found that all of the doped clusters are highly stable and retain the quasi-cage like structures with the exception of $\text{Ti}_2\text{Zn}_{10}\text{O}_{12}$ and $\text{V}_2\text{Zn}_{10}\text{O}_{12}$. The monodoped clusters are all magnetic with the exception of the Ti doped cluster. For the bidoped cases, the Ti and V doped clusters were distorted significantly because of strong covalent Ti–O/V–O bonding. The bidoped clusters show either antiferromagnetic or paramagnetic properties.

Hidalgo et al.⁸⁸⁶ demonstrated the effect of sulfur substitution with $(\text{ZnO})_6$ clusters using DFT and TDDFT calculations. They first investigated the ground-state energies of the $(\text{ZnO})_6$ cluster using the B3LYP/LANL2DZ level of theory. Two variants of this cluster were observed: one is a 2D planar structure and the other is a 3D structure. Excitation energies and absorption wavelengths were calculated using TDDFT, and for the emission wavelength, the excited-state geometry optimization was carried out with Hartree–Fock configuration interaction singles (HF/CIS). In the following year, they published a study about the effects of sulfur substitutional impurities on $(\text{ZnO})_n$ clusters where $n = 4–12$.⁸⁸⁷ They employed the B3LYP/LANL2DZ level of theory in their calculations. They studied the effects of one single sulfur being substituted at each oxygen location within each $(\text{ZnO})_n$ cluster. Bond length, bond angles, binding energies, and electronic properties were discussed after sulfur substitution. The binding energy increased in all of the structures after substitution, and except for a few cases the HOMO–LUMO gap decreased when compared to the pristine form. In 2013, Hidalgo et al.⁸⁸⁸ used hybrid and M06 functionals combined with three different basis sets to calculate the $(\text{ZnO})_{12}$ cage-like nanocluster. B3LYP and B3PW91 hybrid functionals and three M06 functionals with 6-31+G*, LANL2DZ, and the triple- ζ basis set with Stuttgart/Dresden ECP's were employed in the

calculations. They reported that the M06 functionals give good results comparable to the results from hybrid functionals. Their calculated binding energy values are in the range of 3.9–4.3 eV, and ionization potential values obtained were higher than the reported value of 7.99 eV. Their results indicate that this cage is a wide band gap structure.

Kaewruska and Ruangpornvisuti⁸⁸⁹ studied H₂O and NH₃ adsorption on hydrogen terminated ZnO nanoclusters and ZnO graphene-like nanosheets. All possible configurations were optimized with the B3LYP/LANL2DZ level of theory. They found that H₂O adsorption to the zinc oxide nanocluster and graphene-like nanosheets occur via three types of interactions: water oxygen and Zn surface atom, water hydrogen and hydride hydrogen on surface, and water hydrogen and oxygen surface atom. Ammonia adsorption occurs by pointing its nitrogen toward the surface Zn atom, and the angle is approximately perpendicular to the nanosheets and nanoclusters. Small diatomic, triatomic, and tetraatomic gas molecules were recently used to study adsorption abilities of the ZnO sodalite-like cage by Kaewruska and co-workers.⁸⁹⁰ They used the B3LYP/LANL2DZ level of theory, and additional calculations were done with B97D/LANL2DZ to compare the values. The strongest adsorption energies for diatomic and triatomic gases were recorded at monolayer (ML) = 0.082 for O₂ (−14.09 kcal mol^{−1}) and SO₂ (−35.06 kcal mol^{−1}), and NH₃ (−25.41 kcal mol^{−1}).

A cluster assembled material based on Zn₁₂O₁₂ has been investigated by Yong and co-workers.⁸⁹¹ Initially, they performed full-potential linear muffin tin orbital molecular dynamics and GGA minimization to find the lowest energy isomers of the Zn₁₂O₁₂ cluster. It was found that, similar to previous results, a cage structure with six squares and eight hexagons is the most stable configuration for the Zn₁₂O₁₂ cluster. Their periodic calculations showed that assembly can progress by attaching the Zn₁₂O₁₂ cage on a hexagonal site of a second Zn₁₂O₁₂ cage. It was found that the Zn₁₂O₁₂ cage combines with eight hexagons in the adjacent eight Zn₁₂O₁₂ cages to form more stable assemblies. As the assembly continues, these cages form a new 3D nanoporous ZnO phase with a rhombohedral lattice framework. Band analysis shows that this new phase is a semiconductor with a larger band gap value.

In 2012, Yong et al.⁸⁹² studied structures, stabilities, and magnetic properties of Cu-doped Zn_{*n*}O_{*n*} (*n* = 3, 9, 12) clusters with spin-polarized density functional theory. Initially, they performed an extensive search to find the lowest energy isomers of pure (ZnO)_{*n*}, where *n* = 1–13. They observed that ring structures are most stable for *n* = 2–7 and cage and tube structures become dominantly stable for *n* = 8–13. Among these clusters, *n* = 3, 9, and 12 clusters show relatively high stability. These stable clusters were then taken as candidates to investigate the Cu doping. They considered three doping modes: substitutional, exohedral, and endohedral doping with monodoped and bidoped formalities. They reported that among these doped clusters substitutional ones show special stability. The HOMO–LUMO gap decreased in doped clusters due to p–d hybridization. Monodoped clusters show a magnetic moment of 1 μ_B, and the ground states of bidoped clusters have a zero magnetic moment with AF coupled or completely quenched Cu atoms except for Cu₂ZnO₃.

In 2012, Oymak and Erkoç⁸⁵⁷ published a review article on group 12 elements and their small clusters. Both experimental and theoretical details were given with respect to electric dipole

polarizability studies of Zn, Cd, and Hg atoms, and specific attention was provided to Zn and ZnO clusters.

Shewale and co-workers⁸⁹³ reported a first-principle study of interaction of DNA and RNA with a (ZnO)₁₂ cluster. They employed a PBE exchange and correlation functional with a double-ζ with polarization basis set. They have studied nucleic acid bases adenine, guanine, cytosine, thymine, and uracil interacting with the (ZnO)₁₂ cluster. The binding energy is found to be highest at the ring nitrogen site for all nucleobases, the sequence being G < T < U < A < C. Weak van der Waals and covalent forces were ascertained to govern these interactions.

Azpiroz et al.⁸⁹⁴ used ZnO and ZnS with realistic nanostructure models of ~1.5 nm to investigate the electronic, structural, and optical properties by means of DFT/TDDFT calculations. Prismatic shape nanoclusters of (ZnX)₁₁₁ (X = O, S) were formed from bulk wurtzite with two different saturation patterns of the polar surface. These clusters were fully optimized by Car–Parrinello molecular dynamics, and then suitable structures were further optimized with the PBE functional together with a double valence set of Slater type orbitals. Calculated absorption onsets are in excellent agreement with the experimental values (within 0.1–0.2 eV) reported for similarly sized nanoparticles. These clusters also exhibit a well-opened HOMO–LUMO band gap without the presence of possible artificial intraband-gap states. These authors suggested that this computational framework can be used to model groups II–VI semiconductor materials, opening the way to simulate ligand/semiconductor interactions.

Beheshtian, Peyghan, and Bagheri⁸⁹⁵ demonstrated absorption and dissociation of Cl₂ molecules on a ZnO nanocluster. They used the Zn₁₂O₁₂ nanocage with the B3LYP/LANL2DZ level of theory and found that Cl₂ molecules are strongly adsorbed via two mechanisms including chemisorption. It was found that this adsorption process can be exothermic or endothermic based on the adsorption configuration. They also observed that after Cl₂ adsorption the HOMO–LUMO gap decreases and the Fermi level shifts toward lower energies. This Zn₁₂O₁₂ cluster transforms into a p-type semiconductor upon Cl₂ dissociation.

The stability and optical gap of zinc oxide clusters (ZnO)_{*n*}, *n* = 2–18, were investigated by Zhao and co-workers⁸⁵⁸ in conjunction with DFT and TDDFT calculations using the PBE functional. In smaller sized clusters with *n* = 2–5, ring structures showed higher stability, whereas 3D structures are the most stable from *n* = 6–18, and the transition is found to occur at *n* = 5. For small clusters of 2 ≤ *n* ≤ 5, the difference between HOMO–LUMO energy gap and the optical gap was found to be large. When the cluster size increases, this difference becomes small. Nevertheless, they concluded that HOMO–LUMO gaps are sensitive to the structure and insensitive to the cluster size. Structures tend to have greater impact on the optical gap, and they observed a dipole-forbidden transition in the optical gap for different structures.

Mallochi and co-workers⁸⁹⁶ studied the structural and optoelectronic properties of hexagonal prism structures of ZnO and ZnS as a function of length and diameter. They used the BP86/TZVP level of theory in their DFT calculations. They reported that ZnO nanostructures transform from wurtzite to graphitic phase. A model of saturated clusters preserving the wurtzite phase was considered to correlate with the morphological and optoelectronic properties. They found that properties of ZnO graphitic and wurtzite clusters are very

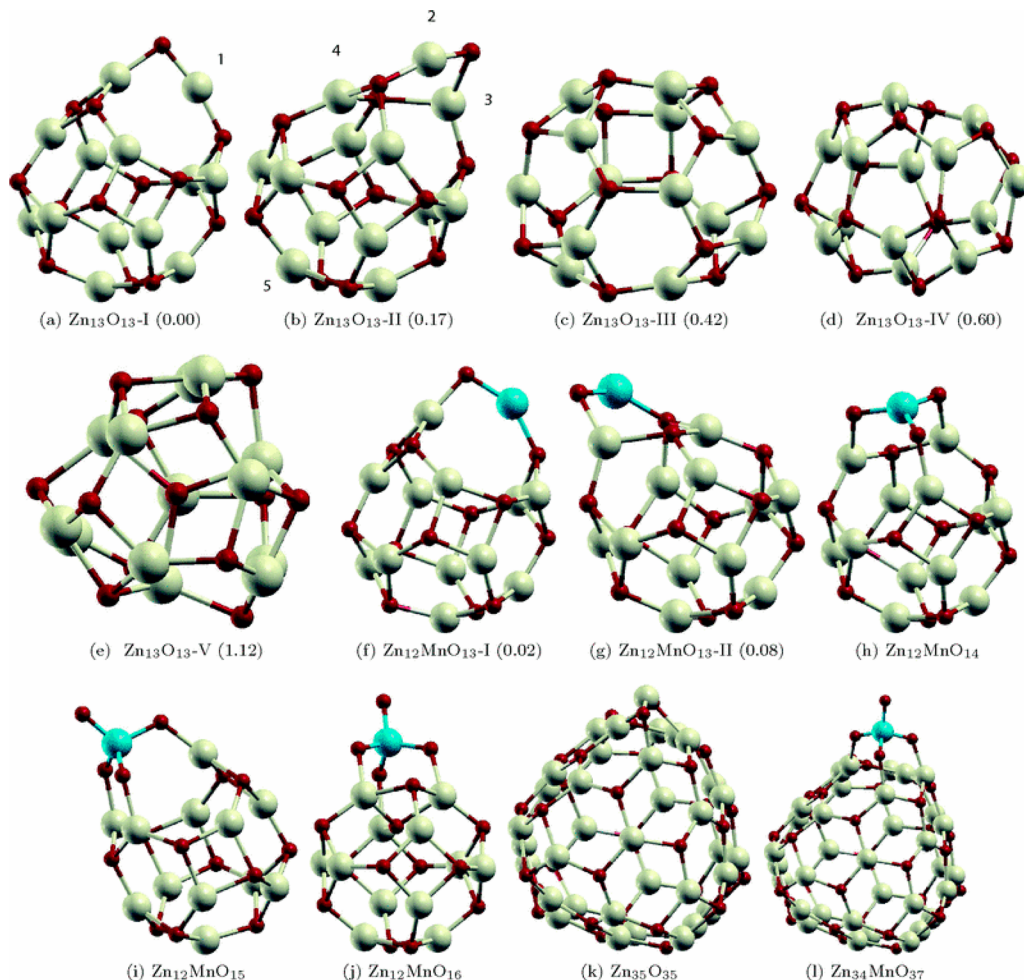


Figure 17. Optimized geometries of doped and undoped ZnO clusters with one Mn atom. Relative energy values are given in parentheses. Numbers in (a) and (b) show Mn doping sites (color code: blue, Mn; red, O; and off-white, Zn). Reprinted with permission from ref 899. Copyright 2012 American Physical Society.

similar. They also performed many-body perturbation theory calculations and concluded that these results are also in good agreement with DFT/TDDFT results. In the same year, Caddeo and Mallocci et al.⁸⁹⁷ reported optoelectronic properties of $(\text{ZnO})_{60}$ isomers. After cutting hexagonal prism structures from bulk wurtzite ZnO, they preoptimized the structures with model potential molecular dynamics simulations. The resulting structures were fully relaxed using DFT at the BP86/TZVP level of theory. Six possible structures of $(\text{ZnO})_{60}$ were studied. It was found that a sodalite structure is the lowest energy structure in agreement with Wang et al.⁸⁷⁶

Chang and Waclawik⁸⁹⁸ investigated experimentally and theoretically the effect of ligands on the growth of ZnO nanoparticles. The adsorption of capping ligands on Zn_nO_n ($n = 4$ or 18) was modeled theoretically. They used the B3LYP/LANL2DZ level of theory in their calculations. Experimentally, they found that tris(hydroxymethyl)aminomethane (THMA) significantly inhibits the growth of ZnO nanoparticles. Their theoretical calculations show that small molecules with multifunctional groups (THMA) adsorb to the ZnO surface with strong bonds and higher interaction energies. These small molecules will stabilize ZnO nanoparticles effectively. Chain hydrocarbon ligands such as *n*-dodecanethiol and *n*-hexadecylamine show much weaker interactions.

Nanavati et al.⁸⁹⁹ performed ab initio calculations on Mn-doped $(\text{ZnO})_n$ ($n = 12, 13, 34, 35$) clusters (Figure 17). They showed the formations of nonstoichiometric $\text{Zn}_{12}\text{MnO}_{15}$ and $\text{Zn}_{34}\text{MnO}_{37}$ obtained from $n = 13$ and 35 become magic with a $1 \mu_B$ magnetic moment. They found that oxygen quenches the magnetic moment of Mn and forms composite structures where MnO_4 is attached to the anion cages of $n = 12$ and 34. They have also replaced Mn with Cr and obtained a neutral nonmagnetic $\text{Zn}_{12}\text{CrO}_{15}$ nanocluster with a large HOMO–LUMO gap of 2.24 eV.

In 2013, Farmanzadeh et al.⁹⁰⁰ investigated the ligand field effect of the adsorption of formaldehyde molecule on the ZnO nanotube surface with the PBE/DNP level of theory. A zigzag (8,0) zinc oxide surface was used with the presence and absence of an external electric field. Their study suggested that external electric fields decrease the HOMO–LUMO gap values and the adsorption energy values. These modifications to the electronic properties of the complex are more noticeable as the electric field increases in a parallel direction to the tube axis. They also concluded that the adsorption process is sensitive to the tube chirality and diameter.

Baei⁹⁰¹ recently reported a study of covalent functionalization of $\text{Zn}_{12}\text{O}_{12}$ nanocluster with thiophene. They reported that the thiophene molecule is physically adsorbed on the surface of the nanocluster. The most stable adsorption configuration was

obtained from orientation with C=C (${}^2\eta$) mode. Natural charge analysis with full natural bond orbital calculations was performed with the B3LYP/6-31G* level of theory for the optimized structures. The charge-transfer value of ${}^2\eta$ and ${}^5\eta$ ($\pi-\pi$ interaction) binding modes shows that π -back bonding characteristics exist in the complex. Theoretical calculations with the B3LYP/LANL2DZ level of theory predict that HOMO–LUMO band gap values change about 0.24–0.72 eV. Furthermore, the decreasing work function shows that the field emission properties of the complex increase upon thiophene adsorption. Later in the same year, Baei and co-workers investigated the energetic, geometric, and electronic properties of one or two hydrogen atoms adsorbed to the $Zn_{12}O_{12}$ nanocluster with the B3LYP/LANL2DZ level of theory.⁹⁰² They demonstrated that one H preferred to be adsorbed atop of an O atom. The average binding energy of two H atoms was found to be higher than that of one hydrogen atom. The HOMO–LUMO gap of the cluster decreased to 0.81 eV from 4.04 eV upon hydrogen adsorption. This suggests that the cluster has transformed to an n-type semiconductor. It was also found that upon hydrogen adsorption, the Fermi level shifts to a higher energy level and decreases the work function facilitating the field electron emission.

Very recently in 2014, Tayebee and co-workers⁹⁰³ studied adsorption properties of aliphatic aldehydes on ZnO nanoclusters and graphene-like systems. The adsorption energies were obtained at the B3LYP/LANL2DZ level of theory. They concluded that surface zinc ions of the central ring of zinc oxide nanoclusters and zinc oxide graphene-like nanosheets interact with oxygen atoms on aldehydes, making the adsorption favorable. It was found that the adsorption energy decreased with longer chain lengths. Iso-butyaldehyde as a branched aldehyde gave the most negative adsorption energy.

4.10.2. Cadmium Oxides. Over the past decade, there have been experimental studies reported on various applications of cadmium oxides. A few examples of these applications include solar cells,⁹⁰⁴ electrochemical capacitors,⁹⁰⁵ thermo electricity,⁹⁰⁶ gas sensors,⁹⁰⁷ etc. However, there have been a very limited number of theoretical papers published for cadmium oxides.

Srinivasaraghavan et al.⁹⁰⁸ recently reported a quantum chemical study of $(CdO)_n$, $n = 1–8$, nanoclusters. They employed the B3LYP exchange and correlation functional with the 6-31G basis set for geometry optimizations. Coordination numbers of Cd and O atoms were found to be very different from the bulk CdO material. They reported that for $n = 1–5$, ring-type structures are the most stable, and for $n \geq 5$, three-dimensional (3D) structures are more favorable than the ring structures. These authors suggest that with the growth of the cadmium oxide clusters, 3D structures are more favorable in energy. A calculated IR spectrum for each cluster was also determined, and these spectra can be used to differentiate the ring structure from 3D structures.

As discussed in the next section, Wang and co-workers⁹⁰⁹ in their study of optical and bonding characteristics of Hg oxide clusters reported Cd doping into Hg oxide clusters as well as Hg doping into Cd oxide clusters.

4.10.3. Mercuric Oxides. Theoretical studies of HgO have been rarely reported. Tossell⁹¹⁰ investigated the oligomerization and the solvolysis of HgO and HgS clusters. Different levels of theories including MP2 and CCSD, along with various density functional methods, were used to study closed ring-type ($HgX)_n$ oligomers ($n = 2, 3, 4$ and $X = O, S$) as well as infinite

1D polymers using periodic boundary conditions. These authors reported that HgX ring oligomers become systematically more stable as n increases and level off around $n = 4–6$. In addition, 1D chain polymers are marginally more stable than the $n = 6$ oligomers. Solvolysis reactions of HgX into species such as $Hg(OH)_2$ and $Hg(SH)_2$ were also studied, and these reactions were more complicated; yet calculated solubility and reactivity are qualitatively in agreement with experiments.

In 2013, Wang and co-workers⁹⁰⁹ studied optical and bonding characteristics of HgX ($X = O, Te, Se$, and S) clusters using the B3LYP/LANL2DZ level of theory. For the oxides, configurations of HgO , Hg_2O_2 , Hg_3O_3 , and Hg_4O_4 were reported. Different configurations for the same cluster have different absorption wavelengths as they have different transition dipole moments, HOMOs, and LUMOs. Cd was doped into the centers of Hg_3O_3 and Hg_4O_4 , and Hg was doped into the centers of Cd_3O_3 and Cd_4O_4 . They observed that doping atoms into the vacancy of pure CdO or HgO clusters changes the geometries and the HOMO–LUMO gaps. These authors also reported that HgTe, HgSe, and HgS have different bonding and spectra than HgO clusters.

4.11. Polyoxometalates

Polyoxometalates (POMs) are polyanionic molecular oxo clusters formed by the condensation of some of the early transition metals like V, Nb, Mo, W, and Ta. Even so, over the past few decades almost all of the elements in the periodic table have somehow been incorporated into the POM framework. These clusters span a wide variety of sizes and shapes and a wide range of applications. A comprehensive review of structure, properties, and reactivity of polyoxometalates emphasizing theoretical reports was published by López et al.⁹¹¹ in mid-2012. In this section, we will concentrate on articles published after this review.

Gao et al.⁹¹² reported a theoretical and experimental study of a pyrene grafted POM hybrid. It was found that pyrene is covalently attached to Mo_6O_{19} via the imido group, making a new organic–inorganic hybrid structure. The electronic absorption peak of this hybrid was observed at 450 nm. This indicates the strong electronic interaction between the organic pyrene imido group and the inorganic hexamolybdate cluster. The geometry of the hybrid system was optimized with the B3LYP/6-31G* level of theory, and the low-lying vertical excitation energies were calculated with TDDFT. TDDFT calculations revealed that the strong peak in the visible region comes from the optically allowed $\pi-\pi^*$ transition of the pyreneimido component.

Miró et al.⁹¹³ synthesized and characterized a new wheel-shaped POM $\{[W_5O_{21}]_3(U^{VI}O_2)_2(\mu-O_2)\}_3^{30-}$ containing well-defined uranyl-peroxide and tungstometalate building blocks. They employed the BP86 exchange and correlation functional with a triple- ζ polarization basis set. It was found from the calculated electrostatic potential that protonation of several μ -oxo bridges occurs to reduce the total charge of the POM. This protonation does not affect the wheel structure of the POM cluster.

The electronic structure and static first hyperpolarizability of organic–inorganic systems based on $[Mo_6O_{19}]^{2-}$ with the chromophore DTE (dithienylperfluorocyclopentene) derivatives have been studied by Teng-Ying Ma et al.⁹¹⁴ They used DFT combined with finite field methods to calculate the second-order nonlinear optical (NLO) coefficients for these structures. The static first hyperpolarizability was calculated

using FF with three functionals, B3LYP, CAM-B3LYP, and LC-BLYP, with the LANL2DZ basis set for Mo and 6-31G(d) for the other atoms. It was shown that photoisomerization significantly changes the geometrical structure from the opening form to the closed-ring form. In the closed-ring form of DTE, its planar structure provides good π conjugation and possesses low $\pi-\pi^*$ transition energies. These authors concluded that the introduction of $[\text{Mo}_6\text{O}_{19}]^{2-}$ and organic group (*N,N*-bis(-4-methoxyphenyl) phenylamino and 2-dicyanomethylene-3-cyano-5-phenyl-5-trifluoromethyl-3,4-dihydrofuran) to the DTE monomer effectively improves the conversion ratio of second-order NLO coefficients between the open- and closed-ring forms. This system was further studied by Teng-Ying Ma et al.⁹¹⁵ shortly thereafter. This time, two POM derivatives were used to bind with the DTE molecule. Two types of structure formalisms were observed: 2D Λ -shaped and W-shaped systems. The CAM-B3LYP and M06-2X functionals were used to study the switching behavior. It was found that charge transfer occurs from DTE to POM and intramolecular charge transfer was shown to improve the static first hyperpolarizability. These authors also investigated second-order NLO of a series of hybrid complexes with porphyrin and α -[MSiW₁₁O₃₉]³⁻ (M = Nb^V or V^V).⁹¹⁶ Geometry optimization was carried out with BP86 combined with a TZP basis set. Additional calculations were also carried out with B3LYP with 6-31G(d) and LANL2DZ basis sets. It was found that substituted metal atom with a large electronegativity (V > Nb) has a large nonlinearity. The metalloporphyrin was found to enhance the π -conjugation and is helpful in enhancing the optical nonlinearity of some complexes. Lengthening of this π -conjugation is helpful for larger optical nonlinearity. It was also reported that the solvent effect plays a major role in the second-order polarizability of the complex. Later, the static second-order NLO responses of lacunary γ -Keggin polyanion derivatives $[\text{XM}_2\text{W}_{10}\text{O}_{38}(\mu\text{-OH})_2]^{n-}$ (X = Si^{IV}, Ge^{IV}, P^V, As^V, M = Al^{III}, Ti^{IV}, V^V; X = Zn^{II}, V^V, M = Al^{III}) were investigated by using DFT methods.⁹¹⁷ Geometry optimizations were carried out with the BP86 exchange correlation function with a triple- ζ polarized basis set; for W atoms, a frozen core composed of 1s to 3spd shells was described by single Slater functions. ALDA was used to calculate the NLO response, and the LB94 potential that corrects the LDA potential in the outer region of the molecule was also used. These authors concluded that the NLO activity of these complexes could be modified by replacing the central heteroatom (X) and the substituted addenda metal atom (M), which reveals a general rule to design the systems with large optical nonlinearity. Later, these authors used the B3LYP/LANL2DZ,6-31G(d) level of theory to investigate the relationship between the reversible redox properties and second-order NLO responses for the photochromic asymmetrical Mn-Anderson type POM covalently linked to one spiropyran complex.⁹¹⁸ They found that the second-order NLO behaviors can be switched by reversible redox and that gaining and losing electrons affects the NLO responses for this complex.

Papulovskiy et al.⁹¹⁹ performed ab initio periodic DFT calculations for over 50 niobate clusters and calculated ⁹³Nb NMR parameters that were in good agreement with the experimental values. Some of the new complexes including AlNbO₄, VNb₉O₂₅, KNb₆O₁₉, and Cs₃NbO₈ are of particular interest due to their catalysis. The four coordinated niobium sites exhibit a small chemical shift span of about 400 ppm, which increases with the coordination number to 900, 1100,

and 1900 ppm for 6, 7, and 8 coordinated niobium sites, respectively. There were two exceptions observed: 5 coordinated sites show significant span and 6 coordinated sites often have the smallest span. Lapina et al.⁹²⁰ have previously reported this general trend of increasing chemical shift with increasing coordination number of niobium. Papulovskiy et al. also reported an additional correlation existing between chemical shift anisotropy and the niobium coordination environment.⁹¹⁹ The chemical shielding span tends to increase with the coordination. The authors suggest these trends will be useful in studying multicomponent and often amorphous niobium oxide catalytic systems.

The electronic structure and bonding features of a series of monoruthenium substituted kegging type POMs have been investigated using DFT by Liu and Guan.⁹²¹ They employed the B3LYP/6-31G(d),LANL2DZ level of theory. The complexes they investigated are $[\{\text{PW}_{11}\text{O}_{39}\}\text{Ru}^{\text{II}/\text{III}}(\text{L})]^{n-}$ (L = DMSO, H₂O, ammonia, and pyridine) and $[\{\text{GeW}_{11}\text{O}_{39}\}\text{Ru}^{\text{II}}(\text{DMSO})_3(\text{H}_2\text{O})]^{6-}$. It was found that both of these complexes have analogous frontier molecular orbital features. The $[\{\text{PW}_{11}\text{O}_{39}\}\text{Ru}^{\text{II}}(\text{DMSO})]^{5-}$ complex has a relatively small HOMO–LUMO gap because of the high HOMO energy level. This difference reported arises from the high composition of POM ligands with antibonding features in the HOMO. It was also shown that Ru(II/III) centers and various ligands have donor–acceptor-type interactions.

Melcamu and co-workers⁹²² designed novel molecular–POM hybrids by combining a POM with nanographene. They employed CAM-B3LYP with LANL2DZ for Mo atoms, and 6-31G(d) and 6-31+G(d) basis sets for other elements. Three systems were used in this study: (NH₂–HBC–NO₂), [NH₂–HBC–Mo₆O₁₈]²⁻, and [Mo₆O₁₈–HBC–NO₂]²⁻ (HBC = hexa-peri-benzocoronene). It was found that the second-order polarizability of the system is enhanced significantly by replacing NO₂ or NH₂ ligands with POM. From TDDFT calculations, they concluded that charge transfer from the polyanion to graphene results in NLO properties of these compounds.

The excitation of decatungstate anion [W₁₀O₃₂]⁴⁻, which is widely used as a photocatalyst, has been investigated recently with relativistic DFT calculations by Ravelli et al.⁹²³ All of the geometries were first optimized with ZORA scalar relativistic corrections (ZSC) at the ZSC-BP86/TZ2P level of theory with an all electron basis set, and excitation spectra were calculated at the COSMO-ZSC-PBE0/TZP-FC level of theory. It is known that upon irradiation, the decatungstate anion ([W₁₀O₃₂]⁴⁻) undergoes one electron reduction to [W₁₀O₃₂]⁵⁻ and protonated [HW₁₀O₃₂]⁴⁻ species. The bireduced species ([W₁₀O₃₂]⁶⁻) is obtained after subsequent disproportionation. The UV–vis spectra of all of the species ([W₁₀O₃₂]⁴⁻, [W₁₀O₃₂]⁵⁻, [HW₁₀O₃₂]⁴⁻, and [W₁₀O₃₂]⁶⁻) involved in decatungstate mediated photochemical reactions were predicted to be in good agreement with experiment.

De Luca and co-workers⁹²⁴ studied the noncovalent interaction between the Keggin POM ($[\text{PMo}_{12}\text{O}_{40}]^{3-}$) and the AUTMAB (acryloyloxyundecyltrimethylammonium bromide) surfactant with DFT. Hydration calculations (using the COSMO model) were also carried out for the POM using X3LYP with a DZ basis set for phosphorus and internal oxygen, DZP for external oxygen, and Stuttgart RSC 1997 ECP for Mo. They calculated the electronic solvation energy of the POM and Br⁻ with the same level of theory to predict the probable exchange on the polymeric surface between these anions at the

water/polymer surface. These calculations predict that there is no net energy gain if the Br^- ion is exchanged with hydrated POM, showing that Br^- cannot be exchanged with this nanosized polyanion to a large extent.

Theoretical investigation of molecular and electronic structures of the heteropolytungstate α -Keggin POM cluster ($[\text{XM}_{12}\text{O}_{40}]^{3-}$, X = P) (Figure 18) and its super reduced state

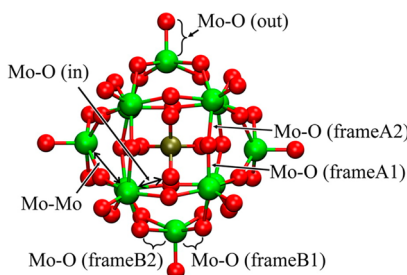


Figure 18. Optimized (BP86/D-SV(P)) geometric structure of $[\text{PMo}_{12}\text{O}_{40}]^{3-}$ and definitions of characteristic bond lengths (color code: green, Mo; red, O; and olive, P). Reprinted with permission from ref 925. Copyright 2014 American Chemical Society.

($[\text{PMo}_{12}\text{O}_{40}]^{27-}$) as well as those of tungsten ($[\text{PW}_{12}\text{O}_{40}]^{3-}$ and $[\text{PW}_{12}\text{O}_{40}]^{27-}$) have been reported recently by Nishimoto et al.⁹²⁵ Geometrical optimizations were carried out with the BP86 and B3LYP exchange correlation functionals and the polarized split valence type def-SV(P) basis set with dispersion correction. This basis set is denoted as D-SV(P) where D- is used to abbreviate the enforcement of dispersion correction. They also employed first-principle molecular dynamics simulations to explore local minima on the potential energy surface where Li atoms are randomly placed as electron donors around the POM cluster surface. The authors reported that super reduction is accompanied by metal–metal bond formation, beginning from the 12th to 14th excess electron transferred to the cluster. Afterward, the number of metal–metal bonds was shown to increase nearly linearly with the number of additionally transferred excess electrons.

5. SEMICONDUCTING METAL CHALCOGENIDE CLUSTERS

This section discusses the theoretical investigation of semiconducting metal chalcogenide clusters, especially $\text{A}^{\text{II}}\text{B}^{\text{VI}}$, $\text{A}^{\text{III}}\text{B}^{\text{VI}}$, and $\text{A}^{\text{IV}}\text{B}^{\text{VI}}$ groups, using ab initio and DFT levels of theory. Clusters presented in the literature may be stoichiometric or nonstoichiometric, naked or ligand-protected, and charged or neutral, so we tried to organize our Review with respect to this classification. The simplest system contains just four atoms, whereas the largest models can consider a few hundred atoms.

5.1. Group 12: $\text{A}^{\text{II}}\text{B}^{\text{VI}}$ ($\text{A}^{\text{II}} = \text{Cd, Zn, Hg}$; $\text{B}^{\text{VI}} = \text{S, Se, Te}$)

5.1.1. Cadmium Chalcogenides: CdS , CdSe , and CdTe . Cadmium chalcogenides have been widely used in quantum dots. Their unique optical properties have led to a multitude of investigations related to biological imaging, solar energy production, etc. The strong experimental interest has also led to significant theoretical attention on these systems.

5.1.1.1. Stoichiometric Bare Clusters. **5.1.1.1.1. Cadmium Sulfide.** Several articles have examined theoretical studies of the structural and electronic properties of cadmium sulfide.^{926–929} The lowest-energy structures and the electronic properties of

small Cd_nS_n ($n = 1–8$) clusters have been studied by using density functional theory by Chu et al.⁹²⁶ For Cd_nS_n clusters with $n = 1–3$, the lowest energy structures are planar, whereas for systems with $n = 4–8$, the three-dimensional structures have the lowest energy. Calculations show that the magic numbers of Cd_nS_n clusters are systems with $n = 3$ and 6. As the cluster size increases, the properties of cadmium sulfide clusters tend to bulk-like ones in binding energy per CdS unit and Mulliken atomic charge.

Large wurtzite and zinc-blende cadmium sulfide Cd_nS_n ($n = 16, 37, 57, 81$) clusters as a function of their size were studied by Joswig et al.⁹²⁷ The calculations were performed by using a linear combination of atomic orbitals and the local density approximation (LCAO DFT LDA) scheme. Spherical cutouts of wurtzite and zinc-blende crystals were considered as the initial structures. During geometry optimization, the largest changes occur in the outer region (up to 2–3 Å for the outermost atoms). In this region, sulfur atoms move away from the center, whereas the cadmium atoms approach the center. A geometry analysis shows that cadmium prefers a high coordination, whereas sulfur atoms for many systems prefer low. For the infinite system, the wurtzite structure is more stable than zinc-blende, whereas for the finite system, the relative stability of these two structures is strongly dependent on the size of the system. Investigation of the electronic properties of these systems indicates a connection between the HOMO–LUMO energy gap and stability: the more stable clusters have a larger energy gap. The HOMO orbital for all clusters was delocalized over the whole cluster, whereas the LUMO was localized between a few surface atoms.

A comparative analysis of stability for nanorods and nanowires of CdSe with different building block geometries has been performed using density functional theory.^{928,929} Clusters ($\text{Cd}_{13}\text{S}_{13})_n$ with $n = 1–6$ that were created from wurtzite and magic-size nanocluster building blocks ($\text{Cd}_{13}\text{S}_{13}$) were made with periodic density functional theory by Sangthong et al.⁹²⁸ Calculations show that the ultrathin nanorods of the magic-cluster-based (“non-bulk-like atomic structures”) structure are more energetically stable than the “correspondingly-sized” bulk-like wurtzite nanorods up to a length of 10 nm. These novel nonbulk-like atomic structures can be potentially useful for new nanoscale properties. Another type of condensed clusters ($\text{Cd}_n\text{S}_n)_m$, where $n = 1–4$ and $m = 1–9$, was presented by Karthikeyan et al.⁹²⁹ The fundamental building blocks of condensed clusters Cd_nS_n ($n = 1–4$) were considered with linear, rhombic, triangular, and square geometries. The most stable condensed systems ($\text{Cd}_n\text{S}_n)_m$ are clusters with building block Cd_3S_3 (triangular isomer), but they can fragment into two small pieces by the application of an external temperature. Electronic properties of condensed clusters with $m > 4$ show a lower energy gap as compared to the bulk CdS system that can be interesting in photocatalytic applications.⁹²⁹

Optical and electronic properties of large cadmium sulfide clusters up to 144 atoms with zinc-blende- and wurtzite-derived structures were studied using the time-dependent extension of a density functional tight-binding method.⁹³⁰ Moreover, the calculations of the single-particle energy eigenvalue have been made for nonrelaxed spherical cutouts of the crystal structure (up to 444 atoms). The comparison of the calculated spectra to the joint densities of states did not show any shift of the lowest-energy transitions, whereas the spectra indicated strong fluctuations in the onset energies depending on the structural

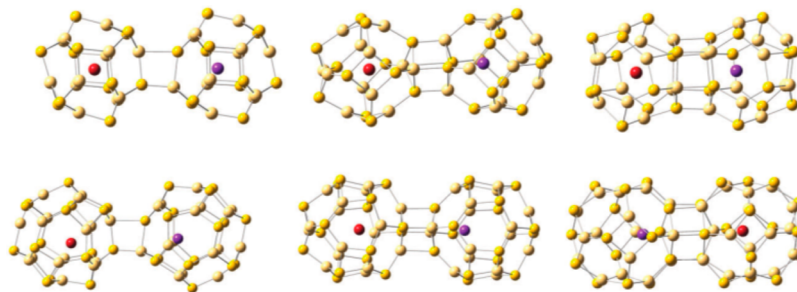


Figure 19. Top: $\text{K}@\text{Cd}_{12}\text{S}_{12}-\text{Br}@\text{Cd}_{12}\text{S}_{12}$ linked together by their edges, squares, and hexagons, respectively, are shown. Bottom: $\text{K}@\text{Cd}_{16}\text{S}_{16}-\text{Br}@\text{Cd}_{16}\text{S}_{16}$ linked together by their edges, squares, and hexagons, respectively, are shown. Violet, K atom; red, Br atom; dark yellow, S atoms; and light yellow, Cd atoms. Reproduced with permission from ref 932. Copyright 2012 PCCP Owner Societies.

properties of the clusters, in particular on the number of single-bonded atoms at the surface. The intense low-lying excitations in the spectra with a large number of unsaturated cadmium atoms indicate that these excitations may be of a collective mode that are observed experimentally in metal clusters as surface plasmon excitations. The HOMO–LUMO gap is a function of the cluster size and decreases with increasing size.

Another interesting type of cadmium sulfide cluster is hollow-cage structures.^{931,932} Geometry optimizations and the calculation of the properties of stoichiometric cadmium sulfide Cd_nS_n ($n = 2-12$) clusters are performed using density functional theory (the BPW91 method with cc-pVDZ-PP for Cd and 6-311+G* for S).⁹³¹ The systems with $n = 2-5$ have ring geometrical configurations, whereas clusters at $n = 6-12$ possess hollow cage structures. Calculated optical spectra show that the most intense features are around 3–4 eV, while low-intensity features appeared at values that are close to the CdS bulk forbidden gap. Also, hollow cadmium sulfide clusters with trapped alkali metals and halogen atoms inside the cavity were studied by Jimenez-Izal et al. using DFT methods (B3LYP with SKBJ and 6-311+G(d)).⁹³² This work focused on analyses of bare Cd_nS_n and endohedral $\text{K}@\text{Cd}_n\text{S}_n-\text{X}@\text{Cd}_n\text{S}_n$ ($n = 12, 16$; X = Cl, Br) clusters (Figure 19). In all of the dimers, the electronic and structural integrity of bare nanoclusters are completely retained. The stability of the dimer decreases with a decreasing number of bonds between monomers. Their results show that it is possible to stabilize new nanoporous polymorphic solid phases of CdS with much larger unit cells as compared to the solid phases found in nature.

5.1.1.1.2. Cadmium Selenide. Several theoretical investigations of the structural, electronic, and optical properties of the small stoichiometric cadmium selenide clusters have been undertaken.^{933,934} Small Cd_nSe_n clusters ($n = 2-8$) were studied by Troparevsky and co-workers using ab initio pseudopotentials within the local density approximation (TDLDA).^{933,934} The investigation of the geometries for these systems shows that Cd atoms have a tendency to be surrounded by bridging chalcogenide atoms.⁹³³ The calculated values of the band gaps oscillate with the changing number of atoms in the CdSe clusters. The binding energies increase significantly with increasing system size up to 6 atoms (Cd_3Se_3), but after this the binding energies became an oscillatory function as well. The results illustrate that clusters Cd_nSe_n with $n = 3$ and 6 are more stable; they exhibit the highest HOMO–LUMO gaps and largest binding energies. Clusters Cd_3Se_3 and Cd_6Se_6 have equivalent triangle and octahedron geometry structures, respectively. The structure,

HOMO–LUMO gaps, and absorption edge indicate “magical” behavior of these clusters.⁹³⁴

For larger CdSe clusters, there are many investigations in the literature about the influence of the cluster size on the structure, electronic, and optical properties.^{935,936} Jose and co-workers⁹³⁵ studied the structural, electronic, and optical properties of CdSe clusters with diameters of up to 2 nm by combining experimental methods (absorption, photoluminescence, and X-ray diffraction spectroscopies) and theoretical DFT calculations. DFT calculations were performed at the B3LYP/LANL2DZ level for Cd_nSe_n ($n = 3, 6, 13$, and 16) clusters. Experimental spectra and calculations show that the minimum building unit of a cadmium selenide cluster is Cd_3Se_3 , which is a six-membered planar ring structure. The HOMO–LUMO gap is increased with the increasing size of the CdSe cluster. Additionally, the absorption spectra were calculated for the smallest Cd_3Se_3 and the largest $\text{Cd}_{16}\text{Se}_{16}$ clusters, including solvent molecules such as triethylphosphine (TEP), triethylphosphine oxide (TEPO), and monoethylamine (MEA). Their results show that the interaction of TEPO is twice as strong as that of TEP with both clusters, whereas neither solvent strongly shifted the absorption band.

A combination of structure enumeration, Monte Carlo searches, and local optimizations were employed for the study of structures of $(\text{CdSe})_n$ ($n = 1-37$) clusters.⁹³⁶ Electronic structure calculations were calculated with density functional theory (B3LYP with VDZ-SD and VDZ-SD* basis sets). Bare magic-size Cd_nSe_n clusters with $n = 9, 12, 16, 18, 21, 24, 28, 32, 33, 35$, and 36 have a high relative stability and were predicted to be cages, cage-core, and tubular structures capped with squares and hexagons, similar to the structures of carbon single-wall nanotubes. Clusters with $n = 34, 37, 47, 52$, and 54 have wurtzite structures and are generally more stable for large clusters.

Furthermore, a number of articles have been dedicated to the investigation and comparison of cadmium selenide with related cadmium sulfide^{938,939} and zinc sulfide⁹³⁷⁻⁹³⁹ systems. Cadmium sulfide and cadmium selenide have been found to exhibit very similar properties.⁹³⁸⁻⁹⁴⁰ Deglmann et al.⁹³⁸ used the Becke–Perdew functional (BP86) and SVP basis set for investigations of small ligand-free CdX (X = S, Se) clusters and large (with up to 198 atoms) CdSe crystals with wurtzite modification. For clusters Cd_nX_n up to $n = 5$, the global minima are ring-like with coordination number two for all atoms, whereas three-dimensional networks are found only for larger clusters. Also, they determined electron affinities, ionization potentials, and electronic excitation spectra for these clusters. Sanville and co-workers combined experimental and theoretical

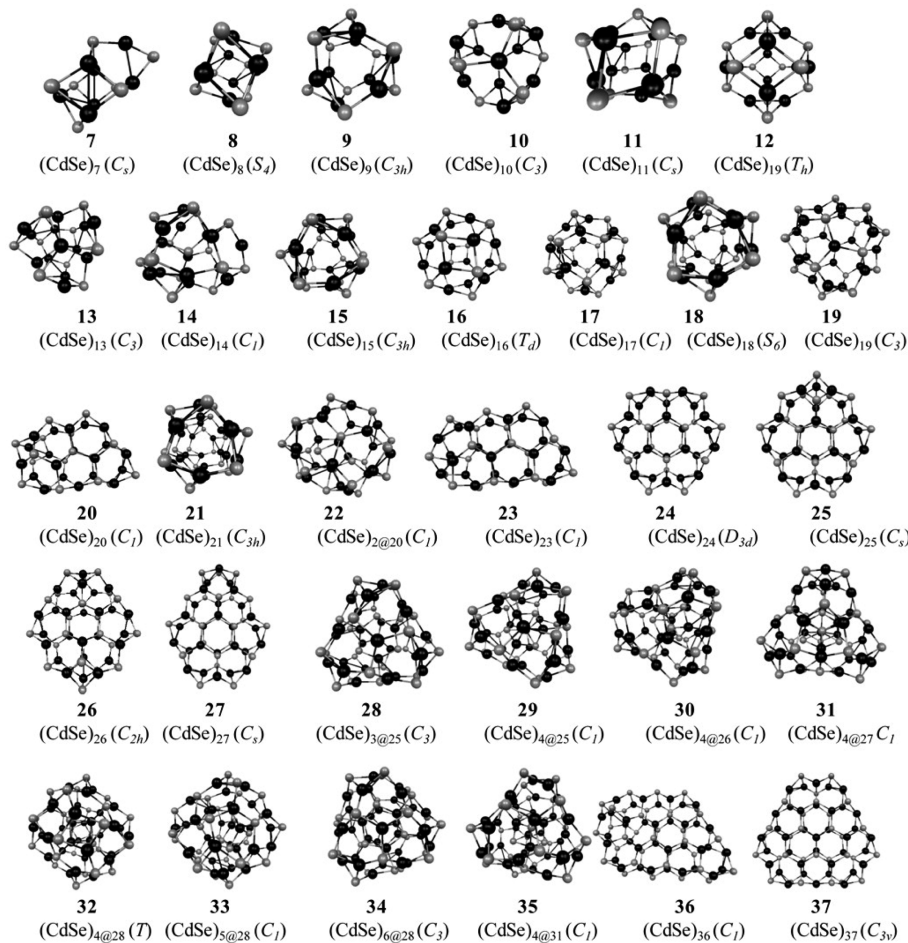


Figure 20. Structures of $(\text{CdSe})_n$ calculated using PBE0. Adapted with permission from ref 937. Copyright 2013 American Chemical Society.

(DFT) methods to study structure and electronic properties of both cadmium sulfide and cadmium selenide Cd_nX_n ($\text{X} = \text{S}, \text{Se}$; $n = 1-16$) clusters.⁹³⁹ The experimental mass spectra showed that clusters with $n = 6$ and 13 were ultrastable. The geometries and properties such as HOMO–LUMO gaps, first excitation energies, vertical ionization energies, and molar atomization energies were calculated for neutral and positively charged Cd_nX_n clusters at the B3LYP level theory with SKBJ and SKBJ(d,2df) basis sets. Small neutral and charged clusters with n less than 5 have planar geometries, but the larger neutral clusters have closed-cage polyhedral geometries, whereas large cationic systems show structures with a pair of two-coordinated atoms. With increasing cluster size, the molar atomization and ionization energies of the neutral clusters trend toward the qualitative values of corresponding bulk parameters, whereas the calculated HOMO–LUMO gaps are shown to trend to the qualitative values of the bulk band gap energies.

The study of size-dependent properties of cadmium selenide Cd_nSe_n clusters with up to 200 atoms in the system was performed using density functional theory with a linear combination of atomic orbitals and the local density approximation (LCAO DFT LDA) by Sarkar et al.⁹⁴⁰ The zinc-blende-, wurtzite-, and rocksalt-derived structures of different sizes $n = 16, 35, 37, 58$, and 83 were considered. The first two geometrical structures of cadmium selenide clusters are more favorable than rock-salt structures and depend significantly on the size of the cluster. In this work, the spherical cutouts of zinc-blende, wurtzite, and rocksalt crystals were

considered as initial structures, which were relaxed to their closest local minimum. With the geometry optimization procedure, the largest changes occur in the outer region of the cluster: Se atoms move away from the center of the cluster, whereas Cd atoms approach the center. The HOMO is localized throughout the whole cluster, whereas the LUMO is centered on atoms near the surface. The HOMO–LUMO energy gap oscillates strongly as a function of the size of the cluster. The geometrical changes during optimization and electronic properties for these CdSe clusters are close to the results for CdS clusters⁹²⁷ described above.

Another comparative investigation of the structures and optical properties of bare Cd_nSe_n and Zn_nS_n ($n = 1-37$) clusters (Figure 20) and their amine-ligated analogs studied with DFT and TDDFT methods was presented by Nguyen et al.⁹³⁷ Bare zinc and cadmium selenide clusters with $n = 8-12$ and 15–19 have spheroidal and tubular structures, whereas cage-core structures are more preferable for $\text{Zn}_{13}\text{S}_{13}$, $\text{Cd}_{13}\text{Se}_{13}$, and $\text{Cd}_{14}\text{Se}_{14}$. Large clusters with $n = 23-27$, 36, 37 and $n = 28-35$ have wurtzite and cage-core structures, respectively. The most stable clusters for zinc sulfide and cadmium selenide are $\text{Zn}_{32}\text{S}_{32}$ and $\text{Cd}_{32}\text{Se}_{32}$ with cubic cores. The properties of small amine-capped clusters with $n = 8-9$, 12–15, 20 are very similar to their bare analogues.

The effect of cluster size on the optical properties has been studied in several articles.^{941,942} Troparevsky et al. investigated wurtzite clusters Cd_nSe_n ($n = 17, 26, 38$) using time-dependent density functional theory and the local density approximation

(LDA and TDLDA).⁹⁴¹ The time-independent LDA calculated spectra show significant differences with respect to the TDLDA spectra. The LDA spectra are red-shifted and have more strong peaks in the low-energy region than TDLDA spectra. Also, TDLDA calculated optical gaps are in good agreement with the experiment data: the measured band gap for cluster Cd₁₇Se₁₇ is equivalent at 3.8 eV, whereas for large clusters this value is close to the bulk value of 1.7 eV. The photoabsorption spectrum of the cadmium selenide cluster Cd₃₄Se₃₄ in the pearl-necklace geometry has also been calculated with the first-principles approach based on DFT within the LDA.⁹⁴² To simulate the pearl-necklace geometry, three types of supercells were used (x , y , and z -directions were shortened). The results vary with respect to the directions in which the cluster was approximated. The supercell where the x direction is shortened gives the most stable Cd₃₄Se₃₄ chain; also, the photoabsorption spectra show the same type of peaks, which is observed experimentally.

Besides studying the structure and optical properties of cadmium selenide clusters, some investigations have focused on highly excited electronic states, phonon-assisted hot electron relaxation dynamics, phonon bottlenecks, etc.^{943–945} First-principles calculations for cadmium selenide quantum dots Cd _{n} Se _{n} ($n = 6, 33, 111$) were studied using a combination of the Hartree–Fock approximation and the symmetry adapted cluster theory with configuration interaction (SAC–CI).⁹⁴³ By investigating the nature of highly excited electronic states in PbSe and CdSe clusters (Figure 21), Isborn and co-workers

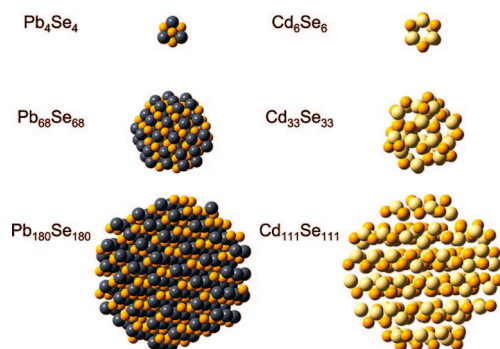


Figure 21. Geometric structure of the PbSe and CdSe QDs used in the calculations. Reprinted with permission from ref 943. Copyright 2008 American Chemical Society.

showed that multiple excitons (MEs) could be generated in CdSe directly upon absorption of a single photon. Optically active multiple excitons were found at high energies. The continuum band structure of CdSe QDs created a mixing of single excitations and MEs at higher energies, indicating that several carrier multiplication (CM) or multiple exciton generation (MEG) mechanisms can be in play.

Chen and co-workers used time-domain nonadiabatic ab initio simulations to study the phonon-assisted hot electron relaxation dynamics in a spherical quantum dot Cd₃₃Se₃₃ (QD) and an elongated quantum dot Cd₅₄Se₅₄ (EQD) with the same diameter.⁹⁴⁴ The elongated structure has the most narrow band gap, and the electron and hole states show higher density with respect to the spherical quantum dot. The band gap shows negative temperature dependence for both the QD and the EQD. The electron–phonon coupling is stronger in the EQD than in the QD. The hot electron decay rate is higher and shows stronger temperature dependence in the EQD than in

the QD. The calculations show that the shapes of nanoclusters can affect the optical and electronic properties. Using time-dependent DFT methods, Kilina et al.⁹⁴⁵ studied the phonon bottleneck in wurzite structure semiconductor quantum dots such as Cd₃₃Se₃₃ and core–shell Cd₃₃Se₃₃/Zn₇₈Se₇₈. These results demonstrated that the phonon bottleneck to the electron–phonon relaxation in semiconductor quantum dots is a special case of the quantum Zeno effect, whereas the conditions necessary for the quantum Zeno effect are also required for the phonon bottleneck. The defects of the shell in the Cd₃₃Se₃₃/Zn₇₈Se₇₈ structure reduce the electron–hole separation and develop the Auger channel.

The effect of the cluster size on electric polarizability and anisotropy for Cd _{n} Se _{n} ($n = 1–16$) clusters was studied with DFT methods (BP86/SVP).⁹⁴⁶ The results show that the electric polarizability values decrease with increasing numbers of atoms in the system n from 1 to 7, with one exception for Cd₅Se₅ clusters where the polarizability value increased. Beyond $n = 7$, the polarizability value does not change significantly. The variation in the anisotropy values for clusters looks almost similar at both static and dynamic frequencies. The HOMO–LUMO energy gap increases for Cd _{n} Se _{n} clusters with n up to 3, whereas beyond (CdSe)₇, no significant changes are observed.

5.1.1.3. Cadmium Telluride. Structure and electronic properties of cadmium telluride clusters (CdTe) were investigated and presented in several articles.^{947,948} Small cadmium telluride clusters Cd _{n} Te _{n} ($n = 2–7$) were studied with density functional theory (B3LYP/LANL2DZ) by Sriram and Chandramouli.⁹⁴⁷ In this article, the authors considered different structures such as linear, ring, and three-dimensional. Their results show that the stability of the system increases with the increasing of system size. The 3-D structures have a higher binding energy as compared to linear and ring structures; the ionization potentials for all 3-D structure are almost identical. 3-D and linear structures have higher dipole moments than ring structures. The HOMO–LUMO gaps and ionization potentials for linear structures are almost similar regardless of size, whereas for rings, these parameters oscillate. The structural and electronic properties of large systems such as (CdTe)_{12 n} ($n = 1–5$) multicage nanochains have been studied by density functional theory (PBE with Double Numerical plus Polarization atomic orbital basis set (DNP)).⁹⁴⁸ The building unit of multicage nanochains is Cd₁₂Te₁₂. The two interconnecting building blocks can be linked in two possible ways by their four-membered rings (IFMR) and by their six-membered rings (ISMR). The results show that these nanochains are more stable than the single cage, whereas the ISMR structure is more energetically favorable than the IFMR. The nanochains with $n \leq 3$ show the typical behavior of quantum dots in that the HOMO–LUMO gaps are sensitive to the length of the nanochains. The longer nanochains ($n \geq 4$) do not show size-dependence of band gaps.

Polarizabilities for CdTe clusters were calculated using the density functional theory level of theory.^{949–951} The dipole polarizabilities, the polarizability anisotropies, and the second hyperpolarizabilities of the ground-state structures of stoichiometric Cd _{n} Te _{n} ($n = 2, 3, 4, 5, 9$) clusters were studied by Karamanis et al. using ab initio and DFT levels of theory.⁹⁴⁹ Also, the effect of the cluster equilibrium geometry on the properties of interest was investigated. The more compact is the predicted structure, the less (hyper)polarizable it becomes. The second hyperpolarizabilities are significantly sensitive to the obtained equilibrium interatomic distances among the

electropositive Cd atoms. Cadmium telluride clusters were found to be far more hyperpolarizable than CdS and CdSe clusters. Wang et al.⁹⁵⁰ studied the structural growth behavior and polarizability for Cd_nTe_n ($n = 1\text{--}14$) clusters using density functional theory. Two types of structures were found: hollow cages and endohedral (core–shell) cages. The hollow cages possess smaller dipole moments and larger polarizabilities than the endohedral ones. The endohedral cages become more stable for $n \geq 12$. A large HOMO–LUMO gap and higher binding energy is observed for Cd₁₃Te₁₃ with the core–shell cage configuration. The results show a cluster geometry and symmetry effect to the dipole moments and polarizabilities. The anisotropies of the cluster polarizability are correlated with the cluster shape. A search of the lowest-energy structures of larger Cd_nTe_n clusters ($n = 15, 16, 20, 24$, and 28) with DFT methods was continued in a later article by Ma et al.⁹⁵¹ Their calculations showed that the endohedral or core–shell cages are more stable than the hollow cages. The hollow cages show smaller dipole moments and larger polarizabilities than the endohedral clusters of the same size.

Structures of different cadmium chalcogenide clusters Cd_nX_n (X = S, Se, Te; $n = 1\text{--}16$) were studied by using the hybrid B3LYP gradient-corrected density functional procedure with the SKBJ basis set.⁹⁵² Different types of structures were considered such as rings, chains, spheroids, distorted spheroids, and cluster tubes. The results show that the most stable structures for clusters Cd_nX_n with $n \leq 5$ are ring-like structures, whereas for larger systems the three-dimensional spheroidal structures are preferable. For all CdX, the largest HOMO–LUMO gaps correspond to the rings and the smallest ones to the cluster tubes.

5.1.1.2. Stoichiometric Ligand-Passivated Clusters.

5.1.1.2.1. Cadmium Selenide. The effects of ligands on the structural, electronic, and optical properties of cadmium selenide were investigated. For passivation of a surface of the cadmium chalcogenide clusters, the different types of ligands were considered. The most widely used ligands are hydrogen, pyridine, amino-, and thio-groups, as well as phosphine and phosphine oxides. In some rare cases for stabilization of these semiconductors, nucleobases (such as adenine and cytosine)^{953,954} and augmented gold clusters⁹⁵⁵ were also used.

The influence of the nature of ligands on the structural and electronic properties has been studied in several articles.^{956–960} Puzder et al.⁹⁵⁶ studied the effect of organic ligand binding on the growth of cadmium selenide semiconductor nanoparticles. The interactions between organic molecules (phosphine oxides, amines, and phosphonic and carboxylic acids) and the surface of wurtzite Cd₁₅Se₁₅ and Cd₃₃Se₃₃ were simulated by ab initio calculations. They found that the dominant binding is between oxygen atoms in the ligands and the Cd atoms on the cluster surfaces. The most strongly bound ligands are phosphonic acid molecules. The calculated relative binding strengths of ligands to different facets support the hypothesis that these binding energies control the relative growth rates of different facets, and therefore the resulting geometry of the nanoparticles. Yang et al. studied the influence of ligands and charges on small and medium size CdSe systems such as Cd₆Se₆ and Cd₁₃Se₁₃ quantum dots using DFT methods.⁹⁵⁷ The bare clusters (wurtzite and cage) and their ligand-passivated structures (ligands are PH₃, PMe₃, NH₃, OPH₂Me) were calculated at the B3LYP/LANL2DZ level of theory. Phosphine and amine ligands could not form a bridging coordination bond between two surface cadmium atoms, while OPH₂Me (TOPO) could.

The binding energy between the CdSe cluster and ligands decreases in the order: Cd–O > Cd–N > Cd–P. Charges on quantum dots show a strong effect on the binding energies and structural and optical properties. Also, their results show that optical properties are controlled by the core structure with the inclusion of surface reorganization.

The effects of different combinations of ligands on the properties of the clusters were studied by Del Ben et al. by DFT methods.⁹⁵⁸ The structures of wurtzite Cd_nSe_n ($n = 13, 19, 33$, and 66) magic-size clusters were protected by various ligands pairs such as formate–hydrogen, acetate–hydrogen, formate–hydrogen–ammonia, and ammonia and methyl amine. The best agreement between the calculated and the experimental optical absorption spectra was achieved for the clusters capped only with the formate–hydrogen pair. For Cd_nSe_n with $n = 33$ and 66, absorption spectra show a clear peak in the low-energy region, without other pronounced features at a higher energy. The excitonic peak arises from three strong transitions from the HOMO, HOMO–1, and HOMO–2 orbitals going to the LUMO orbital. All of these three transitions can be described as charge transfer from surface selenium p states to inner cadmium s states.

Kuznetsov et al. investigated the properties of small and large cadmium chalcogenide clusters using DFT.^{959,960} Calculations for small cadmium selenide and telluride nanoparticles, both bare Cd_nX_n and capped Cd_nX_nR_n (X = Se, Te; $n = 6, 9$; R = amino, thio, or phosphine oxide ligands), were performed using B3LYP/LANL2DZ.⁹⁵⁹ Effects of solvents (water and toluene) on nanoparticle structures and properties were also investigated. Ammonia and phosphine oxide ligands cause HOMO/LUMO energy destabilization in capped nanoparticles. Calculated ionization potentials and electron affinities of CdX clusters with NH₃ and OPH₃ are dramatically reduced as compared to bare structures. SCH₃ groups cause destabilization of the HOMOs of the capped CdX and stabilization of their LUMOs. Investigation for the larger bare Cd₃₃X₃₃ and capped Cd₃₃X₃₃R₂₁ (X = Se, Te; R = NH₃, SCH₃, and OPH₃) quantum dots was performed using DFT (B3LYP/LANL2DZ) theoretical calculations.⁹⁶⁰ The calculated optical gap for bare Cd₃₃Se₃₃ is larger than that for Cd₃₃Te₃₃. The NH₃ ligand does not significantly affect the properties of both clusters. For the SCH₃-capped QD, the binding energy is higher for cadmium telluride. The band gaps for Cd₃₃X₃₃(SCH₃)₂₁ (X = Se, Te) decreased in both cases upon SCH₃ binding. The binding energy for OPH₃ with CdX is very small. The HOMO–LUMO gaps for these Cd₃₃X₃₃(OPH₃)₂₁ complexes are strongly dependent on the chalcogenide atom type. Also, for the Cd₃₃Se₃₃ cluster, the effects of ligand size were studied, and larger ligands such as N(CH₃)₃ and SCH₂CO₂H were used. The trimethylamine does not significantly affect the semiconductor core and is similar to NH₃-ligand, whereas SCH₂CO₂H causes a very strong CdSe core distortion. The inclusion of an implicit solvent in calculation showed that solvent effects have strong influence on the geometries and orbital energies of these clusters.

The electronic structure and optical absorption of a single source precursor (CSP) for CdSe quantum dots were studied with the application of DFT and TDDFT methods.⁹⁶¹ The investigated structure of CSP is the parallelogram Cd₂Se₂ core surrounded by six additional selenium atoms; also, each pair of Se bonds with one diphenylphosphine PPh₂ group (cadmium bis(diselenophosphinate), Cd₂Se₂Se₆(PPh₂)₄). The results show that Cd–Se covalent bonds, which were observed in

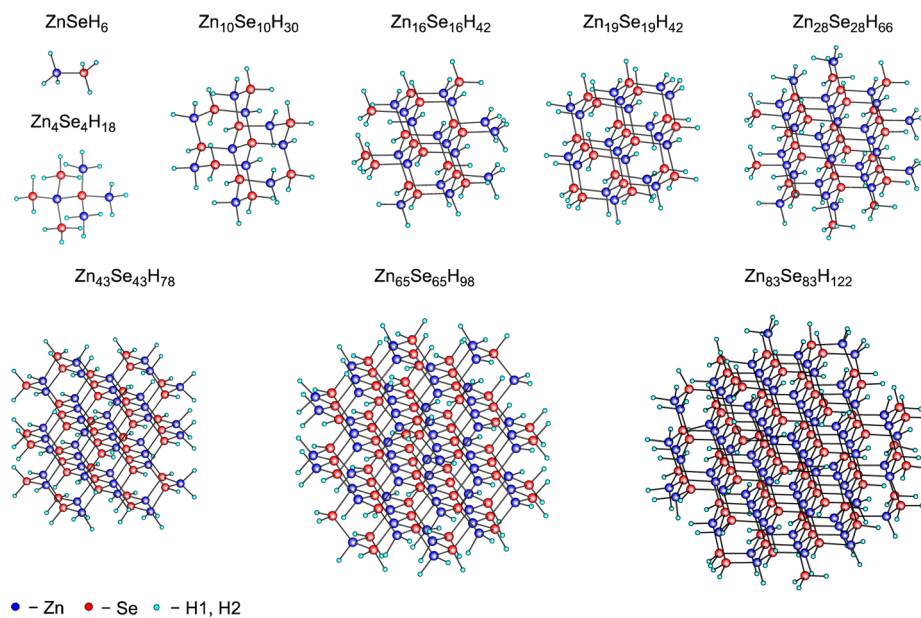


Figure 22. Structures of ZnSe quantum dots passivated with partially charged hydrogen atoms. Reprinted with permission from ref 965. Copyright 2014 Elsevier.

the ligand free Cd_2Se_2 cluster, transformed to a coordination type of bond in the bonds in the single source precursor system. The HOMO and LUMO are localized on individual atoms including the atoms of ligands. The absorption spectrum for this precursor complex is blue-shifted as compared to the bare clusters, which can reflect the involvement of ligand atoms in the electronic transition.

The influence of ligands on the optical properties of the cadmium chalcogenide clusters is presented in a number of articles.^{936,962–966} The structural, electronic, and optical properties of cadmium selenide Cd_nSe_n ($n = 6, 15, 33$, and 45) wurtzite structure clusters with and without ligands were studied by a plane wave implementation of density functional theory (DFT).⁹⁶² Supercells were chosen with at least 10 \AA between replicas to remove spurious periodic interactions. The geometry relaxation of cadmium selenide clusters was performed both in vacuum and in the presence of surfactant ligands (trioctyl phosphine oxide and hexyl-phosphonic acid bound to the surface) to investigate the effect of organic ligands on the atomic geometry of the CdSe nanoclusters. The results show that the structures of ligand-protected clusters are similar to those of unpassivated relaxed structures, but small changes occur locally due to the weak bonds formed between the surface atoms and the ligands. The authors also noted that orbital hybridization effects are significant in CdSe clusters and exhibit behavior similar to that of the bulk cadmium selenide surface. The surface metal atoms prefer to form sp^2 -like bonds with their three nearest anion neighbors. The calculated HOMO–LUMO gaps for the clusters without any surface passivation are $1\text{--}2 \text{ eV}$; the passivating ligands do not affect the optical gap in any significant manner.

Nguyen et al. investigated the optical properties of bare and capped $(\text{CdSe})_n$ ($n = 1\text{--}37$) magic-size quantum dots, and the effects of ligands/solvent on the structural and optical parameters were examined for selected clusters.⁹³⁶ The binding energies decreased in the order $\text{NH}_3 > \text{OP(OH)}_2\text{CH}_3 > \text{H}_2\text{O} > \text{NH}_2\text{CH}_3 > \text{CH}_3\text{COOH} > \text{HCOOH} > \text{OP(CH}_3)_3 > \text{N(CH}_3)_3 > \text{P(CH}_3)_3$. The binding strength decreases with increasing

cluster size. Absorption spectra of ligand-protected clusters are blue-shifted as compared to the bare clusters.

The influence of the solvent and ligand on the structural and optical properties of zinc blende Cd_4Se_4 and wurtzite models of $(\text{Cd}_3\text{Se}_3)_n$ ($n = 1, 2, 3$) nanocrystals was studied with density functional theory (B3LYP/LANL2DZ) by Xu et al.⁹⁶³ The ligands $-\text{S}-\text{CH}_2-\text{CH}_2-\text{COOH}$, $-\text{S}-\text{CH}_2-\text{CH}_2-\text{N}(\text{CH}_3)_2$, $-\text{S}-\text{CH}_2-\text{CH}_2-\text{NH}_2$, $-\text{S}-\text{CH}_2-\text{CH}_2(\text{OH})$, $-\text{S}-\text{CH}_2-\text{CH}-(\text{NH}_2)-\text{COOH}$, $-\text{S}-\text{CH}_2-\text{CH}(\text{OH})-\text{CH}_2(\text{OH})$, and $-\text{S}-\text{CH}_2-\text{COOH}$ were considered. Calculated absorption spectra show that both the solvent and the ligands make the absorption spectra shift to the blue. All transitions of these absorption peaks are from d to p orbitals. Moreover, HOMO–LUMO gaps become smaller with the order of $\text{Cd}_3\text{Se}_3 > (\text{Cd}_3\text{Se}_3)_2 > (\text{Cd}_3\text{Se}_3)_3$. All ligands have a similar influence on CdSe nanocrystals.

Nadler et al.⁹⁶⁴ also examined ligand effects on the optical properties of the bare Cd_nSe_n ($n = 6, 13$, and 34) and methylamine(MA)-capped $\text{Cd}_6\text{Se}_6(\text{MA})_6$, $\text{Cd}_{13}\text{Se}_{13}(\text{MA})_9$, and $\text{Cd}_{34}\text{Se}_{34}(\text{MA})_{22}$ nanoclusters using LR-TDDFT. For the $\text{Cd}_{13}\text{Se}_{13}$ cluster, the absorption spectrum significantly depends on which Cd surface atoms the methylamine ligands are adsorbed to; some $\text{Cd}_{13}\text{Se}_{13}(\text{MA})_9$ clusters show a strong blue-shift in the optical spectrum.

DFT and TDDFT methods were also used to investigate the structures, densities of states, absorption spectra, and optical gaps of spherical CdTe and ZnSe semiconductor quantum dots with sizes up to 2.2 nm passivated by partially charged hydrogen (Figure 22); structures $\text{Cd}_n\text{Te}_n\text{H}_m$ ($n = 1, 4, 10, 16, 19, 28, 43, 65, 83$; $m = 6, 18, 30, 42, 66, 78, 98, 122$) were considered.⁹⁶⁵ The calculations demonstrate that the passivation of the cadmium telluride nanoparticle by hydrogen effectively removes the surface trap states from the gaps and does not affect the energies of the electronic states of semiconductors. In addition, the calculated HOMO–LUMO gaps show size dependence, and the band gaps decreased with increasing cluster diameter.

Azpiroz et al. used DFT and TDDFT methods to investigate the optoelectronic properties of bare and ligand-protected

magic $(\text{CdSe})_{13}$ nanoclusters (ligands are methylamine, pyridine, and aniline).⁹⁶⁶ The core cage configuration $\text{Se}@\text{Cd}_{13}\text{Se}_{12}$ has a lower energy than fullerene- and wurtzite-like structures. All of the ligands exhibit strong interactions with the CdSe core, with calculated bond energies of about 20 kcal/mol. Also, calculations show that the surface ligands and solvent have a strong effect on the optoelectronic properties of $(\text{CdSe})_{13}$. The calculated absorption spectrum of the methylamine-protected $(\text{CdSe})_{13}$ cluster is significantly blue-shifted as compared to the pure cluster. The inclusion of solvent (toluene and water) effects moves the absorption bands of bare CdSe clusters to higher energies.

The influence of passivating ligands (amines, phosphines, phosphine oxides, and pyridines) on the electronic and optical spectra of $\text{Cd}_{33}\text{Se}_{33}$ quantum dots was examined using density functional theory and time-dependent DFT.^{967–972} Kilina et al. examined a cadmium selenide cluster capped by 9 or 21 molecules of methylamine (NH_2Me) and trimethylphosphine oxide (OPMe_3).⁹⁶⁷ Cadmium selenide binds slightly stronger with NH_2Me than with OPMe_3 . In the fully ligated clusters, neither the ligand-localized nor hybridized molecular orbitals appear as trap states inside or near the band gap of the cadmium cluster. The loss of one of the ligands leads to either optically dark or bright additional states inside of the band gap, depending on the position of the leaving ligand on the cluster surface. For these systems, phosphine and pyridines ligands were also considered.⁹⁶⁸ Amine and phosphine oxide ligands provide stronger binding with the QD surface than phosphines and pyridines.

The electronic structure of the ligated $\text{Cd}_{33}\text{Se}_{33}-\text{OPMe}_3$ cluster was also studied with DFT and TDDFT calculations using different atom-localized basis sets and functionals in gas phase and in solvent by Albert et al.⁹⁷¹ They analyzed the sensitivity of geometry, QD–ligand interaction, band gap, and the lowest-energy optical transition of this system on the basis set and solvent. Both geometries and QD–ligand interaction binding energies are strongly dependent on the basis set size. A polar solvent has a dramatic effect on the QD–ligand binding, and decreases the interaction. The effect of the solvent model on the band gap and the lowest optical transition is not as strong as in the case of binding energy. The spectrum is blue-shifted with respect to the calculations in the gas phase.

The interactions between $\text{Cd}_{33}\text{Se}_{33}$ nanocrystals passivated by trioctylphosphine oxide (TOPO) ligands and a series of Ru–polypyridine complexes were studied by a combination of experimental (ATR-FTIR spectra) and theoretical methods.⁹⁷² The theoretical part was performed for $\text{Cd}_{33}\text{Se}_{33}-\text{R}$ (R = acetate and acetic acid groups) using DFT with the hybrid B3LYP functional and the LANL2DZ basis set, in a vacuum and in a solvent. Solvent effects were simulated by a conductor-like polarizable continuum model (CPCM). The geometry optimization was initiated from different starting configurations, unidentate, bridging, or chelating. The binding energy of $\text{Cd}_{33}\text{Se}_{33}$ with acetic acid is significantly smaller than the binding energy with the acetate anion. The HOMO–LUMO gaps for all systems simulated in solvent were ~ 3 eV, which agree well with the lowest absorption peak of the experimentally observed spectrum. The results of DFT modeling are consistent with the experiment.

The time-domain Kohn–Sham (TDKS) method was applied to study phonon-assisted dynamics of electrons and holes in $\text{Cd}_{33}\text{Se}_{33}$ passivated by nine OPMe_3 and NH_2Me ligands.⁹⁶⁹ These calculations show that surface ligands can significantly

affect phonon-assisted relaxation rates at high photoexcitation energies. The interaction of ligands with CdSe clusters leads to new manifold-hybridized orbitals, which are delocalized over surface quantum dot atoms and ligand molecules.

Calculation of IR and Raman spectra was performed for cadmium selenide quantum dots $\text{Cd}_{33}\text{Se}_{33}-\text{R}$ (R = trimethylphosphine oxide (TMPO) and methylamine (MA)) via DFT calculations.⁹⁷⁰ The simulations were carried out in a cubic cell periodically replicated in three dimensions, where the cell was constructed to have at least 8 Å of vacuum between the replicas. The calculated IR and Raman spectra have good agreement with the experimental data. TMPO and MA ligands bind with the semiconductor cluster through Cd atoms. The strongest interaction between the ligand and quantum dot was obtained with TMPO, which forms covalent bonds with the Cd atoms. In the case of MA, the interaction is weaker and realized through a coordination bond. The reported results show that the interaction between the quantum dot and the ligand effects the changes in the ligand vibrational spectra. The main observations for the TMPO and MA spectra include a strong red-shift in the P=O stretching mode frequency and a strong blue-shift of the NH_2 wagging mode frequency, respectively.

Furthermore, some papers are devoted to investigation of the influence of hole-sequestering ligands on the photostability of cadmium selenide dots.⁹⁷³ Tan et al. calculated the charge distribution on ligand-cluster complexes with B3LYP/LANL2DZ for neutral and cationic forms of $\text{Cd}_6\text{Se}_6-\text{R}$, where R = butanethiol, thiophenol (TP), or 4-dimethylaminothiophenol (DMATP). For butanethiol, the entire charge is on the ligand molecule, whereas TP and especially DMATP have a larger part of the charge on the molecule and a smaller charge on the S atom. Calculations show that the more effective electron donor to CdSe is DMATP, which is also more effective at removing the charge away from the oxidation-sensitive thiol group.

Nucleobases were also considered as possible ligands for passivation of the CdSe clusters.^{953,954} Structures and electronic characteristics for bare Cd_nSe_n ($n = 3, 6, 10, 13$), hydrogen-passivated ($\text{Cd}_n\text{Se}_n\text{H}_{2n}$), and cysteine- and adenine-complexes $\text{Cd}_n\text{Se}_n-\text{R}$, $\text{Cd}_n\text{Se}_n\text{H}_{2n}-\text{R}$, and $\text{Cd}_n\text{Se}_n\text{H}_{2n-2}-\text{Ade}$ ($\text{R} = \text{Cys}$, Cys-Cys , Ade) of cadmium selenide clusters were studied with DFT and TDDFT methods (B3LYP with 6-311++G** and LANL2DZ basis sets).^{953,954} The structural investigations show that the nanoclusters $\text{Cd}_n\text{Se}_n\text{H}_{2n}-\text{Cys}$ and $\text{Cd}_n\text{Se}_n\text{H}_{2n}-\text{Cys-Cys}$ contain a four-membered O–Cd–H–Cd ring. The formation of the Cd–S and Cd–OOC bonds is favorable when Cys or Cys–Cys forms covalent bonds with the hydrogen-passivated cluster.⁹⁵³ The calculated electronic spectra of both systems with cysteine and adenine show that spectra for cadmium selenide with Cys-/Ade- are blue-shifted with respect to bare CdSe, whereas hydrogen passivation together with Cys-/Ade- binding is found to lead to a red-shift.^{953,954}

An investigation of the effects of the length on the electronic structure of bare Cd_nSe_n ($n = 6, 10, 14, 26, 38, 74, 110$) nanorods, nanorods passivated by fictitious hydrogen atoms, and nanorods augmented by attaching Au_{13} gold clusters to both ends was presented by Saraf et al.⁹⁵⁵ Their calculations considered nanorods with a length from 4.6 to 116.6 Å and were performed with DFT using a plane-wave basis set. The initial geometries of the bare CdSe nanorods come from the bulk wurtzite structure. For free-standing nanorods, the HOMO arises mainly from p orbitals of Se, but the LUMO

primarily comes from s orbitals of Cd and Se. To create the $\text{Au}_{13}-\text{Cd}_n\text{Se}_n-\text{Au}_{13}$, the bare Au_{13} -clusters were attached to the fully relaxed nanorods. Optimization of these structures produced a “dumbbell-like” structure (nanodumbbell), where the geometry of gold clusters was changed significantly; furthermore, both Cd and Se atoms at the ends of the nanorods are doubly bonded to the gold atoms. Calculation of the local density of states (LDOS) for gold tipped nanorods shows a gap near the nanodumbbell center, and metal-induced gap states (MIGS) emerge near the metal–semiconductor nanocontact. For short nanorods, a full metallization by these metal-induced gap states (MIGS) was found. Also, the end-passivated nanorods and their separated components show charge transfer that is highly localized at the contact region.

5.1.1.3. Nonstoichiometric Bare Clusters. **5.1.1.3.1. Cadmium Selenide.** The study of the size-dependent structural and electronic properties of stoichiometric and nonstoichiometric cadmium selenide (CdSe) clusters with up to 200 atoms in the system was performed using density functional theory with a linear combination of atomic orbitals and a local density approximation (LCAO DFT LDA) by Sarkar et al.⁹⁴⁰ They formed naked nonstoichiometric Cd_mSe_n ($m \neq n$) clusters by placing the center of the sphere at the cadmium or selenium atom. The zinc-blende derived crystal structure of clusters $\text{Cd}_{28}\text{S}_{19}$, $\text{Cd}_{19}\text{S}_{28}$, $\text{Cd}_{79}\text{S}_{68}$, and $\text{Cd}_{68}\text{S}_{79}$ were studied. For these nonstoichiometric clusters, the tendency of the chalcogen atoms to move outward and of the metal atoms to move inward upon structural relaxation, as found for the stoichiometric clusters, is not recovered here. The HOMO–LUMO gap for nonstoichiometric clusters is significantly smaller in comparison to stoichiometric systems.

Time-dependent local density approximation (TDLDA) and GW/Bethe-Salpeter calculations were used to study the optical properties of nonstoichiometric bare CdSe clusters with sizes from 10 to 82 atoms and similar systems passivated by hydrogen.⁹⁷⁴ The results demonstrate that the optical gaps show a strong dependence on cluster size, decreasing with increasing size. The TDDFT calculations show that the lowest-energy excitation is the result of a single-level to single-level transition and that there are no forbidden (dark) transitions before the first bright transition in most clusters. However, GW/Bethe–Salpeter calculations shows that it is a strong mixture of different transitions that gives origin to the lowest-energy excitation, a signature that excitonic effects are important. There are also dark transitions before the first bright transition for all but one of the clusters studied. Radiative decay lifetimes were calculated and are equivalent to about tens to hundreds of picoseconds, whereas the observed experimental lifetimes are of the order of microseconds, which may be explained by the presence of forbidden transitions in these clusters.

5.1.1.3.2. Cadmium Sulfide. Junkermeir et al. studied nonstoichiometric ($\text{Cd}_{140}\text{S}_{141}$, $\text{Cd}_{152}\text{S}_{141}$, $\text{Cd}_{152}\text{S}_{170}$, and $\text{Cd}_{180}\text{S}_{177}$) and two stoichiometric ($\text{Cd}_{132}\text{S}_{132}$ and $\text{Cd}_{140}\text{S}_{140}$) cadmium sulfide clusters via an ab initio tight-binding analysis.⁹⁷⁵ In a bulk crystal, the HOMO and the states just below the HOMO are localized, while the LUMO and those states just above are highly delocalized. Results show that the relaxation process restored the semiconductor nature of the nanocrystal.

5.1.1.4. Nonstoichiometric Ligand-Passivated Clusters. The influence of ligands on the structural, electronic, and optical properties was studied for nonstoichiometric clusters of

cadmium selenide,^{976,977} sulfide,^{977–979} and telluride.⁹⁷⁷ Ligand-stabilized tetrahedral CdSe clusters such as $\text{Cd}_4(\text{SePh})_6\text{Br}_4^{2-}$, $\text{Cd}_8\text{Se}(\text{SePh})_{12}\text{Cl}_4^{2-}$, $\text{Cd}_{10}\text{Se}_4(\text{SePh})_6(\text{PPh}_3)_4$, $\text{Cd}_{17}\text{Se}_4(\text{SeH})_{24}(\text{PH}_3)_4^{2+}$, and $\text{Cd}_{32}\text{Se}_{14}(\text{SeH})_{36}(\text{PH}_3)_4$ were investigated using DFT by Eichkorn et al.⁹⁷⁶ Their results show that clusters $\text{Cd}_4(\text{SePh})_6\text{Br}_4^{2-}$ and $\text{Cd}_{10}\text{Se}_4(\text{SePh})_6(\text{PPh}_3)_4$ have a perfect adamant cage, whereas $\text{Cd}_8\text{Se}(\text{SePh})_{12}\text{Cl}_4^{2-}$, $\text{Cd}_{17}\text{Se}_4(\text{SeH})_{24}(\text{PH}_3)_4^{2+}$, and $\text{Cd}_{32}\text{Se}_{14}(\text{SeH})_{36}(\text{PH}_3)_4$ exhibit wurtzite-type endings. The calculated absorption spectra show a pronounced trend to a smaller band gap for larger cluster cores. The strongest transitions correspond to HOMO–LUMO excitations of charge-transfer type. Calculated spectra of clusters with different sizes show a red-shift with increasing cluster size. Excitations of charged clusters are shifted to the red for anions and to the blue for cations with respect to the neutral systems.

The effect of ligands on the tetrahedral cadmium chalcogenide clusters CdX ($X = \text{S}, \text{Se}, \text{Te}$) was investigated by Gurin.^{977,978} Bare and ligand-protected cadmium sulfide clusters such as $\text{Cd}_4\text{S}_{13}^{18-}$, $\text{Cd}_{17}\text{S}_{28}^{22-}$, $\text{Cd}_4\text{S}_{13}\text{R}_{12}^{6-}$, and $\text{Cd}_{17}\text{S}_{28}\text{R}_{24}^{2+}$ ($\text{R} = \text{H}, \text{CH}_3, \text{CH}_2\text{OH}, \text{CH}_2\text{CH}_2\text{OH}$) were considered using the restricted Hartree–Fock approach.⁹⁷⁸ They found that the bigger ligands bond more strongly with the cluster core. The HOMO–LUMO gap for $\text{Cd}_4\text{S}_{13}^{18-}$ is much larger than that for $\text{Cd}_{17}\text{S}_{28}^{22-}$. The first allowed transition energy for the methyl-terminated $\text{Cd}_{17}\text{S}_{28}$ cluster is near the experimental value for mercaptoethanol-terminated species with the same number of cadmium atoms. The analysis of cadmium chalcogenides CdX ($X = \text{S}, \text{Se}, \text{Te}$)⁹⁷⁷ shows that, despite similar geometries, these clusters show a difference in reactivity and electronic properties. The interatomic distances, effective charges, and HOMO–LUMO transition energies were calculated for these clusters. Complexes $\text{Cd}_{13}\text{S}_{16}\text{H}_{12}^{6+}$, $\text{Cd}_{13}\text{Se}_{16}\text{H}_{12}^{6+}$, and $\text{Cd}_{13}\text{Te}_{16}\text{H}_{12}^{6+}$ show HOMO–LUMO gaps of 8.90, 8.49, and 8.17 eV, respectively, whereas for larger systems $\text{Cd}_{17}\text{X}_{28}\text{H}_{24}^{2+}$ ($\text{X} = \text{S}, \text{Se}, \text{Te}$), the HOMO–LUMO is much smaller and equal to 6.69, 5.88, and 5.89 eV, respectively. Selenide and telluride clusters show longer Cd–X bonds relative to clusters with sulfide. The effective charges for surface chalcogenide atoms are almost the same for clusters with Se and Te, whereas clusters with the sulfur counterpart appear to be more polarized. Density functional theory methods were applied to demonstrate the pronounced effect due to different terminating groups $\text{Cd}_4\text{S}_6\text{R}_6^{2+}$ ($\text{R} = \text{H}, \text{OH}, \text{NH}_2, \text{CH}_3$, and CH_2CH_3). In these complexes, hydrogen and other groups terminate the sulfur atoms and form S–H, S–C, S–O, and S–N bonds. The calculation results show that geometry and density distribution are changed dramatically depending on the type of termination group: the groups with non-hydrogen ligand have a strong effect upon the geometry of the core, while the ethyl group leads to minimal changes both in the electronic structure and in the geometry of the Cd_4S_6 cluster.

The optical properties of the surface passivated hexagonal wurtzite $\text{Cd}_{17}\text{S}_{10}^{4+}$ cluster with different groups such as SH^- , S^{2-} , O^{2-} , and Cu^+ were studied by Aldongarov et al. using DFT calculations (B3LYP and B3PW91 with 6-31+G(d) and LANL2DZ basis sets).⁹⁷⁹ Calculations show that the addition of SH^- and S^{2-} groups decreases singly bonded Cd atoms and increases the band gap in the CdS quantum dots. The presence of oxygen ions on the surface of CdS causes the formation of electronic defects (trap states) in the band gap. The addition of copper ions to the surface tends to form deep trap states, which depend on the location of copper on the CdS surface.

5.1.2. Zinc Chalcogenides: ZnS, ZnSe, and ZnTe. Zinc chalcogenides are semiconducting materials with wider band gaps than the corresponding cadmium chalcogenides. They can often be used as a shell on a cadmium chalcogenide quantum dot to improve its properties. Understanding the structure and optical properties of zinc chalcogenide clusters is of interest for improving these applications.

5.1.2.1. Zinc Sulfide. The most widely investigated zinc chalcogenide nanoclusters are zinc sulfide. The small stoichiometric zinc sulfide Zn_nS_n clusters with n less than 16 were studied using density functional theory (DFT).^{980,981} A structural investigation shows that neutral Zn_nS_n clusters up to $n = 5$ are planar or near-planar ring-like structures, whereas clusters with $n = 6$ and greater exhibit cage-like structures; the hexagonal cluster Zn_3S_3 can be considered as a building unit for larger closed-cage structures. The small positively charged ZnS clusters have planar geometries similar to their neutral analogues, while the crystals with n larger than 5 exhibit cage structures with a pair of two-coordinated atoms.⁹⁸²

The optical properties for the small stoichiometric ZnS clusters were investigated using time-dependent density functional methods.^{983–985} The influence of solvent and ligands on the geometrical and optical properties for the small Zn_nS_n ($n = 3, 4, 6$, and 9) clusters was investigated by Wang et al.⁹⁸³ The calculated (TDDFT/B3LYP/LANL2DZ) optical absorption spectra for these bare structures are blue-shifted with respect to the experimental spectra due to quantum size effects. Solvent effects were included using the PCM model, and results show that the water environment makes the absorption peak obviously blue-shift. Adding ligands ($-S-CH_2-CH_2-COOH$, $-S-CH_2-CH_2-N(CH_3)_2$, $-S-CH_2-CH_2-NH_2$, $-S-CH_2-CH_2(OH)$, $-S-CH_2-CH(NH_2)-COOH$, $-S-CH(OH)-CH_2(OH)$, and $-S-CH_2-COOH$) to the considered naked clusters shows that all ligands have a similar influence on the ZnS clusters: $S-Zn$ bond lengths are elongated, absorption peaks are blue-shifted, and there is no effect on Raman spectra in comparison with results for bare ZnS nanocrystals. Zwijnenburg et al.^{984,985} studied the optical excitation spectra in small polyhedral bare and hydrated Zn_4S_4 and Zn_6S_6 clusters (DFT and TDDFT with B3LYP). The absorption and photoluminescence spectra demonstrate that during relaxation of the excited state the nanostructures break symmetry and one electron localizes on a small number of Zn atoms, whereas the one hole localizes on a small number of S atoms. The effect of water on the optical absorption and photoluminescence spectra of these structures was also investigated.⁹⁸⁵ The results show that the absorption spectra of Zn_4S_4 and Zn_6S_6 in the presence of water are blue-shifted and new peaks appear. Localization of the excited states is also affected by water, and the hydrated ZnS clusters have extra minima.

Medium and large size ZnS clusters can also exhibit geometrical structures such as hollow^{986–996} and ring-like^{991,992,997} isomers. The hollow structures become very popular due to their potential applications in catalysis, drug delivery, high hydrogen storage, medical diagnostics, etc.^{998–1001} The noncarbon fullerene-like structures of Zn_nS_n with $n = 10–47$ have been simulated and studied using density functional theory calculations (B3LYP/SKBJ(d) and PW91/ecp-dnp).^{986,987} The considered “bubble” structures are assembled from 4, 6, and 8 atom rings, and these structures are more stable than the bulk-like clusters. Additionally, hollow Zn_nS_n crystals with $n = 50, 60, 70$, and 80 were considered by

Hamad et al.⁹⁸⁷ The results show that for these large clusters, the onion-like or “double bubble” structures, where one bubble cluster is inserted inside another one, are predicted and more stable. The investigation of the electronic properties shows that the band gap of the “bubble” clusters does not change significantly with the increasing size of the system, and the band gap of the double bubbles is smaller than those of the single bubbles.⁹⁸⁷ In the continuation of these two studies,^{986,987} Hamad and co-workers computed the relative stabilities of clusters Zn_nS_n with $n = 18–560$ (i.e., crystal size up to 4 nm) using simulated annealing and density functional theory.⁹⁸⁸ For systems with $n = 18–80$, the results confirm the previous studies. For large systems, only single and double layer hollow clusters were found, with no triple bubble structures.

Moreover, the structural and electronic properties of ZnS hollow clusters were studied and compared to similar size zinc-blende and wurtzite clusters using the LCAO-DFT-LDA-TB calculation by Pal et al.^{989,990} The calculations⁹⁸⁹ for bubble-like structures Zn_nS_n with $n = 10, 16, 43, 58$, and 68 show that systems with $n = 4–16$ are more stable than the bulk-like structures, whereas for larger clusters the bulk-like structures are preferable. However, the calculations⁹⁹⁰ for single (ZnS) $_n$ and double-layer (ZnS) $_{16}\cdot(ZnS)$ $_n$ ($n = 57, 86, 116$) structures show that all of these hollow structures are more stable in comparison to bulk-like clusters. In both of these articles, the calculated values of the band gap^{989,990} are in good agreement with the results of Hamad et al.⁹⁸⁷ The HOMO–LUMO gaps are higher for hollow clusters than for zinc-blende and wurtzite clusters. The band gap of single- and double-layer hollow clusters decreases with the size of the cluster; however, after $n = 86$ it starts to increase.⁹⁹⁰ The investigation of the HOMO and LUMO orbitals shows that the HOMO is delocalized over the whole cluster, whereas the LUMO is localized at the surface. Calculation of the nonstoichiometric clusters shows that the band gap of these structures is smaller than for stoichiometric systems, and the HOMO and LUMO orbitals are distributed to the outer parts of the cluster.⁹⁸⁹

Furthermore, the investigation of naked and water-passivated Zn_nS_n and Cd_nSe_n clusters with n up to 37 and different geometrical structures were considered using DFT (with B3LYP, CA-B3LYP, CAM-B3LYP, ω B97X, PBE0, PBE, BP86, PW91, and M06 functionals) by Nguyen et al.⁹³⁷ The bare ZnS clusters with $n = 8–12$ and 15–19 are predicted to be spheroidal and tubular structures, with squares and hexagons. For larger clusters, wurtzite and cage-core structures are more preferable. The most stable system is the $Zn_{32}S_{32}$ cluster, which has a cubic core.

The optical properties of hollow zinc sulfide nanoclusters were investigated by TDDFT calculations by Zwijnenburg.^{994–996} Calculated optical absorption spectra⁹⁹⁴ (TD-B3LYP with basis sets def2-SV(P), DZ(D)P, and def2-TZVP) for uncapped Zn_nS_n clusters with n up to 26 display that for some high-symmetry nanostructures, such as Zn_nS_n with $n = 12, 15, 16, 18, 22$, and 26, the first excitation with significant oscillator strength lies at higher energy, whereas the low-symmetry structures ($n = 8$ and 13) show more excitations with large oscillator strength. All of these nanostructures have the strongest intensity peaks between 296 and 264 nm that are in a good agreement with experimental spectra, which is obtained for the approximately similar size nanostructures synthesized in water and methanol. Investigation of the excited-state relaxation of high-symmetry nanostructures⁹⁹⁵ Zn_nS_n with $n = 12, 16, 22$, and 26 shows that the fate of excited states for zinc sulfide

nanostructures involves a cascade of excited minima, separated by barriers, and ends up in a conical intersection between the excited-state energy surface and the ground state. In addition, clusters $Zn_{12}S_{12}$, $Zn_{16}S_{16}$, $Zn_{22}S_{22}$, and $Zn_{26}S_{26}$ demonstrate a photoluminescent (PL) behavior.⁹⁹⁶ The calculation of both bare and water-covered nanoparticles displays two types of PL signals. The first PL signal is located in a visible region of spectra and arises from a singlet–singlet transition that corresponds to an excited-state minimum where an excited electron is untrapped. The second is longer-wavelength and originates from either triplet–singlet or singlet–singlet transitions from excited-state minima in which the excited electron is trapped.

The ring-like ZnS structures were studied and compared to other geometrical structures by Pal et al.^{991,997} These structures can have potential applications in nanometer sensors, resonators, and transducers.⁹⁹⁷ The ring-like, hollow, zinc-blende, and wurtzite structures of the Zn_nS_n with $n = 10, 16, 37, 57$, and 68 were calculated using the genetic algorithm (GA) coupled with the DFTB method. Results show that ring-like structures are energetically more favorable configurations for ZnS than the other known structures. Furthermore, for ring-like structures, the HOMO–LUMO gap has higher values and strongly depends on cluster size (i.e., band gap decreases with an increasing size of cluster).

5.1.2.2. Zinc Selenide and Telluride. Theoretical investigations of the structural, electronic, and optical properties of bare^{965,1002–1004} and ligand-protected¹⁰⁰⁵ ZnSe clusters have also been undertaken. The structural characteristics of small naked stoichiometric clusters of zinc selenide and telluride Zn_nX_n ($X = Se, Te$) with n less than 16 using DFT (B3LYP/SKBJ) were studied.^{1002,1003} The clusters with n up to 5 have been seen to be planar or near-planar rings, and the larger neutral three-dimensional structures have closed-cage polyhedral geometry.

The structural and electronic properties of clusters Zn_mSe_n with $m + n$ up to 200 atoms were studied by Goswami and co-workers using the DFTB method.^{1004,1005} The calculations of naked zinc-blende and wurtzite modification of stoichiometric and nonstoichiometric ZnSe clusters¹⁰⁰⁴ show that the HOMO–LUMO gap decreases with the increase of particle size and the number of singly bonded atoms. Localization of the HOMO and LUMO orbitals for ZnSe is similar to the localization in the CdSe clusters: the HOMO orbital is delocalized over the whole cluster, whereas the LUMO is localized in the surface region. The lowest excitation energy is also affected by cluster size, and is blue-shifted as the cluster size decreases. The stoichiometric wurtzite structures have higher lowest excitation energies than the corresponding zinc-blende clusters. The nonstoichiometric structures have a lower band gap with comparison to the stoichiometric, whereas both HOMO and LUMO orbitals are localized on the surface atoms. To understand how ligands change the optical properties of ZnSe nanostructures, the $-H$ and $-OH$ passivated stoichiometric clusters were calculated.¹⁰⁰⁵ The investigation shows that the surface passivation has a strong influence on the electronic and optical properties: the passivation significantly reduces the size of the cluster and increases the HOMO–LUMO gap. The lower excitation energy of capped clusters is clearly blue-shifted with respect to the bare structures.

The dependence of the electronic and absorption spectra of hydrogen-passivated ZnSe clusters (with sizes up to 2.2 nm) was found by Alnemrat et al. using DFT and TDDFT methods

for $Zn_nSe_nH_m$ ($n = 1, 4, 10, 16, 19, 28, 43, 65, 83; m = 6, 18, 30, 42, 66, 78, 98, 122$) structures (Figure 22).⁹⁶⁵ Their calculations demonstrate that passivation of the ZnSe and CdTe nanoparticles by hydrogen effectively removes the surface trap states from the gaps and does not affect the energies of the electronic states of semiconductors. The band gaps decreased with increasing cluster size.

Small zinc telluride (ZnTe) complexes were studied using DFT methods.^{1003,1006,1007} Results of calculations for the stoichiometric and nonstoichiometric Zn_mTe_n (with $m + n \leq 6$) clusters show that the binding energies of Te rich clusters are significantly larger than those of the Zn-rich clusters.¹⁰⁰⁶ Also, these systems show the quantum size effect, which is similar to other zinc chalcogenide structures: the band gap decreases as the number of atoms in the systems increases. The influence of ligand and solvent on the optical characteristics of the ZnTe clusters for systems with atom numbers up to 18 was studied by Xu et al.¹⁰⁰⁷ Both the solvent (water) and the ligands ($-S-CH_2-CH_2-COOH$, $-S-CH_2-CH_2-N(CH_3)_2$, $-S-CH_2-CH_2-NH_2$, $-S-CH_2-CH_2(OH)$, $-S-CH_2-CH-(NH_2)-COOH$, $-S-CH(OH)-CH_2(OH)$, and $-S-CH_2-COOH$) cause the absorption spectra to shift to the blue.

5.1.3. Mercury Chalcogenides: HgS, HgSe, and HgTe.

Mercury chalcogenides have fewer current applications than other group 12 chalcogenides. Only a few theoretical articles have been published about mercury chalcogenide clusters.^{909,1008,1009} The structural, electronic, and optical properties of the mercury sulfide,⁹⁰⁹ selenide,⁹⁰⁹ and telluride^{909,1008} clusters have been investigated by density functional theory methods. The stoichiometric quadrangles and hexagons of Hg_nX_n ($X = S, Se$, and Te) clusters with $n = 3$ and 4 were studied.⁹⁰⁹ The size of the system has an effect on the HOMO–LUMO gap, which decreases as the number of atoms increases. Moreover, for systems with $n = 3$ the band gap increases in the order $S > Se > Te$, whereas for clusters with $n = 4$ it is reversed, and the HOMO–LUMO gap decreases for $S < Se < Te$. The absorption spectra are shifted to the red with transitions from HgS to HgTe. Calculated lowest vibrational frequencies for the same clusters decrease from HgS to HgTe. The binding energy is the highest for HgS clusters.

Stoichiometric mercury telluride crystals encapsulated within single walled carbon nanotubes (SWNTs) have been studied using the DFT-LDA method.¹⁰⁰⁹ Three different types of 1D-dimensional crystals of HgTe were considered and optimized: 4:4, 3:3, and 2:2 structures. The initial structure for the 4:4 crystal was a $2 \times 2 \times 2$ cubic structure derived from rock salt bulk structure, the 2:2 crystal is a chain motif derived from cinnabar (HgS) bulk structure, and the 3:3 crystal corresponds to a novel structure that was found when HgTe was intercalated within single walled carbon nanotubes (SWNTs). The 1D clusters with the 3:3 coordination-type were found to be the most thermodynamically stable of the three structures. The calculations of clusters $Hg_{4n}Te_{4n}$ and $Hg_{8n}Te_{8n}$ ($n = 2–10$) show that crystals $Hg_{4n}Te_{4n}$ with $n \geq 6$ exhibit 4:4 crystal-type, whereas clusters $Hg_{8n}Te_{8n}$ with $n \geq 4$ prefer the 3:3 structural organization. Also, the results demonstrated that clusters with the $Hg_{8n}Te_{8n}$ unit cell are more stable.

A theoretical examination of the nonstoichiometric Hg_mTe_n clusters with $m \neq n = 13, 16, 19$, and 28 shows that relaxed clusters $Hg_{13}Te_{16}$ and $Hg_{16}Te_{19}$ keep the T_d symmetry of the initial state, whereas other possible structures change it to lower symmetries.¹⁰⁰⁸ The largest structures $Hg_{19}Te_{28}$ and $Hg_{28}Te_{19}$ were obtained by the addition of 12 tellurium and 12 mercury

atoms to the $\text{Hg}_{19}\text{Te}_{16}$ and $\text{Hg}_{16}\text{Te}_{19}$ clusters, respectively. The results show that the added 12 Te atoms have ligand behavior and stabilized the initial $\text{Hg}_{19}\text{Te}_{16}$ core. The HOMO–LUMO gap for all initial states and relaxed clusters $\text{Hg}_{13}\text{Te}_{16}$ and $\text{Hg}_{16}\text{Te}_{19}$ with T_d symmetry is zero or very small, which indicates that these structures have semimetal behavior. After relaxation, when the symmetry is changed, these clusters become semiconductors.

5.2. Group 13: $\text{A}^{\text{III}}\text{B}^{\text{VI}}$ ($\text{A}^{\text{III}} = \text{Ga}$; $\text{B}^{\text{VI}} = \text{S, Te}$)

Articles about DFT or ab initio theoretical investigations of binary semiconductor clusters of group $\text{A}^{\text{III}}\text{B}^{\text{VI}}$ were found only for gallium sulfide¹⁰¹⁰ and gallium telluride.¹⁰¹¹ Gallium(III) sulfide is a semiconductor with applications in electronics and photonics. Gallium(III) telluride is also a semiconductor, but its potential applications are not yet established.

5.2.1. Gallium Sulfide. BelBruno and co-workers¹⁰¹⁰ performed a theoretical study (BPW91/6-311G*) of structures in addition to experimental detection (via a time-of-flight mass spectrometer) of small neutral and cationic Ga_mS_n clusters ($m = 2-4$; $n = 2-7$). The experiment shows that only low molecular weight clusters exist. The theoretical study of structures for these systems led to the proposal that there are no conformers that have “magic number” thermodynamic stability. Furthermore, results for systems with up to 10 atoms suggested that geometrical changes are frequent and that there are no simple reaction pathways connecting successive cluster structures. In addition, there are no obvious addition reaction pathways to build larger clusters from smaller clusters or the Ga_2S_3 molecule.

5.2.2. Gallium Telluride. Seeburrun et al.¹⁰¹¹ studied the structures, vibrational properties, and energetics features of small gallium telluride neutral and anionic clusters Ga_2Te_3 and Ga_3Te_2 using B3LYP, MP2, and CCSD(T) methods with the 6-311G(d) basis set for gallium and the LANL2DZDP ECP basis set for tellurium. The neutral Ga_2Te_3 cluster exhibits a V-shaped configuration with ${}^1\text{A}_1$ ground state, whereas its anion is kite-shaped with ${}^2\text{A}_1$ ground state. The cluster Ga_3Te_2 and its anion Ga_3Te_2^- prefer a three-dimensional D_{3h} geometry with ${}^2\text{A}_2''$ and ${}^1\text{A}_1'$ electronic states, respectively. The calculated adiabatic electron affinity for clusters Ga_2Te_3 and Ga_3Te_2 is 2.78 and 2.86 eV, respectively.

5.3. Group 14: $\text{A}^{\text{IV}}\text{B}^{\text{VI}}$ ($\text{A}^{\text{IV}} = \text{Ge, Pb}$; $\text{B}^{\text{VI}} = \text{S, Se, Te}$)

5.3.1. Germanium Chalcogenides: GeS and GeSe . Germanium chalcogenide semiconductors have potential application in lasers, sensors, photonic applications, optoelectronic applications, etc. A few types of germanium chalcogenide semiconductors are known: amorphous materials^{1012,1013} and glasses.^{1012,1014-1018} The stability and optical properties of these binary semiconductors are dependent on their composition.

5.3.1.1. Germanium Sulfide. The electronic structures of amorphous germanium sulfides were investigated by Hachiya using DFT methods.^{1012,1013} A $\text{Ge}_6\text{S}_{16}\text{H}_8$ cluster similar to the crystalline- GeS_2 structure was optimized using the SVWN/LANL2DZ method, and calculation of the electronic structure for this geometry was performed using B3LYP/6-311G(d).¹⁰¹² Calculation of the valence and conduction band density of states (VB and CB DOS) shows that experimental valence band photoemission spectra are reproduced. States around the band gap are S 3p lone-pair states for the VB top and Ge 4s–S 3p antibonding states for the CB bottom. The normal crystal structure of GeS should contain only Ge–S bonds; however,

sometimes formation of “wrong bonds” such as Ge–Ge or S–S can take place. In this case, electronic properties can be changed. The electronic structure of “wrong bonds” in the amorphous germanium sulfide (GeS) was investigated using the DFT method B3LYP/6-311G(d,p).¹⁰¹³ In this article, the author presented results about the influence of “wrong bonds” in the crystalline- GeS_2 structure on the band gap of amorphous GeS . The crystal-unit Ge_6S_{16} with three different types of bonds was considered: without wrong bonds, with Ge–Ge “wrong bonds”, and with S–S “wrong bonds”. The results show that the narrowing of the band gap with increasing Ge content from GeS_2 composition is due to the lowering of the conduction band bottom with increasing germanium wrong bonds, although the narrowing with increasing S content is moderate due to the presence of the lone-pair states at the valence-band top, which obscure the modification with increasing sulfur wrong bonds.

A theoretical and empirical study of GeS_2 glasses structure and film was made by Mateleshko et al.¹⁰¹⁷ The experimental measurement of germanium sulfide glasses was performed by Raman spectra, whereas the ab initio calculations were carried out using the RHF/6-31G* method for clusters $\text{Ge}_6\text{S}_6\text{H}_4$ and $\text{Ge}_2\text{S}_7\text{H}_6$. In this work, the edge-, corner-sharing, and ethane-like Ge–S structures were considered. The results exhibited good agreement of the experimental Raman data with the most intense bands of quantum-chemical calculated Raman spectra. The electronic structures of the GeS_2 glasses were studied by Holomb and co-workers using the TDDFT level of theory.¹⁰¹⁴ Small Ge_nS_m ($1 < n < 3$ and $1 < m < 9$) clusters were considered. The calculated data allowed the authors to conclude that the optical gap can be managed by the glass composition (percentage sulfur and germanium) and by the melt temperature used for glass preparation. For example, the band gap decreases for theoretical clusters that contain S–S bonds and for real S-rich $\text{Ge}_x\text{S}_{100-x}$ glasses. Also, greatly lowered band gaps were obtained for the germanium-rich glasses with decreasing melt temperature. BelBruno et al.¹⁰¹⁸ studied neutral and cationic Ge_nS_m ($1 \leq n \leq 4$ and $1 \leq m \leq 7$) clusters as models of GeS_2 glasses using the DFT method PBE/6-311G*. Moreover, the empirical investigation of the small germanium sulfide clusters was performed by a time-of-flight mass spectrometer. The experimental results show that only clusters of up to 11 atoms were observed. The theoretical calculation of the global minimum energy conformers for the clusters up to 11 atoms indicates that there are reaction pathways primarily involving atomic addition connecting successive cluster structures. When a kinetic chain reaches the cluster for which the maximum number of Ge–S bonds has been reached, the pathway ends and further addition reactions are thermodynamically unfavorable.

5.3.1.2. Germanium Selenide. Germanium selenide glasses were investigated by Shpotyuk¹⁰¹⁵ and Gurin¹⁰¹⁶ with co-workers. The RHF/6-311G* ab initio method was employed for modeling of quasi-adaptive phases in the $\text{Ge}_x\text{Se}_{100-x}$ ($20 \leq x < 26$) glasses. The results show that for this binary glass with $x < 12$ the structure has a “chain crossing” motif, for systems with $12 \leq x < 23$ the structure is mixed “chain crossing” and “outrigger raft”, and for $x \geq 20$ it is modified “outrigger raft”. In addition, the structure and optical absorption spectra of germanium selenide glasses were studied using DFT and TDDFT levels of theory (B3LYP/LANL2DZ).¹⁰¹⁶ Building units such as $\text{Ge}_6\text{Se}_{16}\text{H}_4$ and $\text{Ge}_6\text{Se}_{16}\text{H}_8$ were considered. The crystal $\text{Ge}_6\text{Se}_{16}\text{H}_8$ does not have –Se–Se– bridges and is more

expanded than $\text{Ge}_6\text{Se}_{16}\text{H}_4$. The results show that both of these clusters have almost the same stability and HOMO–LUMO gaps (3 eV). Calculated optical absorption spectra demonstrate that the major bands of the cluster with –Se–Se– bridges ($\text{Ge}_6\text{Se}_{16}\text{H}_4$) are shifted to the red with respect to the $\text{Ge}_6\text{Se}_{16}\text{H}_8$ cluster.

5.3.2. Lead Chalcogenides: PbS, PbSe, and PbTe. Lead chalcogenides have a number of important industrial applications. For example, PbS is used as a detection element in infrared detectors. Lead selenide is a thermoelectric material and was also one of the first elements used in infrared detectors. PbTe is also a thermoelectric material of interest for use in spacecraft materials.

5.3.2.1. Lead Sulfide. Structural and electronic properties of the stoichiometric PbS nanoclusters have been widely studied using DFT methods.^{1019–1022} The B3LYP functional with the SBKJC basis set for lead and 6-31+G* for sulfur was applied to study the stability of the neutral stoichiometric lead sulfide clusters Pb_nS_n by He et al.¹⁰¹⁹ ($n = 1$ –16) and Zeng and co-workers¹⁰²⁰ (n up to 9). Both of these investigations show that clusters of lead sulfide exhibit the bulk rock salt (galena) structure and follow a simple cubic growth pattern. Investigation of the size-dependence of PbS stability shows that the binding energies increase monotonically from the monomer to the tetramer and shows oscillation for structures with $n > 5$. The lower binding energies are observed for the structures with odd numbers of PbS units.^{1019,1020} The HOMO–LUMO gap shows oscillating behavior with increasing cluster size.¹⁰²⁰

A theoretical study of Pb_nS_n ($n = 1$ –9) was also performed by Xing et al.¹⁰²¹ using the B3LYP method. The structural analysis shows that for some systems the galena structure is not the global minimum. Similar results were obtained by Koirala et al.¹⁰²² for systems Pb_nS_n ($n = 11$ –15) using the B3LYP and PW91 functionals with SBKJC and SDD basis sets for lead and 6-311+G* for sulfur: the large nanoclusters Pb_nS_n ($n = 11$ –15) strongly prefer a two-dimensional stacking of cubes (galena) structure, whereas for some small systems with n less than 10 the galena structure is not the global minimum. The cluster Pb_4S_4 shows magic-number behavior. The results also display the size-dependence of the binding energy and band gap.^{1021,1022} The calculated binding energies and HOMO–LUMO gaps exhibit oscillatory behavior with increasing cluster size.

The large cubic $(\text{PbS})_{4n}$ ($4n = 4, 8, 16, 32, 64, 128$) clusters were investigated by Kiran et al.¹⁰²³ Density functional theory (PW91 functional with DND and DSPP basis sets) calculations were supported by experiments. Their results demonstrated that $(\text{PbS})_{32}$ is the smallest cubic cluster with an inner $(\text{PbS})_4$ core. These $(\text{PbS})_{32}$ clusters are building blocks that can form square and rectangular large crystals with predictable dimensions.

5.3.2.2. Lead Selenide. Structures and optical properties of PbSe clusters were studied using DFT and TDDFT methods by Zeng et al.¹⁰²⁴ Investigation of the geometrical structures of Pb_nSe_n with n up to 10 shows that the structures of these clusters are close to those of PbS, and exhibit cubic and bulk-like structures. The binding energy and HOMO–LUMO gap indicate that the cubic Pb_4Se_4 crystal has a high stability. Moreover, Pb_4Se_4 is considered as a building block for larger clusters. Examination of the photoabsorption spectra shows that including spin–orbit coupling in the calculation has a great influence on the spectra.

Lead selenide semiconductor clusters have unique electronic structures and exhibit a variety of features, which can be controlled by size, shape, and topology. In particular, the phonon-mediated relaxation of electronic excitations in semiconductor quantum dots and generation of the multiple excitons can play a critical role in a variety of applications.¹⁰²⁵ Multiple excitons (MEs) and the electron–phonon bottleneck in the lead selenide quantum dots (QD) Pb_nSe_n ($n = 16, 68$, and 180) were studied using time-domain ab initio simulations with nonadiabatic molecular dynamics.¹⁰²⁵ The calculations of optical spectra show that for these PbSe QD the phonon bottleneck to the electron–phonon relaxation does not exist due to the high density of electron and hole states. Later work from this group has been dedicated to theoretical study of the electron–phonon relaxation in $\text{Pb}_{68}\text{Se}_{68}$ semiconductor clusters and showed that the phonon bottleneck is avoided through two relaxation pathways: surface state and multiphonon processes.^{1026,1027} The theoretical investigation demonstrated that MEs are located in the cluster spectra above an energy threshold; furthermore, PbSe creates energy windows in which MEs dominate as compared to single excitons.¹⁰²⁵ Isborn et al.⁹⁴³ have shown that multiple excitons in PbSe (Figure 21) can be generated directly in the crystal upon absorption of a single photon.

The effects of the dopants, defects, and charging on the excited states and optical absorption spectra of small stoichiometric and nonstoichiometric lead selenide clusters (Pb_4Se_4 , Pb_4Se_4^- , and Pb_3Se_4) were studied using ab initio calculations (SAC-CI method with LANL2DZ basis set) by Fisher et al.¹⁰²⁸ These results suggested that cluster modifications have a significant effect on the electronic and optical properties of this type of system. The defects create new states, which are mixed with the original states and shift spectra to the higher energy region. Dopants and charging show the same effects on the cluster properties. The multiexcitons (ME) and intraband transitions (IB) + single-exciton (SE) configurations show similar trends for anionic and n-doped clusters, whereas the IB + SE configurations are more preferable over ME in the cationic clusters.

5.3.2.3. Lead Telluride. Nonstoichiometric¹⁰²⁹ and stoichiometric^{1029,1030} lead telluride clusters were theoretically investigated using ab initio and DFT methods. Gong and co-workers studied structures and stabilities of small Pb_nTe_n (where $m + n \leq 6$) clusters by the DFT B3LYP method with CEP-121G, LANL2DZ, and SDD basis sets.¹⁰²⁹ Their calculations show that stoichiometric clusters are more stable than nonstoichiometric species. For nonstoichiometric systems, they concluded that Pb-rich clusters are respectively more stable than Te-rich systems. Analysis of the dissociation energies demonstrated that stoichiometric clusters $(\text{PbTe})_n$ with $n = 1$ –3 are the most stable and can be considered as building blocks in the cluster-assembled materials. The HOMO–LUMO gaps (1.87–3.55 eV) indicate semiconductor-like behavior.

Structural evolution and stabilities of the stoichiometric Pb_nTe_n clusters with up to 40 atoms in the system were studied using the ab initio level theory with local density approximation (LDA) by Mulugeta et al.¹⁰³⁰ Geometry analyses show that for small systems with $n \leq 5$ the structures with Pb–Pb bonds are energetically more favorable. Calculated binding energies, energies of fragmentation, and band gaps indicated that the Pb_4Te_4 system is a magic cluster. For large clusters with $n > 5$, the isomers that contained Pb–Te bonds have the lowest

energies. Moreover, clusters with $n = 11\text{--}20$ strongly prefer the two-dimensional stacking of cubes structures.

6. SUMMARY

A wide variety of metal, metal oxide, and metal chalcogenide clusters and nanoparticles have been studied theoretically using quantum mechanical methods. For pure metals, most of the theoretical work performed to date has focused on noble metals because they are resistant to oxidation and thus are generally stable in their metallic form. Noble metal clusters and nanoparticles of elements such as Pd, Pt, and Au are of interest for catalytic applications. Other noble metal clusters such as Ag and Au are commonly studied because of their unique optical properties. Bare clusters of earlier transition metals are typically of interest for their potential magnetic properties. In general, these clusters are not as heavily studied as those of the noble metals, which may be due in part to theoretical challenges of ascertaining the correct lowest energy isomer and spin state for systems with many interacting d orbitals. Of the main group metals, aluminum is one of the most investigated systems; this is due in part to its electronic structure arising from delocalized sp atomic orbitals and to its usefulness in both metallic and oxide forms.

Of the transition metal oxides, titanium oxide, zirconium oxide, vanadium oxide, manganese oxide, iron oxide, cobalt oxide, and zinc oxide clusters and nanoparticles have been studied in great detail theoretically. These oxides have significant industrial applications as semiconducting materials, catalysts, pigments, battery materials, and magnetic recording devices. In consequence, it is not surprising that the structures and properties of small clusters and larger nanoparticles of these materials have been of great theoretical interest. Surprisingly, ruthenium oxide, which is of significant experimental interest as a water splitting catalyst, has not yet received the degree of theoretical attention that other common oxides have enjoyed.

For chalcogenide compounds, most of the theoretical work that has been done has focused on cadmium chalcogenides as well as some work with zinc sulfide. As for the metal and metal oxide clusters, this interest is not surprising given the wide variety of experimental applications for these systems. Stoichiometric and nonstoichiometric clusters have been explored. To date, most of the work has examined clusters without ligands, although recent work is beginning to investigate ligand-protected clusters and nanoparticles. Additional work on ligand-protected chalcogenides is desirable because the ligands are known to affect surface structure, electronic states, optical properties, etc., of experimental chalcogenide compounds.

Structures and relative isomer energies have been some of the principal aims of these studies. In concert, researchers have also examined overall binding energies, fragmentation energies, etc. In addition, many investigations have focused on electronic properties such as HOMO–LUMO gaps, densities of states, ionization potentials, and electron affinities. Furthermore, optical properties such as UV–vis absorption spectra have been studied for a number of clusters and nanoparticles. Electronic and optical properties have been of significant interest for noble metal and semiconductor clusters. Magnetic properties, particularly magnetic moments, have also been of interest especially for early transition metal clusters. Occasionally, nonlinear optical or chiroptical properties, X-ray

absorption properties, and other physical properties have been studied for the systems discussed in this work.

Most of the work performed on these systems to date has employed density functional theory, although HF and post-HF methods have also been utilized. For the near future, it is unlikely that post-HF methods will be routinely applied to these large systems, so DFT is likely to remain the method of choice. Researchers working in this area must keep in mind the quality and applicability of various exchange-correlation functionals when considering their results for the structures, spin states, ionization potentials, electron affinities, HOMO–LUMO gaps, optical absorption spectra, and other properties of these clusters. Where available, comparison with experiment provides useful validation of theoretical predictions.

AUTHOR INFORMATION

Corresponding Author

*E-mail: cmaikens@ksu.edu.

Notes

The authors declare no competing financial interest.

Biographies



Amendra Fernando received his Bachelor of Science (Special Degree) in Computational Chemistry from University of Colombo, Sri Lanka, in 2010. He is currently a Ph.D. candidate in the Aikens group at Kansas State University. His research is focused on fundamental understanding and mechanistic exploration of transition metal oxides for water splitting. His research interests are theoretical and computational studies in materials science, photochemistry, and catalysis.



K. L. Dimuthu M. Weerawardene received her Bachelor of Science degree in Computational Chemistry from University of Colombo in Sri Lanka in 2011. She is now a third year Ph.D. student under the

direction of Christine M. Aikens at Kansas State University. Her research mainly focuses on using quantum chemical methods to study structure and dynamics of noble metal nanoclusters.



Natalia V. Karimova obtained her Master Degree diploma in 2008 and her doctoral degree in 2011 at the Irkutsk State University, laboratory of Quantum Chemistry, Russia. Her area of interest was the ab initio study of the acetylene classical reactions in superbasic media. At the present time, she is a Ph.D. student at Kansas State University. Her current work is related to the theoretical investigation of electronic and optical properties for plasmonic silver nanoparticles, silver nanowires, and gold nanoclusters by using density functional theory methods.



Christine M. Aikens completed her Bachelor of Science degree at the University of Oklahoma in 2000. She received her Ph.D. in 2005 from Iowa State University under the direction of Mark S. Gordon and then performed postdoctoral research with George C. Schatz at Northwestern University. In 2007, she joined the faculty at Kansas State University, where her research focuses on the physical and chemical properties of metal-containing nanoparticles and clusters.

ACKNOWLEDGMENTS

We are thankful for financial support from the National Science Foundation (Grant nos. CHE-0955515, CHE-1213771, and EPS-0903806), the Air Force Office of Scientific Research (AFOSR Award no. FA9550-09-1-0451), the Department of Energy (DOE Award no. DE-SC0012273), and Kansas State University. C.M.A. is grateful to the Alfred P. Sloan Foundation for a Sloan Research Fellowship (2011-2013) and the Camille and Henry Dreyfus Foundation for a Camille Dreyfus Teacher-Scholar Award (2011-2016).

ABBREVIATIONS

MO	molecular orbital
----	-------------------

HOMO	highest occupied MO
LUMO	lowest unoccupied MO
DOS	density of states
PDOS	projected density of states
IP	ionization potentials
EA	electron affinity
PES	photoelectron spectroscopy
DVM	discrete variational (DV) method
MD	molecular dynamics
AIMD	ab initio molecular dynamics
BO LSD MD	Born–Oppenheimer local-spin-density MD
LCAO	linear combination of atomic orbitals
LCGTO	linear combination of Gaussian-type orbitals
LCGTO-FF-DF	LCGTO fitting-functions density functional
LCPSAO	linear combination of norm-conserving pseudopotential atomic orbitals
SCF-X α -SW	self-consistent-field-X α scattered wave
TSDS	taboo search in descriptor space
QM/MM	quantum mechanics/molecular mechanics
ONIOM	our own n -layered integrated molecular orbital and molecular mechanics
1D	one-dimensional
2D	two-dimensional
3D	three-dimensional
fcc	face-centered cubic
bcc	body-centered cubic
hcp	hexagonal close packed
icos	icosahedral
TO	truncated octahedral
CN	coordination number
XRD	X-ray diffraction
CD	circular dichroism
IR	infrared
IRMPD	infrared multi photon dissociation spectra
SERS	surface-enhanced Raman scattering
TIED	trapped ion electron diffraction
NMR	nuclear magnetic resonance
EPR	electron paramagnetic resonance
ENDOR	electron nuclear double resonance
ELDOR	electron–electron double resonance
XAS	X-ray absorption spectroscopy
XANES	X-ray absorption near edge structure
NEXAFS	near edge X-ray absorption fine structure
EXAFS	extended X-ray absorption fine structure
AFM	antiferromagnetic
FM	ferromagnetic
MAE	magnetic anisotropy energies
OEC	oxygen evolving complex
PSII	photosystem II
POM	polyoxometalate

REFERENCES

- (1) Knight, W. D.; Clemenger, K.; de Heer, W. A.; Saunders, A.; Chou, M. Y.; Cohen, M. L. *Phys. Rev. Lett.* **1984**, *52*, 2141.
- (2) de Heer, W. A. *Rev. Mod. Phys.* **1993**, *65*, 611.
- (3) Leuchten, R. E.; Harms, A. C.; Castleman, A. W. *J. Chem. Phys.* **1989**, *91*, 2753.
- (4) Khanna, S. N.; Jena, P. *Phys. Rev. Lett.* **1992**, *69*, 1664.
- (5) Khanna, S. N.; Jena, P. *Phys. Rev. B* **1995**, *51*, 13705.
- (6) Bergeron, D. E.; Castleman, A. W.; Morisato, T.; Khanna, S. N. *Science* **2004**, *304*, 84.
- (7) Bonačić-Koutecký, V.; Fantucci, P.; Koutecký, J. *Chem. Rev.* **1991**, *91*, 1035.

- (8) Castleman, A. W.; Khanna, S. N. *J. Phys. Chem. C* **2009**, *113*, 2664.
- (9) Jena, P. *J. Phys. Chem. Lett.* **2013**, *4*, 1432.
- (10) Walter, M.; Akola, J.; Lopez-Acevedo, O.; Jadzinsky, P. D.; Calero, G.; Ackerson, C. J.; Whetten, R. L.; Grönbeck, H.; Häkkinen, H. *Proc. Natl. Acad. Sci. U.S.A.* **2008**, *105*, 9157.
- (11) Ceperley, D. M.; Alder, B. *J. Phys. Rev. Lett.* **1980**, *45*, 566.
- (12) Perdew, J. P.; Zunger, A. *Phys. Rev. B* **1981**, *23*, 5048.
- (13) Vosko, S. H.; Wilk, L.; Nusair, M. *Can. J. Phys.* **1980**, *58*, 1200.
- (14) Becke, A. D. *Phys. Rev. A* **1988**, *38*, 3098.
- (15) Perdew, J. P. *Phys. Rev. B* **1986**, *33*, 8822.
- (16) Perdew, J. P.; Chevary, J. A.; Vosko, S. H.; Jackson, K. A.; Pederson, M. R.; Singh, D. J.; Fiolhais, C. *Phys. Rev. B* **1992**, *46*, 6671.
- (17) Perdew, J. P.; Burke, K.; Ernzerhof, M. *Phys. Rev. Lett.* **1996**, *77*, 3865.
- (18) Becke, A. D. *J. Chem. Phys.* **1993**, *98*, 5648.
- (19) Lee, C.; Yang, W.; Parr, R. G. *Phys. Rev. B* **1988**, *37*, 785.
- (20) Adamo, C.; Barone, V. *J. Chem. Phys.* **1999**, *110*, 6158.
- (21) Perdew, J. P.; Tao, J.; Staroverov, V. N.; Scuseria, G. E. *Phys. Rev. Lett.* **2003**, *91*, 146401.
- (22) Zhao, Y.; Truhlar, D. G. *Theor. Chem. Acc.* **2008**, *120*, 215.
- (23) Casida, M. E. In *Recent Advances in Density Functional Methods*; Chong, D. P., Ed.; World Scientific: Singapore, 1995.
- (24) van Leeuwen, R.; Baerends, E. J. *Phys. Rev. A* **1994**, *49*, 2421.
- (25) Gritsenko, O. V.; Schipper, P. R. T.; Baerends, E. J. *Chem. Phys. Lett.* **1999**, *302*, 199.
- (26) Schipper, P. R. T.; Gritsenko, O. V.; van Gisbergen, S. J. A.; Baerends, E. J. *J. Chem. Phys.* **2000**, *112*, 1344.
- (27) Yanai, T.; Tew, D.; Handy, N. C. *Chem. Phys. Lett.* **2004**, *393*, 51.
- (28) Hay, P. J.; Wadt, W. R. *J. Chem. Phys.* **1985**, *82*, 270.
- (29) Wadt, W. R.; Hay, P. J. *J. Chem. Phys.* **1985**, *82*, 284.
- (30) Hay, P. J.; Wadt, W. R. *J. Chem. Phys.* **1985**, *82*, 299.
- (31) Stevens, W. J.; Basch, H.; Krauss, M. *J. Chem. Phys.* **1984**, *81*, 6026.
- (32) Stevens, W. J.; Krauss, M.; Basch, H.; Jasien, P. G. *Can. J. Chem.* **1992**, *70*, 612.
- (33) Cundari, T. R.; Stevens, W. J. *J. Chem. Phys.* **1993**, *98*, 5555.
- (34) Jensen, F. *Introduction to Computational Chemistry*, 2nd ed.; John Wiley & Sons Ltd.: West Sussex, 2007.
- (35) Cramer, C. J. *Essentials of Computational Chemistry: Theories and Models*, 2 ed.; John Wiley and Sons: Chichester, West Sussex, England, 2004.
- (36) Ivanov, S. A.; Arachchige, I.; Aikens, C. M. *J. Phys. Chem. A* **2011**, *115*, 8017.
- (37) Reuse, F. A.; Khanna, S. N. *Chem. Phys. Lett.* **1995**, *234*, 77.
- (38) Reuse, F. A.; Khanna, S. N.; Bernal, S. *Phys. Rev. B* **1995**, *52*, R11650.
- (39) Reuse, F. A.; Khanna, S. N. *Eur. Phys. J. D* **1999**, *6*, 77.
- (40) Reddy, B. V.; Nayak, S. K.; Khanna, S. N.; Rao, B. K.; Jena, P. J. *Phys. Chem. A* **1998**, *102*, 1748.
- (41) Duan, H. M.; Gong, X. G.; Zheng, Q. Q.; Lin, H. Q. *J. Appl. Phys.* **2001**, *89*, 7308.
- (42) Sahoo, S.; Rollmann, G.; Entel, P. *Phase Transitions* **2005**, *78*, 723.
- (43) Longo, R. C.; Gallego, L. *J. Phys. Rev. B* **2006**, *74*, 193409.
- (44) Aguilera-Granja, F.; García-Fuente, A.; Vega, A. *Phys. Rev. B* **2008**, *78*, 134425.
- (45) Onal, I.; Sayar, A.; Uzun, A.; Ozkar, S. *J. Comput. Theor. Nanosci.* **2009**, *6*, 1.
- (46) Yilmazer, N. D.; Fellah, M. F.; Onal, I. *Turk. J. Chem.* **2012**, *36*, 55.
- (47) Singh, R.; Kroll, P. *Phys. Rev. B* **2008**, *78*, 245404.
- (48) Song, W.; Lu, W.-C.; Zang, Q.-j.; Wang, C. Z.; Ho, K. M. *Int. J. Quantum Chem.* **2012**, *112*, 1717.
- (49) Song, W.; Lu, W.-C.; Zang, Q.-j.; Li, Q.-x. *Chem. Res. Chin. Univ.* **2012**, *28*, 291.
- (50) Zhang, Q.-M.; Wells, J. C.; Gong, X. G.; Zhang, Z. *Phys. Rev. B* **2004**, *69*, 205413.
- (51) Wang, Q.; Lim, K. H.; Yang, S.-W.; Yang, Y.; Chen, Y. *Theor. Chem. Acc.* **2011**, *128*, 17.
- (52) Wang, L.-L.; Johnson, D. D. *J. Am. Chem. Soc.* **2009**, *131*, 14023.
- (53) Das, N. K.; Shoji, T. *J. Phys. Chem. C* **2012**, *116*, 13353.
- (54) Das, N. K.; Shoji, T. *J. Alloys Compd.* **2013**, *580*, 37.
- (55) Aguilera-Granja, F.; Longo, R. C.; Gallego, L. J.; Vega, A. *J. Chem. Phys.* **2010**, *132*, 184507.
- (56) Reddy, B. V.; Khanna, S. N. *Phys. Rev. Lett.* **1993**, *70*, 3323.
- (57) Estiu, G. L.; Zener, M. C. *J. Phys. Chem.* **1994**, *98*, 4793.
- (58) Watari, N.; Ohnishi, S. *Phys. Rev. B* **1998**, *58*, 1665.
- (59) Moseler, M.; Häkkinen, H.; Barnett, R. N.; Landman, U. *Phys. Rev. Lett.* **2001**, *86*, 2545.
- (60) Chang, C. M.; Chou, M. Y. *Phys. Rev. Lett.* **2004**, *93*, 133401.
- (61) Kumar, V.; Kawazoe, Y. *Phys. Rev. B* **2002**, *66*, 144413.
- (62) Futschek, T.; Marsman, M.; Hafner, J. *J. Phys.: Condens. Matter* **2005**, *17*, 5927.
- (63) Rogan, J.; García, G.; Valdivia, J. A.; Orellana, W.; Romero, A. H.; Ramírez, R.; Kiwi, M. *Phys. Rev. B* **2005**, *72*, 115421.
- (64) Wang, L.-L.; Johnson, D. D. *Phys. Rev. B* **2007**, *75*, 235405.
- (65) Sun, Y.; Zhang, M.; Fournier, R. *Phys. Rev. B* **2008**, *77*, 075435.
- (66) Sun, Y.; Fournier, R.; Zhang, M. *Phys. Rev. A* **2009**, *79*, 043202.
- (67) Köster, A. M.; Calaminici, P.; Orgaz, E.; Roy, D. R.; Reveles, J. U.; Khanna, S. N. *J. Am. Chem. Soc.* **2011**, *133*, 12192.
- (68) Reveles, J. U.; Köster, A. M.; Calaminici, P.; Khanna, S. N. *J. Chem. Phys.* **2012**, *136*, 114505.
- (69) Park, N.; Sung, D.; Lim, S.; Moon, S.; Hong, S. *Appl. Phys. Lett.* **2009**, *94*, 073105.
- (70) Aguilera-Granja, F.; Vega, A.; Rogan, J.; Orellana, W.; García, G. *Eur. Phys. J. D* **2007**, *44*, 125.
- (71) Jennison, D. R.; Schultz, P. A.; Sears, M. P. *J. Chem. Phys.* **1997**, *106*, 1856.
- (72) Nava, P.; Sierka, M.; Ahlrichs, R. *Phys. Chem. Chem. Phys.* **2003**, *5*, 3372.
- (73) Yudanov, I. V.; Sahnoun, R.; Neyman, K. M.; Rösch, N. *J. Chem. Phys.* **2002**, *117*, 9887.
- (74) Yudanov, I. V.; Sahnoun, R.; Neyman, K. M.; Rösch, N.; Hoffmann, J.; Schauermann, S.; Johánek, V.; Unterhalt, H.; Rupprechter, G.; Libuda, J.; Freund, H.-J. *J. Phys. Chem. B* **2003**, *107*, 255.
- (75) Yudanov, I. V.; Neyman, K. M.; Rösch, N. *Phys. Chem. Chem. Phys.* **2004**, *6*, 116.
- (76) Neyman, K. M.; Inntam, C.; Gordienko, A. B.; Yudanov, I. V.; Rösch, N. *J. Chem. Phys.* **2005**, *122*, 174705.
- (77) Yudanov, I. V.; Neyman, K. M.; Rösch, N. *Phys. Chem. Chem. Phys.* **2006**, *8*, 2396.
- (78) Viñes, F.; Illas, F.; Neyman, K. M. *J. Phys. Chem. A* **2008**, *112*, 8911.
- (79) Neyman, K. M.; Sahnoun, R.; Inntam, C.; Hengrasmee, S.; Rösch, N. *J. Phys. Chem. B* **2004**, *108*, 5424.
- (80) Paz-Borbón, L. O.; Johnston, R. L.; Barcaro, G.; Fortunelli, A. *Eur. Phys. J. D* **2009**, *52*, 131.
- (81) Pittaway, F.; Paz-Borbón, L. O.; Johnston, R. L.; Arslan, H.; Ferrando, R.; Mottet, C.; Barcaro, G.; Fortunelli, A. *J. Phys. Chem. C* **2009**, *113*, 9141.
- (82) Paz-Borbón, L. O.; Johnston, R. L.; Barcaro, G.; Fortunelli, A. *J. Chem. Phys.* **2008**, *128*, 134517.
- (83) Yudanov, I. V.; Neyman, K. M. *Phys. Chem. Chem. Phys.* **2010**, *12*, 5094.
- (84) Zanti, G.; Peeters, D. *J. Phys. Chem. A* **2010**, *114*, 10345.
- (85) Liu, X.; Tian, D.; Meng, C. *Comput. Theor. Chem.* **2012**, *999*, 246.
- (86) Liu, X.; Tian, D.; Meng, C. *Chem. Phys.* **2013**, *415*, 179.
- (87) Bruma, A.; Ismail, R.; Paz-Borbón, L. O.; Arslan, H.; Barcaro, G.; Fortunelli, A.; Li, Z. Y.; Johnston, R. L. *Nanoscale* **2013**, *5*, 646.
- (88) Barman, S.; Kanhere, D. G.; Das, G. P. *J. Phys.: Condens. Matter* **2009**, *21*, 396001.
- (89) Mu, Y.; Han, Y.; Wang, J.; Wan, J.-g.; Wang, G. *Phys. Rev. A* **2011**, *84*, 053201.

- (90) Wei, L.; Yao, X.; Tian, X.; Cao, M.; Chen, W.; She, Y.; Zhang, S. *Comput. Theor. Chem.* **2011**, *966*, 375.
- (91) Negreiros, F. R.; Kuntová, Z.; Barcaro, G.; Rossi, G.; Ferrando, R.; Fortunelli, A. *J. Chem. Phys.* **2010**, *132*, 234703.
- (92) Negreiros, F. R.; Barcaro, G.; Kuntová, Z.; Rossi, G.; Ferrando, R.; Fortunelli, A. *Surf. Sci.* **2011**, *605*, 483.
- (93) Messmer, R. P.; Knudson, S. K.; Johnson, K. H.; Diamond, J. B.; Yang, C. Y. *Phys. Rev. B* **1976**, *13*, 1396.
- (94) Xu, W.-X.; Schierbaum, K. D.; Goepel, W. *Int. J. Quantum Chem.* **1997**, *62*, 427.
- (95) Aprà, E.; Fortunelli, A. *J. Mol. Struct.* **2000**, *501*, 251.
- (96) Aprà, E.; Fortunelli, A. *J. Phys. Chem. A* **2003**, *107*, 2934.
- (97) Watari, N.; Ohnishi, S. *J. Chem. Phys.* **1997**, *106*, 7531.
- (98) Lin, X.; Ramer, N. J.; Rappe, A. M.; Hass, K. C.; Schneider, W. F.; Trout, B. L. *J. Phys. Chem. B* **2001**, *105*, 7739.
- (99) Bazin, D.; Sayers, D.; Rehr, J. J.; Mottet, C. *J. Phys. Chem. B* **1997**, *101*, 5332.
- (100) Ankudinov, A. L.; Rehr, J. J.; Low, J. J.; Bare, S. R. *J. Chem. Phys.* **2002**, *116*, 1911.
- (101) Xiao, L.; Wang, L. *J. Phys. Chem. A* **2004**, *108*, 8605.
- (102) Yang, S. H.; Drabold, D. A.; Adams, J. B.; Ordejon, P.; Glassford, K. *J. Phys.: Condens. Matter* **1997**, *9*, L39.
- (103) Futschek, T.; Hafner, J.; Marsman, M. *J. Phys.: Condens. Matter* **2006**, *18*, 9703.
- (104) Aprà, E.; Baletto, F.; Ferrando, R.; Fortunelli, A. *Phys. Rev. Lett.* **2004**, *93*, 065502.
- (105) Kumar, V.; Kawazoe, Y. *Phys. Rev. B* **2008**, *77*, 205418.
- (106) Ryu, J. H.; Han, S. S.; Kim, D. H.; Henkelman, G.; Lee, H. M. *ACS Nano* **2011**, *5*, 8515.
- (107) Oemry, F.; Nakanishi, H.; Kasai, H.; Maekawa, H.; Osumi, K.; Sato, K. *J. Alloys Compd.* **2014**, *594*, 93.
- (108) Ferrando, R.; Jellinek, J.; Johnston, R. L. *Chem. Rev.* **2008**, *108*, 845.
- (109) Okumura, M.; Sakane, S.; Kitagawa, Y.; Kawakami, T.; Toshima, N.; Yamaguchi, K. *Res. Chem. Intermed.* **2008**, *34*, 737.
- (110) Barcaro, G.; Ferrando, R.; Fortunelli, A.; Rossi, G. *J. Phys. Chem. Lett.* **2010**, *1*, 111.
- (111) Barcaro, G.; Fortunelli, A.; Polak, M.; Rubinovich, L. *Nano Lett.* **2011**, *11*, 1766.
- (112) Häkkinen, H. *Chem. Soc. Rev.* **2008**, *37*, 1847.
- (113) Häberlen, O. D.; Chung, S.-C.; Rösch, N. *Int. J. Quantum Chem.* **1994**, *S28*, 595.
- (114) Häberlen, O. D.; Chung, S.-C.; Stener, M.; Rösch, N. *J. Chem. Phys.* **1997**, *106*, 5189.
- (115) Garzón, I. L.; Beltrán, M. R.; Posada-Amarillas, A.; Ordejón, P.; Artacho, E.; Sánchez-Portal, D.; Soler, J. M. *Phys. Rev. Lett.* **1998**, *81*, 1600.
- (116) Garzón, I. L.; Michaelian, K.; Beltrán, M. R.; Posada-Amarillas, A.; Ordejón, P.; Artacho, E.; Sánchez-Portal, D.; Soler, J. M. *Eur. Phys. J. D* **1999**, *9*, 211.
- (117) Michaelian, K.; Rendón, N.; Garzón, I. L. *Phys. Rev. B* **1999**, *60*, 2000.
- (118) Soler, J. M.; Beltrán, M. R.; Michaelian, K.; Garzón, I. L.; Ordejón, P.; Sánchez-Portal, D.; Artacho, E. *Phys. Rev. B* **2000**, *61*, 5771.
- (119) Garzón, I. L.; Reyes-Nava, J. A.; Rodríguez-Hernández, J. L.; Sigal, I.; Beltrán, M. R.; Michaelian, K. *Phys. Rev. B* **2002**, *66*, 073403.
- (120) Häkkinen, H.; Moseler, M.; Kostko, O.; Morgner, N.; Hoffmann, M. A.; von Issendorff, B. *Phys. Rev. Lett.* **2004**, *93*, 093401.
- (121) Häkkinen, H.; Moseler, M. *Comput. Mater. Sci.* **2006**, *35*, 332.
- (122) Huang, W.; Ji, M.; Dong, C.-D.; Gu, X.; Wang, L.-M.; Gong, X.; Wang, L.-S. *ACS Nano* **2008**, *2*, 897.
- (123) Dong, C.-D.; Gong, X. G. *J. Chem. Phys.* **2010**, *132*, 104301.
- (124) Wang, J.; Wang, G.; Zhao, J. *Phys. Rev. B* **2002**, *66*, 035418.
- (125) Li, J.; Li, X.; Zhai, H.-J.; Wang, L.-S. *Science* **2003**, *299*, 864.
- (126) Wang, J.; Wang, G.; Zhao, J. *Chem. Phys. Lett.* **2003**, *380*, 716.
- (127) Fernández, E. M.; Soler, J. M.; Garzón, I. L.; Balbás, L. C. *Phys. Rev. B* **2004**, *70*, 165403.
- (128) Wu, K.; Li, J.; Lin, C. *Chem. Phys. Lett.* **2004**, *388*, 353.
- (129) Xie, R.-H.; Bryant, G. W.; Zhao, J.; Kar, T.; Smith, V. H., Jr. *Phys. Rev. B* **2005**, *71*, 125422.
- (130) Aikens, C. M.; Schatz, G. C. *J. Phys. Chem. A* **2006**, *110*, 13317.
- (131) Idrobo, J. C.; Walkosz, W.; Yip, S. F.; Öğüt, S.; Wang, J.; Jellinek, J. *Phys. Rev. B* **2007**, *76*, 205422.
- (132) Castro, A.; Marques, M. A. L.; Romero, A. H.; Oliveira, M. J. T.; Rubio, A. *J. Chem. Phys.* **2008**, *129*, 144110.
- (133) Koppen, J. V.; Hapka, M.; Szczęśniak, M. M.; Chałasiński, G. *J. Chem. Phys.* **2012**, *137*, 114302.
- (134) Anak, B.; Bencharif, M.; Rabilloud, F. *RSC Adv.* **2014**, *4*, 13001.
- (135) Yoon, B.; Koskinen, P.; Huber, B.; Kostko, O.; von Issendorff, B.; Häkkinen, H.; Moseler, M.; Landman, U. *ChemPhysChem* **2007**, *8*, 157.
- (136) King, R. B.; Chen, Z.; von Ragué Schleyer, P. *Inorg. Chem.* **2004**, *43*, 464.
- (137) Zubarev, D. Y.; Boldyrev, A. I. *J. Phys. Chem. A* **2009**, *113*, 866.
- (138) Lechtken, A.; Neiss, C.; Stairs, J.; Schooss, D. *J. Chem. Phys.* **2008**, *129*, 154304.
- (139) Kryachko, E. S.; Remacle, F. *Int. J. Quantum Chem.* **2007**, *107*, 2922.
- (140) Fa, W.; Luo, C.; Dong, J. *Phys. Rev. B* **2005**, *72*, 205428.
- (141) Fa, W.; Dong, J. *J. Chem. Phys.* **2006**, *124*, 114310.
- (142) Tian, D.; Zhao, J. *J. Phys. Chem. A* **2008**, *112*, 3141.
- (143) Zhao, H.-Y.; Ning, H.; Wang, J.; Su, X.-J.; Guo, X.-G.; Liu, Y. *Phys. Lett. A* **2010**, *374*, 1033.
- (144) Yang, A.; Fa, W.; Dong, J. *Phys. Lett. A* **2010**, *374*, 4506.
- (145) Johansson, M. P.; Sundholm, D.; Vaara, J. *Angew. Chem., Int. Ed.* **2004**, *43*, 2678.
- (146) Gu, X.; Ji, M.; Wei, S. H.; Gong, X. G. *Phys. Rev. B* **2004**, *70*, 205401.
- (147) Ji, M.; Gu, X.; Li, X.; Gong, X.; Li, J.; Wang, L.-S. *Angew. Chem., Int. Ed.* **2005**, *44*, 7119.
- (148) Tian, D.; Li, J.; Zhao, Y.; Zhao, J.; Guo, X. *Comput. Mater. Sci.* **2011**, *50*, 2359.
- (149) Gao, Y.; Zeng, X. C. *J. Am. Chem. Soc.* **2005**, *127*, 3698.
- (150) Wang, J.; Jellinek, J.; Zhao, J.; Chen, Z.; King, R. B.; von Ragué Schleyer, P. *J. Phys. Chem. A* **2005**, *109*, 9265.
- (151) Tian, D.; Zhao, J.; Wang, B.; King, R. B. *J. Phys. Chem. A* **2007**, *111*, 411.
- (152) Karttunen, A. J.; Linnolahti, M.; Pakkanen, T. A.; Pyykko, P. *Chem. Commun.* **2008**, 465.
- (153) Jiang, D.-e.; Walter, M. *Phys. Rev. B* **2011**, *84*, 193402.
- (154) Liu, X.-J.; Hamilton, I.; Krawczyk, R. P.; Schwerdtfeger, P. *J. Comput. Chem.* **2012**, *33*, 311.
- (155) Wang, J.; Ning, H.; Ma, Q.-M.; Liu, Y.; Li, Y.-C. *J. Chem. Phys.* **2008**, *129*, 134705.
- (156) Zhao, L.-X.; Lei, Y.-M.; Zhang, M.; Feng, X.-J.; Luo, Y.-H. *Phys. B (Amsterdam, Neth.)* **2009**, *404*, 1705.
- (157) Xing, X.; Yoon, B.; Landman, U.; Parks, J. H. *Phys. Rev. B* **2006**, *74*, 165423.
- (158) Bulusu, S.; Li, X.; Wang, L.-S.; Zeng, X. C. *J. Phys. Chem. C* **2007**, *111*, 4190.
- (159) Jalbout, A. F.; Contreras-Torres, F. F.; Pérez, L. A.; Garzón, I. L. *J. Phys. Chem. A* **2008**, *112*, 353.
- (160) Lechtken, A.; Schooss, D.; Stairs, J. R.; Blom, M. N.; Furche, F.; Morgner, N.; Kostko, O.; von Issendorff, B.; Kappes, M. M. *Angew. Chem., Int. Ed.* **2007**, *46*, 2944.
- (161) Gu, X.; Bulusu, S.; Li, X.; Zeng, X. C.; Li, J.; Gong, X. G.; Wang, L.-S. *J. Phys. Chem. C* **2007**, *111*, 8228.
- (162) Santizo, I. E.; Hidalgo, F.; Pérez, L. A.; Noguez, C.; Garzón, I. L. *J. Phys. Chem. C* **2008**, *112*, 17533.
- (163) Shao, N.; Huang, W.; Gao, Y.; Wang, L.-M.; Li, X.; Wang, L.-S.; Zeng, X. C. *J. Am. Chem. Soc.* **2010**, *132*, 6596.
- (164) Shao, N.; Huang, W.; Mei, W.-N.; Wang, L. S.; Wu, Q.; Zeng, X. C. *J. Phys. Chem. C* **2014**, *118*, 6887.
- (165) Stener, M.; Nardelli, A.; De Francesco, R.; Fronzoni, G. *J. Phys. Chem. C* **2007**, *111*, 11862.
- (166) Durante, N.; Fortunelli, A.; Broyer, M.; Stener, M. *J. Phys. Chem. C* **2011**, *115*, 6277.

- (167) Weissker, H. C.; Mottet, C. *Phys. Rev. B* **2011**, *84*, 165443.
- (168) Burgess, R. W.; Keast, V. J. *J. Phys. Chem. C* **2011**, *115*, 21016.
- (169) Lian, K.-Y.; Salek, P.; Jin, M.; Ding, D. *J. Chem. Phys.* **2009**, *130*, 174701.
- (170) Guidez, E. B.; Aikens, C. M. *Nanoscale* **2012**, *4*, 4190.
- (171) Liao, M.-S.; Bonifassi, P.; Leszczynski, J.; Ray, P. C.; Huang, M.-J.; Watts, J. D. *J. Phys. Chem. A* **2010**, *114*, 12701.
- (172) Guidez, E. B.; Aikens, C. M. *J. Phys. Chem. C* **2013**, *117*, 12325.
- (173) Piccini, G.; Havenith, R. W. A.; Broer, R.; Stener, M. *J. Phys. Chem. C* **2013**, *117*, 17196.
- (174) Lopez-Lozano, X.; Barron, H.; Mottet, C.; Weissker, H.-C. *Phys. Chem. Chem. Phys.* **2014**, *16*, 1820.
- (175) Burgess, R. W.; Keast, V. J. *J. Phys. Chem. C* **2014**, *118*, 3194.
- (176) Magyar, R. J.; Mujica, V.; Marquez, M.; Gonzalez, C. *Phys. Rev. B* **2007**, *75*, 144421.
- (177) Luo, W.; Pennycook, S. J.; Pantelides, S. T. *Nano Lett.* **2007**, *7*, 3134.
- (178) Pundlik, S. S.; Kalyanaraman, K.; Waghmare, U. V. *J. Phys. Chem. C* **2011**, *115*, 3809.
- (179) Gusso, M. *J. Phys.: Condens. Matter* **2006**, *18*, 1211.
- (180) Majumdar, D.; Roszak, S.; Leszczynski, J. *Can. J. Chem. Eng.* **2012**, *99*, 9999, 1.
- (181) Zhang, H.-F.; Stender, M.; Zhang, R.; Wang, C.; Li, J.; Wang, L.-S. *J. Phys. Chem. B* **2004**, *108*, 12259.
- (182) Aikens, C. M.; Schatz, G. C. In *Nanoparticles: Synthesis, Stabilization, Passivation, and Functionalization* (ACS Symposium Series); Nagarajan, R., Hatton, T. A., Eds.; American Chemical Society: New York, 2008.
- (183) Provorse, M. R.; Aikens, C. M. *Comput. Theor. Chem.* **2012**, *987*, 16.
- (184) Hull, J. M.; Provorse, M. R.; Aikens, C. M. *J. Phys. Chem. A* **2012**, *116*, 5445.
- (185) Larsson, J. A.; Nolan, M.; Greer, J. C. *J. Phys. Chem. B* **2002**, *106*, 5931.
- (186) Genest, A.; Krüger, S.; Gordienko, A. B.; Rösch, N. Z. *Naturforsch.* **2004**, *59b*, 1585.
- (187) Periyasamy, G.; Durgun, E.; Raty, J.-Y.; Remacle, F. *J. Phys. Chem. C* **2010**, *114*, 15941.
- (188) Barngrover, B. M.; Aikens, C. M. *J. Phys. Chem. A* **2013**, *117*, 5377.
- (189) López-Lozano, X.; Pérez, L. A.; Garzón, I. L. *Phys. Rev. Lett.* **2006**, *97*, 233401.
- (190) Pérez, L. A.; López-Lozano, X.; Garzón, I. L. *Eur. Phys. J. D* **2009**, *52*, 123.
- (191) Tlahuice-Flores, A. *J. Mol. Model.* **2013**, *19*, 1937.
- (192) Hidalgo, F.; Noguez, C.; Olvera de la Cruz, M. *Nanoscale* **2014**, *6*, 3325.
- (193) Gao, Y.; Shao, N.; Pei, Y.; Chen, Z.; Zeng, X. C. *ACS Nano* **2011**, *5*, 7818.
- (194) Kanoun, M. B.; Cavallo, L. *J. Phys. Chem. C* **2014**, *118*, 13707.
- (195) Sánchez-González, Á.; Muñoz-Losa, A.; Vukovic, S.; Corni, S.; Mennucci, B. *J. Phys. Chem. C* **2010**, *114*, 1553.
- (196) Jennison, D. R.; Schultz, P. A. *J. Chem. Phys.* **1997**, *106*, 1856.
- (197) Schooss, D.; Blom, M. N.; Parks, J. H.; Issendorff, B. v.; Haberland, H.; Kappes, M. M. *Nano Lett.* **2005**, *5*, 1972.
- (198) Xing, X.; Danell, R. M.; Garzón, I. L.; Michaelian, K.; Blom, M. N.; Burns, M. M.; Parks, J. H. *Phys. Rev. B* **2005**, *72*, 081405.
- (199) Blom, M. N.; Schooss, D.; Stairs, J.; Kappes, M. M. *J. Chem. Phys.* **2006**, *124*, 244308.
- (200) Bonačić-Koutecký, V.; Burda, J.; Mitrić, R.; Ge, M.; Zampella, G.; Fantucci, P. *J. Chem. Phys.* **2002**, *117*, 3120.
- (201) Yang, M.; Jackson, K.; Jellinek, J. *J. Chem. Phys.* **2006**, *125*, 144308.
- (202) Baishya, K.; Idrobo, J. C.; Öğüt, S.; Yang, M.; Jackson, K.; Jellinek, J. *Phys. Rev. B* **2008**, *78*, 075439.
- (203) Tian, D.; Zhang, H.; Zhao, J. *Solid State Commun.* **2007**, *144*, 174.
- (204) Pereiro, M.; Baldomir, D. *Phys. Rev. A* **2007**, *75*, 033202.
- (205) Harb, M.; Rabilloud, F.; Simon, D.; Rydlo, A.; Lecoultrre, S.; Conus, F.; Rodrigues, V.; Félix, C. *J. Chem. Phys.* **2008**, *129*, 194108.
- (206) Yan, S.-Y.; Zhang, W.; Zhao, Z.-X.; Lu, W.-C.; Zhang, H.-X. *Theor. Chem. Acc.* **2012**, *131*, 1.
- (207) Chen, M.; Dyer, J. E.; Li, K.; Dixon, D. A. *J. Phys. Chem. A* **2013**, *117*, 8298.
- (208) Taherkhani, F.; Negreiros, F. R.; Parsafar, G.; Fortunelli, A. *Chem. Phys. Lett.* **2010**, *498*, 312.
- (209) Aikens, C. M.; Li, S.; Schatz, G. C. *J. Phys. Chem. C* **2008**, *112*, 11272.
- (210) Mayer, A.; González, A. L.; Aikens, C. M.; Schatz, G. C. *Nanotechnology* **2009**, *20*, 195204.
- (211) Khan, S. A.; Senapati, D.; Senapati, T.; Bonifassi, P.; Fan, Z.; Singh, A. K.; Neeley, A.; Hill, G.; Ray, P. C. *Chem. Phys. Lett.* **2011**, *512*, 92.
- (212) Yan, J.; Gao, S. *Phys. Rev. B* **2008**, *78*, 235413.
- (213) Johnson, H. E.; Aikens, C. M. *J. Phys. Chem. A* **2009**, *113*, 4445.
- (214) Liao, M.-S.; Bonifassi, P.; Leszczynski, J.; Ray, P. C.; Huang, M.-J.; Watts, J. D. *J. Phys. Chem. A* **2010**, *114*, 12701.
- (215) Guidez, E. B.; Aikens, C. M. *J. Phys. Chem. C* **2013**, *117*, 12325.
- (216) Bae, G.-T.; Aikens, C. M. *J. Phys. Chem. C* **2012**, *116*, 10356.
- (217) He, Y.; Zeng, T. *J. Phys. Chem. C* **2010**, *114*, 18023.
- (218) Weissker, H.-C.; Whetten, R. L.; Lopez-Lozano, X. *Phys. Chem. Chem. Phys.* **2014**, *16*, 12495.
- (219) Barcaro, G.; Sementa, L.; Fortunelli, A.; Stener, M. *J. Phys. Chem. C* **2014**, *118*, 12450.
- (220) Vincenot, J.; Aikens, C. In *Advances in the Theory of Atomic and Molecular Systems*; Piecuch, P., Maruani, J., Delgado-Barrio, G., Wilson, S., Eds.; Springer: Netherlands, 2009; Vol. 20.
- (221) Bae, G.-T.; Aikens, C. M. *J. Phys. Chem. A* **2012**, *116*, 8260.
- (222) Silverstein, D. W.; Jensen, L. *J. Chem. Phys.* **2010**, *132*, 194302.
- (223) Rabilloud, F. *J. Phys. Chem. A* **2013**, *117*, 4267.
- (224) Chen, H.; Ratner, M. A.; Schatz, G. C. *J. Phys. Chem. C* **2011**, *115*, 18810.
- (225) Chen, H.; Ratner, M. A.; Schatz, G. C. *J. Phys. Chem. C* **2012**, *118*, 1755.
- (226) Tielens, F.; Saeys, M.; Tourwé, E.; Marin, G. B.; Hubin, A.; Geerlings, P. *J. Phys. Chem. A* **2002**, *106*, 1450.
- (227) Tobita, M.; Yasuda, Y. *J. Phys. Chem. C* **2008**, *112*, 13851.
- (228) Zhao, L. L.; Jensen, L.; Schatz, G. C. *J. Am. Chem. Soc.* **2006**, *128*, 2911.
- (229) Jensen, L.; Zhao, L. L.; Schatz, G. C. *J. Phys. Chem. C* **2007**, *111*, 4756.
- (230) Morton, S. M.; Jensen, L. *J. Am. Chem. Soc.* **2009**, *131*, 4090.
- (231) Moore, J. E.; Morton, S. M.; Jensen, L. *J. Phys. Chem. Lett.* **2012**, *3*, 2470.
- (232) Gaff, J.; Franzen, S. *Chem. Phys.* **2012**, *397*, 34.
- (233) Valley, N.; Jensen, L.; Autschbach, J.; Schatz, G. C. *J. Chem. Phys.* **2010**, *133*, 054103.
- (234) Zhao, L. L.; Jensen, L.; Schatz, G. C. *Nano Lett.* **2006**, *6*, 1229.
- (235) Luo, J.; Wang, P.; Fang, Y. *Vib. Spectrosc.* **2014**, *70*, 162.
- (236) Zhang, X.; Wang, P.; Sheng, S.; Zhang, L.; Fang, Y. *Spectrochim. Acta, Part A* **2014**, *121*, 430.
- (237) Wang, M.; Spataru, T.; Lombardi, J. R.; Birke, R. L. *J. Phys. Chem. C* **2007**, *111*, 3044.
- (238) Jensen, L. *J. Phys. Chem. A* **2009**, *113*, 4437.
- (239) Lang, X.-F.; Yin, P.-G.; You, T.-T.; Jiang, L.; Guo, L. *ChemPhysChem* **2011**, *12*, 2468.
- (240) Brewer, K. E.; Aikens, C. M. *J. Phys. Chem. A* **2010**, *114*, 8858.
- (241) Zhuang, Z.; Shi, X.; Chen, Y.; Zuo, M. *Spectrochim. Acta, Part A* **2011**, *79*, 1593.
- (242) Sánchez-González, A.; Corni, S.; Mennucci, B. *J. Phys. Chem. C* **2011**, *115*, 5450.
- (243) Bokareva, O. S.; Kühn, O. *Chem. Phys.* **2014**, *435*, 40.
- (244) Xie, R.; He, T.-j.; He, L.; Chen, D.-m.; Liu, F.-c. *Chin. J. Chem. Phys.* **2006**, *19*, 406.
- (245) El-Khoury, P. Z.; Hess, W. P. *Chem. Phys. Lett.* **2013**, *581*, 57.
- (246) Hidalgo, F.; Noguez, C. *ACS Nano* **2012**, *7*, 513.

- (247) Ricart, J. M.; Torras, J.; Illas, F.; Rubio, J. *Surf. Sci.* **1994**, *307*–*309*, 107.
- (248) Wang, J.; Wang, G.; Zhao, J. *Chem. Phys. Lett.* **2003**, *380*, 716.
- (249) Fernández, E. M.; Soler, J. M.; Garzón, I. L.; Balbás, L. C. *Phys. Rev. B* **2004**, *70*, 165403.
- (250) Lacaze-Dufaure, C.; Blanc, C.; Mankowski, G.; Mijoule, C. *Surf. Sci.* **2007**, *601*, 1544.
- (251) Itoh, M.; Kumar, V.; Adschari, T.; Kawazoe, Y. *J. Chem. Phys.* **2009**, *131*, 174510.
- (252) Yang, M.; Yang, F.; Jackson, K. A.; Jellinek, J. *J. Chem. Phys.* **2010**, *132*, 064306.
- (253) Jellinek, J.; Acioli, P. H. *J. Chem. Phys.* **2003**, *118*, 7783.
- (254) Baishya, K.; Idrobo, J. C.; Öğüt, S.; Yang, M.; Jackson, K. A.; Jellinek, J. *Phys. Rev. B* **2011**, *83*, 245402.
- (255) Jiang, M.; Zeng, Q.; Zhang, T.; Yang, M.; Jackson, K. A. *J. Chem. Phys.* **2012**, *136*, 104501.
- (256) Ziashahabi, A.; Ghodselahi, T.; Heidari saani, M. *J. Phys. Chem. Solids* **2013**, *74*, 929.
- (257) Calaminici, P.; Pérez-Romero, M.; Vásquez-Pérez, J. M.; Köster, A. M. *Comput. Theor. Chem.* **2013**, *1021*, 41.
- (258) Anak, B.; Bencharif, M.; Rabilloud, F. *RSC Adv.* **2014**, *4*, 13001.
- (259) Pacchioni, G.; Bagus, P. S. *Chem. Phys.* **1993**, *177*, 373.
- (260) Bagus, P. S.; Pacchioni, G. *J. Chem. Phys.* **1995**, *102*, 879.
- (261) Gomes, J. R. B.; Gomes, J. A. N. F. *Surf. Sci.* **2000**, *446*, 283.
- (262) Domínguez-Ariza, D.; Sousa, C.; Harrison, N. M.; Ganduglia-Pirovano, M. V.; Illas, F. *Surf. Sci.* **2003**, *522*, 185.
- (263) Illas, F.; López, N.; Ricart, J. M.; Clotet, A.; Conesa, J. C.; Fernández-García, M. *J. Phys. Chem. B* **1998**, *102*, 8017.
- (264) Rodriguez, J. A.; Goodman, D. W. *Science* **1992**, *257*, 897.
- (265) Fernández-García, M.; Conesa, J. C.; Clotet, A.; Ricart, J. M.; López, N.; Illas, F. *J. Phys. Chem. B* **1998**, *102*, 141.
- (266) Häkkinen, H.; Barnett, R. N.; Landman, U. *Phys. Rev. Lett.* **1999**, *82*, 3264.
- (267) Garzón, I. L.; Roviera, C.; Michaelian, K.; Beltrán, M. R.; Ordejón, P.; Junquera, J.; Sánchez-Portal, D.; Artacho, E.; Soler, J. M. *Phys. Rev. Lett.* **2000**, *85*, 5250.
- (268) Häkkinen, H.; Walter, M.; Grönbeck, H. *J. Phys. Chem. B* **2006**, *110*, 9927.
- (269) Hidalgo, F.; Sánchez-Castillo, A.; Garzón, I. L.; Noguez, C. *Eur. Phys. J. D* **2009**, *52*, 179.
- (270) Batista, R. J. C.; Mazzoni, M. S. C.; Garzón, I. L.; Beltrán, M. R.; Chacham, H. *Phys. Rev. Lett.* **2006**, *96*, 116802.
- (271) Jadzinsky, P. D.; Calero, G.; Ackerson, C. J.; Bushnell, D. A.; Kornberg, R. D. *Science* **2007**, *318*, 430.
- (272) Noguez, C.; Garzon, I. L. *Chem. Soc. Rev.* **2009**, *38*, 757.
- (273) Jiang, D.-e. *Acta Phys. Chim. Sin.* **2010**, *26*, 999.
- (274) Aikens, C. M. *J. Phys. Chem. Lett.* **2011**, *1*, 2594.
- (275) Aikens, C. M. *Mol. Simul.* **2012**, *38*, 607.
- (276) Häkkinen, H. *Nat. Chem.* **2012**, *4*, 443.
- (277) Pei, Y.; Zeng, X. C. *Nanoscale* **2012**, *4*, 4054.
- (278) Jiang, D.-e. *Nanoscale* **2013**, *5*, 7149.
- (279) Iwasa, T.; Nobusada, K. *Chem. Phys. Lett.* **2007**, *441*, 268.
- (280) Iwasa, T.; Nobusada, K. *J. Phys. Chem. C* **2007**, *111*, 45.
- (281) Akola, J.; Walter, M.; Whetten, R. L.; Häkkinen, H.; Grönbeck, H. *J. Am. Chem. Soc.* **2008**, *130*, 3756.
- (282) Heaven, M. W.; Dass, A.; White, P. S.; Holt, K. M.; Murray, R. W. *J. Am. Chem. Soc.* **2008**, *130*, 3754.
- (283) Zhu, M.; Aikens, C. M.; Hollander, F. J.; Schatz, G. C.; Jin, R. J. *Am. Chem. Soc.* **2008**, *130*, 5883.
- (284) Zhu, M.; Eckenhoff, W. T.; Pintauer, T.; Jin, R. *J. Phys. Chem. C* **2008**, *112*, 14221.
- (285) Aikens, C. M. *J. Phys. Chem. C* **2008**, *112*, 19797.
- (286) Aikens, C. M. *J. Phys. Chem. A* **2009**, *113*, 10811.
- (287) Day, P. N.; Nguyen, K. A.; Pachter, R. *J. Chem. Theory Comput.* **2010**, *6*, 2809.
- (288) Parker, J. F.; Kacprzak, K. A.; Lopez-Acevedo, O.; Häkkinen, H.; Murray, R. W. *J. Phys. Chem. C* **2010**, *114*, 8276.
- (289) Aikens, C. M. *J. Phys. Chem. Lett.* **2010**, *1*, 2594.
- (290) Guo, R.; Murray, R. W. *J. Am. Chem. Soc.* **2005**, *127*, 12140.
- (291) Akola, J.; Kacprzak, K. A.; Lopez-Acevedo, O.; Walter, M.; Grönbeck, H.; Häkkinen, H. *J. Phys. Chem. C* **2010**, *114*, 15986.
- (292) Jung, J.; Kang, S.; Han, Y.-K. *Nanoscale* **2012**, *4*, 4206.
- (293) Schaaff, T. G.; Whetten, R. L. *J. Phys. Chem. B* **2000**, *104*, 2630.
- (294) Sánchez-Castillo, A.; Noguez, C.; Garzón, I. L. *J. Am. Chem. Soc.* **2010**, *132*, 1504.
- (295) Tlahuice-Flores, A.; Whetten, R. L.; Jose-Yacaman, M. *J. Phys. Chem. C* **2013**, *117*, 20867.
- (296) Grönbeck, H. *Nanoscale* **2012**, *4*, 4178.
- (297) Tlahuice-Flores, A. *Mol. Simul.* **2013**, *39*, 428.
- (298) Tlahuice-Flores, A.; Whetten, R. L.; Jose-Yacaman, M. *J. Phys. Chem. C* **2013**, *117*, 12191.
- (299) Mäkinen, V.; Häkkinen, H. *Eur. Phys. J. D* **2012**, *66*, 1.
- (300) Lopez-Acevedo, O.; Häkkinen, H. *Eur. Phys. J. D* **2011**, *63*, 311.
- (301) Liu, C.; Lin, S.; Pei, Y.; Zeng, X. C. *J. Am. Chem. Soc.* **2013**, *135*, 18067.
- (302) Lopez-Acevedo, O.; Kacprzak, K. A.; Akola, J.; Häkkinen, H. *Nat. Chem.* **2010**, *2*, 329.
- (303) Kauffman, D. R.; Alfonso, D.; Matranga, C.; Qian, H.; Jin, R. J. *Am. Chem. Soc.* **2012**, *134*, 10237.
- (304) Li, G.; Jiang, D.-e.; Liu, C.; Yu, C.; Jin, R. *J. Catal.* **2013**, *306*, 177.
- (305) Wu, Z.; Jiang, D.-e.; Mann, A. K. P.; Mullins, D. R.; Qiao, Z.-A.; Allard, L. F.; Zeng, C.; Jin, R.; Overbury, S. H. *J. Am. Chem. Soc.* **2014**, *136*, 6111.
- (306) Jupally, V. R.; Kota, R.; Van Dornshuld, E.; Mattern, D. L.; Tschumper, G. S.; Jiang, D.-e.; Dass, A. *J. Am. Chem. Soc.* **2011**, *133*, 20258.
- (307) Mathew, A.; Natarajan, G.; Lehtovaara, L.; Häkkinen, H.; Kumar, R. M.; Subramanian, V.; Jaleel, A.; Pradeep, T. *ACS Nano* **2013**, *8*, 139.
- (308) Zhu, M.; Aikens, C. M.; Hendrich, M. P.; Gupta, R.; Qian, H.; Schatz, G. C.; Jin, R. *J. Am. Chem. Soc.* **2009**, *131*, 2490.
- (309) Venzo, A.; Antonello, S.; Gascón, J. A.; Guryanov, I.; Leapman, R. D.; Perera, N. V.; Sousa, A.; Zamuner, M.; Zanella, A.; Maran, F. *Anal. Chem.* **2011**, *83*, 6355.
- (310) Antonello, S.; Perera, N. V.; Ruzzi, M.; Gascón, J. A.; Maran, F. *J. Am. Chem. Soc.* **2013**, *135*, 15585.
- (311) Dainese, T.; Antonello, S.; Gascón, J. A.; Pan, F.; Perera, N. V.; Ruzzi, M.; Venzo, A.; Zoleo, A.; Rissanen, K.; Maran, F. *ACS Nano* **2014**, *8*, 3904.
- (312) Fields-Zinna, C. A.; Crowe, M. C.; Dass, A.; Weaver, J. E. F.; Murray, R. W. *Langmuir* **2009**, *25*, 7704.
- (313) Jiang, D.-e.; Dai, S. *Inorg. Chem.* **2009**, *48*, 2720.
- (314) Kacprzak, K. A.; Lehtovaara, L.; Akola, J.; Lopez-Acevedo, O.; Häkkinen, H. *Phys. Chem. Chem. Phys.* **2009**, *11*, 7123.
- (315) Walter, M.; Moseler, M. *J. Phys. Chem. C* **2009**, *113*, 15834.
- (316) Negishi, Y.; Kurashige, W.; Niihori, Y.; Iwasa, T.; Nobusada, K. *Phys. Chem. Chem. Phys.* **2010**, *12*, 6219.
- (317) Qian, H.; Jiang, D.-e.; Li, G.; Gayathri, C.; Das, A.; Gil, R. R.; Jin, R. *J. Am. Chem. Soc.* **2012**, *134*, 16159.
- (318) Ulises Reveles, J.; Clayborne, P. A.; Reber, A. C.; Khanna, S. N.; Pradhan, K.; Sen, P.; Pederson, M. R. *Nat. Chem.* **2009**, *1*, 310.
- (319) Jiang, D.-e.; Whetten, R. L. *Phys. Rev. B* **2009**, *80*, 115402.
- (320) Zhou, M.; Cai, Y. Q.; Zeng, M. G.; Zhang, C.; Feng, Y. P. *Appl. Phys. Lett.* **2011**, *98*, 143103/1.
- (321) Chen, X.; Strange, M.; Häkkinen, H. *Phys. Rev. B* **2012**, *85*, 085422/1.
- (322) Negishi, Y.; Iwai, T.; Ide, M. *Chem. Commun.* **2010**, *46*, 4713.
- (323) Guidez, E. B.; Mäkinen, V.; Häkkinen, H.; Aikens, C. M. *J. Phys. Chem. C* **2012**, *116*, 20617.
- (324) Tlahuice-Flores, A. *J. Nanopart. Res.* **2013**, *15*, 1.
- (325) Kauffman, D. R.; Alfonso, D.; Matranga, C.; Qian, H.; Jin, R. *J. Phys. Chem. C* **2013**, *117*, 7914.
- (326) Kumara, C.; Aikens, C. M.; Dass, A. *J. Phys. Chem. Lett.* **2014**, *5*, 461.
- (327) Negishi, Y.; Munakata, K.; Ohgake, W.; Nobusada, K. *J. Phys. Chem. Lett.* **2012**, *3*, 2209.

- (328) Kurashige, W.; Yamaguchi, M.; Nobusada, K.; Negishi, Y. *J. Phys. Chem. Lett.* **2012**, *3*, 2649.
- (329) Kurashige, W.; Munakata, K.; Nobusada, K.; Negishi, Y. *Chem. Commun.* **2013**, *49*, 5447.
- (330) Kurashige, W.; Yamazoe, S.; Yamaguchi, M.; Nishido, K.; Nobusada, K.; Tsukuda, T.; Negishi, Y. *J. Phys. Chem. Lett.* **2014**, *5*, 2072.
- (331) Jiang, D.-e.; Tiago, M.; Luo, W.; Dai, S. *J. Am. Chem. Soc.* **2008**, *130*, 2777.
- (332) Jiang, D.-e.; Luo, W.; Tiago, M. L.; Dai, S. *J. Phys. Chem. C* **2008**, *112*, 13905.
- (333) Pei, Y.; Gao, Y.; Zeng, X. *C. J. Am. Chem. Soc.* **2008**, *130*, 7830.
- (334) Lopez-Acevedo, O.; Tsunoyama, H.; Tsukuda, T.; Häkkinen, H.; Aikens, C. M. *J. Am. Chem. Soc.* **2010**, *132*, 8210.
- (335) Qian, H.; Eckenhoff, W. T.; Zhu, Y.; Pintauer, T.; Jin, R. *J. Am. Chem. Soc.* **2010**, *132*, 8280.
- (336) Negishi, Y.; Igarashi, K.; Munakata, K.; Ohgake, W.; Nobusada, K. *Chem. Commun.* **2012**, *48*, 660.
- (337) Molina, B.; Sanchez-Castillo, A.; Knoppe, S.; Garzon, I. L.; Bürgi, T.; Tlahuice-Flores, A. *Nanoscale* **2013**, *5*, 10956.
- (338) Gao, Y.; Shao, N.; Zeng, X. *C. ACS Nano* **2008**, *2*, 1497.
- (339) Li, Y.; Galli, G.; Gygi, F. *ACS Nano* **2008**, *2*, 1896.
- (340) Reimers, J. R.; Wang, Y.; Cankurtaran, B. O.; Ford, M. J. *J. Am. Chem. Soc.* **2010**, *132*, 8378.
- (341) Lopez-Acevedo, O.; Clayborne, P. A.; Häkkinen, H. *Phys. Rev. B* **2011**, *84*, 035434.
- (342) Heinecke, C. L.; Ni, T. W.; Malola, S.; Mäkinen, V.; Wong, O. A.; Häkkinen, H.; Ackerson, C. J. *J. Am. Chem. Soc.* **2012**, *134*, 13316.
- (343) Gao, Y. *J. Phys. Chem. C* **2013**, *117*, 8983.
- (344) Hulkko, E.; Lopez-Acevedo, O.; Koivisto, J.; Levi-Kalsman, Y.; Kornberg, R. D.; Pettersson, M.; Häkkinen, H. *J. Am. Chem. Soc.* **2011**, *133*, 3752.
- (345) Knoppe, S.; Wong, O. A.; Malola, S.; Häkkinen, H.; Bürgi, T.; Verbiest, T.; Ackerson, C. J. *J. Am. Chem. Soc.* **2014**, *136*, 4129.
- (346) Lopez-Acevedo, O.; Akola, J.; Whetten, R. L.; Grönbeck, H.; Häkkinen, H. *J. Phys. Chem. C* **2009**, *113*, 5035.
- (347) Malola, S.; Häkkinen, H. *J. Phys. Chem. Lett.* **2011**, *2*, 2316.
- (348) Kumara, C.; Dass, A. *Nanoscale* **2011**, *3*, 3064.
- (349) Koivisto, J.; Malola, S.; Kumara, C.; Dass, A.; Häkkinen, H.; Pettersson, M. *J. Phys. Chem. Lett.* **2012**, *3*, 3076.
- (350) Malola, S.; Lehtovaara, L.; Häkkinen, H. *J. Phys. Chem. C* **2014**, *118*, 20002.
- (351) MacDonald, M. A.; Zhang, P.; Qian, H.; Jin, R. *J. Phys. Chem. Lett.* **2010**, *1*, 1821.
- (352) Bahena, D.; Bhattacharai, N.; Santiago, U.; Tlahuice, A.; Ponce, A.; Bach, S. B. H.; Yoon, B.; Whetten, R. L.; Landman, U.; Jose-Yacaman, M. *J. Phys. Chem. Lett.* **2013**, *4*, 975.
- (353) Weissker, H. C.; Escobar, H. B.; Thanthirige, V. D.; Kwak, K.; Lee, D.; Ramakrishna, G.; Whetten, R. L.; López-Lozano, X. *Nat. Commun.* **2014**, *5*, 3785.
- (354) Zeng, C.; Qian, H.; Li, T.; Li, G.; Rosi, N. L.; Yoon, B.; Barnett, R. N.; Whetten, R. L.; Landman, U.; Jin, R. *Angew. Chem., Int. Ed.* **2012**, *124*, 13291.
- (355) Zeng, C.; Liu, C.; Pei, Y.; Jin, R. *ACS Nano* **2013**, *7*, 6138.
- (356) Zeng, C.; Li, T.; Das, A.; Rosi, N. L.; Jin, R. *J. Am. Chem. Soc.* **2013**, *135*, 10011.
- (357) Knoppe, S.; Malola, S.; Lehtovaara, L.; Bürgi, T.; Häkkinen, H. *J. Phys. Chem. A* **2013**, *117*, 10526.
- (358) Das, A.; Li, T.; Nobusada, K.; Zeng, C.; Rosi, N. L.; Jin, R. *J. Am. Chem. Soc.* **2013**, *135*, 18264.
- (359) Das, A.; Li, T.; Li, G.; Nobusada, K.; Zeng, C.; Rosi, N. L.; Jin, R. *Nanoscale* **2014**, *6*, 6458.
- (360) Song, Y.; Wang, S.; Zhang, J.; Kang, X.; Chen, S.; Li, P.; Sheng, H.; Zhu, M. *J. Am. Chem. Soc.* **2014**, *136*, 2963.
- (361) Zhu, M.; Qian, H.; Jin, R. *J. Phys. Chem. Lett.* **2010**, *1*, 1003.
- (362) Crasto, D.; Malola, S.; Brosofsky, G.; Dass, A.; Häkkinen, H. *J. Am. Chem. Soc.* **2014**, *136*, 5000.
- (363) Shaw, C. F., III. *Chem. Rev.* **1999**, *99*, 2589.
- (364) Bau, R. *J. Am. Chem. Soc.* **1998**, *120*, 9380.
- (365) Daniel, M.-C.; Astruc, D. *Chem. Rev.* **2004**, *104*, 293.
- (366) Shao, N.; Pei, Y.; Gao, Y.; Zeng, X. *C. J. Phys. Chem. A* **2009**, *113*, 629.
- (367) Kacprzak, K. A.; Lopez-Acevedo, O.; Häkkinen, H.; Grönbeck, H. *J. Phys. Chem. C* **2010**, *114*, 13571.
- (368) Jiang, D.-e.; Whetten, R. L.; Luo, W.; Dai, S. *J. Phys. Chem. C* **2009**, *113*, 17291.
- (369) Jiang, D.-e.; Chen, W.; Whetten, R. L.; Chen, Z. *J. Phys. Chem. C* **2009**, *113*, 16983.
- (370) Pei, Y.; Gao, Y.; Shao, N.; Zeng, X. *C. J. Am. Chem. Soc.* **2009**, *131*, 13619.
- (371) Tlahuice, A.; Garzón, I. L. *Phys. Chem. Chem. Phys.* **2012**, *14*, 3737.
- (372) Tlahuice, A.; Garzón, I. L. *Phys. Chem. Chem. Phys.* **2012**, *14*, 7321.
- (373) Jiang, D.-e. *Chem.—Eur. J.* **2011**, *17*, 12289.
- (374) Pei, Y.; Pal, R.; Liu, C.; Gao, Y.; Zhang, Z.; Zeng, X. *C. J. Am. Chem. Soc.* **2012**, *134*, 3015.
- (375) Jiang, D.-e.; Overbury, S. H.; Dai, S. *J. Am. Chem. Soc.* **2013**, *135*, 8786.
- (376) Tlahuice-Flores, A.; Jose-Yacamán, M.; Whetten, R. L. *Phys. Chem. Chem. Phys.* **2013**, *15*, 19557.
- (377) Yu, Y.; Luo, Z.; Chevrier, D. M.; Leong, D. T.; Zhang, P.; Jiang, D.-e.; Xie, J. *J. Am. Chem. Soc.* **2014**, *136*, 1246.
- (378) Jiang, D.-e.; Walter, M.; Akola, J. *J. Phys. Chem. C* **2010**, *114*, 15883.
- (379) Pei, Y.; Lin, S.; Su, J.; Liu, C. *J. Am. Chem. Soc.* **2013**, *135*, 19060.
- (380) Zeng, C.; Chen, Y.; Li, G.; Jin, R. *Chem. Commun.* **2014**, *50*, 55.
- (381) Malola, S.; Lehtovaara, L.; Knoppe, S.; Hu, K.-J.; Palmer, R. E.; Bürgi, T.; Häkkinen, H. *J. Am. Chem. Soc.* **2012**, *134*, 19560.
- (382) Malola, S.; Lehtovaara, L.; Häkkinen, H. *J. Phys. Chem. Lett.* **2014**, *5*, 1329.
- (383) Nimmala, P. R.; Yoon, B.; Whetten, R. L.; Landman, U.; Dass, A. *J. Phys. Chem. A* **2013**, *117*, 504.
- (384) Tlahuice-Flores, A.; Santiago, U.; Bahena, D.; Vinogradova, E.; Conroy, C. V.; Ahuja, T.; Bach, S. B. H.; Ponce, A.; Wang, G.; José-Yacamán, M.; Whetten, R. L. *J. Phys. Chem. A* **2013**, *117*, 10470.
- (385) Malola, S.; Lehtovaara, L.; Enkovaara, J.; Häkkinen, H. *ACS Nano* **2013**, *7*, 10263.
- (386) Jiang, D.-e.; Walter, M. *Nanoscale* **2012**, *4*, 4234.
- (387) Tlahuice-Flores, A.; Black, D. M.; Bach, S. B. H.; Jose-Yacamán, M.; Whetten, R. L. *Phys. Chem. Chem. Phys.* **2013**, *15*, 19191.
- (388) McPartlin, M.; Mason, R.; Malatesta, L. *Chem. Commun.* **1969**, *334*.
- (389) Mollenhauer, D.; Gaston, N. *J. Comput. Chem.* **2014**, *35*, 986.
- (390) Bellon, P.; Manassero, M.; Sansoni, M. *J. Chem. Soc., Dalton Trans.* **1972**, *1481*.
- (391) Nunokawa, K.; Onaka, S.; Ito, M.; Horibe, M.; Yonezawa, T.; Nishihara, H.; Ozeki, T.; Chiba, H.; Watase, S.; Nakamoto, M. *J. Organomet. Chem.* **2006**, *691*, 638.
- (392) Schulz-Dobrick, M.; Jansen, M. Z. *Anorg. Allg. Chem.* **2007**, *633*, 2326.
- (393) Copley, R. C. B.; Mingos, D. M. P. *J. Chem. Soc., Dalton Trans.* **1996**, *479*.
- (394) Mingos, D. M. P. *J. Chem. Soc., Dalton Trans.* **1976**, *1163*.
- (395) Spivey, K.; Williams, J. I.; Wang, L. *Chem. Phys. Lett.* **2006**, *432*, 163.
- (396) Dufour, F.; Fresch, B.; Durupthy, O.; Chaneac, C.; Remacle, F. *J. Phys. Chem. C* **2014**, *118*, 4362.
- (397) Provorse, M. R.; Aikens, C. M. *J. Am. Chem. Soc.* **2010**, *132*, 1302.
- (398) Hadley, A.; Aikens, C. M. *J. Phys. Chem. C* **2010**, *114*, 18134.
- (399) Lopez-Acevedo, O.; Kacprzak, K. A.; Akola, J.; Häkkinen, H. *Nat. Chem.* **2010**, *2*, 329.
- (400) Chen, X.; Häkkinen, H. *J. Am. Chem. Soc.* **2013**, *135*, 12944.
- (401) Briant, C. E.; Theobald, B. R. C.; White, J. W.; Bell, L. K.; Mingos, D. M. P.; Welch, A. J. *J. Chem. Soc., Chem. Commun.* **1981**, *5*, 201.

- (402) Li, J.; Wang, S.-G. *J. Mol. Model.* **2010**, *16*, 505.
- (403) Fresch, B.; Hanozin, E.; Dufour, F.; Remacle, F. *Eur. Phys. J. D* **2012**, *66*, 326.
- (404) Yang, H.; Wang, Y.; Lei, J.; Shi, L.; Wu, X.; Mäkinen, V.; Lin, S.; Tang, Z.; He, J.; Häkkinen, H.; Zheng, L.; Zheng, N. *J. Am. Chem. Soc.* **2013**, *135*, 9568.
- (405) Knoppe, S.; Lehtovaara, L.; Häkkinen, H. *J. Phys. Chem. A* **2014**, *118*, 4214.
- (406) Shichibu, Y.; Negishi, Y.; Watanabe, T.; Chaki, N. K.; Kawaguchi, H.; Tsukuda, T. *J. Phys. Chem. C* **2007**, *111*, 7845.
- (407) Teo, B. K.; Keating, K. *J. Am. Chem. Soc.* **1984**, *106*, 2224.
- (408) Nobusada, K.; Iwasa, T. *J. Phys. Chem. C* **2007**, *111*, 14279.
- (409) Iwasa, T.; Nobusada, K.; Nakajima, A. *J. Phys. Chem. C* **2013**, *117*, 24586.
- (410) Goh, J.-Q.; Malola, S.; Häkkinen, H.; Akola, J. *J. Phys. Chem. C* **2013**, *117*, 22079.
- (411) Teo, B. K.; Shi, X.; Zhang, H. *J. Am. Chem. Soc.* **1992**, *114*, 2743.
- (412) Häkkinen, H.; Walter, M.; Grönbeck, H. *J. Phys. Chem. B* **2006**, *110*, 9927.
- (413) Schmid, G.; Pfeil, R.; Boese, R.; Bandermann, F.; Meyer, S.; Calis, G. H. M.; van der Velden, J. W. A. *Chem. Ber.* **1981**, *114*, 3634.
- (414) Schmid, G. *Chem. Soc. Rev.* **2008**, *37*, 1909.
- (415) Periyasamy, G.; Remacle, F. *Nano Lett.* **2009**, *9*, 3007.
- (416) Genest, A.; Krüger, S.; Rösch, N. Z. *Naturforsch.* **2009**, *64b*, 1246.
- (417) Pei, Y.; Shao, N.; Gao, Y.; Zeng, X. C. *ACS Nano* **2010**, *4*, 2009.
- (418) Walter, M.; Moseler, M.; Whetten, R. L.; Häkkinen, H. *Chem. Sci.* **2011**, *2*, 1583.
- (419) Fackler, J. P.; McNeal, C. J.; Pignolet, L. H.; Winpenny, R. E. P. *J. Am. Chem. Soc.* **1989**, *111*, 6434.
- (420) Lopez-Acevedo, O.; Rintala, J.; Virtanen, S.; Femoni, C.; Tiozzo, C.; Grönbeck, H.; Pettersson, M.; Häkkinen, H. *J. Am. Chem. Soc.* **2009**, *131*, 12573.
- (421) Bakr, O. M.; Amendola, V.; Aikens, C. M.; Wenseleers, W.; Lee, R.; Dal Negro, L.; Schatz, G. C.; Stellacci, F. *Angew. Chem., Int. Ed.* **2009**, *48*, 5921.
- (422) Yang, H.; Wang, Y.; Huang, H.; Gell, L.; Lehtovaara, L.; Malola, S.; Häkkinen, H.; Zheng, N. *Nat. Commun.* **2013**, *4*, 2422.
- (423) Desiréddy, A.; Conn, B. E.; Guo, J.; Yoon, B.; Barnett, R. N.; Monahan, B. M.; Kirschbaum, K.; Griffith, W. P.; Whetten, R. L.; Landman, U.; Bigioni, T. P. *Nature* **2013**, *501*, 399.
- (424) Yang, H.; Wang, Y.; Yan, J.; Chen, X.; Zhang, X.; Häkkinen, H.; Zheng, N. *J. Am. Chem. Soc.* **2014**, *136*, 7197.
- (425) Chakraborty, I.; Govindarajan, A.; Erusappan, J.; Ghosh, A.; Pradeep, T.; Yoon, B.; Whetten, R. L.; Landman, U. *Nano Lett.* **2012**, *12*, 5861.
- (426) Bertorelle, F.; Hamouda, R.; Rayane, D.; Broyer, M.; Antoine, R.; Dugourd, P.; Gell, L.; Kulesza, A.; Mitić, R.; Bonačić-Koutecký, V. *Nanoscale* **2013**, *5*, 5637.
- (427) Michaelian, K.; Beltrán, M. R.; Garzón, I. L. *Phys. Rev. B* **2002**, *65*, 041403.
- (428) Wang, J.; Wang, G.; Zhao, J. *Phys. Rev. A* **2003**, *68*, 013201.
- (429) Iokibe, K.; Tachikawa, H.; Azumi, K. *J. Phys. B: At., Mol. Opt. Phys.* **2007**, *40*, 427.
- (430) Johansson, M. P.; Pyykkö, P. *Phys. Chem. Chem. Phys.* **2004**, *6*, 2907.
- (431) Piotrowski, M. J.; Piquini, P.; Silva, J. L. F. D. *Phys. Rev. B* **2010**, *81*, 155446.
- (432) Gutsev, G. L.; Weatherford, C. W.; Belay, K. G.; Ramachandran, B. R.; Jena, P. *J. Chem. Phys.* **2013**, *138*, 164303.
- (433) Zhao, J. *Phys. Rev. A* **2001**, *64*, 043204.
- (434) Wang, Y.; Flad, H.-J.; Dolg, M. *Phys. Rev. B* **2000**, *61*, 2362.
- (435) Hartke, B.; Flad, H.-J.; Dolg, M. *Phys. Chem. Chem. Phys.* **2001**, *3*, 5121.
- (436) Gaston, N.; Schwerdtfeger, P. *Phys. Rev. B* **2006**, *74*, 024105.
- (437) Yuan, H. K.; Chen, H.; Ahmed, A. S.; Zhang, J. F. *Phys. Rev. B* **2006**, *74*, 144434.
- (438) Li, X.-B.; Wang, H.-Y.; Luo, J.-S.; Guo, Y.-D.; Wu, W.-D.; Tang, Y.-J. *Chin. Phys. B* **2009**, *18*, 3414.
- (439) Wang, J. *Phys. Rev. B* **2007**, *75*, 155422.
- (440) Wang, J.; Wang, Y.; Wu, G.; Zhang, X.; Zhao, X.; Yang, M. *Phys. Chem. Chem. Phys.* **2009**, *11*, 5980.
- (441) Wu, G.; Wang, J.; Lu, Y.; Yang, M. *J. Chem. Phys.* **2008**, *128*, 224315.
- (442) Wang, Y.; Wu, G.; Du, J.; Yang, M.; Wang, J. *J. Phys. Chem. A* **2012**, *116*, 93.
- (443) Wang, M.; Qiu, G.; Huang, X.; Du, Z.; Li, Y. *J. Phys.: Condens. Matter* **2009**, *21*, 046004(1).
- (444) Tian, F.-Y.; Wang, Y.-X. *Int. J. Quantum Chem.* **2010**, *110*, 1573.
- (445) Zhao, J.; Qiu, Q.; Wang, B.; Wang, J.; Wang, G. *Solid State Commun.* **2001**, *118*, 157.
- (446) Villanueva, M. S.; Tejeda, P. H. H.; Pal, U.; Rivas-Silva, J. F.; Mora, J. V. R.; Ascencio, J. A. *J. Phys. Chem. A* **2006**, *110*, 10274.
- (447) Villanueva, M. S.; Romero, A. H.; Hernández, A. B. *Nanotechnology* **2009**, *20*, 465709.
- (448) Castro, M.; Liu, S.-R.; Zhai, H.-J.; Wang, L.-S. *J. Chem. Phys.* **2003**, *118*, 2116.
- (449) Wang, S.-Y.; Duan, W.; Zhao, D.-L.; Wang, C.-Y. *Phys. Rev. B* **2002**, *65*, 165424.
- (450) Wang, S.-Y.; Yu, J.-Z.; Mizuseki, H.; Yan, J.-A.; Kawazoe, Y.; Wang, C.-Y. *J. Chem. Phys.* **2004**, *120*, 8463.
- (451) Lee, B.; Lee, G. W. *J. Chem. Phys.* **2007**, *127*, 164316.
- (452) Medina, J.; deCoss, R.; Tapia, A.; Canto, G. *Eur. Phys. J. B* **2010**, *76*, 427.
- (453) Wang, S.-Y.; Duan, W.; Wang, C.-Y. *J. Phys. B: At., Mol. Opt. Phys.* **2002**, *35*, 4015.
- (454) Xiang, J.; Wei, S. H.; Yan, X. H.; You, J. Q.; Mao, Y. L. *J. Chem. Phys.* **2004**, *120*, 4251.
- (455) Du, J.; Sun, X.; Chen, J.; Jiang, G. *J. Phys. B: At., Mol. Opt. Phys.* **2010**, *43*, 205103(1).
- (456) Wang, H.; Hu, N.; Tao, D.-J.; Lu, Z.-H.; Nie, J.; Chen, X.-S. *Comput. Theor. Chem.* **2011**, *977*, 50.
- (457) Verkhovtsev, A. V.; Hanauske, M.; Yakubovich, A. V.; Solov'yov, A. V. *Comput. Mater. Sci.* **2013**, *76*, 80.
- (458) Salahub, D. R.; Messmer, R. P. *Surf. Sci.* **1981**, *106*, 415.
- (459) Liu, F.; Khanna, S. N.; Jena, P. *Phys. Rev. B* **1991**, *43*, 8179.
- (460) Lee, K.; Callaway, J. *Phys. Rev. B* **1993**, *48*, 15358.
- (461) Lee, K.; Callaway, J. *Phys. Rev. B* **1994**, *49*, 13906.
- (462) Alvarado, P.; Dorantes-Dávila, J.; Dreysse, H. *Nanostruct. Mater.* **1993**, *3*, 331.
- (463) Kortus, J.; Pederson, M. R.; Hellberg, C. S.; Khanna, S. N. *Eur. Phys. J. D* **2001**, *16*, 177.
- (464) Ratsch, C.; Fielicke, A.; Kirilyuk, A.; Behler, J.; Helden, G. v.; Meijer, G.; Scheffler, M. *J. Chem. Phys.* **2005**, *122*, 124302.
- (465) Wu, G.; Yang, M.; Guo, X.; Wang, J. *Comput. Chem.* **2012**, *33*, 1854.
- (466) Cheng, H.; Wang, L.-S. *Phys. Rev. Lett.* **1996**, *77*, 51.
- (467) Reddy, B. V.; Khanna, S. N.; Jena, P. *Phys. Rev. B* **1999**, *60*, 15597.
- (468) Nayak, S. K.; Nooijen, M. *J. Phys. Chem. A* **1999**, *103*, 9853.
- (469) Briere, T. M.; Sluiter, M. H. F.; Kumar, V.; Kawazoe, Y. *Phys. Rev. B* **2002**, *66*, 064412.
- (470) Bobadova-Parvanova, P.; Jackson, K. A.; Srinivas, S.; Horoi, M. *Phys. Rev. A* **2003**, *67*, 061202.
- (471) Bobadova-Parvanova, P.; Jackson, K. A.; Srinivas, S.; Horoi, M. *J. Chem. Phys.* **2005**, *122*, 014310.
- (472) Kabir, M.; Mookerjee, A.; Kanhere, D. G. *Phys. Rev. B* **2006**, *73*, 224439.
- (473) Xie, Y.; Blackman, J. A. *Phys. Rev. B* **2006**, *73*, 214436.
- (474) Gutsev, G. L.; Mochena, M. D.; B, C. W., Jr.; Zheng, W.-J.; Thomas, O. C.; Bowen, K. H. *J. Chem. Phys.* **2008**, *129*, 044310.
- (475) Longo, R. C.; Carrete, J.; Gallego, L. J. *J. Chem. Phys.* **2009**, *131*, 046101.
- (476) Datta, S.; Kabir, M.; Mookerjee, A.; Saha-Dasgupta, T. *Phys. Rev. B* **2011**, *83*, 075425.

- (477) Dunlap, B. I. *Z. Phys. D: At., Mol. Clusters* **1991**, *19*, 255.
- (478) Diéguez, O.; Alemany, M. M. G.; Rey, C.; Ordejón, P.; Gallego, L. *J. Phys. Rev. B* **2001**, *63*, 205407.
- (479) Bobadova-Parvanova, P.; Jackson, K. A.; Srinivas, S.; Horoi, M. *Phys. Rev. B* **2002**, *66*, 195402.
- (480) Duan, H. M.; Zheng, Q. Q. *Phys. Lett. A* **2001**, *280*, 333.
- (481) Aguilera-Granja, F.; Vega, A.; Balbás, L. C. *J. Mex. Chem. Soc.* **2012**, *S6*, 331.
- (482) Postnikov, A. V.; Entel, P.; Soler, J. M. *Eur. Phys. J. D* **2003**, *25*, 261.
- (483) Köhler, C.; Seifert, G.; Frauenheim, T. *Chem. Phys.* **2005**, *309*, 23.
- (484) Šípr, O.; Košuth, M.; Ebert, H. *Phys. Rev. B* **2004**, *70*, 174423.
- (485) Rollmann, G.; Entel, P.; Sahoo, S. *Comput. Mater. Sci.* **2006**, *35*, 275.
- (486) Rollmann, G.; Gruner, M. E.; Hucht, A.; Meyer, R.; Entel, P.; Tiago, M. L.; Chelikowsky, J. R. *Phys. Rev. Lett.* **2007**, *99*, 083402.
- (487) Ma, Q.-M.; Xie, Z.; Wang, J.; Liu, Y.; Li, Y.-C. *Solid State Commun.* **2007**, *142*, 114.
- (488) Gutsev, G. L.; Weatherford, C. A.; Jena, P.; Johnson, E.; Ramachandran, B. R. *J. Phys. Chem. A* **2012**, *116*, 10218.
- (489) Wu, M.; Kandalam, A. K.; Gutsev, G. L.; Jena, P. *Phys. Rev. B* **2012**, *86*, 174410.
- (490) Sahoo, S.; Hucht, A.; Gruner, M. E.; Rollmann, G.; Entel, P.; Postnikov, A.; Ferrer, J.; Fernández-Seivane, L.; Richter, M.; Fritsch, D.; Sil, S. *Phys. Rev. B* **2010**, *82*, 054418.
- (491) Li, Z.-q.; Gu, B.-l. *Phys. Rev. B* **1993**, *47*, 13611.
- (492) Miura, K.; Kimura, H.; Imanaga, S. *Phys. Rev. B* **1994**, *50*, 10335.
- (493) Ma, Q.-M.; Xie, Z.; Wang, J.; Liu, Y.; Li, Y.-C. *Phys. Lett. A* **2006**, *358*, 289.
- (494) Ma, Q. M.; Liu, Y.; Xie, Z.; Wang, J. *J. Phys.: Conf. Ser.* **2006**, *29*, 163.
- (495) Datta, S.; Kabir, M.; Ganguly, S.; Sanyal, B.; Saha-Dasgupta, T.; Mookerjee, A. *Phys. Rev. B* **2007**, *76*, 014429.
- (496) Dong, C. D.; Gong, X. G. *Phys. Rev. B* **2008**, *78*, 020409.
- (497) Piotrowski, M. J.; Piquini, P.; Cândido, L.; Silva, J. L. F. D. *Phys. Chem. Chem. Phys.* **2011**, *13*, 17242.
- (498) Tereshchuk, P. L. *Comput. Mater. Sci.* **2011**, *50*, 991.
- (499) Aguilera-Granja, F.; Montejano-Carrizalez, J. M.; Guirado-López, R. A. *Phys. Rev. B* **2006**, *73*, 115422.
- (500) Jinlong, Y.; Chuanyun, X.; Shangda, X.; Kelin, W. *Phys. Rev. B* **1993**, *48*, 12155.
- (501) Lv, J.; Zhang, F.-Q.; Jia, J.-F.; Xu, X.-H.; Wu, H.-S. *J. Mol. Struct.* **2010**, *955*, 14.
- (502) Piotrowski, M. J.; Piquini, P.; Silva, J. L. F. D. *J. Phys. Chem. C* **2012**, *116*, 18432.
- (503) Islam, M. F.; Khanna, S. N. *J. Phys.: Condens. Matter* **2014**, *26*, 125303.
- (504) Kaiming, D.; Jinlong, Y.; Chuanyun, X.; Kelin, W. *Phys. Rev. B* **1996**, *54*, 11907.
- (505) Kumar, V.; Kawazoe, Y. *Phys. Rev. B* **2002**, *65*, 125403.
- (506) Kumar, V.; Kawazoe, Y. *Eur. Phys. J. D* **2003**, *24*, 81.
- (507) Zhang, W.; Zhao, H.; Wang, L. *J. Phys. Chem. B* **2004**, *108*, 2140.
- (508) Li, S.; Li, H.; Liu, J.; Xue, X.; Tian, Y.; He, H.; Jia, Y. *Phys. Rev. B* **2007**, *76*, 045410.
- (509) Jinlong, Y.; Toigo, F.; Kelin, W.; Manhong, Z. *Phys. Rev. B* **1994**, *50*, 7173.
- (510) Reddy, B. V.; Nayak, S. K.; Khanna, S. N.; Rao, B. K.; Jena, P. *Phys. Rev. B* **1999**, *59*, 5214.
- (511) Bae, Y.-C.; Osanai, H.; Kumar, V.; Kawazoe, Y. *Phys. Rev. B* **2004**, *70*, 195413.
- (512) Bae, Y.-C.; Kumar, V.; Osanai, H.; Kawazoe, Y. *Phys. Rev. B* **2005**, *72*, 125427.
- (513) Cox, A. J.; Louderback, J. G.; Apsel, S. E.; Bloomfield, L. A. *Phys. Rev. B* **1994**, *49*, 12295.
- (514) Zhang, W.; Xiao, L.; Hirata, Y.; Pawluk, T.; Wang, L. *Chem. Phys. Lett.* **2004**, *383*, 67.
- (515) Jones, R. O. *J. Chem. Phys.* **1993**, *99*, 1194.
- (516) Cheng, H.-P.; Berry, R. S.; Whetten, R. L. *Phys. Rev. B* **1991**, *43*, 10647.
- (517) Yi, J.-Y.; Oh, D. J.; Bernholc, J. *Phys. Rev. Lett.* **1991**, *67*, 1594.
- (518) Röthlisberger, U.; Andreoni, W.; Giannozzi, P. *J. Chem. Phys.* **1992**, *96*, 1248.
- (519) Akola, J.; Häkkinen, H.; Manninen, M. *Phys. Rev. B* **1998**, *58*, 3601.
- (520) Duque, F.; Mananes, A. *Eur. Phys. J. D* **1999**, *9*, 223.
- (521) Akola, J.; Manninen, M.; Häkkinen, H.; Landman, U.; Li, X.; Wang, L.-S. *Phys. Rev. B* **1999**, *60*, R11297.
- (522) Akola, J.; Manninen, M.; Häkkinen, H.; Landman, U.; Li, X.; Wang, L.-S. *Phys. Rev. B* **2000**, *62*, 13216.
- (523) Akola, J.; Manninen, M. *Phys. Rev. B* **2001**, *63*, 193410.
- (524) Rao, B. K.; Jena, P. *J. Chem. Phys.* **1999**, *111*, 1890.
- (525) Fournier, R. *J. Chem. Theory Comput.* **2007**, *3*, 921.
- (526) Candido, L.; Rabelo, J. N. T. *Phys. Rev. B* **2012**, *85*, 245404.
- (527) Chuang, F.-C.; Wang, C. Z.; Ho, K. H. *Phys. Rev. B* **2006**, *73*, 125431.
- (528) Zhang, W.; Lu, W.-C.; Sun, J.; Wang, C. Z.; Ho, K. M. *Chem. Phys. Lett.* **2008**, *455*, 232.
- (529) Aguado, A.; Lopez, J. M. *J. Chem. Phys.* **2009**, *130*, 064704.
- (530) Drebov, N.; Ahlrichs, R. *J. Chem. Phys.* **2010**, *132*, 164703.
- (531) Aguado, A.; Lopez, J. M. *J. Phys. Chem. B* **2006**, *110*, 14020.
- (532) Starace, A. K.; Neal, C. M.; Cao, B.; Jarrold, M. F.; Aguado, A.; Lopez, J. M. *J. Chem. Phys.* **2008**, *129*, 144702.
- (533) Neal, C. M.; Starace, A. K.; Jarrold, M. F.; Joshi, K.; Krishnamurty, S.; Kanhere, D. G. *J. Phys. Chem. C* **2007**, *111*, 17788.
- (534) Pushpa, R.; Narasimhan, S.; Waghmare, U. *J. Chem. Phys.* **2004**, *121*, 5211.
- (535) Mananes, A.; Duque, F.; Mendez, F.; Lopez, M. J.; Alonso, J. A. *J. Chem. Phys.* **2003**, *119*, 5128.
- (536) Liu, Y.; Hua, Y.; Jiang, M.; Xu, M.; Yu, F.; Chen, J. *Eur. Phys. J. D* **2013**, *67*, 194.
- (537) Kim, J. C.; Kim, K. H.; Jung, J.; Han, Y.-K. *J. Comput. Chem.* **2007**, *29*, 1626.
- (538) Reber, A. C.; Roach, P. J.; Woodward, W. H.; Khanna, S. N.; Castleman, A. W. *J. Phys. Chem. A* **2012**, *116*, 8085.
- (539) Abreu, M. B.; Powell, C.; Reber, A. C.; Khanna, S. N. *J. Am. Chem. Soc.* **2012**, *134*, 20507.
- (540) Clayborne, P. A.; Lopez-Acevedo, O.; Whetten, R. L.; Grönbeck, H.; Häkkinen, H. *J. Chem. Phys.* **2011**, *135*, 094701.
- (541) Kumar, V. *Phys. Rev. B* **1998**, *57*, 8827.
- (542) Rao, B. K.; Khanna, S. N.; Jena, P. *Phys. Rev. B* **2000**, *62*, 4666.
- (543) Khanna, S. N.; Rao, B. K.; Jena, P. *Phys. Rev. B* **2002**, *65*, 125105.
- (544) Otero, N.; Alsenoy, C. V.; Karamanis, P.; Pouchan, C. *Comput. Theor. Chem.* **2013**, *1021*, 114.
- (545) Kumar, V.; Bhattacharjee, S.; Kawazoe, Y. *Phys. Rev. B* **2000**, *61*, 8541.
- (546) Lu, Q. L.; Luo, Q. Q.; Jalbout, A. F.; Wan, J. G.; Wang, G. H. *Eur. Phys. J. D* **2009**, *51*, 219.
- (547) Khanna, S. N.; Ashman, C.; Rao, B. K.; Jena, P. *J. Chem. Phys.* **2001**, *114*, 9792.
- (548) Roach, P. J.; Woodward, W. H.; Reber, A. C.; Khanna, S. N.; Castleman, A. W. *J. Phys. Rev. B* **2010**, *81*, 195404.
- (549) Zope, R. R.; Baruah, T. *Phys. Rev. B* **2001**, *64*, 053202.
- (550) Sun, H.; Bai, Y.; Cheng, H.; Xu, N.; Wang, B.; Wang, G. *J. Mol. Struct.* **2013**, *1031*, 22.
- (551) Iwasa, T.; Nakajima, A. *Chem. Phys. Lett.* **2013**, *582*, 100.
- (552) Iwasa, T.; Nakajima, A. *J. Phys. Chem. C* **2013**, *117*, 21551.
- (553) Breaux, G. A.; Benirschke, R. C.; Sugai, T.; Kinnear, B. S.; Jarrold, M. F. *Phys. Rev. Lett.* **2003**, *91*, 215508.
- (554) Chacko, S.; Joshi, K.; Kanhere, D. G.; Blundell, S. A. *Phys. Rev. Lett.* **2004**, *92*, 135506.
- (555) Gaston, N.; Parker, A. J. *Chem. Phys. Lett.* **2011**, *501*, 375.
- (556) Balasubramanian, K.; Feng, P. Y. *Chem. Phys. Lett.* **1988**, *146*, 155.
- (557) Zhao, Y.; Xu, W.; Li, Q. *J. Phys. Chem. A* **2004**, *108*, 7448.

- (558) Song, B.; Cao, P.-l. *J. Chem. Phys.* **2005**, *123*, 144312.
- (559) Drebov, N.; Weigend, F.; Ahlrichs, R. *J. Chem. Phys.* **2011**, *135*, 044314.
- (560) Sai, L.; Zhao, J.; Huang, X.; Wang, J. *J. Nanosci. Nanotechnol.* **2012**, *12*, 132.
- (561) Schebarchov, D.; Gaston, N. *Phys. Chem. Chem. Phys.* **2011**, *13*, 21109.
- (562) Schnepf, A.; Stößer, G.; Schnöckel, H. *Angew. Chem., Int. Ed.* **2002**, *41*, 1882.
- (563) Hartig, J.; Stößer, A.; Hauser, P.; Schnöckel, H. *Angew. Chem., Int. Ed.* **2007**, *46*, 1658.
- (564) Schnepf, A.; Weckert, E.; Linti, G.; Schnöckel, H. *Angew. Chem., Int. Ed.* **1999**, *38*, 3381.
- (565) Schebarchov, D.; Gaston, N. *Phys. Chem. Chem. Phys.* **2012**, *14*, 9912.
- (566) Gong, X. G.; Zheng, Q. Q.; Han, R. S. *Solid State Commun.* **1995**, *94*, 735.
- (567) Yi, J.-Y. *Phys. Rev. B* **2000**, *61*, 7277.
- (568) Henry, D. J. *J. Phys. Chem. C* **2012**, *116*, 24814.
- (569) Henry, D. J. *J. Phys. Chem. C* **2013**, *117*, 26269.
- (570) Şentürk, S.; Ekincioğlu, Y. Z. *Naturforsch.* **2012**, *67a*, 289.
- (571) Guo, L. *Comput. Mater. Sci.* **2009**, *45*, 951.
- (572) Guo, L. *J. Cluster Sci.* **2012**, *24*, 575.
- (573) Lu, Z.-Y.; Wang, C.-Z.; Ho, K.-M. *Phys. Rev. B* **2000**, *61*, 2329.
- (574) Majumder, C.; Kumar, V.; Mizuseki, H.; Kawazoe, Y. *Phys. Rev. B* **2001**, *64*, 233405.
- (575) Schäfer, S.; Assadollahzadeh, B.; Mehring, M.; Schwerdtfeger, P.; Schäfer, R. *J. Phys. Chem. A* **2008**, *112*, 12312.
- (576) Matxain, J. M.; Piris, M.; Formoso, E.; Mercero, J. M.; Lopez, X.; Ugalde, J. M. *ChemPhysChem* **2007**, *8*, 2096.
- (577) Kandalam, A. K.; Chen, G.; Jena, P. *Appl. Phys. Lett.* **2008**, *92*, 143109.
- (578) Chen, X.; Deng, K.; Liu, Y.; Tang, C.; Yuan, Y.; Tan, W.; Wang, X. *J. Chem. Phys.* **2008**, *129*, 094301.
- (579) Iñiguez, M. P.; Lopez, M. J.; Alonso, J. A.; Soler, J. M. *ZPhys.-D: At., Mol. Clusters* **1988**, *11*, 163.
- (580) Rubio, A.; Balbas, L. C.; Alonso, J. A. *Physica B* **1990**, *167*, 19.
- (581) Molina, L. M.; Lopez, M. J.; Rubio, A.; Balbas, L. C.; Alonso, J. A. *Adv. Quantum Chem.* **1998**, *33*, 329.
- (582) Wang, B.; Zhao, J.; Chen, X.; Shi, D.; Wang, G. *Phys. Rev. A* **2005**, *71*, 033201.
- (583) Rajesh, C.; Majumder, C.; Rajan, M. G. R.; Kulshreshtha, S. K. *Phys. Rev. B* **2005**, *72*, 235411.
- (584) Rajesh, C.; Majumder, C. *J. Chem. Phys.* **2007**, *126*, 244704.
- (585) Li, X.-P.; Lu, W.-C.; Zang, Q.-J.; Chen, G.-J.; Wang, C. Z.; Ho, K. M. *J. Phys. Chem. A* **2009**, *113*, 6217.
- (586) Lei, Y.-M.; Zhao, L.-X.; Feng, X.-J.; Zhang, M.; Luo, Y.-H. *THEOCHEM* **2010**, *948*, 11.
- (587) Rajesh, C.; Majumder, C. *Chem. Phys. Lett.* **2006**, *430*, 101.
- (588) Rajesh, C.; Majumder, C. *J. Chem. Phys.* **2008**, *128*, 024308.
- (589) Chen, D.-L.; Tian, W. Q.; Sun, C.-C. *Phys. Rev. A* **2007**, *75*, 013201.
- (590) Esenturk, E. N.; Fettinger, J.; Eichhorn, B. *J. Am. Chem. Soc.* **2006**, *128*, 9178.
- (591) Chen, X.; Deng, K.; Liu, Y.; Tang, C.; Yuan, Y.; Hu, F.; Wu, H.; Huang, D.; Tan, W.; Wang, X. *Chem. Phys. Lett.* **2008**, *462*, 275.
- (592) Bai, Y.-J.; Cheng, H.-Y.; Sun, H.-Q.; Xu, N.; Deng, K.-M. *Physica B* **2011**, *406*, 3781.
- (593) Charkin, O. P.; Klimenko, N. M.; Charkin, D. O. *Russ. J. Inorg. Chem.* **2009**, *54*, 717.
- (594) Zhao, Y. X.; Ding, X. L.; Ma, Y. P.; Wang, Z. C.; He, S. G. *Theor. Chem. Acc.* **2010**, *127*, 449.
- (595) Wu, X.-N.; Xu, B.; Meng, J.-H.; He, S.-G. *Int. J. Mass Spectrom.* **2012**, *310*, 57.
- (596) Stevenson, S.; Mackey, M. A.; Stuart, M. A.; Phillips, J. P.; Easterling, M. L.; Chancellor, C. J.; Olmstead, M. M.; Balch, A. L. *J. Am. Chem. Soc.* **2008**, *130*, 11844.
- (597) Valencia, R.; Rodríguez-Fortea, A.; Stevenson, S.; Balch, A. L.; Poblet, J. M. *Inorg. Chem.* **2009**, *48*, 5957.
- (598) Mercado, B. Q.; Olmstead, M. M.; Beavers, C. M.; Easterling, M. L.; Stevenson, S.; Mackey, M. A.; Coumbe, C. E.; Phillips, J. D.; Phillips, J. P.; Poblet, J. M.; Balch, A. L. *Chem. Commun.* **2010**, *46*, 279.
- (599) Popov, A. A.; Chen, N.; Pinzón, J. R.; Stevenson, S.; Echegoyen, L. A.; Dunsch, L. *J. Am. Chem. Soc.* **2012**, *134*, 19607.
- (600) Dai, B.; Deng, K.; Yang, J. *Chem. Phys. Lett.* **2002**, *364*, 188.
- (601) Yang, Z.; Xiong, S.-J. *J. Chem. Phys.* **2008**, *129*, 124308.
- (602) Yang, Z.; Xiong, S. J. *J. Phys. Chem. A* **2009**, *114*, 54.
- (603) Rahane, A. B.; Murkute, P. A.; Deshpande, M. D.; Kumar, V. J. *Phys. Chem. A* **2013**, *117*, 5542.
- (604) Qu, Z. W.; Kroes, G.-J. *J. Phys. Chem. C* **2007**, *111*, 16808.
- (605) Valdés, A.; Kroes, G. J. *J. Phys. Chem. C* **2010**, *114*, 1701.
- (606) Wang, T.-H.; Fang, Z.; Gist, N. W.; Li, S.; Dixon, D. A.; Gole, J. L. *J. Phys. Chem. C* **2011**, *115*, 9344.
- (607) Fujishima, A.; Honda, K. *Nature* **1972**, *238*, 37.
- (608) Gong, Y.; Zhou, M.; Andrews, L. *Chem. Rev.* **2009**, *109*, 6765.
- (609) Sun, C.; Liu, L.-M.; Selloni, A.; Lu, G. Q.; Smith, S. C. *J. Mater. Chem.* **2010**, *20*, 10319.
- (610) Jeong, K. S.; Chang, C.; Sedlmayr, E.; Sülzle, D. *J. Phys. B: At., Mol. Opt. Phys.* **2000**, *33*, 3417.
- (611) Yu, W.; Freas, R. B. *J. Am. Chem. Soc.* **1990**, *112*, 7126.
- (612) Hagfeldt, A.; Bergstroem, R.; Siegbahn, H. O. G.; Lunell, S. J. *Phys. Chem.* **1993**, *97*, 12725.
- (613) Albaret, T.; Finocchi, F.; Noguera, C. *Appl. Surf. Sci.* **1999**, *144–145*, 672.
- (614) Mikheeva, E. P.; Kachurovskaya, N. A.; Zhidomirov, G. M. *Kinet. Catal.* **2002**, *43*, 223.
- (615) Persson, P.; Gebhardt, J. C. M.; Lunell, S. J. *Phys. Chem. B* **2003**, *107*, 3336.
- (616) Hamad, S.; Catlow, C. R. A.; Woodley, S. M.; Lago, S.; Mejías, J. A. *J. Phys. Chem. B* **2005**, *109*, 15741.
- (617) Qu, Z. W.; Kroes, G.-J. *J. Phys. Chem. B* **2006**, *110*, 8998.
- (618) Qu, Z. W.; Zhu, H. *J. Comput. Chem.* **2010**, *31*, 2038.
- (619) Lundqvist, M. J.; Nilsing, M.; Persson, P.; Lunell, S. *Int. J. Quantum Chem.* **2006**, *106*, 3214.
- (620) Jirkovsky, J.; Macounova, K.; Dietz, H.; Plieth, W.; Krtík, P.; Zalis, S. *Collect. Czech. Chem. Commun.* **2007**, *72*, 171.
- (621) West, R. H.; Beran, G. J. O.; Green, W. H.; Kraft, M. *J. Phys. Chem. A* **2007**, *111*, 3560.
- (622) Calatayud, M.; Maldonado, L.; Minot, C. *J. Phys. Chem. C* **2008**, *112*, 16087.
- (623) Calatayud, M.; Minot, C. *J. Phys. Chem. C* **2009**, *113*, 12186.
- (624) Li, S. G.; Dixon, D. A. *J. Phys. Chem. A* **2008**, *112*, 6646.
- (625) Chen, M.; Dixon, D. A. *J. Chem. Theory Comput.* **2013**, *9*, 3189.
- (626) Iacomino, A.; Cantele, G.; Ninno, D.; Marri, I.; Ossicini, S. *Phys. Rev. B* **2008**, *78*, 075405.
- (627) Zhang, D.; Liu, P.; Liu, C. *J. Phys. Chem. C* **2008**, *112*, 16729.
- (628) Zhang, D.; Sun, H.; Liu, J.; Liu, C. *J. Phys. Chem. C* **2008**, *113*, 21.
- (629) Andreev, A. S.; Chizhov, Y. V. *High Energy Chem.* **2009**, *43*, 561.
- (630) Andreev, A. S.; Kuznetsov, V. N.; Chizhov, Y. V. *J. Phys. Chem. C* **2012**, *116*, 18139.
- (631) Andreev, A. S.; Kuznetsov, V. N.; Chizhov, Y. V. *J. Mol. Model.* **2013**, *19*, 5063.
- (632) Sui, R.; Lo, J. M. H.; Charpentier, P. A. *J. Phys. Chem. C* **2009**, *113*, 21022.
- (633) De Francesco, R.; Stener, M.; Fronzoni, G. *Phys. Chem. Chem. Phys.* **2009**, *11*, 1146.
- (634) Shevlin, S. A.; Woodley, S. M. *J. Phys. Chem. C* **2010**, *114*, 17333.
- (635) Valdés, Á.; Qu, Z. W.; Kroes, G. J.; Rossmeisl, J.; Nørskov, J. K. *J. Phys. Chem. C* **2008**, *112*, 9872.
- (636) Zhanpeisov, N. U. *Kinet. Catal.* **2010**, *51*, 849.
- (637) Nunzi, F.; De Angelis, F. *J. Phys. Chem. C* **2011**, *115*, 2179.
- (638) De Angelis, F.; Fantacci, S.; Mosconi, E.; Nazeeruddin, M. K.; Grätzel, M. *J. Phys. Chem. C* **2011**, *115*, 8825.
- (639) Sousa, C.; Tosoni, S.; Illas, F. *Chem. Rev.* **2012**, *113*, 4456.

- (640) Auvinen, S.; Alatalo, M.; Haario, H.; Jalava, J.-P.; Lamminmäki, R.-J. *J. Phys. Chem. C* **2011**, *115*, 8484.
- (641) Syzgantseva, O. A.; Gonzalez-Navarrete, P.; Calatayud, M.; Bromley, S.; Minot, C. *J. Phys. Chem. C* **2011**, *115*, 15890.
- (642) Stodt, D.; Hattig, C. *J. Chem. Phys.* **2012**, *137*, 114705.
- (643) Du, H. B.; Jia, Y.; Zhang, R. Q. *J. Theor. Comput. Chem.* **2013**, *12*, 1250094.
- (644) Iwaszuk, A.; Mulheran, P. A.; Nolan, M. *J. Mater. Chem. A* **2013**, *1*, 2515.
- (645) Lee, C.; Aikens, C. M. *Comput. Theor. Chem.* **2013**, *1013*, 32.
- (646) Oprea, C. I.; Panait, P.; Lungu, J.; Stamate, D.; Dumbrava, A.; Cimpoeus, F.; Girtu, M. A. *Int. J. Photoenergy* **2013**, 893850.
- (647) Berardo, E.; Hu, H.-S.; Shevlin, S. A.; Woodley, S. M.; Kowalski, K.; Zwijnenburg, M. A. *J. Chem. Theory Comput.* **2014**, *10*, 1189.
- (648) Herrera, B.; Gracia, F.; Araya, P.; Toro-Labbé, A. *J. Mol. Model.* **2009**, *15*, 405.
- (649) Johnson, G. E.; Mitrić, R.; Tyo, E. C.; Bonačić-Koutecký, V.; Castleman, A. W. *J. Am. Chem. Soc.* **2008**, *130*, 13912.
- (650) Isobe, Y.; Fuse, M.; Kobayashi, K. *J. Nucl. Sci. Technol.* **1994**, *31*, 546.
- (651) Foschini, C. R.; Filho, O. T.; Juiz, S. A.; Souza, A. G.; Oliveira, J. B. L.; Longo, E.; Leite, E. R.; Paskocimas, C. A.; Varela, J. A. *J. Mater. Sci.* **2004**, *39*, 1935.
- (652) Chen, S.-G.; Yin, Y.-S.; Wang, D.-P. *J. Am. Ceram. Soc.* **2005**, *88*, 1041.
- (653) Kuwabara, A.; Katamura, J.; Ikuhara, Y.; Sakuma, T. *J. Am. Ceram. Soc.* **2002**, *85*, 2557.
- (654) Walther, P.; Puchberger, M.; Kogler, F. R.; Schwarz, K.; Schubert, U. *Phys. Chem. Chem. Phys.* **2009**, *11*, 3640.
- (655) Johnson, G. E.; Mitrić, R.; Nössler, M.; Tyo, E. C.; Bonačić-Koutecký, V.; Castleman, A. W. *J. Am. Chem. Soc.* **2009**, *131*, 5460.
- (656) Johnson, G. E.; Mitrić, R.; Bonačić-Koutecký, V.; Castleman, A. W., Jr. *Chem. Phys. Lett.* **2009**, *475*, 1.
- (657) Li, S.; Dixon, D. A. *J. Phys. Chem. A* **2010**, *114*, 2665.
- (658) Woodley, S. M.; Hamad, S.; Catlow, C. R. A. *Phys. Chem. Chem. Phys.* **2010**, *12*, 8454.
- (659) Nößler, M.; Mitrić, R.; Bonačić-Koutecký, V. *J. Phys. Chem. C* **2012**, *116*, 11570.
- (660) Boulet, P.; Knöfel, C.; Kuchta, B.; Hornebecq, V.; Llewellyn, P. *J. Mol. Model.* **2012**, *18*, 4819.
- (661) Cerón, M.; Herrera, B.; Araya, P.; Gracia, F.; Toro-Labbé, A. *J. Mol. Model.* **2013**, *19*, 2885.
- (662) Lousada, C. M.; Johansson, A. J.; Brinck, T.; Jonsson, M. *Phys. Chem. Chem. Phys.* **2013**, *15*, 5539.
- (663) Hermann, K.; Witko, M.; Družinic, R. *Faraday Discuss.* **1999**, *114*, 53.
- (664) Wang, H. Q.; Li, H. F.; Kuang, X. Y. *Phys. Chem. Chem. Phys.* **2012**, *14*, 5272.
- (665) Michalak, A.; Witko, M.; Hermann, K. *Surf. Sci.* **1997**, *375*, 385.
- (666) Perdew, J. P.; Chevary, J. A.; Vosko, S. H.; Jackson, K. A.; Pederson, M. R.; Singh, D. J.; Fiolhais, C. *Phys. Rev. B* **1992**, *46*, 6671.
- (667) Witko, M.; Hermann, K.; Tokarz, R. *Catal. Today* **1999**, *50*, 553.
- (668) Hermann, K.; Witko, M.; Družinic, R.; Tokarz, R. *Top. Catal.* **2000**, *11*, 67.
- (669) Hermann, K.; Witko, M.; Družinic, R.; Tokarz, R. *Appl. Phys. A: Mater. Sci. Process.* **2001**, *72*, 429.
- (670) Haras, A.; Witko, M.; Salahub, D. R.; Hermann, K.; Tokarz, R. *Surf. Sci.* **2001**, *491*, 77.
- (671) Zazhigalov, V. A.; Haber, J.; Stoch, J.; Kharlamov, A. I.; Bogutskaya, L. V.; Bacherikova, I. V.; Kowal, A. *Solid State Ionics* **1997**, *101–103*, 1257.
- (672) Czekaj, I.; Hermann, K.; Witko, M. *Surf. Sci.* **2003**, *545*, 85.
- (673) Haber, J.; Witko, M. *J. Catal.* **2003**, *216*, 416.
- (674) Tokarz-Sobieraj, R.; Witko, M.; Gryboś, R. *Catal. Today* **2005**, *99*, 241.
- (675) Kolczewski, C.; Hermann, K.; Gulmond, S.; Kuhlenbeck, H.; Freund, H. *J. Surf. Sci.* **2007**, *601*, 5394.
- (676) Cavalleri, M.; Hermann, K.; Knop-Gericke, A.; Havecker, M.; Herbert, R.; Hess, C.; Oestreich, A.; Dobler, J.; Schlogl, R. *J. Catal.* **2009**, *262*, 215.
- (677) Hejduk, P.; Witko, M.; Hermann, K. *Top. Catal.* **2009**, *52*, 1105.
- (678) Vyboishchikov, S. F.; Sauer, J. *J. Phys. Chem. A* **2000**, *104*, 10913.
- (679) Vyboishchikov, S. F.; Sauer, J. *J. Phys. Chem. A* **2001**, *105*, 8588.
- (680) Asmis, K. R.; Santambrogio, G.; Brummer, M.; Sauer, J. *Angew. Chem., Int. Ed.* **2005**, *44*, 3122.
- (681) Feyel, S.; Döbler, J.; Schröder, D.; Sauer, J.; Schwarz, H. *Angew. Chem., Int. Ed.* **2006**, *45*, 4681.
- (682) Calatayud, M.; Andrés, J.; Beltrán, A. *J. Phys. Chem. A* **2001**, *105*, 9760.
- (683) Najbar, M.; Banas, J.; Korchowiec, J.; Bialas, A. *Catal. Today* **2002**, *73*, 249.
- (684) Anstrom, M.; Topsoe, N. Y.; Dumesic, J. A. *J. Catal.* **2003**, *213*, 115.
- (685) Justes, D. R.; Mitric, R.; Moore, N. A.; Bonacic-Koutecky, V.; Castleman, A. W. *J. Am. Chem. Soc.* **2003**, *125*, 6289.
- (686) Matsuda, Y.; Bernstein, E. R. *J. Phys. Chem. A* **2005**, *109*, 3803.
- (687) Jakubikova, E.; Bernstein, E. R. *J. Phys. Chem. A* **2007**, *111*, 13339.
- (688) De Francesco, R.; Stener, M.; Causa, M.; Toffoli, D.; Fronzoni, G. *Phys. Chem. Chem. Phys.* **2006**, *8*, 4300.
- (689) Fronzoni, G.; De Francesco, R.; Stener, M. *J. Chem. Phys.* **2012**, *137*, 244308.
- (690) Charkin, O. P.; Klimentko, N. M.; Charkin, D. O. *Russ. J. Inorg. Chem.* **2008**, *53*, 568.
- (691) Ma, J. B.; Wu, X. N.; Zhao, X. X.; Ding, X. L.; He, S. G. *Phys. Chem. Chem. Phys.* **2010**, *12*, 12223.
- (692) Ma, J.-B.; Zhao, Y.-X.; He, S.-G.; Ding, X.-L. *J. Phys. Chem. A* **2012**, *116*, 2049.
- (693) Li, X. N.; Wu, X. N.; Ding, X. L.; Xu, B.; He, S. G. *Chem.—Eur. J.* **2012**, *18*, 10998.
- (694) Ard, S.; Dibble, C. J.; Akin, S. T.; Duncan, M. A. *J. Phys. Chem. C* **2011**, *115*, 6438.
- (695) Saldias, M.; Paredes-Garcia, V.; Vega, A.; Canon-Mancisidor, W.; Le Fur, E.; Venegas-Yazigi, D.; Spodine, E. *Polyhedron* **2012**, *41*, 120.
- (696) Wang, H.-Q.; Li, H.-F. *Comput. Theor. Chem.* **2013**, *1006*, 70.
- (697) Compere, C.; Costa, D.; Jolly, L. H.; Mauger, E.; Giessner-Prettre, C. *New J. Chem.* **2000**, *24*, 993.
- (698) Wang, X.; Neukermans, S.; Vanhoutte, F.; Janssens, E.; Verschoren, G.; Silverans, R. E.; Lievens, P. *Appl. Phys. B: Laser Opt.* **2001**, *73*, 417.
- (699) Bergeron, D. E.; Castleman, A. W.; Jones, N. O.; Khanna, S. N. *Nano Lett.* **2004**, *4*, 261.
- (700) Li, S.; Dixon, D. A. *J. Phys. Chem. A* **2006**, *110*, 6231.
- (701) Zhai, H.-J.; Li, S.; Dixon, D. A.; Wang, L.-S. *J. Am. Chem. Soc.* **2008**, *130*, 5167.
- (702) Li, S.; Guenther, C. L.; Kelley, M. S.; Dixon, D. A. *J. Phys. Chem. C* **2011**, *115*, 8072.
- (703) Li, S. G.; Zhai, H. J.; Wang, L. S.; Dixon, D. A. *J. Phys. Chem. A* **2012**, *116*, 5256.
- (704) Tokarz-Sobieraj, R.; Hermann, K.; Witko, M.; Blume, A.; Mestl, G.; Schlogl, R. *Surf. Sci.* **2001**, *489*, 107.
- (705) Wei, Y.; Zhang, T.; Lang, Z.; Yan, L.; Su, Z. *Dyes Pigm.* **2014**, *102*, 6.
- (706) Zhao, L.; Chiu, C.-c.; Genest, A.; Rösch, N. *Comput. Theor. Chem.* **2014**, *1045*, 57.
- (707) Sun, Q.; Rao, B. K.; Jena, P.; Stolicic, D.; Kim, Y. D.; Gantefor, G.; Castleman, A. W. *J. Chem. Phys.* **2004**, *121*, 9417.
- (708) David Jeba Singh, D. M.; Pradeep, T.; Thirumoorthy, K.; Balasubramanian, K. *J. Phys. Chem. A* **2010**, *114*, 5445.
- (709) Zouni, A.; Witt, H.-T.; Kern, J.; Fromme, P.; Krauss, N.; Saenger, W.; Orth, P. *Nature* **2001**, *409*, 739.

- (710) Kamiya, N.; Shen, J.-R. *Proc. Natl. Acad. Sci. U.S.A.* **2003**, *100*, 98.
- (711) Ferreira, K. N.; Iverson, T. M.; Maghlaoui, K.; Barber, J.; Iwata, S. *Science* **2004**, *303*, 1831.
- (712) Loll, B.; Kern, J.; Saenger, W.; Zouni, A.; Biesiadka, J. *Nature* **2005**, *438*, 1040.
- (713) Guskov, A.; Kern, J.; Gabdulkhakov, A.; Broser, M.; Zouni, A.; Saenger, W. *Nat. Struct. Mol. Biol.* **2009**, *16*, 334.
- (714) Umena, Y.; Kawakami, K.; Shen, J.-R.; Kamiya, N. *Nature* **2011**, *473*, 55.
- (715) McEvoy, J. P.; Brudvig, G. W. *Chem. Rev.* **2006**, *106*, 4455.
- (716) McEvoy, J. P.; Gascon, J. A.; Batista, V. S.; Brudvig, G. W. *Photochem. Photobiol. Sci.* **2005**, *4*, 940.
- (717) Mullins, C. S.; Pecoraro, V. L. *Coord. Chem. Rev.* **2008**, *252*, 416.
- (718) Sproviero, E.; McEvoy, J.; Gascón, J.; Brudvig, G.; Batista, V. *Photosynth. Res.* **2008**, *97*, 91.
- (719) Sproviero, E.; Newcomer, M.; Gascón, J.; Batista, E.; Brudvig, G.; Batista, V. *Photosynth. Res.* **2009**, *102*, 455.
- (720) Sproviero, E. M.; Gascón, J. A.; McEvoy, J. P.; Brudvig, G. W.; Batista, V. S. *Coord. Chem. Rev.* **2008**, *252*, 395.
- (721) Yamazaki, H.; Shouji, A.; Kajita, M.; Yagi, M. *Coord. Chem. Rev.* **2010**, *254*, 2483.
- (722) Siegbahn, P. E. M. *J. Photochem. Photobiol., B* **2011**, *104*, 94.
- (723) Kusunoki, M. *J. Photochem. Photobiol., B* **2011**, *104*, 100.
- (724) Williamson, A.; Conlan, B.; Hillier, W.; Wydrzynski, T. *Photosynth. Res.* **2011**, *107*, 71.
- (725) Liu, X.; Wang, F. *Coord. Chem. Rev.* **2012**, *256*, 1115.
- (726) Najafpour, M. M.; Rahimi, F.; Aro, E.-M.; Lee, C.-H.; Allakhverdiev, S. I. *J. R. Soc., Interface* **2012**, *9*, 2383.
- (727) Vinyard, D. J.; Ananyev, G. M.; Charles Dismukes, G. *Annu. Rev. Biochem.* **2013**, *82*, 577.
- (728) Pokhrel, R.; Brudvig, G. W. *Phys. Chem. Chem. Phys.* **2014**, *16*, 11812.
- (729) Hirahara, M.; Shoji, A.; Yagi, M. *Eur. J. Inorg. Chem.* **2014**, *2014*, 595.
- (730) Rüttinger, W.; Dismukes, G. C. *Chem. Rev.* **1997**, *97*, 1.
- (731) Zieman, P. J.; Castleman, A. W. *Phys. Rev. B* **1992**, *46*, 13480.
- (732) Nayak, S. K.; Jena, P. *Phys. Rev. Lett.* **1998**, *81*, 2970.
- (733) Nayak, S. K.; Jena, P. *J. Am. Chem. Soc.* **1999**, *121*, 644.
- (734) Han, M. J.; Ozaki, T.; Yu, J. *J. Chem. Phys.* **2005**, *123*, 034306.
- (735) Kim, B. S.; Lee, D. Y.; Lee, H. W.; Chung, W. S. *Adv. Mater. Res.* **2007**, *969*.
- (736) Kanan, D. K.; Carter, E. A. *J. Mater. Chem. A* **2013**, *1*, 9246.
- (737) Wu, J.-Z.; De Angelis, F.; Carrell, T. G.; Yap, G. P. A.; Sheats, J.; Car, R.; Dismukes, G. C. *Inorg. Chem.* **2005**, *45*, 189.
- (738) Kuznetsov, A. E.; Geletti, Y. V.; Hill, C. L.; Musaev, D. G. *J. Phys. Chem. A* **2010**, *114*, 11417.
- (739) Bashkin, J. S.; Chang, H. R.; Streib, W. E.; Huffman, J. C.; Hendrickson, D. N.; Christou, G. *J. Am. Chem. Soc.* **1987**, *109*, 6502.
- (740) Wang, S.; Folting, K.; Streib, W. E.; Schmitt, E. A.; McCusker, J. K.; Hendrickson, D. N.; Christou, G. *Angew. Chem., Int. Ed. Engl.* **1991**, *30*, 305.
- (741) Wang, S.; Huffman, J. C.; Folting, K.; Streib, W. E.; Lobkovsky, E. B.; Christou, G. *Angew. Chem., Int. Ed. Engl.* **1991**, *30*, 1672.
- (742) Messinger, J. *Phys. Chem. Chem. Phys.* **2004**, *6*, 4764.
- (743) Pantazis, D. A.; Orio, M.; Petrenko, T.; Zein, S.; Lubitz, W.; Messinger, J.; Neese, F. *Phys. Chem. Chem. Phys.* **2009**, *11*, 6788.
- (744) Yano, J.; Kern, J.; Sauer, K.; Latimer, M. J.; Pushkar, Y.; Biesiadka, J.; Loll, B.; Saenger, W.; Messinger, J.; Zouni, A.; Yachandra, V. K. *Science* **2006**, *314*, 821.
- (745) Siegbahn, P. E. M. *Chem.—Eur. J.* **2008**, *14*, 8290.
- (746) Siegbahn, P. E. M. *Acc. Chem. Res.* **2009**, *42*, 1871.
- (747) Ames, W.; Pantazis, D. A.; Krewald, V.; Cox, N.; Messinger, J.; Lubitz, W.; Neese, F. *J. Am. Chem. Soc.* **2011**, *133*, 19743.
- (748) Cox, N.; Rapatskiy, L.; Su, J.-H.; Pantazis, D. A.; Sugiura, M.; Kulik, L.; Dorlet, P.; Rutherford, A. W.; Neese, F.; Boussac, A.; Lubitz, W.; Messinger, J. *J. Am. Chem. Soc.* **2011**, *133*, 3635.
- (749) Cox, N.; Messinger, J. *Biochim. Biophys. Acta, Bioenerg.* **2013**, *1827*, 1020.
- (750) Lundberg, M.; Siegbahn, P. E. M. *Phys. Chem. Chem. Phys.* **2004**, *6*, 4772.
- (751) Siegbahn, P. E. M. *Chem.—Eur. J.* **2006**, *12*, 9217.
- (752) Siegbahn, P. E. M. *Dalton Trans.* **2009**, *10063*.
- (753) Siegbahn, P. E. M. *J. Am. Chem. Soc.* **2009**, *131*, 18238.
- (754) Siegbahn, P. E. M. *ChemPhysChem* **2011**, *12*, 3274.
- (755) Siegbahn, P. E. M. *Phys. Chem. Chem. Phys.* **2012**, *14*, 4849.
- (756) Siegbahn, P. E. M. *Biochim. Biophys. Acta, Bioenerg.* **2013**, *1827*, 1003.
- (757) Siegbahn, P. E. M.; Blomberg, M. R. A. *J. Chem. Theory Comput.* **2013**, *10*, 268.
- (758) Sproviero, E. M.; Gascón, J. A.; McEvoy, J. P.; Brudvig, G. W.; Batista, V. S. *J. Chem. Theory Comput.* **2006**, *2*, 1119.
- (759) Sproviero, E. M.; Gascon, J. A.; McEvoy, J. P.; Brudvig, G. W.; Batista, V. S. *J. Inorg. Biochem.* **2006**, *100*, 786.
- (760) Sproviero, E. M.; Gascón, J. A.; McEvoy, J. P.; Brudvig, G. W.; Batista, V. S. *J. Am. Chem. Soc.* **2008**, *130*, 6728.
- (761) Sproviero, E. M.; Gascón, J. A.; McEvoy, J. P.; Brudvig, G. W.; Batista, V. S. *J. Am. Chem. Soc.* **2008**, *130*, 3428.
- (762) Luber, S.; Rivalta, I.; Umena, Y.; Kawakami, K.; Shen, J.-R.; Kamiya, N.; Brudvig, G. W.; Batista, V. S. *Biochemistry* **2011**, *50*, 6308.
- (763) Pal, R.; Negre, C. F. A.; Vogt, L.; Pokhrel, R.; Ertem, M. Z.; Brudvig, G. W.; Batista, V. S. *Biochemistry* **2013**, *52*, 7703.
- (764) Petrie, S.; Stranger, R.; Pace, R. J. *Angew. Chem., Int. Ed.* **2010**, *49*, 4233.
- (765) Petrie, S.; Stranger, R.; Pace, R. J. *Chem.—Eur. J.* **2010**, *16*, 14026.
- (766) Petrie, S.; Gatt, P.; Stranger, R.; Pace, R. J. *Phys. Chem. Chem. Phys.* **2012**, *14*, 4651.
- (767) Petrie, S.; Gatt, P.; Stranger, R.; Pace, R. J. *Phys. Chem. Chem. Phys.* **2012**, *14*, 11333.
- (768) Kusunoki, M. *Biochim. Biophys. Acta, Bioenerg.* **2007**, *1767*, 484.
- (769) Kusunoki, M. *Biochim. Biophys. Acta, Bioenerg.* **2008**, *1777*, 477.
- (770) Galstyan, A.; Robertazzi, A.; Knapp, E. W. *J. Am. Chem. Soc.* **2012**, *134*, 7442.
- (771) Saito, T.; Shoji, M.; Kanda, K.; Isobe, H.; Yamanaka, S.; Kitagawa, Y.; Yamada, S.; Kawakami, T.; Okumura, M.; Yamaguchi, K. *Int. J. Quantum Chem.* **2012**, *112*, 121.
- (772) Pecoraro, V. L.; Baldwin, M. J.; Caudle, M. T.; Hsieh, W.-Y.; Law, N. A. *Pure Appl. Chem.* **1998**, *70*, 925.
- (773) Iwata, S.; Barber, J. *Curr. Opin. Struct. Biol.* **2004**, *14*, 447.
- (774) Yachandra, V. K.; Sauer, K.; Klein, M. P. *Chem. Rev.* **1996**, *96*, 2927.
- (775) Yamanaka, S.; Saito, T.; Kanda, K.; Isobe, H.; Umena, Y.; Kawakami, K.; Shen, J. R.; Kamiya, N.; Okumura, M.; Nakamura, H.; Yamaguchi, K. *Int. J. Quantum Chem.* **2012**, *112*, 321.
- (776) Yamanaka, S.; Isobe, H.; Kanda, K.; Saito, T.; Umena, Y.; Kawakami, K.; Shen, J. R.; Kamiya, N.; Okumura, M.; Nakamura, H.; Yamaguchi, K. *Chem. Phys. Lett.* **2011**, *511*, 138.
- (777) Kanda, K.; Yamanaka, S.; Saito, T.; Umena, Y.; Kawakami, K.; Shen, J.-R.; Kamiya, N.; Okumura, M.; Nakamura, H.; Yamaguchi, K. *Chem. Phys. Lett.* **2011**, *506*, 98.
- (778) Ichino, T.; Yamaguchi, K.; Yoshioka, Y. *Chem. Lett.* **2012**, *41*, 18.
- (779) Isobe, H.; Shoji, M.; Yamanaka, S.; Umena, Y.; Kawakami, K.; Kamiya, N.; Shen, J. R.; Yamaguchi, K. *Dalton Trans.* **2012**, *41*, 13727.
- (780) Yamaguchi, K.; Isobe, H.; Yamanaka, S.; Saito, T.; Kanda, K.; Shoji, M.; Umena, Y.; Kawakami, K.; Shen, J. R.; Kamiya, N.; Okumura, M. *Int. J. Quantum Chem.* **2013**, *113*, 525.
- (781) Yamaguchi, K.; Yamanaka, S.; Isobe, H.; Saito, T.; Kanda, K.; Umena, Y.; Kawakami, K.; Shen, J. R.; Kamiya, N.; Okumura, M.; Nakamura, H.; Shoji, M.; Yoshioka, Y. *Int. J. Quantum Chem.* **2013**, *113*, 453.
- (782) Lang, S. M.; Fleischer, I.; Bernhardt, T. M.; Barnett, R. N.; Landman, U. *Nano Lett.* **2013**, *13*, 5549.
- (783) Kurashige, Y.; Chan, G. K.-L.; Yanai, T. *Nat. Chem.* **2013**, *5*, 660.

- (784) Yue, J.; Jiang, X.; Kaneti, Y. V.; Yu, A. InTech; available from <http://www.intechopen.com/books/howtoreference/smarnanoparticles-technology/experimental-and-theoretical-studies-on-low-dimensional-iron-oxide-nanostructures>, 2012.
- (785) Ding, X. L.; Xue, W.; Ma, Y. P.; Wang, Z. C.; He, S. G. *J. Chem. Phys.* **2009**, *130*, 014303.
- (786) Wang, L.-S.; Fan, J.; Lou, L. *Surf. Rev. Lett.* **1996**, *03*, 695.
- (787) Wang, L.-S.; Wu, H.; Desai, S. R. *Phys. Rev. Lett.* **1996**, *76*, 4853.
- (788) Sakurai, M.; Sumiyama, K.; Sun, Q.; Kawazoe, Y. *J. Phys. Soc. Jpn.* **1999**, *68*, 3497.
- (789) Wang, Q.; Sun, Q.; Sakurai, M.; Yu, J. Z.; Gu, B. L.; Sumiyama, K.; Kawazoe, Y. *Phys. Rev. B* **1999**, *59*, 12672.
- (790) Sun, Q.; Wang, Q.; Parlinski, K.; Yu, J. Z.; Hashi, Y.; Gong, X. G.; Kawazoe, Y. *Phys. Rev. B* **2000**, *61*, 5781.
- (791) Sun, Q.; Sakurai, M.; Wang, Q.; Yu, J. Z.; Wang, G. H.; Sumiyama, K.; Kawazoe, Y. *Phys. Rev. B* **2000**, *62*, 8500.
- (792) Sun, Q.; Kandalam, A. K.; Wang, Q.; Jena, P.; Kawazoe, Y.; Marquez, M. *Phys. Rev. B* **2006**, *73*, 134409.
- (793) Sun, Q.; Reddy, Marquez, M.; Jena, P.; Gonzalez, C.; Wang, Q. *J. Phys. Chem. C* **2007**, *111*, 4159.
- (794) Kortus, J.; Pederson, M. R. *Phys. Rev. B* **2000**, *62*, 5755.
- (795) Shiroishi, H.; Oda, T.; Hamada, I.; Fujima, N. *Polyhedron* **2005**, *24*, 2472.
- (796) Jones, N. O.; Reddy, B. V.; Rasouli, F.; Khanna, S. N. *Phys. Rev. B* **2005**, *72*, 165411.
- (797) Van Natter, R. M.; Coleman, J. S.; Lund, C. R. F. *J. Mol. Catal. A: Chem.* **2008**, *292*, 76.
- (798) Van Natter, R. M.; Coleman, J. S.; Lund, C. R. F. *J. Mol. Catal. A: Chem.* **2009**, *311*, 17.
- (799) Taguchi, T.; Stamatatos, T. C.; Abboud, K. A.; Jones, C. M.; Poole, K. M.; O'Brien, T. A.; Christou, G. *Inorg. Chem.* **2008**, *47*, 4095.
- (800) López, S.; Romero, A. H.; Mejía-López, J.; Mazo-Zuluaga, J.; Restrepo, J. *Phys. Rev. B* **2009**, *80*, 085107.
- (801) Zueva, E. M.; Sameera, W. M. C.; Piñero, D. M.; Chakraborty, I.; Devlin, E.; Baran, P.; Lebruskova, K.; Sanakis, Y.; McGrady, J. E.; Raptis, R. G. *Inorg. Chem.* **2011**, *50*, 1021.
- (802) Ohshima, K.; Komukai, T.; Moriyama, R.; Misaizu, F. *J. Phys. Chem. A* **2014**, *118*, 3899.
- (803) Dong, H.; Zhang, L.; Zhou, X. *Theor. Chem. Acc.* **2014**, *133*, 1.
- (804) Brunschwig, B. S.; Chou, M. H.; Creutz, C.; Ghosh, P.; Sutin, N. *J. Am. Chem. Soc.* **1983**, *105*, 4832.
- (805) Elizarova, G. L.; Matvienko, L. G.; Lozhkina, N. V.; Parmon, V. N.; Zamaraev, K. I. *React. Kinet. Catal. Lett.* **1981**, *16*, 191.
- (806) Shafirovich, V. Y.; Khannanov, N. K.; Strelets, V. V. *Nouv. J. Chim.* **1980**, *4*, 81.
- (807) Shafirovich, V. Y.; Strelets, V. V. *Nouv. J. Chim.* **1978**, *2*, 199.
- (808) Du, P.; Eisenberg, R. *Energy Environ. Sci.* **2012**, *5*, 6012.
- (809) Kanan, M. W.; Nocera, D. G. *Science* **2008**, *321*, 1072.
- (810) Risch, M.; Khare, V.; Zaharieva, I.; Gerencser, L.; Chernev, P.; Dau, H. *J. Am. Chem. Soc.* **2009**, *131*, 6936.
- (811) Kanan, M. W.; Yano, J.; Surendranath, Y.; Dincă, M.; Yachandra, V. K.; Nocera, D. G. *J. Am. Chem. Soc.* **2010**, *132*, 13692.
- (812) Surendranath, Y.; Kanan, M. W.; Nocera, D. G. *J. Am. Chem. Soc.* **2010**, *132*, 16501.
- (813) Dau, H.; Limberg, C.; Reier, T.; Risch, M.; Roggan, S.; Strasser, P. *ChemCatChem* **2010**, *2*, 724.
- (814) Artero, V.; Chavarot-Kerlidou, M.; Fontecave, M. *Angew. Chem., Int. Ed.* **2011**, *50*, 7238.
- (815) Artero, V.; Fontecave, M. *Chem. Soc. Rev.* **2013**, *42*, 2338.
- (816) McAlpin, J. G.; Stich, T. A.; Casey, W. H.; Britt, R. D. *Coord. Chem. Rev.* **2012**, *256*, 2445.
- (817) Sartorel, A.; Bonchio, M.; Campagna, S.; Scandola, F. *Chem. Soc. Rev.* **2013**, *42*, 2262.
- (818) McCool, N. S.; Robinson, D. M.; Sheats, J. E.; Dismukes, G. C. *J. Am. Chem. Soc.* **2011**, *133*, 11446.
- (819) Pramanik, A.; Koyasu, K.; Nakajima, A.; Kaya, K. *J. Phys. Chem. A* **2002**, *106*, 4891.
- (820) Xie, Y.; Dong, F.; Heinbuch, S.; Rocca, J. J.; Bernstein, E. R. *Phys. Chem. Chem. Phys.* **2010**, *12*, 947.
- (821) Yin, S.; Xue, W.; Ding, X. L.; Wang, W. G.; He, S. G.; Ge, M. F. *Int. J. Mass Spectrom.* **2009**, *281*, 72.
- (822) Mattioli, G.; Risch, M.; Amore Bonapasta, A.; Dau, H.; Guidoni, L. *Phys. Chem. Chem. Phys.* **2011**, *13*, 15437.
- (823) Mattioli, G.; Giannozzi, P.; Amore Bonapasta, A.; Guidoni, L. *J. Am. Chem. Soc.* **2013**, *135*, 15353.
- (824) Wang, L.-P.; Van Voorhis, T. *J. Phys. Chem. Lett.* **2011**, *2*, 2200.
- (825) Mavros, M. G.; Tsuchimochi, T.; Kowalczyk, T.; McIsaac, A.; Wang, L.-P.; Van Voorhis, T. *Inorg. Chem.* **2014**, *S3*, 6386.
- (826) McAlpin, J. G.; Stich, T. A.; Ohlin, C. A.; Surendranath, Y.; Nocera, D. G.; Casey, W. H.; Britt, R. D. *J. Am. Chem. Soc.* **2011**, *133*, 15444.
- (827) Hu, X. L.; Piccinin, S.; Laio, A.; Fabris, S. *ACS Nano* **2012**, *6*, 10497.
- (828) Li, X.; Siegbahn, P. E. M. *J. Am. Chem. Soc.* **2013**, *135*, 13804.
- (829) Kwapien, K.; Piccinin, S.; Fabris, S. *J. Phys. Chem. Lett.* **2013**, *4*, 4223.
- (830) Mainardi, D. S.; Balbuena, P. B. *J. Phys. Chem. A* **2003**, *107*, 10370.
- (831) Harding, D. J.; Davies, R. D. L.; Mackenzie, S. R.; Walsh, T. R. *J. Chem. Phys.* **2008**, *129*, 124304.
- (832) Harding, D. J.; Mackenzie, S. R.; Walsh, T. R. *Chem. Phys. Lett.* **2009**, *469*, 31.
- (833) Zhou, X.; Yang, J. X.; Li, C. *J. Phys. Chem. A* **2012**, *116*, 9985.
- (834) Nagai, J.; Morisaki, S. *Solid State Ionics* **2003**, *165*, 149.
- (835) Nagai, J. *Proc. SPIE* **2001**, *4458*, 164.
- (836) Lang, S. M.; Fleischer, I.; Bernhardt, T. M.; Barnett, R. N.; Landman, U. *J. Am. Chem. Soc.* **2012**, *134*, 20654.
- (837) Lang, S. M.; Fleischer, I.; Bernhardt, T. M.; Barnett, R. N.; Landman, U. *J. Phys. Chem. A* **2014**, *118*, 8572.
- (838) Kwon, G.; Ferguson, G. A.; Heard, C. J.; Tyo, E. C.; Yin, C.; DeBartolo, J.; Seifert, S.; Winans, R. E.; Kropf, A. J.; Greeley, J.; Johnston, R. L.; Curtiss, L. A.; Pellin, M. J.; Vajda, S. *ACS Nano* **2013**, *7*, 5808.
- (839) Hermes, A. C.; Hamilton, S. M.; Cooper, G. A.; Kerpal, C.; Harding, D. J.; Meijer, G.; Fielicke, A.; Mackenzie, S. R. *Faraday Discuss.* **2012**, *157*, 213.
- (840) Kerpal, C.; Harding, D. J.; Hermes, A. C.; Meijer, G.; Mackenzie, S. R.; Fielicke, A. *J. Phys. Chem. A* **2012**, *117*, 1233.
- (841) Titmuss, S.; Wander, A.; King, D. A. *Chem. Rev.* **1996**, *96*, 1291.
- (842) Luo, Y.; Li, S.; Ren, Q.; Liu, J.; Xing, L.; Wang, Y.; Yu, Y.; Jia, Z.; Li, J. *Cryst. Growth Des.* **2006**, *7*, 87.
- (843) Ma, L.; Lin, Y.; Wang, Y.; Li, J.; Wang, E.; Qiu, M.; Yu, Y. *J. Phys. Chem. C* **2008**, *112*, 18916.
- (844) Ma, L.-L.; Li, J.-L.; Sun, H.-Z.; Qiu, M.-Q.; Wang, J.-B.; Chen, J.-Y.; Yu, Y. *Mater. Res. Bull.* **2010**, *45*, 961.
- (845) Poizot, P.; Laruelle, S.; Gruegeon, S.; Dupont, L.; Tarascon, J. M. *Nature* **2000**, *407*, 496.
- (846) Yu, Y.; Du, F.-P.; Yu, J. C.; Zhuang, Y.-Y.; Wong, P.-K. *J. Solid State Chem.* **2004**, *177*, 4640.
- (847) Yu, Y.; Ma, L.-L.; Huang, W.-Y.; Li, J.-L.; Wong, P.-K.; Yu, J. C. *J. Solid State Chem.* **2005**, *178*, 1488.
- (848) Jeong, S. S.; Mittiga, A.; Salza, E.; Masci, A.; Passerini, S. *Electrochim. Acta* **2008**, *53*, 2226.
- (849) Siripala, W.; Ivanovskaya, A.; Jaramillo, T. F.; Baeck, S.-H.; McFarland, E. W. *Sol. Energy Mater. Sol. Cells* **2003**, *77*, 229.
- (850) Minami, T.; Miyata, T.; Ihara, K.; Minamino, Y.; Tsukada, S. *Thin Solid Films* **2006**, *494*, 47.
- (851) Mittiga, A.; Salza, E.; Sarto, F.; Tucci, M.; Vasanthi, R. *Appl. Phys. Lett.* **2006**, *88*, 163502.
- (852) Onishi, T.; Takano, Y.; Yamaki, D.; Yamaguchi, K. *Mol. Cryst. Liq. Cryst.* **2002**, *379*, 507.
- (853) Yang, F.; Sun, Q.; Ma, L. L.; Jia, Y.; Luo, S. J.; Liu, J. M.; Geng, W. T.; Chen, J. Y.; Li, S.; Yu, Y. *J. Phys. Chem. A* **2010**, *114*, 8417.
- (854) Fellah, M.; Santen, R.; Onal, I. *Catal. Lett.* **2011**, *141*, 762.
- (855) Fellah, M.; Onal, I. *Catal. Lett.* **2012**, *142*, 22.

- (856) Trushin, E. V.; Zilberberg, I. L. *Chem. Phys. Lett.* **2013**, *560*, 37.
- (857) Oymak, H.; Erkoç, S. *Int. J. Mod. Phys. B* **2012**, *26*, 1230003.
- (858) Zhao, H. X.; Chen, X. S.; Dong, R. B.; Lu, W. *J. Nanosci. Nanotechnol.* **2012**, *12*, 138.
- (859) Catlow, C. R. A.; Bromley, S. T.; Hamad, S.; Mora-Fonz, M.; Sokol, A. A.; Woodley, S. M. *Phys. Chem. Chem. Phys.* **2010**, *12*, 786.
- (860) Catlow, C. R. A.; French, S. A.; Sokol, A. A.; Al-Sunaidi, A. A.; Woodley, S. M. *J. Comput. Chem.* **2008**, *29*, 2234.
- (861) Lai, W. J. *J. Mol. Struct. (THEOCHEM)* **1992**, *257*, 217.
- (862) Martins, J. B. L.; Andrés, J.; Longo, E.; Taft, C. A. *J. Mol. Struct. (THEOCHEM)* **1995**, *330*, 301.
- (863) Matxain, J. M.; Fowler, J. E.; Ugalde, J. M. *Phys. Rev. A* **2000**, *62*, 053201.
- (864) Matxain, J. M.; Mercero, J. M.; Fowler, J. E.; Ugalde, J. M. *J. Am. Chem. Soc.* **2003**, *125*, 9494.
- (865) Lü, X.; Xu, X.; Wang, N.; Zhang, Q.; Ehara, M.; Nakatsuji, H. *Chem. Phys. Lett.* **1998**, *291*, 445.
- (866) Staemmler, V.; Fink, K.; Meyer, B.; Marx, D.; Kunat, M.; Gil Girol, S.; Burghaus, U.; Wöll, C. *Phys. Rev. Lett.* **2003**, *90*, 106102.
- (867) Lopes Martins, J. B.; Longo, E.; Rodríguez Salmon, O. D.; Espinoza, V. A. A.; Taft, C. A. *Chem. Phys. Lett.* **2004**, *400*, 481.
- (868) Fink, K. *Phys. Chem. Chem. Phys.* **2006**, *8*, 1482.
- (869) Liu, H.; Wang, S.; Zhou, G.; Wu, J.; Duan, W. *J. Chem. Phys.* **2006**, *124*.
- (870) Jain, A.; Kumar, V.; Kawazoe, Y. *Comput. Mater. Sci.* **2006**, *36*, 258.
- (871) Reber, A. C.; Khanna, S. N.; Hunjan, J. S.; Beltrán, M. R. *Chem. Phys. Lett.* **2006**, *428*, 376.
- (872) Reber, A. C.; Khanna, S. N.; Hunjan, J. S.; Beltran, M. R. *Eur. Phys. J. D* **2007**, *43*, 221.
- (873) Steudel, R.; Steudel, Y. *Chem.—Eur. J.* **2006**, *12*, 8589.
- (874) Wang, B. L.; Nagase, S.; Zhao, J. J.; Wang, G. H. *J. Phys. Chem. C* **2007**, *111*, 4956.
- (875) Wang, B. L.; Wang, X. Q.; Chen, G. B.; Nagase, S. G.; Zhao, J. *J. Chem. Phys.* **2008**, *128*, 144710.
- (876) Wang, B.; Wang, X.; Zhao, J. *J. Phys. Chem. C* **2010**, *114*, 5741.
- (877) Li, C.; Guo, W.; Kong, Y.; Gao, H. *Appl. Phys. Lett.* **2007**, *90*, 223102.
- (878) Zhao, M.; Xia, Y.; Tan, Z.; Liu, X.; Mei, L. *Phys. Lett. A* **2007**, *372*, 39.
- (879) Carrasco, J.; Illas, F.; Bromley, S. T. *Phys. Rev. Lett.* **2007**, *99*, 235502.
- (880) Zhu, Z.; Chutia, A.; Sahnoun, R.; Koyama, M.; Tsuboi, H.; Hatakeyama, N.; Endou, A.; Takaba, H.; Kubo, M.; Del Carpio, C. A.; Miyamoto, A. *Jpn. J. Appl. Phys.* **2008**, *47*, 2999.
- (881) Al-Sunaidi, A. A.; Sokol, A. A.; Catlow, C. R. A.; Woodley, S. M. *J. Phys. Chem. C* **2008**, *112*, 18860.
- (882) Sokol, A. A.; Catlow, C. R. A.; Miskufova, M.; Shevlin, S. A.; Al-Sunaidi, A. A.; Walsh, A.; Woodley, S. M. *Phys. Chem. Chem. Phys.* **2010**, *12*, 8438.
- (883) Woodley, S. B.; Sokol, A. A.; Catlow, C. R. A.; Al-Sunaidi, A. A.; Woodley, S. M. *J. Phys. Chem. C* **2013**, *117*, 27127.
- (884) Cheng, X.; Li, F.; Zhao, Y. *J. Mol. Struct. (THEOCHEM)* **2009**, *894*, 121.
- (885) Chen, Q.; Wang, J. *Chem. Phys. Lett.* **2009**, *474*, 336.
- (886) Hidalgo, M. A. F.; Jimenez, D. B.; Glossman-Mitnik, D. *J. Mol. Struct. (THEOCHEM)* **2010**, *957*, 100.
- (887) Flores-Hidalgo, M. A.; Barraza-Jiménez, D.; Glossman-Mitnik, D. *Comput. Theor. Chem.* **2011**, *965*, 154.
- (888) Flores-Hidalgo, M. A.; Glossman-Mitnik, D.; Galvan, D. H.; Barraza-Jimenez, D. *J. Chin. Chem. Soc.* **2013**, *60*, 1082.
- (889) Kaewruksa, B.; Ruangpornvisuti, V. *J. Mol. Struct.* **2011**, *994*, 276.
- (890) Kaewruksa, B.; Pipornpong, W.; Wanno, B.; Ruangpornvisuti, V. *Comput. Theor. Chem.* **2013**, *1020*, 100.
- (891) Yong, Y.; Song, B.; He, P. *J. Phys. Chem. C* **2011**, *115*, 6455.
- (892) Yong, Y. L.; Wang, Z.; Liu, K.; Song, B.; He, P. M. *Comput. Theor. Chem.* **2012**, *989*, 90.
- (893) Shewale, V.; Joshi, P.; Mukhopadhyay, S.; Deshpande, M.; Pandey, R.; Hussain, S.; Karna, S. P. *J. Phys. Chem. C* **2011**, *115*, 10426.
- (894) Azpiroz, J. M.; Mosconi, E.; Angelis, F. D. *J. Phys. Chem. C* **2011**, *115*, 25219.
- (895) Beheshtian, J.; Peyghan, A. A.; Bagheri, Z. *Appl. Surf. Sci.* **2012**, *258*, 8171.
- (896) Mallocci, G.; Chiodo, L.; Rubio, A.; Mattoni, A. *J. Phys. Chem. C* **2012**, *116*, 8741.
- (897) Caddeo, C.; Mallocci, G.; De Angelis, F.; Colombo, L.; Mattoni, A. *Phys. Chem. Chem. Phys.* **2012**, *14*, 14293.
- (898) Chang, J.; Waclawik, E. R. *J. Nanopart. Res.* **2012**, *14*, 1012.
- (899) Nanavati, S. P.; Sundararajan, V.; Mahamuni, S.; Ghaisas, S. V.; Kumar, V. *Phys. Rev. B* **2012**, *86*, 205320.
- (900) Farmanzadeh, D.; Tabari, L. *Comput. Theor. Chem.* **2013**, *1016*, 1.
- (901) Baei, M. T. *J. Cluster Sci.* **2013**, *24*, 749.
- (902) Baei, M. T.; Peyghan, A. A.; Bagheri, Z. *C. R. Chim.* **2013**, *16*, 122.
- (903) Tayebee, R.; Zamand, N.; Hosseini-nasr, A.; Kargar Razi, M. *J. Mol. Struct.* **2014**, *1065–1066*, 135.
- (904) Yakuphanoglu, F.; Caglar, M.; Caglar, Y.; Ilican, S. *J. Alloys Compd.* **2010**, *506*, 188.
- (905) Chang, J.; Todkar, V. V.; Mane, R. S.; Ham, D.; Ganesh, T.; Han, S. H. *Physica E* **2009**, *41*, 1741.
- (906) Salunkhe, R. R.; Dhawale, D. S.; Gujar, T. P.; Lokhande, C. D. *Mater. Res. Bull.* **2009**, *44*, 364.
- (907) Salunkhe, R. R.; Dhawale, D. S.; Dubal, D. P.; Lokhande, C. D. *Sens. Actuators, B* **2009**, *140*, 86.
- (908) Srinivasaraghavan, R.; Chandiramouli, R.; Jeyaprakash, B. G.; Seshadri, S. *Spectrochim. Acta, Part A* **2013**, *102*, 242.
- (909) Wang, C.; Xu, S.; Cui, Y. *New J. Chem.* **2013**, *37*, 3303.
- (910) Tossell, J. A. *J. Phys. Chem. A* **2006**, *110*, 2571.
- (911) Lopez, X.; Carbo, J. J.; Bo, C.; Poblet, J. M. *Chem. Soc. Rev.* **2012**, *41*, 7537.
- (912) Gao, J.; Liu, X.; Liu, Y.; Yu, L.; Feng, Y.; Chen, H.; Li, Y.; Rakesh, G.; Huan, C. H. A.; Sum, T. C.; Zhao, Y.; Zhang, Q. *Dalton Trans.* **2012**, *41*, 12185.
- (913) Miró, P.; Ling, J.; Qiu, J.; Burns, P. C.; Gagliardi, L.; Cramer, C. J. *Inorg. Chem.* **2012**, *51*, 8784.
- (914) Ma, T.-Y.; Ma, N.-N.; Yan, L.-K.; Guan, W.; Su, Z.-M. *J. Mol. Graphics Modell.* **2013**, *40*, 110.
- (915) Ma, T.-Y.; Ma, N. N.; Yan, L.-K.; Zhang, T.; Su, Z.-M. *J. Phys. Chem. A* **2013**, *117*, 10783.
- (916) Zhang, T.; Ma, N.; Yan, L.; Wen, S.; Ma, T.; Su, Z. *J. Mol. Graphics Modell.* **2013**, *46*, 59.
- (917) Zhang, T.; Ma, N.; Yan, L.; Wen, S.; Su, Z. *Chem. Phys. Lett.* **2013**, *557*, 123.
- (918) Zhang, T.; Ma, N.; Yan, L.; Ma, T.; Su, Z. *Dyes Pigm.* **2014**, *106*, 105.
- (919) Papulovskiy, E.; Shubin, A. A.; Terskikh, V. V.; Pickard, C. J.; Lapina, O. B. *Phys. Chem. Chem. Phys.* **2013**, *15*, 5115.
- (920) Lapina, O. B.; Khabibulin, D. F.; Romanenko, K. V.; Gan, Z.; Zuev, M. G.; Krasil'nikov, V. N.; Fedorov, V. E. *Solid State Nucl. Magn. Reson.* **2005**, *28*, 204.
- (921) Liu, C.-G.; Guan, X.-H. *Mol. Phys.* **2013**, *111*, 3733.
- (922) Melcamu, Y. Y.; Wen, S.; Yan, L.; Zhang, T.; Su, Z. *Mol. Simul.* **2012**, *39*, 214.
- (923) Ravelli, D.; Dondi, D.; Fagnoni, M.; Albini, A.; Bagno, A. *Phys. Chem. Chem. Phys.* **2013**, *15*, 2890.
- (924) De Luca, G.; Bisignano, F.; Figoli, A.; Galiano, F.; Furia, E.; Mancuso, R.; Saoncella, O.; Carraro, M.; Bonchio, M.; Gabriele, B. *J. Phys. Chem. B* **2014**, *118*, 2396.
- (925) Nishimoto, Y.; Yokogawa, D.; Yoshikawa, H.; Awaga, K.; Irle, S. *J. Am. Chem. Soc.* **2014**, *136*, 9042.
- (926) Chu, H.-Y.; Liu, Z.-X.; Qiu, G.-L.; Kong, D.-G.; Wu, S.-X.; Li, Y.-C.; Du, Z.-L. *Chin. Phys. B* **2008**, *17*, 2478.
- (927) Joswig, J.-O.; Springborg, M.; Seifert, G. *J. Phys. Chem. B* **2000**, *104*, 2617.

- (928) Sangthong, W.; Limtrakul, J.; Illasa, F.; Bromley, S. T. *Nanoscale* **2010**, *2*, 72.
- (929) Karthikeyan, S.; Deepika, E.; Murugan, P. *J. Phys. Chem. C* **2012**, *116*, 5981.
- (930) Joswig, J.-O.; Seifert, G.; Niehaus, T. A.; Springborg, M. *J. Phys. Chem. B* **2003**, *107*, 2897.
- (931) Gutsev, G. L.; O'Neal, R. H., Jr.; Belay, K. G.; Weatherford, C. A. *Chem. Phys.* **2010**, *368*, 113.
- (932) Jimenez-Izal, E.; Matxain, J. M.; Piris, M.; Ugalde, J. M. *Phys. Chem. Chem. Phys.* **2012**, *14*, 9676.
- (933) Troparevsky, M. C.; Chelikowsky, J. R. *J. Chem. Phys.* **2001**, *114*, 943.
- (934) Troparevsky, M. C.; Kronik, L.; Chelikowsky, J. R. *Phys. Rev. B* **2001**, *65*, 033311.
- (935) Jose, R.; Zhanpeisov, N. U.; Fukumura, H.; Baba, Y.; Ishikawa, M. *J. Am. Chem. Soc.* **2006**, *128*, 629.
- (936) Nguyen, K. A.; Day, P. N.; Pachter, R. *J. Phys. Chem. C* **2010**, *114*, 16197.
- (937) Nguyen, K. A.; Pachter, R.; Day, P. N. *J. Chem. Theory Comput.* **2013**, *9*, 3581.
- (938) Deglmann, P.; Ahlrichs, R.; Tsereteli, K. *J. Chem. Phys.* **2002**, *116*, 1585.
- (939) Sanville, E.; Burnin, A.; BelBruno, J. *J. J. Phys. Chem. A* **2006**, *110*, 2378.
- (940) Sarkar, P.; Springborg, M. *Phys. Rev. B* **2003**, *68*, 235409.
- (941) Troparevsky, M. C.; Kronik, L.; Chelikowsky, J. R. *J. Chem. Phys.* **2003**, *119*, 2284.
- (942) Nagaoka, M.; Ishii, S.; Noguchi, Y.; Ohno, K. *Mater. Trans.* **2008**, *49*, 2420.
- (943) Isborn, C. M.; Kilina, S. V.; Li, X.; Prezhdo, O. V. *J. Phys. Chem. C* **2008**, *112*, 18291.
- (944) Chen, L.; Bao, H.; Tan, T.; Prezhdo, O. V.; Ruan, X. *J. Phys. Chem. C* **2011**, *115*, 11400.
- (945) Kilina, S. V.; Neukirch, A. J.; Habenicht, B. F.; Kilin, D. S.; Prezhdo, O. V. *Phys. Rev. Lett.* **2013**, *110*, 180404.
- (946) Jha, P. C.; Seal, P.; Sen, S.; Ogren, H.; Chakrabarti, S. *Comput. Mater. Sci.* **2008**, *44*, 728.
- (947) Sriram, S.; Chandiramouli, R. *Res. Chem. Intermed.* **2013**, *1*.
- (948) Wu, Z.; Zhang, Y.; Huang, S.; Zhang, S. *Comput. Mater. Sci.* **2013**, *68*, 238.
- (949) Karamanis, P.; Pouchan, C. *Chem. Phys. Lett.* **2009**, *474*, 162.
- (950) Wang, J.; Ma, L.; Zhao, J.; Jackson, K. A. *J. Chem. Phys.* **2009**, *130*, 214307.
- (951) Ma, L.; Wang, J.; Wang, G. *Chem. Phys. Lett.* **2012**, *552*, 73.
- (952) Matxain, J. M.; Mercero, J. M.; Fowler, J. E.; Ugalde, J. M. *J. Phys. Chem. A* **2004**, *108*, 10502.
- (953) Chung, S.-Y.; Lee, S.; Liu, C.; Neuhauser, D. *J. Phys. Chem. B* **2008**, *113*, 292.
- (954) Kim, H.-S.; Jang, S.-W.; Chung, S.-Y.; Lee, S.; Lee, Y.; Kim, B.; Liu, C.; Neuhauser, D. *J. Phys. Chem. B* **2009**, *114*, 471.
- (955) Saraf, D.; Kshirsagar, A. *arXiv.org, e-Print Arch., Condens. Matter* **2013**, *1*.
- (956) Puzder, A.; Williamson, A. J.; Zaitseva, N.; Galli, G.; Manna, L.; Alivisatos, A. P. *Nano Lett.* **2004**, *4*, 2361.
- (957) Yang, P.; Tretiak, S.; Ivanov, S. *J. Cluster Sci.* **2011**, *22*, 405.
- (958) Del Ben, M.; Havenith, R. W. A.; Broer, R.; Stener, M. *J. Phys. Chem. C* **2011**, *115*, 16782.
- (959) Kuznetsov, A. E.; Balamurugan, D.; Skourtis, S. S.; Beratan, D. *N. J. Phys. Chem. C* **2012**, *116*, 6817.
- (960) Kuznetsov, A. E.; Beratan, D. N. *J. Phys. Chem. C* **2014**, *118*, 7094.
- (961) Wang, X.; Zeng, Q.; Shi, J.; Jiang, G.; Yang, M.; Liu, X.; Enright, G.; Yu, K. *Chem. Phys. Lett.* **2013**, *568–569*, 125.
- (962) Puzder, A.; Williamson, A. J.; Gygi, F.; Galli, G. *Phys. Rev. Lett.* **2004**, *92*, 217401.
- (963) Xu, S.; Wang, C.; Cui, Y. *J. Mol. Model.* **2010**, *16*, 469.
- (964) Nadler, R.; Sanz, J. *Theor. Chem. Acc.* **2013**, *132*, 1.
- (965) Alnemrat, S.; Ho Park, Y.; Vasiliev, I. *Physica E* **2014**, *57*, 96.
- (966) Azpiroz, J. M.; Matxain, J. M.; Infante, I.; Lopez, X.; Ugalde, J. *M. Phys. Chem. Chem. Phys.* **2013**, *15*, 10996.
- (967) Kilina, S.; Ivanov, S.; Tretiak, S. *J. Am. Chem. Soc.* **2009**, *131*, 7717.
- (968) Fischer, S. A.; Crotty, A. M.; Kilina, S. V.; Ivanov, S. A.; Tretiak, S. *Nanoscale* **2012**, *4*, 904.
- (969) Kilina, S.; Velizhanin, K. A.; Ivanov, S.; Prezhdo, O. V.; Tretiak, S. *ACS Nano* **2012**, *6*, 6515.
- (970) Abueela, A. M.; Mohamed, T. A.; Prezhdo, O. V. *J. Phys. Chem. C* **2012**, *116*, 14674.
- (971) Albert, V. V.; Ivanov, S. A.; Tretiak, S.; Kilina, S. V. *J. Phys. Chem. C* **2011**, *115*, 15793.
- (972) Koposov, A. Y.; Cardolaccia, T.; Albert, V.; Badaeva, E.; Kilina, S.; Meyer, T. J.; Tretiak, S.; Sykora, M. *Langmuir* **2011**, *27*, 8377.
- (973) Tan, Y.; Jin, S.; Hamers, R. J. *J. Phys. Chem. C* **2012**, *117*, 313.
- (974) Lopez del Puerto, M.; Tiago, M.; Chelikowsky, J. *Phys. Rev. B* **2008**, *77*, 045404.
- (975) Junkermeier, C.; Lewis, J.; Bryant, G. *Phys. Rev. B* **2008**, *77*, 205125.
- (976) Eichkorn, K. *Chem. Phys. Lett.* **1998**, *288*, 235.
- (977) Gurin, V. S. *SPIE-Int. Soc. Opt. Eng.* **2004**, 216.
- (978) Gurin, V. S. *Surf. Rev. Lett.* **2000**, *7*, 161.
- (979) Aldongarov, A.; Irgibaeva, I.; Hermansson, K.; Agren, H. *Mol. Phys.* **2014**, *112*, 674.
- (980) Matxain, J. M.; Fowler, J. E.; Ugalde, J. M. *Phys. Rev. A* **2000**, *61*, 053201.
- (981) Lalsare, D.; Kshirsagar, A. *Bull. Mater. Sci.* **2012**, *35*, 1055.
- (982) Burnin, A.; Sanville, E.; BelBruno, J. *J. J. Phys. Chem. A* **2005**, *109*, 5026.
- (983) Wang, C.; Xu, S.; Ye, L.; Lei, W.; Cui, Y. *J. Struct. Chem.* **2010**, *21*, 1215.
- (984) Zwijnenburg, M. A.; Sousa, C.; Illas, F.; Bromley, S. T. *J. Chem. Phys.* **2011**, *134*, 064511.
- (985) Zwijnenburg, M. A.; Illas, F.; Bromley, S. T. *Phys. Chem. Chem. Phys.* **2011**, *13*, 9311.
- (986) Spano, E.; Hamad, S.; Catlow, C. R. A. *J. Phys. Chem. B* **2003**, *107*, 10337.
- (987) Hamad, S.; Catlow, C. R. A.; Spano, E.; Matxain, J. M.; Ugalde, J. M. *J. Phys. Chem. B* **2005**, *109*, 2703.
- (988) Hamad, S.; Catlow, C. R. A. *J. Cryst. Growth* **2006**, *294*, 2.
- (989) Pal, S.; Goswami, B.; Sarkar, P. *J. Chem. Phys.* **2005**, *123*, 044311.
- (990) Pal, S.; Goswami, B.; Sarkar, P. *J. Phys. Chem. C* **2008**, *112*, 6307.
- (991) Pal, S.; Sharma, R.; Goswami, B.; Sarkar, P.; Bhattacharyya, S. P. *J. Chem. Phys.* **2009**, *130*, 214703.
- (992) Woodley, S. M.; Sokol, A. A.; Catlow, C. R. A. *Z. Anorg. Allg. Chem.* **2004**, *630*, 2343.
- (993) Spanó, E.; Hamad, S.; Richard, C.; Catlow, A. *Chem. Commun.* **2004**, *864*.
- (994) Zwijnenburg, M. A. *Nanoscale* **2011**, *3*, 3780.
- (995) Zwijnenburg, M. A. *Phys. Chem. Chem. Phys.* **2013**, *15*, 11119.
- (996) Zwijnenburg, M. A. *Nanoscale* **2012**, *4*, 3711.
- (997) Pal, S.; Sharma, R.; Goswami, B.; Sarkar, P. *Chem. Phys. Lett.* **2009**, *467*, 365.
- (998) Kim, S.-W.; Kim, M.; Lee, W. Y.; Hyeon, T. *J. Am. Chem. Soc.* **2002**, *124*, 7642.
- (999) Hua, Z.; Shuyuan, Z.; Shuan, P.; Gongpu, L.; Jianguo, H. *Nanotechnology* **2004**, *15*, 945.
- (1000) Yan, C.; Xue, D. *J. Phys. Chem. B* **2006**, *110*, 7102.
- (1001) Tartaj, P.; del Puerto Morales, M.; Veintemillas-Verdaguer, S.; González-Carreño, T.; Serna, C. J. *J. Phys. D: Appl. Phys.* **2003**, *36*, R182.
- (1002) Sanville, E.; Burnin, A.; BelBruno, J. *J. J. Phys. Chem. A* **2006**, *110*, 2378.
- (1003) Matxain, J. M.; Mercero, J. M.; Fowler, J. E.; Ugalde, J. M. *Phys. Rev. A* **2001**, *64*, 053201.
- (1004) Goswami, B.; Pal, S.; Sarkar, P.; Seifert, G.; Springborg, M. *Phys. Rev. B* **2006**, *73*, 205312.

- (1005) Goswami, B.; Pal, S.; Sarkar, P. *Phys. Rev. B* **2007**, *76*, 045323.
- (1006) Pekoz, R.; Erkoc, S. *Physica E* **2008**, *40*, 2921.
- (1007) Xu, S.; Wang, C.; Cui, Y. *J. Mol. Struct.* **2009**, *938*, 133.
- (1008) Wang, X. Q.; Clark, S. J.; Abram, R. A. *Phys. Rev. B* **2004**, *70*, 235328.
- (1009) Kuganathan, N.; Green, J. C. *Int. J. Quantum Chem.* **2008**, *108*, 797.
- (1010) BelBruno, J. J.; Sanville, E.; Burnin, A.; Muhangi, A. K.; Malyutin, A. *Chem. Phys. Lett.* **2009**, *478*, 132.
- (1011) Seeburrun, N.; Soopramanien, M.; Abdallah, H.; Archibong, E.; Ramasami, P. *J. Mater. Sci.* **2012**, *47*, 4332.
- (1012) Hachiya, K. *J. Non-Cryst. Solids.* **2002**, *312–314*, 566.
- (1013) Hachiya, K. *J. Non-Cryst. Solids.* **2003**, *321*, 217.
- (1014) Holomb, R.; Mitsa, V.; Johansson, P. *J. Optoelectron. Adv. Mater.* **2005**, *7*, 1881.
- (1015) Shpotyuk, O.; Golovchak, R.; Boyko, V.; Kozyukhin, S. *Phys. Status Solidi C* **2010**, *7*, 921.
- (1016) Gurin, V.; Shpotyuk, O.; Boyko, V. *Physics, Chemistry and Applications of Nanostructures - Proceedings of the International Conference Nanomeeting*, 2013; p 158.
- (1017) Mateleshko, N.; Mitsa, V.; Holomb, R. *Phys. B (Amsterdam, Neth.)* **2004**, *349*, 30.
- (1018) BelBruno, J. J.; Burnin, A. *Phys. Chem. Chem. Phys.* **2010**, *12*, 8557.
- (1019) He, J.; Liu, C.; Li, F.; Sa, R.; Wu, K. *Chem. Phys. Lett.* **2008**, *457*, 163.
- (1020) Zeng, H.; Schelly, Z. A.; Ueno-Noto, K.; Marynick, D. S. *J. Phys. Chem. A* **2005**, *109*, 1616.
- (1021) Xing, H.; Xu, S.; Ding, Z.; Huang, Y.; Chen, X.; Wang, J.; Shi, Y. *Phys. Lett.* **2008**, *372*, 4694.
- (1022) Koirala, P.; Kiran, B.; Kandalam, A. K.; Fancher, C. A.; de Clercq, H. L.; Li, X.; Bowen, K. H. *J. Chem. Phys.* **2011**, *135*, 134311/1.
- (1023) Kiran, B.; Kandalam, A. K.; Rallabandi, R.; Koirala, P.; Li, X.; Tang, X.; Wang, Y.; Fairbrother, H.; Gantefor, G.; Bowen, K. *J. Chem. Phys.* **2012**, *136*, 024317/1.
- (1024) Zeng, Q.; Shi, J.; Jiang, G.; Yang, M.; Wang, F.; Chen, J. *J. Chem. Phys.* **2013**, *139*, 104302.
- (1025) Prezhdo, O. V. *Chem. Phys. Lett.* **2008**, *460*, 1.
- (1026) Kilina, S. V.; Kilin, D. S.; Prezhdo, O. V. *ACS Nano* **2009**, *3*, 93.
- (1027) Kilina, S. V.; Kilin, D. S.; Prezhdo, V. V.; Prezhdo, O. V. *J. Phys. Chem. C* **2011**, *115*, 21641.
- (1028) Fischer, S. A.; Isborn, C. M.; Prezhdo, O. V. *Chem. Sci.* **2011**, *2*, 400.
- (1029) Gong, X. X.; Du, J. G.; Jiang, G. *Acta Phys. Chim. Sin.* **2010**, *26*, 1669.
- (1030) Mulugeta, Y.; Woldegehebriel, H. *Comput. Theor. Chem.* **2014**, *1039*, 40.